Title
A Molecular Approach for Dechiphering and Designing Cobalt Water Oxidation Catalysts

Author
Nguyen, Andy

Publication Date
2016

Peer reviewed|Thesis/dissertation

A Molecular Approach for Deciphering and Designing Cobalt Water Oxidation Catalysts

By

Andy Ich Nguyen

A dissertation submitted in partial satisfaction of the requirements for the degree of

Doctor of Philosophy
in
Chemistry

in the Graduate Division
of the
University of California, Berkeley

Committee in charge:
Prof. T. Don Tilley (Chair)
Prof. Jeffrey R. Long
Prof. John Arnold
Prof. Alexis T. Bell

Summer 2016

Abstract

A Molecular Approach for Deciphering and Designing Cobalt Water Oxidation Catalysts

By

Andy Ich Nguyen

Doctor of Philosophy in Chemistry
University of California, Berkeley
Professor T. Don Tilley, Chair

Chapter 1: **Efficient C-H Bond Activations *via* O_2 Cleavage by a Dianionic Cobalt(II) Complex**

A dianionic, square planar cobalt(II) complex reacts with O_2 in the presence of acetonitrile to give a cyanomethylcobalt(III) complex formed by C–H bond cleavage. Interestingly, the group-transfer reagents PhIO, IO_4^-, and *p*-tolyl azide react similarly to give the same cyanomethylcobalt(III) complex. Competition studies with various hydrocarbon substrates indicate that the rate of C–H bond cleavage greatly depends on the pK_a of the C–H bond, rather than on the C–H bond dissociation energy. Kinetic isotope experiments reveal a moderate KIE value of *ca.* 3.5 using either O_2 or PhIO. The possible involvement of a Co(IV)-oxo species in this chemistry is discussed.

Chapter 2: **Mechanistic Investigations of Water Oxidation by a Cobalt Oxide Analogue: Evidence for a Highly Oxidized Intermediate and Exclusive Terminal Oxo Participation**

Artificial photosynthesis (AP) promises to replace our dependence on fossil energy resources *via* conversion of sunlight into sustainable, carbon-neutral fuels. However, large-scale AP implementation remains impeded by a dearth of cheap, efficient catalysts for the oxygen evolution reaction (OER). Cobalt oxide materials can catalyze the OER and are potentially scalable due to the abundance of cobalt in the earth's crust; but unfortunately, the activity of these materials is insufficient for practical AP implementation. Attempts to improve cobalt oxide's activity have been stymied by limited mechanistic understanding that stems from the inherent difficulty of characterizing structure and reactivity at surfaces of heterogeneous materials. While previous studies on cobalt oxide revealed the intermediacy of the unusual Co(IV) oxidation state, much remains unknown, including whether bridging or terminal oxo ligands form O_2 and what the relevant oxidation states are. We have addressed these issues by employing a homogenous model for cobalt oxide, the $[Co^{III}_4]$ cubane ($Co_4O_4(OAc)_4py_4$, py = pyridine, OAc = acetate), that can be oxidized to the $[Co^{IV}Co^{III}_3]$ state, and upon addition of one equivalent of sodium hydroxide, the $[Co^{III}_4]$ cubane is regenerated with stoichiometric formation of O_2. Oxygen isotopic labelling experiments demonstrate that the cubane core remains intact during this stoichiometric oxygen evolution reaction, implying that terminal oxo ligands are responsible for forming O_2. The OER is also examined with stopped-flow UV-visible spectroscopy, and its kinetic behavior is modelled, to surprisingly reveal that O_2 formation requires disproportionation of the $[Co^{IV}Co^{III}_3]$ state to generate an even higher oxidation state, formally $[Co^{V}Co^{III}_3]$ or

$[Co^{IV}_2Co^{III}_2]$. The mechanistic understanding provided by these results should accelerate the development of OER catalysts leading to increasingly efficient AP systems.

Chapter 3: **Prediction of redox potentials for Co_4O_4 cubanes over a 1400 mV range: Implications for the feasibility of formal Co(V)–Oxo species**

Synthetic methods were developed for generating new Co_4O_4 cubanes comprising highly electron-deficient ligands, electron-rich ligands, and ligands with secondary hydrogen-bond donors. The synthetic methods also allowed for cubanes with mixed carboxylates. A two-dimensional linear free energy relationship (LFER) was found to accurately predict the $[Co^{III}_4O_4]^{4+}/[Co^{IV}Co^{III}_3O_4]^{5+}$ and $[Co^{IV}Co^{III}_3O_4]^{5+}/[Co^{IV}_2Co^{III}_2O_4]^{6+}$ redox potentials as a function of the pK_a of the ligands bound to the cubane. These redox potentials span a maximum of 1420 mV. Comparing cubanes containing intramolecular hydrogen-bonds with those lacking hydrogen-bonds allowed for the rationalization of the different redox potentials previously seen for the same cubane in water versus polar aprotic solvents. Finally, application of the LFER to the proposed, non-isolable intermediates in cubane-mediated water oxidation allowed estimation of their redox potentials and support for their plausibility.

Chapter 4: **Tunable, site-isolated Co_4O_4 oxygen-evolution catalysts uniformly dispersed within porous frameworks**

Three-dimensional porous coordination-polymers composed of Co_4O_4 cubanes and several organic linkers were synthesized as new, tunable heterogeneous oxygen evolution reaction (OER) catalysts. Frameworks were synthesized either by substituting the acetate ligands of the cubane, $Co_4O_4(OAc)_4py_4$ (OAc = acetate, py = pyridine), with tricarboxylic acids, or by substituting the pyridine linkers with tripyridyl ligands. Although these solids lack long-range periodicity, their structures were well characterized by a suite of techniques, including X-ray absorption spectroscopy (XAS), extended x-ray absorption fine structure (EXAFS), and pair-distribution function analysis (PDF). Evidence for their high surface areas come from thermogravimetric analysis and gas sorption data. The tripyridyl-linked frameworks were significantly more stable than the tricarboxylate-linked frameworks towards the high pH conditions used in the OER. Stoichiometric O_2 evolution occurs by addition of the oxidized coordination-polymers into pH 14 solutions, demonstrating the retention of the molecular cubane precursor's OER reactivity. Finally, thin films of these polymers on glassy carbon perform as OER electrocatalysts. Their overpotential is tuned by the basicity of the linker ligands, demonstrating these as tuneable heterogeneous OER electrocatalysts.

Chapter 5: **Carboxylate-Supported Mixed Manganese-Cobalt Oxido Cubane and Dangler Clusters**

In a single step, manganese(IV) is readily incorporated into an oxido-cobalt(III) scaffold by rational, self-assembly of permanganate, cobalt(II) acetate and pyridine to form the cubane oxo cluster $MnCo_3O_4(OAc)_5py_3$ (OAc = acetate, py = pyridine), **1-OAc**. The electronic properties of the cubane are tuned by exchange of the μ^1-acetate ligand for Cl^- (**1-Cl**), NO_3^- (**1-NO$_3$**), and pyridine (**[1-py]$^+$**). Addition of a fifth Co(II) to **1-OAc** forms $MnCo_4O_4(OAc)_6(NO_3)py_3$ (**2**), reminiscent of the "dangler" motif of photosystem II. The electronic states of these clusters were examined by electron paramagnetic spectroscopy (EPR) and SQUID magnetometry. Cyclic voltammetry of the clusters in organic solvents demonstrates an accessible $[MnCo_3O_4]^{5+}/[MnCo_3O_4]^{6+}$ redox couple that is modulated by the nature of the ligand on Mn. Yet, DFT showed redox process occur at a Co-ion rather than the Mn-ion. Interestingly, the addition of the dangler ion gave four accessible redox states, perhaps suggesting a role for the dangler ion found in photosystem II.

To my teachers, my friends, and my family

Table of Contents

Acknowledgements

As I write this Ph.D. thesis, I realize this means I will soon be able to say to others, "That's *Dr.* Nguyen to you, sir/ma'am!" At last, I will join the upper echelons of society. It was a team effort to get to this point, and if it weren't for the encouragement of many people, I might not have even pursued this path. The following list contains those most impactful people in shaping me as a chemist, but is nowhere near comprehensive.

I cannot thank my parents enough for always fostering a love of knowledge and learning, and an expectation of excellence and hard work. They supported my obsessions, willingly or begrudgingly, whether it was with dinosaurs, astronomy, chemistry or art, skateboarding, and music. I will always appreciate them allowing me to setup a sketchy chemistry lab in the garage (moved from the original location in my bedroom closet), and patiently dealing with the occasional smoke and noxious fumes. From them I learned that it was important to do what you love, as long as you do it well, and do it creatively.

I am deeply indebted to the teachers in my life. I was never that straight-A's, overachieving student, but my high-school chemistry teacher, Dr. Beverley Matsuda, believed in me more than any other teacher. Before I started college, she said to me, "If you are not majoring in chemistry, I'm going to have to change your mind." At that time, I had no solidified career goals, but her statement helped defined my identity. Almost equally influential was professor Alan Heyduk, whom I worked for at UCI. He set expectations very high, and in that way, instilled in me how to be a rigorous chemist and, in the end, the confidence to pursue a career in chemistry.

Arriving at Berkeley, I feel lucky to have chosen to work in the lab of T. Don Tilley. The academic freedom in his lab nourished creativity and independence. As an advisor, he was supportive – allowing a safe environment for new and crazy ideas – while critical enough to force those ideas to their greatest potentials. Of my colleagues, I am most grateful to have met Kurt M. Van Allsburg, fellow collaborator and good friend, who has always entertained and enabled my craziest ideas. And of course, many thanks to Rosemary Tilley, for keeping us absent-minded lab rats from drowning in bureaucracy.

I am grateful for the opportunities to work with many collaborators (their names are listed in the chapters of the thesis). Their expertise and dedication made the science in each chapter more complete and more rigorous. Needless to say, this work could not have been done without them.

I thank the incredible staff at Berkeley, Tony Iavarone, Kathy Durkin, and Antonio DiPasquale, who provided invaluable assistance.

Finally, it is really the friends who help you get by. I'm forever glad to have befriended Pascual Oña-Burgos, Donatela Bellone, Ben Kriegel, Felix Neumeyer, and Gavin Kiel. My greatest and warmest acknowledgement goes to Julia Oktawiec, with whom I truly learned that happiness does make all aspects of life, including work, more fulfilling and exciting.

Preface

Why do we still use pollutive fossil fuels instead of cleaner and more abundant solar energy? We depend on fossil fuels to produce energy for nearly all the essentials of modern civilization, such as the production of industrial goods, electricity, and transportation. Not considering that fossil fuels are a limited resource, the burning of fossil fuels comes at a deadly cost: the massive release of CO_2, a potent greenhouse gas, into our atmosphere, drastically altering our planet's climate. If the status quo is upheld, Earth will no longer be a desirable habitat for us. But fossil fuels are so plentiful, easy to use, and easy to transport. While the energy from the sun is indeed many-fold more plentiful and infinitely cleaner, we do not know of a good way to capture and store that energy. Sunlight is intermittent, but modern society never sleeps.

Many organisms, such as bacteria and plants, have already mastered the conversion of sunlight into a storable form of energy. This marvelous process is called photosynthesis, and it works by first converting sunlight into an electrical current. The energy of this electrical current is funneled into water, an abundant resource, to make dioxygen (O_2) and hydrogen-equivalents. These hydrogen-equivalents are coupled with another abundant molecule, CO_2, to make fuel for these organisms. The net reaction is the conversion of water and CO_2 into O_2 and carbohydrates. Incredible molecular and supramolecular machines present inside these photosynthetic cells catalyze this deceptively simple reaction. Since its initial discovery over 200 years ago, we still do not completely understand how photosynthesis operates from a chemical standpoint. Thus, if only we can decipher the chemistries of photosynthesis, perhaps we may have a chance of adapting it for our own needs, and evolve civilization into an era of sustainability and environmental harmony.

Chemists, tasked with the goal of developing "artificial phototosynthesis" (AP), have discovered promising materials capable of turning light into fuels. In its simplest form, an AP device consists of a few materials: a photovoltaic for sunlight to electricity conversion, and catalysts that utilize the electrical energy to split water into storable fuels, O_2 and H_2. The efficiency of these materials, however, pales in comparison to that of natural photosynthesis, and the rate at which sunlight is converted into fuel is too much slow to meet the demands of modern technology. Of the several parts required in a basic AP device, the catalyst for oxidizing water into O_2 has the lowest efficiency, and is one of the main limiting factors for AP. The O_2-evolution reaction (OER) is also chemically the most demanding reaction, requiring the orchestrated transport of four electrons and four protons. No earth-abundant material has yet been found to catalyze the OER efficiently enough for a practical AP device. However, there are good leads. In theory, the power of chemistry should allow for the modification of these promising leads into more efficient catalysts. But, like the case with natural photosynthesis, we barely understand how these artificial, "simpler" catalysts work. Chemists cannot rationally modify a system that they do not fully understand.

It is the goal of this thesis to contribute to that necessary understanding. We begin with designing model systems simple enough that we can know almost everything about. Then we build up complexity, eventually converging to that of the real system. It is a slow method, but a surer one. We call this bottom-up approach the molecular approach, meaning that any material we wish to design, regardless of size or complexity, must be understood at its fundamental level – the molecular level. While materials can be described in terms of bulk properties (i.e. color, durability, shape, catalytic activity), it is the molecular building blocks of that material that determines those properties. Molecular knowledge is then the ultimate knowledge for creating new materials.

This thesis targets OER catalysts based on cobalt. Cobalt oxides (CoO_x) and its derivatives comprise one of the most active classes of OER catalysts. CoO_x are polymeric materials, with units of Co and O atoms in an infinitely extended lattice, and exist in many different phases and forms. These bulk materials are difficult to study and understand due to their heterogeneous nature, with ill-defined active sites. We address this issue using a molecular approach – synthesizing small molecular models of CoO_x, starting with models containing just one Co, building up to four Co atoms, and eventually applying these model systems to extended materials. With these models, we provide evidence for feasibility the elusive Co(IV)–oxo intermediate often proposed in OER, decipher the mechanism of OER by cobalt, and design new heterogeneous OER catalysts with well-defined active sites. Finally, molecular models were developed for the even more active OER catalysts, Mn-doped-CoO_x, demonstrating the generality of this approach. We hope the findings in this thesis emphasize the contributions that fundamental, molecular knowledge can provide for designing practical catalysts, particularly for one as important as the OER.

Chapter 1:

Efficient C-H Bond Activations *via* O_2 Cleavage by a Dianionic Cobalt(II) Complex*

---

* This work is based upon work previously published, included with permission from all authors:

Nguyen, A. I., Hadt, R. G., Solomon, E. I., Tilley, T. D. *Chem. Sci.,* **2014**, *5*, 2874-2878.

Author contributions: Andy I. Nguyen formulated the project, synthesized all materials, and performed mechanistic studies. Ryan G. Hadt and Edward I. Solomon (Stanford University) measured and analyzed all EPR spectra.

1.1 Introduction

An important challenge for the development of new catalytic oxidations is the utilization of O_2 from the air, as this reactant should enable the most atom-economical, cost effective and environmentally benign oxidations. In this context, the development of cobalt-based catalysts is particularly promising, since several types of homogeneous and heterogeneous cobalt catalysts are already known to utilize oxygen in oxidations of organic compounds.[1] Much of this chemistry is thought to proceed *via* peroxy intermediates that initiate the generation of organic radicals.[2] However, high-valent cobalt oxo intermediates have been postulated for certain oxidations, such as benzylic alcohol oxidation, amine oxidation, and epoxidation.[1] Despite abundant circumstantial evidence for cobalt-mediated O_2 cleavage, there has been no observation of a cobalt oxo species as the direct product of this type of O_2 activation. Notably, the generation of a cobalt(IV) oxo intermediate *via* O_2 cleavage would seem to be difficult given ligand field arguments,[3] and the fact that numerous cobalt(II) complexes have been shown to reversibly bind O_2 to give superoxo or μ-peroxo complexes without O_2 cleavage.[6]

This contribution describes attempts to promote O–O bond cleavage in a μ-peroxo intermediate to access a high-valent oxo species, with use of a tetraanionic ligand. The tetrananionic ligand ^{Br}HBA-Et (Scheme 1) provides a strong ligand field that features hard donor atoms, and ligands of this type have been shown to support a number of metal complexes in high oxidation states.[9] This approach has led to observation of clean C–H bond activations of acetonitrile and other hydrocarbons upon reaction of a dianionic cobalt(II) complex with O_2. Furthermore, the use of oxo- and imido-transfer agents is shown to produce reactive intermediates with similar characteristics, implying that putative cobalt(IV) oxo and imido complexes[5] may be generated in these cases. Most importantly, this report describes a cobalt system that utilizes O_2 cleavage in promoting unusual C–H bond activations.

1.2 Results and Discussion

Deprotonation of (^{Br}HBA-Et)H_4, *N*,*N*'-(ethane-1,2-diyl)bis(5-bromo-2-hydroxybenzamide), with four equivalents of KH in THF, followed by treatment with $CoCl_2$ and then salt metathesis with a tetraalkylammonium (^{n}Bu$_4$N$^+$ or Me$_4$N$^+$) chloride gave the dianionic complexes [^{n}Bu$_4$N]$_2$[(^{Br}HBA-Et)Co] ([^{n}Bu$_4$N]$_2$**1**) and [Me$_4$N]$_2$[(^{Br}HBA-Et)Co] ([Me$_4$N]$_2$**1**) as orange, crystalline solids in 58% and 47% yields, respectively (Scheme 1). The complex [^{n}Bu$_4$N]$_2$**1** is a low spin, S = 1/2 Co(II) complex, as demonstrated by the solution magnetic moment (1.98 μ_B, 298 K). A rhombic signal in the 77 K X-band EPR spectrum (g_1 = 1.956, g_2 = 2.29, g_3 = 3.15) with hyperfine coupling to the I = 7/2 ^{59}Co nucleus ($|A_1|$ = 81 MHz, $|A_2|$ = 285 MHz, $|A_3|$ = 300 MHz) is consistent with an $(xy)^2(z^2)^2(yz)^2(xz)^1$ or $(xy)^2(z^2)^2(xz)^2(yz)^1$ ground state (Supporting Information, Figure S3). Single crystal X-ray diffraction revealed that [^{n}Bu$_4$N]$_2$**1** contains a nearly square planar cobalt center (sum of angles about Co = 360.2(4)°), with Co–N and Co–O bond distances that both average to 1.87 Å (Figure 1). Cyclic voltammetry reveals a reversible one-electron redox event at $E_{1/2}$ = –0.22 V (vs NHE) corresponding to the Co(II)/Co(III) couple (Supporting Information Figure S6). This redox couple is more

negative than that for cobalt complexes supported by salen[8a] ($E_{1/2}$ = +0.25 V vs NHE), porphyrin[8b] ($E_{1/2}$ = +0.68 V vs NHE), corrole[8c] ($E_{1/2}$ = +0.03 V vs NHE), 1,1'-(ethane-1,2-diyl)bis(3-*tert*-butylurea)[4a] ($E_{1/2}$ = –0.086 V vs NHE), and 2,2',2''-nitrilo-tris(*N*-isopropylacetamide)[4b] ($E_{1/2}$ = +0.44 V vs NHE) ligands.

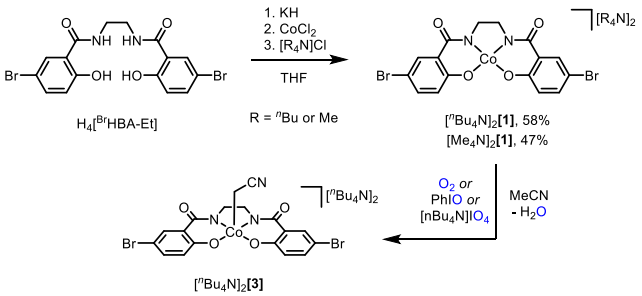

Scheme 1. Synthesis of $[^n\text{Bu}_4\text{N}]_2$**1**, $[^n\text{Me}_4\text{N}]_2$**1**, and $[^n\text{Bu}_4\text{N}]_2$**3**.

The one-electron oxidation of $[^n\text{Bu}_4\text{N}]_2$**1** by AgCl in THF afforded the Co(III) complex $[^n\text{Bu}_4\text{N}][(^{Br}\text{HBA-Et})\text{Co}]$ ($[^n\text{Bu}_4\text{N}]$**2**), which gives a deep purple solution in acetonitrile (λ_{max} = 560 nm, ε = 6800 M^{-1} cm^{-1}; 98% isolated yield). Solution magnetic moment measurements characterize $[^n\text{Bu}_4\text{N}]$**2** as having an S = 1 (2.88 μ_B, 298 K) ground state. X-ray crystallography (Supporting Information, Figure S1) reveals that Co is in a nearly square planar geometry (sum of angles about Co = 360.5(2)°). The average Co–N and Co–O bond distances are contracted to 1.84 Å and 1.83 Å, respectively, relative to analogous values for $[^n\text{Bu}_4\text{N}]_2$**1**. Presumably, the electron-rich nature of the ligand in [**2**]$^-$ stabilizes the four-coordinate cobalt(III) center and substantially reduces its Lewis acidity. This geometry contrasts with that of most cobalt(III) compounds which prefer an octahedral coordination environment with a diamagnetic ground state.

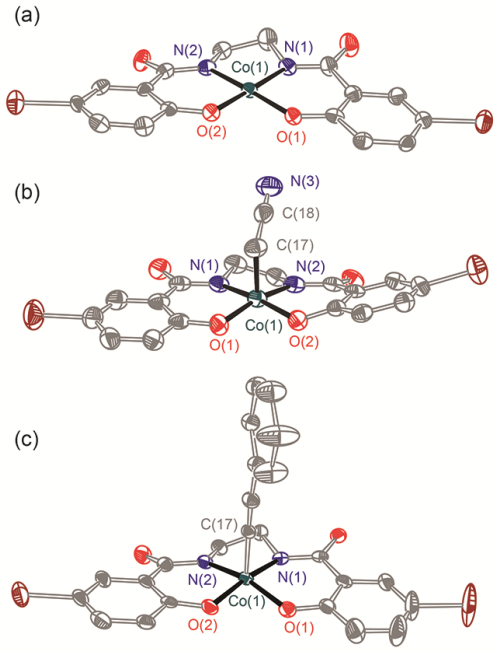

Figure 1. ORTEP diagrams of (a) [^{n}Bu$_4$N]$_2$**1**, (b) [^{n}Bu$_4$N]$_2$**3**, and (c) [^{n}Bu$_4$N]$_2$**4**. Thermal ellipsoids are drawn at 50%, and the solvent molecule, [^{n}Bu$_4$N]$^+$ cations, and hydrogen atoms are omitted for clarity.

Reaction of 0.25 equivalents of dry dioxygen with [^{n}Bu$_4$N]$_2$**1** in acetonitrile-d_3 resulted in a rapid color change from orange to dark brown, and generation of [^{n}Bu$_4$N]$_2$**3**-d_2 in 88% yield by ^{1}H NMR spectroscopy with respect to [^{n}Bu$_4$N]$_2$**1**. Use of excess dry dioxygen (1 atm) in the reaction with [^{n}Bu$_4$N]$_2$**1** in acetonitrile produced [^{n}Bu$_4$N]$_2$**3** in only 50% yield with respect to [^{n}Bu$_4$N]$_2$**1**. This lower yield is probably due to oxidation of the cyanomethyl ligand of [^{n}Bu$_4$N]$_2$**3** by the excess O_2, to form [^{n}Bu$_4$N]**2** which was isolated from the reaction solution in 12% yield and identified by NMR spectroscopy. The complex [^{n}Bu$_4$N]$_2$**3**, isolated as green crystals, was shown by X-ray crystallography to possess a cyanomethyl ligand (Figure 1b). Thus, reaction of [^{n}Bu$_4$N]$_2$**1** with O_2 results in activation of the relatively strong C–H bond of acetonitrile (BDE_{C-H} = 96 kcal/mol, pK_a = 31.1 in DMSO).

Interestingly, reactions of [^{n}Bu$_4$N]$_2$**1** with oxo-transfer reagents also resulted in formation of [^{n}Bu$_4$N]$_2$**3**. Thus, reaction of 0.5 of an equivalent of tetra-*n*-butylammonium periodate, [^{n}Bu$_4$N]IO$_4$, with [^{n}Bu$_4$N]$_2$**1** in acetonitrile resulted in quantitative formation of [^{n}Bu$_4$N]$_2$**3** after 30 min (by ^{1}H NMR spectroscopy). A control experiment using potassium iodate (KIO_3) and 18-crown-6 with [^{n}Bu$_4$N]$_2$**1** in acetonitrile revealed no reaction over this time, demonstrating that all oxo-transfer reactivity is derived from the periodate anion. Similarly, reaction of 0.5 equivalents of PhIO with [^{n}Bu$_4$N]$_2$**1** gave [^{n}Bu$_4$N]$_2$**3** in 46% yield (by ^{1}H NMR spectroscopy). The lower yield for this reaction is attributed to its heterogeneous nature.

Notably, Valentine and co-workers have shown that iodosylbenzene is activated as an oxo-transfer reagent in the presence of both redox-active and non-redox-active metal

ions (e.g., Co, and Zn), without the generation of an oxo ligand at the metal center. In these cases, iodosylbenzene undergoes Lewis-acid activation toward oxo-transfer to olefins (epoxidation) in the presence of metal salts in acetonitrile solvent, apparently with no activation of the latter.[9] For comparison, a mixture of iodosylbenzene (1 equivalent), $[^{n}Bu_4N]_2$**1**, and cyclohexene in acetonitrile gave no transformation of the olefin during complete conversion of $[^{n}Bu_4N]_2$**1**, with formation of $[^{n}Bu_4N]_2$**3** in 46% yield, as monitored by ^{1}H NMR spectroscopy and gas-chromatography-mass-spectrometry (GC-MS). Thus, any intermediate formed by the interaction of iodosylbenzene with $[^{n}Bu_4N]_2$**1** seems to have *low* electrophilicity and is unreactive toward cyclohexene. This appears to reflect the observed, low Lewis acidity for the cobalt(II) center of $[^{n}Bu_4N]_2$**1**, with its strongly donating ligand and dianionic nature. Thus, Lewis acid activation of iodosylbenzene seems unlikely with $[^{n}Bu_4N]_2$**1**, and the highly reducing nature of this complex is more consistent with a redox event and oxo-transfer from iodosylbenzene. Thus, the observed reaction chemistry appears to suggest that a cobalt oxo intermediate forms upon reaction with O_2 or oxo-transfer reagents.

To investigate the nature of the C–H bond activation step, a competition experiment between toluene ($BDE_{C–H}$ = 86 kcal/mol, pK_a = 41 in DMSO) and acetonitrile-d_3 as substrates (1:1 molar mixture) was performed using PhIO or O_2 as the oxidant. Significantly, $[^{n}Bu_4N]_2$**3**-d_2 was the only organocobalt species observed by ^{1}H NMR spectroscopy, and no trace of a toluene-activated product was detected. By ^{2}H NMR spectroscopy, the reaction mixture contained no detectable amounts of deuterated toluene products that might form via initial toluene activation, followed by metathesis with acetonitrile-d_3. In addition, a competition experiment involving 10 equivalents of 9,10-dihydroanthracene, a more acidic substrate ($BDE_{C–H}$ = 78 kcal/mol, pK_a = 30 in DMSO),[10] in acetonitrile-d_3 solvent produced anthracene (13%) and 9,10-anthraquinone (12%) using PhIO or O_2, respectively, as oxidant.[11] The formation of 9,10-anthraquinone with O_2 as the oxidant may result from reaction of $^3O_2$ with the 9-anthracenyl radical formed by initial C–H bond abstraction.[12] Thus, C–H bond activations in this system appear to be promoted by acidic character in the C–H bond. This was further indicated by reactions of $[^{n}Bu_4N]_2$**1** in acetonitrile with O_2 or PhIO in the presence of phenylacetylene (10 equivalents), which contains a very acidic but strong C–H bond ($BDE_{C–H}$ = ~133 kcal/mol, pK_a = 28 in DMSO).[13] This reaction quantitatively (by ^{1}H NMR spectroscopy) forms the diamagnetic, green cobalt alkynyl complex $[^{n}Bu_4N]_2[(^{Br}HBA\text{-}Et)Co–C{\equiv}CPh]$ ($[^{n}Bu_4N]_2$**4**, $\nu_{C\equiv C}$ = 2106 cm^{-1}). The structure of $[^{n}Bu_4N]_2$**4** was confirmed by X-ray crystallography (Figure 1c). The strong preference for more acidic substrates suggests that in the C–H bond activation step, proton transfer may precede electron transfer (*vide infra*).

A kinetic isotope effect (KIE) for reaction of acetonitrile in the presence of $[^{n}Bu_4N]_2$**1** and O_2 was obtained from a competition experiment involving a 1:1 mixture of acetonitrile and acetonitrile-d_3. Quantification of the $[^{n}Bu_4N]_2$**3**/$[^{n}Bu_4N]_2$**3**-d_2 ratio by high-resolution electrospray mass spectrometry gave a KIE value of 3.3(2). Interestingly, the analogous reaction with PhIO as the oxidant provided a KIE value that is essentially identical, 3.6(2). This moderate primary KIE value is consistent with an early or late transition state for the C–H bond activation step, and heterolytic C–H bond cleavage.

Coupled with the selectivities described above, these results suggest that a common intermediate is formed by reactions of PhIO or O_2 with $[^nBu_4N]_2$**1**, which activates C–H bonds by a heterolytic mechanism involving considerable proton-transfer character. Note that highly basic metal oxo complexes are expected to exhibit a moderate primary KIE in C–H bond activations.[14]

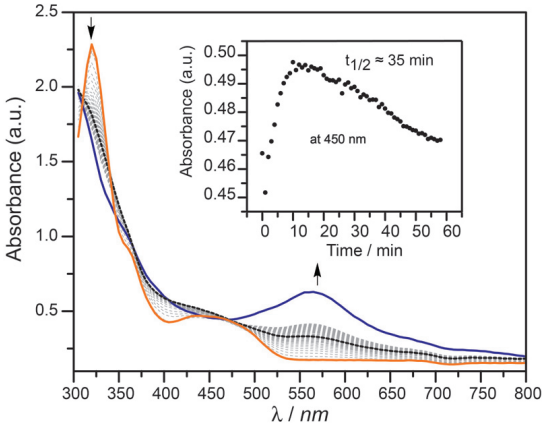

Figure 2. UV-vis time trace of $[^nBu_4N]_2$1 reaction with 1 atm O_2 at –63°C in 1:1 MeCN/THF. Orange trace is $[^nBu_4N]_2$1; purple trace is at t = 60 min; dashed-black trace is t = 10 min.

In an attempt to observe an intermediate in the O_2-mediated activation of acetonitrile, a 1:1 THF/MeCN solution of $[^nBu_4N]_2$**1** at –63°C was treated with O_2 (1 atm) and the reaction progress was followed by UV-vis spectroscopy. After 10 min, a new absorbance at ca. 400-450 nm, which decayed over the course of 1 h ($t_{1/2}$ ≈ 35 min), was observed (Figure 2). EPR spectroscopy (X-band, 77 K; Supporting Information, Figure S4) was used to characterize this intermediate, generated by addition of dry O_2 at room temperature to an *n*-butyronitrile solution of $[^nBu_4N]_2$**1** in the EPR tube. This experiment allowed observation of a new S = ½ signal with hyperfine coupling to ^{59}Co (g_1 = 2.026, g_2 = 2.028, g_3 = 2.13, $|A_1|$ = 57 MHz, $|A_2|$ = 43 MHz, $|A_3|$ = 85 MHz), the appearance of which after 30 seconds was accompanied by elimination of the signal for $[^nBu_4N]_2$**1**. After 10 minutes at room temperature, the intensity of the new signal diminished (to ~10% of the original intensity, by integration of the EPR signal) with no appearance of new signals, consistent with the formation of EPR-silent products. However, when the solution was degassed by a freeze-pump-thaw cycle after acquisition of the first spectrum, the S = ½ signal diminished and the signal for $[^nBu_4N]_2$**1** increased (Supporting Information, Figure S5). This behavior is consistent with reversible O_2 coordination to the cobalt(II) center to form the η^1-superoxo complex $[^nBu_4N]_2[(^{Br}HBA\text{-}Et)Co(O_2)]$, $[^nBu_4N]_2$**5** (Scheme 2).[4] In addition, analysis of the reaction mixture of $[Me_4N]_2$**1** with O_2 in acetonitrile after approximately 10 seconds at room temperature by high-resolution ESI-MS revealed the presence of a dianion with m/z = 264.42, and an isotopic distribution consistent with the terminal cobalt(IV) oxo complex $[^nBu_4N]_2[(^{Br}HBA\text{-}Et)CoO]$, $[^nBu_4N]_2$**6** (Supporting Information Figure S4).

The observations of [^{n}Bu$_4$N]$_2$**5** and [^{n}Bu$_4$N]$_2$**6** implicate these species as potential intermediates that directly engage in C–H bond-cleavage reactions. However, the results described above are most consistent with involvement of the oxo complex [**6**]$^{2-}$ in this chemistry. Firstly, metal superoxo complexes often exhibit much higher k_H/k_D values in intermolecular C–H bond activations (a range of k_H/k_D = 6.3 to 50 is typical).[15] The substrate competition experiments are consistent with initial proton abstraction from a C–H bond, but the *p*Ka of hydrogen superoxide (pK_a = 12 in DMF)[16, 17] suggests that such species should not be basic enough to accomplish such deprotonations. Furthermore, the observed reaction chemistry for O_2 closely parallels that observed with oxo-transfer reagents PhIO and IO_4^-, suggesting a cobalt(IV) oxo species as a common intermediate. Thus, the reaction with O_2 presumably involves binding of cobalt(II) to the initially formed superoxo complex [**5**]$^{2-}$, followed by O–O bond cleavage to generate the oxo compex [**6**]$^{2-}$. This oxo complex is presumed to react with hydrocarbons *via* proton- and electron-transfers to produce hydroxide and the cobalt(III) complex [**2**]$^{2-}$. This would generate the cyanomethyl radical $NCCH_2^{\bullet}$, and rapid trapping of this species by [**1**]$^{2-}$ would give [**3**]$^{2-}$. The cobalt(III) hydroxide species, proposed as the direct product of a proton-coupled-electron-transfer to [**6**]$^{2-}$, is expected to provide a second pathway to the [**3**]$^{2-}$ product, *via* deprotonation of acetonitrile. This hypothesis is supported by the observed reaction of [**2**]$^{2-}$ with (18-crown-6⊂K)OH in acetonitrile over 1 h, to give [**3**]$^{2-}$ in quantitative yield.

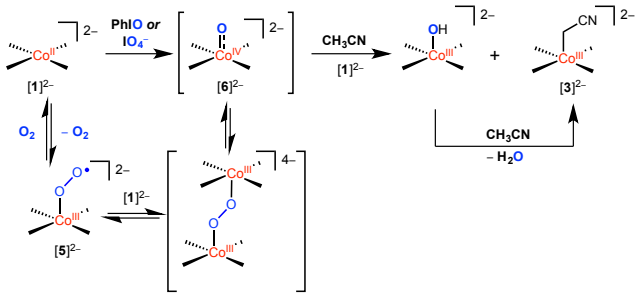

Scheme 2. Proposed mechanism for the formation of [**3**]$^{2-}$ by the reaction of [**1**]$^{2-}$ with O_2 or oxo-transfer reagents.

The reaction of [^{n}Bu$_4$N]$_2$**1** with the oxo-transfer reagents PhIO and IO_4^- suggest the possibility of a putative cobalt(IV) oxo complex. Consistent with this hypothesis, [^{n}Bu$_4$N]$_2$**1** was observed to react with *p*-tolyl azide, a nitrene transfer reagent, in acetonitrile-d_3 to cleanly produce [^{n}Bu$_4$N]$_2$**3** and 1 equiv of toluidine-d_2 (by ^{1}H NMR and ^{2}H NMR spectroscopy). This reaction is tentatively proposed to proceed *via* a cobalt(IV) imido species and a mechanism analogous to that proposed above for the cobalt(IV) oxo species (Scheme 3).

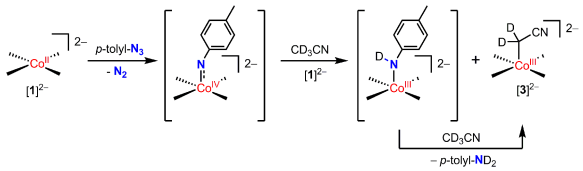

Scheme 3. Proposed mechanism for the formation of $[\mathbf{3}]^{2-}$ by the reaction of $[\mathbf{1}]^{2-}$ with tolyl azide.

1.3 Conclusions

In summary, the reaction of O_2 with $[^{n}Bu_4N]_2\mathbf{1}$ forms a cyanomethylcobalt(III) complex, $[^{n}Bu_4N]_2\mathbf{3}$, that results from an intermolecular C–H bond activation of acetonitrile. Oxo- and nitrene-transfer reagents are observed to induce the same reactivity, suggesting that cobalt(IV)-oxo and –imido species are key intermediates. Note that Schaefer and coworkers reported that, in the presence of O_2, a (salen)cobalt(II) species activates acetone to form a Co–C bond. No mechanistic details were provided, but this process may proceed *via* a cobalt-oxo intermediate that abstracts proton from acetone (which is about 7 orders of magnitude more acidic than acetonitrile).[18] The well-behaved system described above is expected to provide opportunities to establish mechanistic details for O_2 activation by cobalt(II), and perhaps the microscopic reverse, O–O bond formation. Along these lines, future efforts will target kinetic and low-temperature spectroscopic studies to better characterize the intermediates resulting from O_2 activation.

1.4 Acknowledgements

This work was supported by the Director, Office of Science, Office of Basic Energy Sciences of the US Department of Energy under contract No. DE-AC02-05CH11231 and the National Institutes of Health (Grant GM 40392 to E.I.S.). R.G.H. acknowledges a Gerhard Casper Stanford Graduate Fellowship and the Achievement Rewards for College Scientist (ARCS) Foundation. The authors thank Dr. Antonio Iavarone (QB3 Chemistry Mass Spectrometry Facility) for high-resolution ESI mass-spectrometry measurements, Apurva Pradhan for assistance with UV-vis measurements, and Dr. John J. Curley for stimulating discussions.

1.5 References

(1) Chakrabarty, R., Sarmah, P., Saha, B., Chakravorty, S., Das, B. K. *Inorg. Chem.* **2009**, *48*, 6371-6379; (b) Chakrabarty, R., Bora, S. J., Das, B. K. *Inorg. Chem.* **2007**, *46*, 9450-9462; (c) Jain, S. L., Sain, D. *Angew. Chem., Int. Ed.* **2003**, *42*, 1265-1267; (d) Caetano, B. L., Rocha, L. A., Molina, E., Rocha, Z. N., Ricci, G.; Calefi, P. S., de Lima, O. J., Mello, C., Nassar, E. J., Ciuffi, K. J. *Applied Catalysis A: General*, **2006**, *311*, 122-134; (e) Song, Y. J., Hyun, M. Y., Lee, J. H., Lee, H. G., Kim, J. H., Jang, S. P., Noh, J. Y., Kim, Y.; Kim, S., Lee, S. J., Kim, C. *Chem. Eur. J.* **2012**, *18*, 6094-6101; (f) Koola, J. D., Kochi, J. K. *J. Org. Chem,* **1987**, *52*, 4545-4553; (g) Chavez, F. A., Rowland, J. M., Olmstead, M. M., Mascharak, P. K. *J. Am. Chem. Soc.* **1998**, *120*, 9015-9027; (h) Hanzlik, R. P., Williamson, D. *J. Am. Chem.*

Soc. **1976**, *98*, 6570-6573; (i) Sobkowiak, A., Sawyer, D. T. *J. Am. Chem. Soc.* **1991**, *113*, 9520-9523; (j) Penniyamurthy, T., Bhatia, B., Reddy, M. M., Maikap, G. C., Iqbal, J. *Tetrahedron* **1997**, *53*, 7649-7670; (k) Fukuzumi, S., Okamoto, K., Tokuda, Y., Gros, C. P., Guilard, R. *J. Am. Chem. Soc.* **2004**, *126*, 17059-17066.

(2) (a) Sheldon, R. A., Kochi, J. K. Metal-Catalyzed Oxidations of Organic Compounds; Academic Press: New York, 1981; (b) Chavez, F. A., Mascharak, P. K. *Acc. Chem. Res.* **2000**, *33*, 539-545.

(3) Winkler, J. R., Gray, H. B. *Struct. Bond.* **2012**, *142*, 17-28.

(4) (a) Larsen, P. L., Parolin, T. J., Powell, D. R., Hendrich, M. P.; Borovik, A. S. *Angew. Chem. Int. Ed.* **2003**, *42*, 85-89; (b) Lucas, R. L., Zart, M. K., Murkerjee, J., Sorrell, T. N., Powell, D. R., Borovik, A. S. *J. Am. Chem. Soc.* **2006**, *128*, 15476-15489.

(5) (a) Hopmann, K. H., Ghosh, A. *ACS Catal.* **2011**, *1*, 597-600; (b) Lyakovskyy, V., Olivios Suarez, A. I., Lu, H., Jiang, H., Zhang, P. X., de Bruin, B. *J. Am. Chem. Soc.* **2011**, *133*, 12264-12273.

(6) (a) Fritch, J. R., Christoph, G. G., Schaefer, W. P. *Inorg. Chem.* **1973**, *12*, 2170-2175; (b) Schaefer, W. P., Marsh, R. E. *J. Am. Chem. Soc.* **1966**, *88*, 178-179; (c) Gall, R. S., Rogers, J. F., Schaefer, W. P., Christoph, G. G. *J. Am. Chem. Soc.* **1976**, 5135-5144; (d) C. Floriani and F. Calderazzo, *J. Chem. Soc. A,* **1969**, 946; (e) Collman, J. P., Gagne, R. R., Kouba, J., Ljusberg-Wahren, H. *J. Am. Chem. Soc.*, **1974**, 96, 6800–6802.

(7) (a) Collins, T. J., Powell, R. D., Slebodnick, C., Uffelman, E. S. *J. Am. Chem. Soc.* **1990**, *112*, 899-901; (b) Tiago de Oliveira, F., Chanda, A., Banerjee, D., Shan, X., Mondal, S., Que Jr., L., Bominaar, E. L., Münck, E., Collins, T. J. *Science*, **2007**, *315*, 835-838; (c) Anson, F. C., Collins, T. J., Coots, R. J., Gipson, S. L., Richmond, T. G. *J. Am. Chem. Soc.* **1984**, *106*, 5037-5038; (d) Anson, F. C.; Collins, T. J.; Richmond, T. G.; Santarsiero, B. D.; Toth, J. E.; Treco, B. G. R. T. *J. Am. Chem. Soc.* **1987**, 2974-2979; e) Collins, T. J.; Nichols, T. R.; Uffelman, E. S. *J. Am. Chem. Soc.* **1991**, *113*, 4708-4709.

(8) (a) Ortiz, B., Park, S.-M. *Bull. Korean Chem. Soc.* **2000**, *21*, 405-411; (b) Shi, C., Anson, F. C. *Inorg. Chem.* **1998**, *37*, 1037-1043; (c) Kadish, K. M., Shen, J., Frémond, L., Chen, P., El Ojaimi, M., Chkounda, M.; Gros, C. P.; Barbe, J.-M., Ohkubo, K., Fukuzumi, S., Guilard, R. *Inorg. Chem.* **2008**, *47*, 6726-6737.

(9) (a) VanAtta, R. B., Franklin, C. C., Valentine, J. S. *Inorg. Chem.*, **1984**, *23*, 4121–4123; (b) Nam, W., Valentine, J. S. *J. Am. Chem. Soc.*, **1990**, *112*, 4977–4979; (c) Yang, Y., Diederich, F., Valentine, J. S. *J. Am. Chem. Soc.*, **1991**, *113*, 7195–7205.

(10) Bordwell, F. G., Cheng, J.-P., Ji, G.-Z., Satish, A. V., Zhang, X. *J. Am. Chem. Soc.* **1991**, *113*, 9790-9795.

(11) The remaining products were $[^{n}Bu_4N]_2$**3** and $[^{n}Bu_4N]$**2** formed by the activation of acetonitrile.

(12) Hawthorne, J. O., Schowalter, K. A., Simon, A. W., Wilt, M. H., Morgan, M. S. *Oxidation of Organic Compound*s, American Chemical Society, 1968; Vol 75, pp 203-215.

(13) Luo, Y-R. Comprehensive Handbook of Chemical Bond Energies; Taylor & Francis: 2006.

(14) Parsell, T. H., Yang, M.-Y., Borovik, A. S. *J. Am. Chem. Soc.* **2009**, *131*, 2762-2763.
(15) (a) Cho, J., Woo, J., Nam, W. *J. Am. Chem. Soc.* **2010**, *132,* 5958-5959; (b) Peterson, R. L., Himes, R. A., Kotani, H., Suenobu, T., Tian, L., Siegler, M. A., Solomon, E. I., Fukuzumi, S., Karlin, K. D. *J. Am. Chem. Soc.* **2011**, *133*, 1702-1705; (c) Klinman, J. P. *Chem. Rev.*, **1996**, 2541-2561; (d) Prigge, S. R., Eipper, B. A., Mains, R. E., Amzel, L. M. *Science*, **2004**, *304*, 864-867; (e) Lee, Y.-M., Hong, S., Morimoto, Y., Shin, W., Fukuzumi, S., Nam, W. *J. Am. Chem. Soc.*, **2010**, *132*, 10668-10670; (f) Cho, K.-B., Kang, H., Woo, J., Park, J. P., Seo, M. S., Cho, J., Nam, W. *Inorg. Chem.* **2014**, *53*, 645-652.
(16) Chin, D-H., Chiericato, G., Nanni, E. J. Jr., Sawyer, D. T. *J. Am. Chem. Soc.* **1982**, *104*, 1296-1299.
(17) The p*K*a values in DMF are comparable to values in DMSO. Maran, F., Celadon, D., Severin, M. G., Vianello, E. *J. Am. Chem. Soc.* **1991**, *113*, 9320-9329.
(18) Schaefer, W. P., Waltzman, R.; Huie, B. T. *J. Am. Chem. Soc.*, **1978**, *100*, 5063-5067.

Supporting Information for **Chapter 1**

Experimental Details

General Considerations. All manipulations were carried out using Schlenk techniques under a purified N_2 atmosphere or in a Vacuum Atmospheres drybox. Solvents (spectroscopic grade) were purchased from Aldrich. Dry THF was prepared by passage through a VAC drying column. Acetonitrile was dried with CaH_2, and then fractionally distilled from CaH_2 under N_2. Acetonitrile used for crystallization was vacuum transferred from P_2O_5. *n*-Butyronitrile (^{n}PrCN) was dried by distillation over CaH_2. Dry solvents were stored under N_2 in Straus flasks. Cobalt(II) chloride, potassium hydride, 5-bromo-salicylic acid, ethylenediamine, iodosylbenzene (PhIO), 9,10-dihydroanthracene, and triphenylphosphine were purchased from Aldrich and used as received. NMR spectra were recorded on Bruker AVB-400, AVQ-400 and AV-300 spectrometers at room temperature. d_3-MeCN and d_6-DMSO were purchased from Cambridge Isotopes and dried over 3Å sieves under N_2. ^{1}H NMR spectra were referenced to residual protio solvent peaks (δ 2.94 for CD_3CN, δ 2.50 for $(CD_3)_2SO$). $^{13}C\{^1H\}$ NMR spectra were referenced to solvent resonances (δ 118.26 for CD_3CN, δ 39.51 for $(CD_3)_2SO$). Elemental analyses were carried out by the College of Chemistry Microanalytical Laboratory at the University of California, Berkeley. Infrared spectra were recorded on a Bruker Alpha P attenuated total reflectance instrument. UV-vis spectra were obtained on a Varian Cary 300 Bio or Varian Cary 50 BIO UV–visible spectrophotometer with a Unisoko cryostat attachment for stirring and temperature control in 1-cm air-free quartz cells. X-band electron paramagnetic resonance (EPR) spectra were obtained using a Bruker EMX spectrometer. X-band spectra were obtained at 77 K in a liquid nitrogen finger dewar using an ER 041 XG microwave bridge and an ER 4102ST cavity (parameters for recording the X-band EPR data: 9.63 GHz frequency, 1 mW microwave power, and 10 G modulation amplitude). X-band data were simulated using the Easy Spin program. Mass spectrometry measurements were performed at the QB3 Mass Spectrometry Facility at UC Berkeley using a quadrupole time-of-flight mass spectrometer (Q-TOF Premier, Waters, Milford, MA) that was equipped with an electrospray ionization (ESI) source. ESI source voltages were adjusted for optimum desolvation and transmission of ions of interest prior to recording mass spectra. Cyclic voltammograms were obtained with a BASi Epsilon potentiostat at room temperature using a glassy carbon working electrode (7 mm diameter), a platinum counter electrode, and a silver wire floating reference. All potentials were referenced against an $[Cp_2Fe]^{0/+}$ internal standard in acetonitrile.

Preparation of (^{Br}HBA-Et)H_4, *N*,*N*'-(ethane-1,2-diyl)*bis*(5-bromo-2-hydroxybenzamide). 5-Bromo-salicylic acid (5.4 g, 25 mmol) was combined with acetic anhydride (5 mL) and sulfuric acid (3 drops). The mixture was heated to 80 °C for 10 min. Water (100 mL) was added to the solid mass and the resulting solid was collected by filtration (5.6 g). The solid was dissolved in oxalyl chloride (6 mL) and DMF (2 drops) over 1 h. The volatile materials were removed *in vacuo* and the resulting residue was triturated twice with dichloromethane to give a white solid. The solid was dissolved in 100 mL of THF and the resulting solution was cooled to 0 °C. Ethylenediamine (0.72

mL, 11 mmol) was added dropwise and the resulting solution was stirred for 30 min. Triethylamine (4.5 mL, 32 mmol) in 100 mL of THF was added and the stirring was continued for 45 min at room temperature. The solution was filtered and the filtrate was evaporated to dryness and then washed with cold ethanol (0°C, 50 mL) to give a white solid. The solid from the last filtration was washed with 500 mL of water. The combined solids were dissolved in a solvent mixture of 200 mL water / 150 mL ethanol containing 1.5 g (37 mmol) of sodium hydroxide. The solution was refluxed for 30 min and then quenched with 3.5 mL of HCl (12.1 M). The resulting mixture was cooled to 0 °C and then filtered to give the product as a white solid (3.12 g, 55%).
^{1}H NMR (400 MHz, d_6-DMSO) δ: 3.49 (m, 4H, –CH_2CH_2–), 6.89 (d, 2H, $^3J_{HH}$ = 8.7, aryl-*H*), 7.55 (dd, 2H, $^3J_{HH}$ = 8.7, $^4J_{HH}$ = 2.2, aryl-*H*), 8.03 (d, 2H, $^4J_{HH}$ = 2.2, aryl-*H*), 9.01 (t, 2H, $^3J_{HH}$ = 5.3, N–*H*), 12.53 (s, 2H, O–*H*); HRMS (ESI) for $C_{16}H_{13}Br_2N_2O_4$ [M – H^+]$^-$ 456.92, found 456.9214.

Preparation of [^{n}Bu$_4$N]$_2$[(^{Br}HBA-Et)Co] ([^{n}Bu$_4$N]$_2$1). Potassium hydride (0.102 g, 2.54 mmol), **(^{Br}HBA-Et)H$_4$** (0.292 g, 0.640), and 10 mL of THF were combined in a 20 mL vial, and the resulting reaction mixture was stirred for 16 h. $CoCl_2$ (0.083 g, 0.640 mmol) was then added and the dark green solution was stirred for 16 h. Tetra-*n*-butylammonium chloride (0.354 g, 1.27 mmol) was then added and the stirring was continued for 2 h. The orange precipitate was collected by filtration and extracted into 15 mL of acetonitrile. The extract was evaporated *in vacuo* to give an orange crystalline solid (0.371 g, 58%). Anal. Calcd for $C_{48}H_{82}Br_2CoN_4O_4$: C, 57.77; H, 8.28; N, 5.61. Found: C, 57.17; H, 8.30; N, 5.28. IR (neat) ν/cm^{-1}: 2959, 2931, 2873, 1577, 1550, 1489, 1460, 1406, 1520, 1326, 1263, 1228, 1143, 1110, 882, 819, 681, 736, 656, 625, 535, 465, 419. UV-vis (MeCN) λ_{max}/nm (ε/M^{-1} cm^{-1}): 450 (2200), 320 (17,000), 217 (62,000). Magnetic Susceptibility (298 K, MeCN) μ_B: 1.98.

Preparation of [^{n}Me$_4$N]$_2$[(^{Br}HBA-Et)Co] ([Me$_4$N]$_2$1•2CH$_3$CN). Potassium hydride (0.145 g, 3.61 mmol), **(^{Br}HBA-Et)H$_4$** (0.4127 g, 0.900 mmol), and 10 mL of THF were combined in a 20 mL vial, and the resulting reaction mixture was stirred for 16 h. $CoCl_2$ (0.117 g, 0.900 mmol) was then added and the resulting green solution was stirred for 3 h. Tetra-*n*-methylammonium chloride (0.197 g, 1.80 mmol) was then added and stirring was continued for 16 h. The orange precipitate was collected by filtration and extracted into 15 mL of MeCN. The extract was evaporated *in vacuo* to give an orange crystalline solid (0.293 g, 44%). Anal. Calcd for $C_{48}H_{82}Br_2CoN_4O_4$•2CH_3CN: C, 45.24; H, 5.42; N, 11.30. Found: C, 45.0; H, 5.51; N, 11.0.

Preparation of [^{n}Bu$_4$N][(^{Br}HBA-Et)Co] ([^{n}Bu$_4$N]2). AgCl (0.0291 g, 0.205 mmol) was added to a slurry of [^{n}Bu$_4$N]$_2$**1** (0.205 g, 0.205 mmol) in 10 mL of THF. The reaction mixture was stirred for 45 minutes, and then 3 mL of Et_2O was added to precipitate [^{n}Bu$_4$N]Cl. Filtration of the reaction mixture through a celite plug and evaporation of the resulting purple solution afforded a purple solid (0.155 g, 98%). Figure S1 shows the x-ray crystal structure with selected bond lengths.
Anal. Calcd for $C_{32}H_{46}Br_2CoN_3O_4$: C, 50.87; H, 6.14; N, 5.56. Found: C, 50.0; H, 5.90; N, 5.29. ^{1}H NMR (400 MHz, CD_3CN) δ: -28.05 (s, 2H, aryl-*H*), 0.72 (t, 12H, $^3J_{HH}$ =

6.5, ($CH_3CH_2CH_2CH_2$)$_4$N), 1.05 (sex, 8H, $^3J_{HH}$ = 6.5, ($CH_3CH_2CH_2CH_2$)$_4$N), 1.28 (br, 8H, ($CH_3CH_2CH_2CH_2$)$_4$N), 2.73 (t, 8H, $^3J_{HH}$ = 6.3, ($CH_3CH_2CH_2CH_2$)$_4$N), 19.00 (s, 2H, aryl-*H*), 29.93 (s, 2H, aryl-*H*), 318.04 (s, 2H, –CH_2CH_2–). IR (neat) ν/cm^{-1}: 2956, 2931, 2868, 1580, 1552, 1520, 1456, 1409, 1298, 1145, 1093, 882, 821, 740, 685, 630, 583, 538, 487, 464, 424. UV-vis (MeCN) λ_{max}/nm (ε/M^{-1} cm^{-1}): 560 (6800), 378 (3000), 303 (10,000), 250 (15,000), 214 (38,000). Magnetic Susceptibility (298 K, MeCN) μ_B: 2.88.

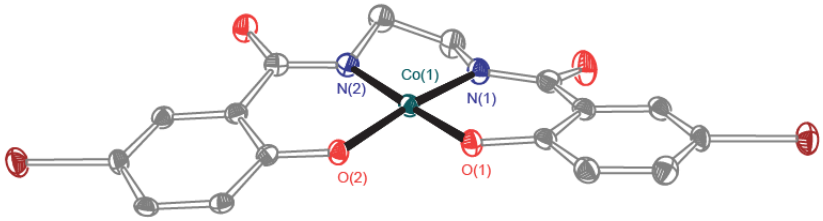

Figure S1. ORTEP diagram of [^{n}Bu$_4$N]$_2$**2**. Thermal ellipsoids are drawn at 50%, hydrogen atoms and ^{n}Bu$_4$N$^+$ cations are omitted for clarity. Selected bond distances (Å) and angles (deg) for [1]: N(1)–Co(1) 1.834(2), N(2)–Co(1) 1.836(2), O(1)–Co(1) 1.831(2), O(2)–Co(1) 1.830(2); O(2)–Co(1)–N(2) 94.90(9), N(2)–Co(1)–N(1) 86.41(10), N(1)–Co(1)–O(1) 95.22(9), O(2)–Co(1)–O(1) 83.98(8).

Preparation of [^{n}Bu$_4$N]$_2$[(^{Br}HBA-Et)Co(CH_2CN)] ([^{n}Bu$_4$N]$_2$3). A MeCN solution (5 mL) of [^{n}Bu$_4$N]$_2$**1** (0.107 g, 0.107 mmol) in a Schlenk tube was degassed with one freeze-pump-thaw cycle, and this solution was exposed to 1 atm of dry O_2 at room temperature. The reaction mixture was stirred for 2 h at room temperature to produce a dark brown solution. The volatile materials were removed *in vacuo* to afford a brown residue. The residue was dissolved in 3 mL of THF, and 3 mL of Et_2O was added to yield a green oily residue and a purple solution. The purple solution was decanted away from the oil, and evaporated *in vacuo* to give [^{n}Bu$_4$N][**2**] (0.010 g, 12% based on [^{n}Bu$_4$N]$_2$**1**), identified by ^{1}H NMR spectroscopy. The green oil was stirred vigorously in 10 mL of Et_2O to give [^{n}Bu$_4$N]$_2$**3** as a green solid, which was collected by filtration (0.056 g, 50% based on [^{n}Bu$_4$N]$_2$**1**). Single crystals suitable for X-ray diffraction were obtained by vapor diffusion of Et_2O into a saturated solution of [^{n}Bu$_4$N]$_2$**3** in THF.

Anal. Calcd for $C_{50}H_{84}Br_2CoN_5O_4$: C, 57.86; H, 8.16; N, 6.75. Found: C, 57.58; H, 8.05; N, 7.07. ^{1}H NMR (400 MHz, CD_3CN) δ: 0.93 (t, 24H, $^3J_{HH}$ = 6.8, ($CH_3CH_2CH_2CH_2$)$_4$N), 1.31 (sex, 16H, $^3J_{HH}$ = 6.8, ($CH_3CH_2CH_2CH_2$)$_4$N), 1.53 (br, 16H, ($CH_3CH_2CH_2CH_2$)$_4$N), 1.54 (s, 2H, CH_2CN) 3.04 (br, 16H, ($CH_3CH_2CH_2CH_2$)$_4$N), 3.50 (m, 4H, –CH_2CH_2–), 6.93 (d, 2H, $^3J_{HH}$ = 8.4, aryl-*H*), 6.98 (dd, 2H, $^3J_{HH}$ = 8.4, $^4J_{HH}$ = 2, aryl-*H*), 8.01 (d, 2H, $^4J_{HH}$ = 2, aryl-*H*). ^{13}C{^{1}H} NMR (100.62 MHz, CD_3CN) δ: 13.72 (($CH_3CH_2CH_2CH_2$)$_4$N), 20.30 (($CH_3CH_2CH_2CH_2$)$_4$N), 24.20 (($CH_3CH_2CH_2CH_2$)$_4$N), 50.34 (–CH_2CH_2–), 59.15 (($CH_3CH_2CH_2CH_2$)$_4$N), 104.15 (aryl-*C*), 126.33 (aryl-*C*), 131.89 (aryl-*C*), 133.26 (aryl-*C*), 169.59 (aryl-*C*), 170.96 (*C*=O). IR (neat) ν/cm^{-1}: 2961, 2931, 2873, 2203 (C≡N), 1580, 1552, 1520, 1452, 1409, 1309, 1261, 1228, 1145, 1108, 1093, 1025, 882, 819, 739,

680, 648, 628, 535, 465, 440, 423. UV-vis (MeCN) λ_{max}/nm (ε/M^{-1} cm^{-1}): 800 (1300), 217 (68,000).

Generation of [^{n}Bu$_4$N]$_2$[(^{Br}HBA-Et)Co(CH$_2$CN)] ([^{n}Bu$_4$N]$_2$3) by stoichiometric O$_2$. In a J. Young tube, [^{n}Bu$_4$N]$_2$**1** (0.031 g, 0.031 mmol) was dissolved in 0.6 mL of CD_3CN. The solution was degassed by a freeze-pump-thaw cycle. A rubber septum with a needle was fitted on the J. Young tube and the headspace was degassed by pulling vacuum. A syringe containing 0.2 mL dry O_2 (0.0078 mmol) was inserted into the septum, and the J. Young seal was opened to allow the O_2 to diffuse into the tube. The reaction was complete after 16 h, and [^{n}Bu$_4$N]$_2$**3** was formed along 88% yield by ^{1}H NMR spectroscopy (with respect to [^{n}Bu$_4$N]$_2$**1**), using 1,4-dimethoxybenzene or [^{n}Bu$_4$N]$^+$ as an internal standard.

Generation of [^{n}Bu$_4$N]$_2$[(^{Br}HBA-Et)Co(CH$_2$CN)] ([^{n}Bu$_4$N]$_2$3) by PhIO. In a J. Young tube, [^{n}Bu$_4$N]$_2$**1** (0.037 g, 0.037 mmol) and PhIO (0.0041 g, 0.018 mmol) were dissolved in 0.6 mL of CD_3CN. The reaction was complete after 16 h, and [^{n}Bu$_4$N]$_2$**3** was formed along with iodobenzene in quantitative yield by ^{1}H NMR spectroscopy (with respect to both iodosylbenzene and [^{n}Bu$_4$N]$_2$**1**), using 1,4-dimethoxybenzene or [^{n}Bu$_4$N]$^+$ as an internal standard.

Generation of [^{n}Bu$_4$N]$_2$[(^{Br}HBA-Et)Co(CH$_2$CN)] ([^{n}Bu$_4$N]$_2$3) by [^{n}Bu$_4$N]IO$_4$. In a J. Young tube, [^{n}Bu$_4$N]$_2$**1** (0.050 g, 0.050 mmol) was dissolved in ~1 mL of CD_3CN, and [^{n}Bu$_4$N]IO$_4$ (0.010 g, 0.025 mmol) was added slowly in small batches with stirring. The reaction was complete after 0.5 h, and [^{n}Bu$_4$N]$_2$**3** was formed in near quantitative yield (96% with respect to [^{n}Bu$_4$N]$_2$**1**) by ^{1}H NMR spectroscopy, using either 1,4-dimethoxybenzene (0.0055g) or [^{n}Bu$_4$N]$^+$ as an internal standard.

Preparation of [^{n}Bu$_4$N]$_2$[(^{Br}HBA-Et)Co(CCPh)] ([^{n}Bu$_4$N]$_2$4). To a MeCN solution (5 mL) of [^{n}Bu$_4$N]$_2$**1** (0.100 g, 0.107 mmol) was added phenylacetylene (0.102 g, 1.10 mmol). Iodosylbenzene (0.011 g, 0.050 mmol) was added, and the resulting reaction mixture was stirred for 3 h. Diethyl ether (15 mL) was added to the solution and a green crystalline solid formed overnight. The mother liquor was decanted and the solid was dried in vacuo to yield 0.084 g (76%) of the product.
^{1}H NMR (400 MHz, CD_3CN) δ: 0.92 (br, 24H, (C*H*$_3$CH$_2$CH$_2$CH$_2$)$_4$N), 1.29 (br, 16H, (CH$_3$C*H*$_2$CH$_2$CH$_2$)$_4$N), 1.52 (br, 16H, (CH$_3$C*H*$_2$CH$_2$CH$_2$)$_4$N), 3.03 (br, 16H, (CH$_3$CH$_2$CH$_2$C*H*$_2$)$_4$N), 3.45 (m, 2H, –C*H*$_2$C*H*$_2$–), 3.67 (m, 2H, –C*H*$_2$C*H*$_2$–), 6.84–7.00 (m, 9H, aryl-*H*), 8.04 (br, 2H, aryl-*H*). ^{13}C{^{1}H} NMR (100.62 MHz, CD_3CN) δ: 13.85 ((*C*H$_3$CH$_2$CH$_2$CH$_2$)$_4$N), 20.29 ((CH$_3$*C*H$_2$CH$_2$CH$_2$)$_4$N), 24.29 ((CH$_3$CH$_2$*C*H$_2$CH$_2$)$_4$N), 51.15 (–*C*H$_2$*C*H$_2$–), 59.14 ((CH$_3$CH$_2$CH$_2$*C*H$_2$)$_4$N), 105.28 (aryl-*C*), 114.93 (Ph*C*≡C–), 125.51 (aryl-*C*), 125.83 (aryl-*C*), 127.26 (aryl-*C*), 128.83 (aryl-*C*), 132.24 (aryl-*C*), 132.93 (aryl-*C*), 133.04 (aryl-*C*), 168.94 (aryl-*C*), 171.41 (*C*=O). IR (neat) ν/cm^{-1}: 2958, 2934, 2870, 2106 (C≡C), 1576, 1555, 1519, 1458, 1440, 1410, 1317, 1265, 1229, 878, 814; HRMS (ESI) for $C_{24}H_{15}Br_2CoN_2O_4$ $[M]^{2-}$ m/z = 306.94, found 306.94.

Generation of $[^nBu_4N]_2[(^{Br}HBA\text{-}Et)Co(CCPh)]$ ($[^nBu_4N]_2$4) by O_2. A J. Young tube containing $[^nBu_4N]_2$**1** (0.025 g, 0.025 mmol) and phenylacetylene (0.026 g, 0.25 mmol) was degassed by one freeze-pump-thaw cycle. Excess dry O_2 (1 atm) was added to the reaction mixture. After 1 h, a green solution was obtained. ^{1}H NMR spectroscopy showed quantitative formation of $[^nBu_4N]_2$**4** by integration against 1,4-dimethoxybenzene internal standard (0.003 g, 0.022 mmol).

Reaction of $[^nBu_4N]_2$1, KIO_3, and 18-crown-6 in MeCN. Potassium iodate (0.005 g, 0.025 mmol) was added to a MeCN solution (0.6 mL) containing $[^nBu_4N]_2$**1** (0.050 g, 0.050 mmol) and 18-crown-6 (0.006 g, 0.025 mmol). The reaction was allowed to react for 16 h. No color change was observed indicating no generation of $[^nBu_4N]_2$**3**.

Reaction of $[^nBu_4N]_2$1, PhIO, and cyclohexene. PhIO (0.011 g, 0.050 mmol) was added to a d_3-MeCN solution (0.6 mL) containing $[^nBu_4N]_2$**1** (0.050 g, 0.050 mmol) and excess cyclohexene (0.042 g, 0.50 mmol). The reaction was allowed to react for 16 h, and analyzed by ^{1}H NMR spectroscopy which showed a 46% yield of $[^nBu_4N]_2$**3**, and no change in cyclohexene integration (no new shifts corresponding to any new organic products were observed either) using $[^nBu_4N]^+$ as an internal standard. Gas-chromatography mass spectrometry only showed peaks for cyclohexene, 1,4-dimethoxybenzene, and iodobenzene.

Reaction of $[^nBu_4N]_2$1, O_2, and 9,10-dihydroanthracene. Excess O_2 was added to a d_3-MeCN slurry (0.6 mL) containing $[^nBu_4N]_2$**1** (0.0403 g, 0.0404 mmol) and 9,10-dihydroanthracene (0.072 g, 0.404 mmol). The reaction mixture was analyzed by ^{1}H NMR spectroscopy after 24 h, which showed a 12% yield of anthraquinone using $[^nBu_4N]^+$ as an internal standard.

Reaction of $[^nBu_4N]_2$1, PhIO, and 9,10-dihydroanthracene. PhIO (0.004 g, 0.020 mmol) was added to a d_3-MeCN slurry (0.6 mL) containing $[^nBu_4N]_2$**1** (0.020 g, 0.020 mmol) and 9,10-dihydroanthracene (0.036 g, 0.20 mmol). The reaction mixture was analyzed by ^{1}H NMR spectroscopy after 45 minutes, which showed a 13% yield of anthracene using $[^nBu_4N]^+$ as an internal standard.

UV-vis measurement of $[^nBu_4N]_2$1 + O_2. Dry O_2 (1 atm) was added to a Teflon sealed, air-tight quartz cuvette containing a solution of $[^nBu_4N]_2$**1** in 1:1 MeCN/THF (3.0 mL, 8.5×10^{-5} M) at –63°C. A measurement was taken every minute for 60 minutes from the point of O_2 addition. To record the spectrum of the completed reaction, the cuvette was then allowed to warm up to room temperature for 10 minutes, and then cooled back down to –63°C before the spectrum was recorded.

Preparation of $[6]^{2-}$ ESI-MS sample. Dry O_2 was added via a blunt syringe to a vial capped with a rubber septum containing a solution of $[Me_4N]_2$**1** in MeCN (1 mM). At room temperature, an aliquot from the reaction mixture was analyzed after approximately 30 s. Figure S2 shows the full spectrum and inset shows the zoomed up region for $[6]^{2-}$.

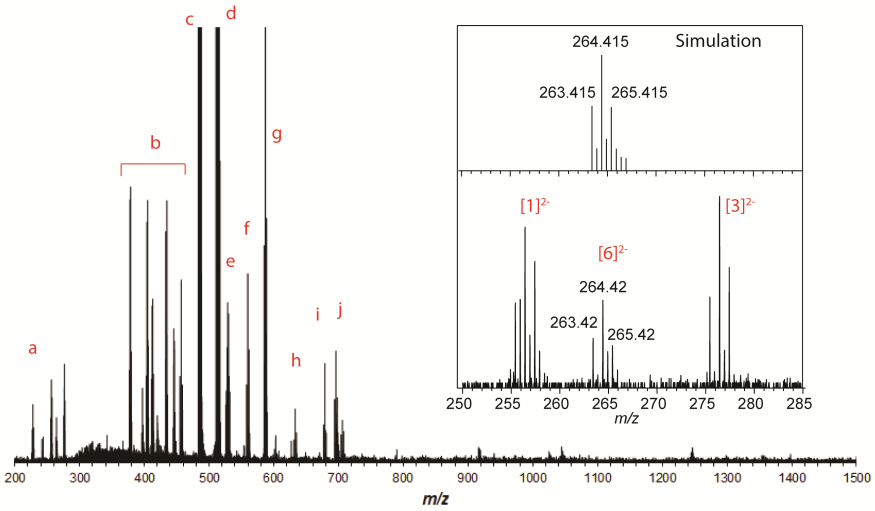

Figure S2. Negative-ion ESI-MS (full and close up of region-of-interest). Other ions identified are: (a) *227.96*, $[LH_2]^{2-}$, (b) *378.86*, $[LH_4(\text{-Br})]^{-}$, (c) various monobrominated complexes, indicated by a doublet pattern (debromination in ESI), (d) *485.39*, $[(LH_2)_2Co^{II}]^{2-}$, (e) **[2]**$^{-}$, (f) *528.83*, $[LCoO]^{-}$, (g) *580.93*, $[(LCo^{II})(Me_4N)]^{-}$, (h) *632.93*, $[(LH)Co^{II}(\text{formate})(Me_4N)]^{-}$, (i) *678.94*, $[(LH_2)Co^{II}(\text{formate})_2(Me_4N)]^{-}$, (j) *696.04*, $[(LCo^{II})(H_2O)(OH)(Me_4N)_2]^{-}$. No peaks could be assigned to the species $[LCo^{III}OH]^{2-}$, $[(LCo^{III})_2O]^{4-}$, $[LCo^{III}O_2]^{-}$, $([LCo^{III})_2O_2]^{4-}$, or their adducts with either Na^{+} or Me_4N^{+}. (L= **[^{Br}HBA-Et]**$^{4-}$)
**Note*: Relative abundance is not representative of relative concentrations in solution.

Preparation of $[^{n}Bu_4N]_2$1 EPR sample. A solution of $[^{n}Bu_4N]_2$**1** in ^{n}PrCN (5 mM) in a quartz EPR tube was prepared. The solution was cooled to 77 K. Figure S3 shows the simulated and experimental EPR spectrum.

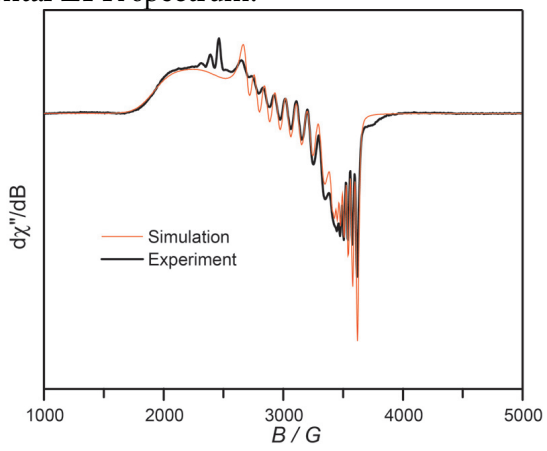

Figure S3. Simulated and experimental spectrum for **[1]**$^{2-}$.

Observation of [5]$^{2-}$ generated from O_2, by EPR. Dry O_2 was added to a quartz EPR tube capped with a rubber septum containing a solution of $[^{n}Bu_4N]_2$**1** in ^{n}PrCN (5 mM). The reaction mixture was maintained at room temperature for approximately 30 s and

then was immediately cooled to 77 K. Figure S4 shows the simulated and experimental EPR spectrum.

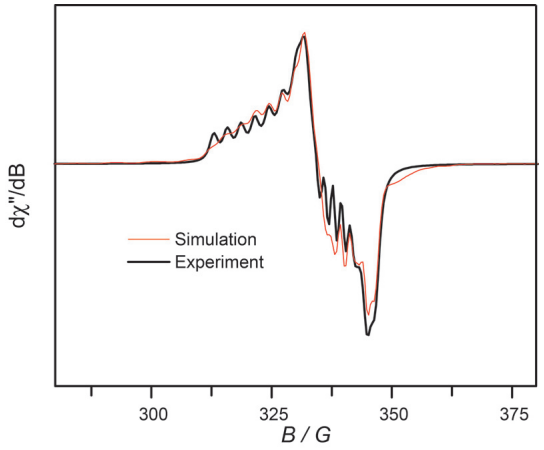

Figure S4. Simulated and experimental spectrum for **[5]**$^{2-}$.

Reversible formation of [5]$^{2-}$ observed by EPR. An EPR spectrum was acquired of a Teflon sealed J. Young tube containing a solution of [^{n}Bu$_4$N]$_2$**1** in MeCN (5 mM). The solution was degassed by one freeze-pump-thaw cycle and dry O_2 was added to the vessel and the reaction mixture was maintained at room temperature for approximately 60 s, and then it was rapidly cooled to 77 K and an EPR spectrum was acquired. The solution was then degassed by one freeze-pump-thaw cycle, cooled to 77 K, and an EPR spectrum was acquired. Figure S5 shows the overlay of the two spectra.

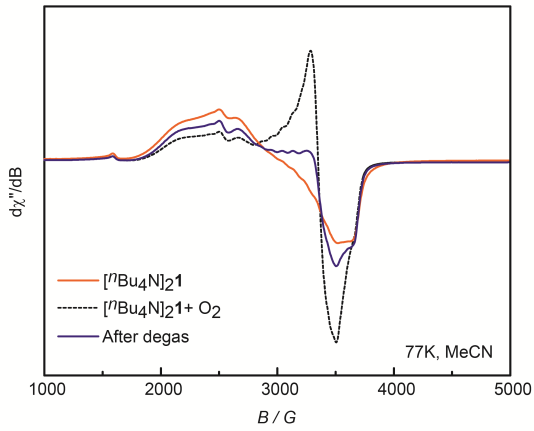

Figure S5. EPR spectra of the reaction mixture before O_2 addition, after O_2 addition, and after degassing.

Analysis of complete reaction mixture ([^{n}Bu$_4$N]$_2$1 + O_2) by EPR. Dry O_2 was added to a quartz EPR tube capped with a rubber septum containing a solution of [^{n}Bu$_4$N]$_2$**1** in ^{n}PrCN (5 mM). The reaction was allowed to occur at room temperature for approximately 10 min, and the reaction mixture was then rapidly cooled to 77 K.

Preparation of $[^nBu_4N]_2$1 sample for cyclic voltammetry. A solution of **[1]**$^{2-}$ (1.04×10^{-3} M, 10 mL) in 0.10 M tetra-*n*-butylammonium hexafluorophosphate acetonitrile solution was prepared in a N_2 filled glovebox at room temperature. Potentials were then referenced to ferrocene internal standard.

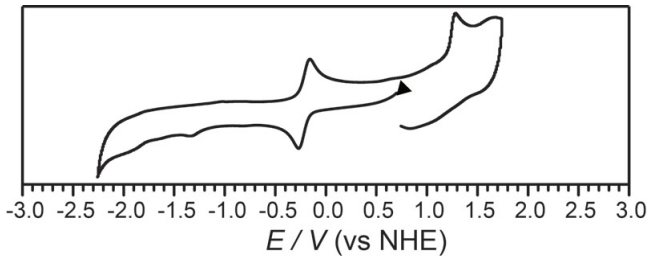

Figure S6. Cyclic voltammagram of $[^nBu_4N]_2$**1** at 100 mv/s (without ferrocene).

X-ray Crystallography Details

X-ray diffraction data were collected using Bruker AXS three-circle diffractometers coupled to a CCD detector with either QUAZAR multilayer mirror- or graphite-monochromated Mo Kα radiation (λ = 0.71073 Å). The structures were solved by direct methods using SHELXS and refined against F^2 on all data by full-matrix least squares with SHELXL-97. All non-hydrogen atoms were refined anisotropically; hydrogen atoms were included into the model at their geometrically calculated positions and refined using a riding model.

Chapter 2:

Mechanistic Investigations of Water Oxidation by a Cobalt Oxide Analogue: Evidence for a Highly Oxidized Intermediate and Exclusive Terminal Oxo Participation*

---

* This work is based upon work previously published, included with permission from all authors:

Nguyen, A. I., Ziegler, M. S., Oña-Burgos, P., Sturzbecher-Hohne, M., Kim, W., Bellone, D. E., Tilley, T. D. *J. Am. Chem. Soc.*, **2015**, *137*, 12865-12872.

Author contributions: Andy I. Nguyen formulated the project, synthesized all materials, measured electrochemical data, and performed mechanistic studies. Micah S. Ziegler and A.I.N quantified the O_2 evolution. Pascual Oña-Burgos measured and analyzed NMR spectroscopic data. Manuel Sturzbecher-Hohne (LBL) measured the stopped-flow UV-vis data. Wooyul Kim (LBL) and A.I.N. performed the isotopic labeling experiments. Donatela E. Bellone and A.I.N. solved the kinetic equations. A.I.N performed the numerical kinetic simulations.

2.1 Introduction

Society's current and future energy demands require sustainable resources that do not contribute to global climate change.[1] While the sun provides abundant energy, conversion of solar energy into a storable, transportable, easily accessible form is not yet economically feasible.[2,3] An ideal system would artificially replicate natural photosynthesis, which involves the endergonic 4-electron oxidation of water to O_2 and four protons (eq 1), and the subsequent storage of captured solar energy in the chemical bonds of a fuel.[4] However, without a catalyst this transformation is inefficient; therefore, research on solar fuel production has focused heavily on the discovery of increasingly efficient water oxidation catalysts (WOCs).[5–8] Mechanistic details of this catalysis, including that of the natural process in photosystem II, is limited but expected to provide important design principles that will enable optimization of catalyst efficiency.[9,10] Much of the mystery associated with such mechanisms concerns the O–O bond-forming event, although several possibilities seem plausible.[8,11]

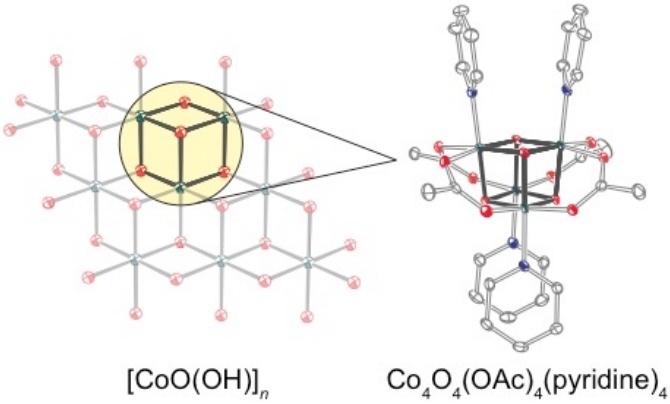

Figure 1. Structural comparison of cobalt oxyhydroxide (CoOOH)[12] with cobalt cubane (**1**). Red, green, blue, and gray spheres or ellipsoids represent O, Co, N, and C, respectively.

$$2H_2O \rightarrow 4H^+ + 4e^- + O_2 \qquad (1)$$

Cobalt oxide materials are among the most promising catalysts for water oxidation, due to their robust structures, inherent activity, and most importantly, the natural abundance of cobalt.[13–16] Unfortunately, thorough structural characterizations and mechanistic studies of the active species for cobalt oxide catalysts are inherently difficult, given their heterogeneous nature.[17,18] For heterogeneous catalysts like this, information about the structure and reactivity of the active site can be gained by studying appropriately designed, molecular models. However, while a few soluble, molecular cobalt compounds are reported to behave as active water oxidation catalysts under photochemical or electrochemical conditions, their associated mechanisms remain poorly defined.[8,19–21] Such investigations are complicated by the difficulty in establishing the integrity of molecular cobalt catalysts under operating conditions, as these compounds may simply serve as precursors to a heterogeneous cobalt oxide catalyst.[22,23] Thus, to date the mechanisms available to soluble and insoluble cobalt-based catalysts for WOC are not well understood.

Herein, we provide experimental evidence for the mechanism of WOC as catalyzed by a molecular cobalt oxide cluster. This cluster, $Co_4O_4(OAc)_4py_4$ (**1**), was first synthesized in 1998 by Beattie et al., and is an attractive model compound due to its resemblance to a subunit of extended cobalt oxides (Figure 1).[24] The Nocera and Britt groups have employed **1** as a model for the cobalt phosphate (CoP_i) water oxidation catalyst in electron paramagnetic resonance (EPR) spectroscopy studies.[25] Its promise as a functional model for water oxidation catalysis has been examined by the groups of Dismukes, Scandola, and Sun, and Nocera.[26–29] In support of **1** as a possible WOC candidate, DFT calculations by Siegbahn and coworkers demonstrated the existence of an energetically feasible pathway for O–O bond formation by **1** *via* a Co(V) intermediate, but their results do not have experimental support.[30] Similarly, theoretical calculations on other cobalt systems suggest that Co(V) is likely the true active intermediate, although the lack of experimental evidence for such species renders it controversial.[31–33] The investigations described below involve a combination of electrochemistry, stoichiometric reactivity, spectroscopy, and kinetic experiments to observe and identify many key intermediates and reaction steps of WOC involving **1**. In particular, the conversion of hydroxide to oxygen is shown to occur at a molecular $[Co_4O_4]$ cubane center, and the O–O bond formation is demonstrated *via* a clean stoichiometric reaction from an isolated Co(IV) intermediate. Kinetic studies reveal an unusual mechanism implicating formation of a formal $[Co(III)_3Co(V)]$ or $[Co(III)_2Co(IV)_2]$ intermediate prior to O_2 release. To our knowledge, this is the first example of an isolated WOC intermediate shown to cleanly form O_2 in the absence of exogenous oxidant. Taken together, these data form a clearer picture of how water oxidation is mediated by **1**, and also gives broader implications of how cobalt-oxide materials may mediate water oxidation. These should provide a basis for the rational design of more efficient and robust cobalt-based catalysts.

2.2 Electrochemistry and reaction chemistry

Cubane complex **1** was purified by column chromatography to remove impurities from the crude product obtained using the published synthesis.[29,34] In addition, compound **1** was treated with tetrasodium diaminoethanetetracarboxylate (Na_4EDTA) in the workup to remove any trace Co(II) impurities. To more thoroughly investigate the stability and chemistry of cubane **1** in aqueous solution, cyclic voltammetry was performed over the pH range of 0.0 to 12. From pH 4 to 10, a 1 mM solution of **1** displays a fully reversible redox couple at $E_{1/2}$ = 1.25 V (vs. NHE), corresponding to a one-electron $[Co(III)_4]/[Co(III)_3Co(IV)]$ redox couple (**1**/**1**$^+$) (Figure 2a). In agreement with the results of Nocera and coworkers, purified **1** does not exhibit noticeable catalysis over this pH range, indicating that these samples do not contain Co(II) impurities. This reversible couple shifts linearly with pH to more oxidizing potentials below pH 4, at a rate (63 mV/pH unit) that indicates a 1 H^+, 1 e^- redox process (Figure S3). The peak potential remains constant below pH 0.7 (to 0), and this behavior is consistent with protonation of cubane **1** to **1**H$^+$, and a pK_a value of 3.5 for **1**. For comparison, the dicationic cobalt cubane complex $[Co_4O_4(OAc)_2(bipy)_4]^{2+}$ exhibits similar behavior, with a pK_a value of 3.15.[35]

Increasing the pH to 12 results in a significant rise in current density for the anodic wave and bubble formation that is consistent with the catalytic oxidation of hydroxide to oxygen (Figure 2b). By ^{1}H NMR spectroscopy, a solution of **1** (10 mM in D_2O) at pD 12 shows partial conversion to a new species (*vide infra*), but the total integration of all cobalt species decreased by only 0.9% after 2.5 hours, implying that there is only minor decomposition into insoluble or paramagnetic compounds (Figure S4). This electrocatalysis corresponds to an overpotential η of 728 mV at a current density of ~2 mA cm^{-2} (TOF = 2 s^{-1}, Supporting Information). The catalytic wave was mostly retained in the presence of 0.25 mM Na_4EDTA, suggesting that catalytic activity is not due to Co(II), though it should be noted that $EDTA^{4-}$ is readily oxidized at E > 1.1 V vs NHE, which may account for slight differences in the shapes of the catalytic waves in the presence of Na_4EDTA.[36,37] Furthermore, rinsing the glassy carbon electrode with water removed all catalytic species that might have been on the electrode, as evidenced by the lack of catalysis in the cyclic voltammogram in a solution containing only electrolyte at pH 12 (Figure S1A). The electrocatalytic activity of **1** is also significantly different from that of Co(II) under these conditions (Figure S1A). From the cyclic voltammetry and control experiments, it seems that very pure samples of **1** exhibit true homogeneous water oxidation catalysis at pH 12. To acquire a better understanding of the chemical behavior of complexes **1** and **1**$^+$ at different pH values, attempts were made to isolate and/or observe the species responsible for the electrochemistry described above.

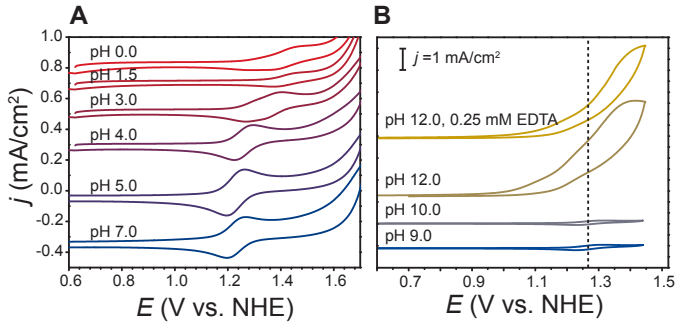

Figure 2. Cyclic voltammograms (100 mV/s) of 1.0 mM **1** in H_2O with 0.1 M Na_2SO_4 electrolyte at (a) pH 0.0 – 7.0 and (b) pH 9.0 – 12.0. The dashed line in (b) shows the **1/1**$^+$ redox couple.

The pH–dependent behavior of **1** suggests that the protonated cubane, **1**H$^+$, is present at lower pH values, and the existence of this complex was established by its isolation and characterization. Addition of 1 equiv of 4-toluenesulfonic acid (TsOH) to **1** in methanol afforded **[1H]OTs** in quantitative yield, and the structure of **[1H]OTs•4MeCN** was determined by X-ray crystallography (Figure S10A). With respect to **1**, the Co–OH bonds of **[1H]OTs** are elongated to an average length of 1.897(2) Å, while the remaining Co–O bond lengths remain unchanged with an average of 1.865(2) Å (**1** has a Co–O bond length range of 1.860 –1.876 Å).[34] A close contact of 2.586(2) Å between an oxygen atom of the cubane (O(4)) and the tosylate oxygen atom O(13) is consistent with O···H···O hydrogen bonding. The ^{1}H NMR spectrum of

[1H]OTs in CD_3CN at room temperature suggests that the molecule is C_s symmetric with broadened resonances, suggesting slow proton exchange on the NMR timescale. Furthermore, the infrared spectrum contains a broad peak at 3400 cm^{-1}, assigned to an O–H stretching mode.

The presence of a fully reversible redox couple over a wide pH range indicates that the chemical oxidation of **1** (or $\mathbf{1}H^+$) to $\mathbf{1}^+$ is feasible in water. Indeed, the oxidized cubane **[1]PF$_6$** has previously been isolated from the oxidation of **1** in acetonitrile.[29] In water, the reaction of **1** with 1 equiv of ceric ammonium nitrate, followed by addition of NH_4PF_6, resulted in precipitation of **[1]PF$_6$** as a black solid in 75% yield (Scheme 1, reaction A). Recrystallization from CH_2Cl_2/hexane afforded analytically pure single crystals of **[1]PF$_6$•CH$_2$Cl$_2$** for X-ray diffraction analysis (Figure S10B). The Co–O bond distances in the cubane core of **[1]PF$_6$** are in agreement with those reported in the literature.[29,38]

The oxidized cubane **[1]PF$_6$** is soluble in a mixture of neutral water and acetonitrile (9:1 by volume), but appears to form an acidic *aqua* complex under these conditions. Thus, a decrease in the observed pH from 8.2 to 5.9 (with 0.4 mM **[1]PF$_6$**) is consistent with acidification of H_2O *via* coordination to cobalt, that is $\mathbf{1(H_2O)}^+ \rightleftharpoons \mathbf{1(OH)} + H^+$. The ^{1}H NMR spectrum of **[1]PF$_6$** in pure CD_3CN consists of four very broad resonances corresponding to equivalent acetate (10.17 ppm) and pyridine (6.62 ppm, 6.15 ppm, 2.62 ppm) resonances. For a sample of **[1]PF$_6$** dissolved in 9:1 D_2O/CD_3CN, the same broad ^{1}H NMR resonances for **[1]PF$_6$** are observed, along with a set of four new resonances that correspond to a 23% conversion of **[1]PF$_6$** to a new species (Figure S5). The 8:8:4:12 ratio for these resonances is consistent with the presence of a new cubane species with four acetate and four pyridine ligands. The new resonances are paramagnetically shifted, as indicated by a pyridine-*H* chemical shift at 2.50 ppm, and an acetate-C*H*$_3$ resonance at 3.50 ppm. These results are consistent with the presence of a new Co(IV)-containing cubane cluster with an acidic *aqua* ligand, $\mathbf{1(H_2O)}^+$. Thus, an aqueous solution of **[1]PF$_6$** contains $\mathbf{1}^+$ and $\mathbf{1(H_2O)}^+$ in equilibrium, and the acidity of the latter species also implies the presence of **1(OH)** (Scheme 1, reaction B).

Scheme 1. Observed stoichiometric intermediates starting with **1**.

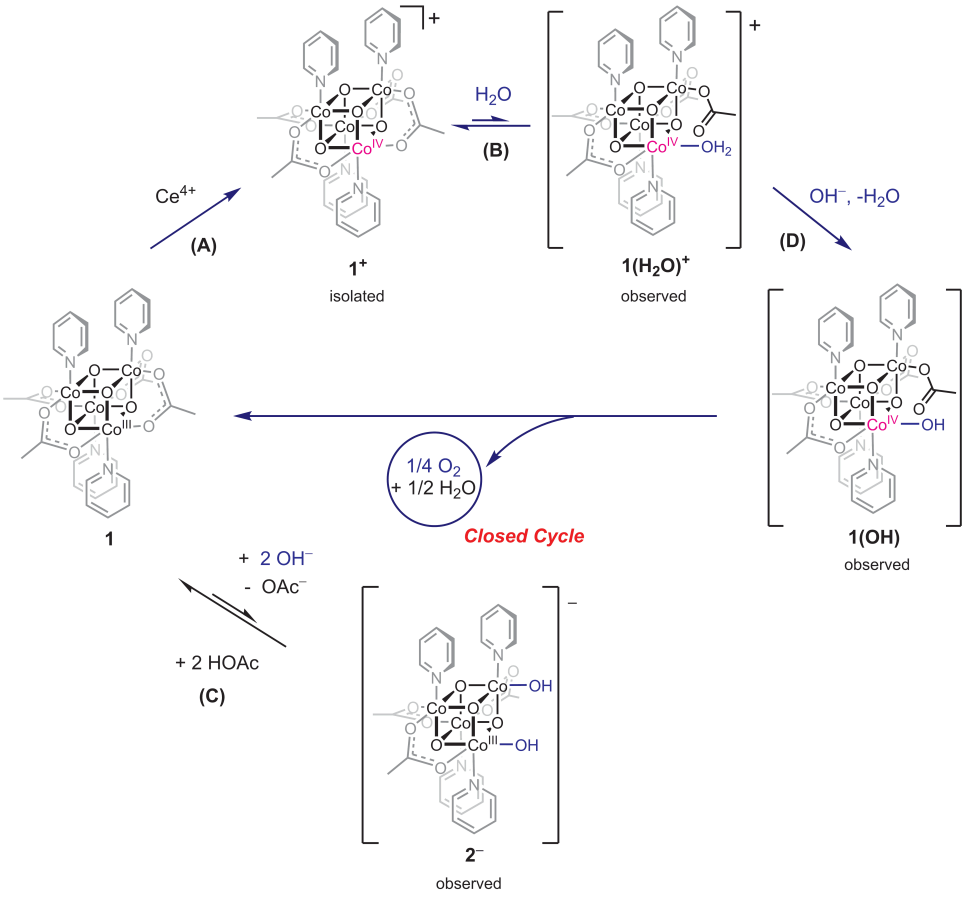

The species responsible for the anodic wave observed at pH 12 was targeted in the stoichiometric reaction of 1 equiv of NaOH with **1** in D_2O. By ^1H NMR spectroscopy, this reaction results in an equilibrium involving **1**, free acetate, and a new complex. Since many pyridine ligand resonances for the new complex overlap, ^1H TOCSY NMR spectroscopy was used to resolve them, and the resulting assignments are consistent with a C_2-symmetric cubane complex possessing two types of pyridine ligands in a 1:1 ratio (Figure S6). Furthermore, two new acetate ligand resonances are present in a 6:3 ratio, and integration of the pyridine and acetate peaks shows that the new species possesses four pyridine and three acetate ligands. This is confirmed by ^1H pulsed field gradient spin-echo (PGSE) diffusion NMR spectroscopy, which shows that the new acetate and pyridine resonances belong to the same species having a hydrodynamic radius that is similar to that of **1** (r_H = 7.0 Å for **1**, and 6.8 Å for the new species). This information is most consistent with a [Co(III)$_4$]-dihydroxide complex, $[Co_4O_4(OAc)_3py_4(OH)_2]^-$ (**2**$^-$), formed by substitution of an acetate ligand by two hydroxide ions (Scheme 1, reaction C). The chemical identity of **2**$^-$ and the presence of hydroxide ligands was furthered evidenced by addition of 1 equiv of acetic acid to the reaction mixture, which reformed **1** in quantitative yield by ^1H NMR spectroscopy. Note that the structural *syn*-dihydroxide motif assigned to **2**$^-$ has been proposed in the literature as an active site for O_2 evolution

in cobalt-oxide materials.[17,30,31,39] Thus, an appealing mechanism for O_2 formation observed in the cyclic voltammogram involves electrochemical oxidation of $\mathbf{2}^-$ to the $[Co(III)_3Co(IV)]$-dihydroxide state, followed by formation of the O–O bond. The possibility of a Co(IV)-hydroxide complex as a catalyst for water oxidation prompted us to pursue the observation or isolation of such a species.

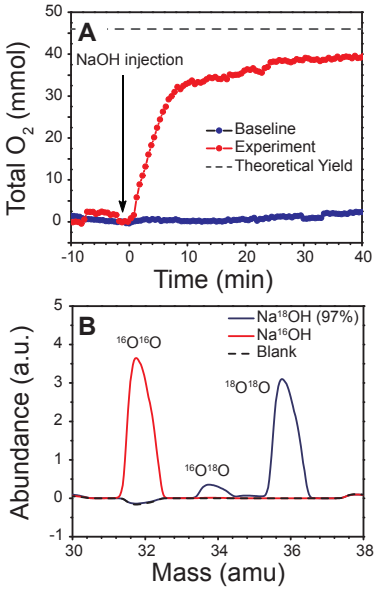

Figure 3. Measurement of O_2 from the reaction of **[1]PF$_6$** and NaOH. (A) Quantification by fluorescence probe. (B) Isotopic quantification by mass spectrometry.

A conceivable pathway to a Co(IV)–hydroxide complex in this system is by the associative addition of hydroxide to $\mathbf{1}^+$. Interestingly, reaction of **[1]PF$_6$** with 1 equiv of NaOH (*aq*) in CD_3CN quantitatively produced **1** (by ^{1}H NMR spectroscopy), indicating a net 1-electron reduction of $\mathbf{1}^+$ by hydroxide anion. On a larger scale, this reaction produced noticeable amounts of gas, suggesting the possibility of O_2 as a product of hydroxide oxidation by $\mathbf{1}^+$. Quantitative measurement by an O_2–sensing probe revealed a ~75% yield of O_2 with respect to **1**, though the yield is most likely higher since a non-trivial amount of unmeasured bubbles adhered to the wall of the flask (Figure 3A). Mass spectrometric measurement of the head space confirmed the presence of $^{32}O_2$, and when ~97% enriched $Na^{18}OH$ (in $H_2{}^{18}O$) was employed, 90% $^{36}O_2$ (94% theoretical) and 10% $^{34}O_2$ (5.9% theoretical) were detected (Figure 3B). High-resolution electrospray ionization mass spectrometry (ESI-MS) analysis of the solution after reaction with $Na^{18}OH$ showed no measurable incorporation of ^{18}O into **1**, meaning that the O-atoms within the cluster do not exchange with OH^-/H_2O on the timescale of the experiment (Figure S2). Significantly, this isotopic labeling experiment reveals that the O–O bond is formed solely from OH^- and *not* from the μ-O-atoms within the cuboidal core of $\mathbf{1}^+$. Note that while oxygen isotopic labeling studies with a cobalt oxide (Co-Pi) catalyst could not conclusively distinguish between mechanisms involving terminal versus bridging oxo/hydroxide ligands,[39] the results in this work favor mechanisms for which

only terminal oxo/hydroxide ligands are involved in O–O bond formation. Furthermore, the reaction of $\mathbf{1}^+$ with hydroxide supports the importance of the cobalt(IV) oxidation state in O_2 evolution by cobalt catalysts. The quantitative reduction of $\mathbf{1}^+$ by hydroxide to regenerate **1** and give O_2 completes a conceivable catalytic cycle, for which each stoichiometric step of the cycle has been observed (Scheme 1, reaction D).

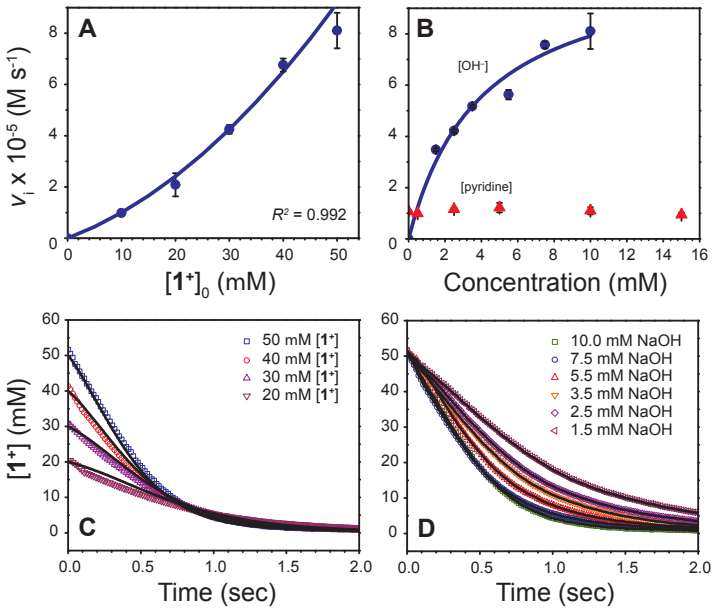

Figure 4. Kinetic plots. (A) Initial rate versus $[\mathbf{1}^+]$ (with 10 mM $[OH^-]$). (B) Initial rate versus $[OH^-]$ (•), and [pyridine] (with 5 mM $[OH^-]$) (▲). (C) and (D) Numerical kinetic modelling. The black solid lines are the fits from the model, and the shapes represent the measured values.

2.3 Kinetics and proposed mechanism

To gain further information on the mechanism of the reaction between $\mathbf{[1]PF_6}$ and NaOH, a kinetics analysis of the reaction by stopped-flow UV-vis spectroscopy was conducted in 9:1 H_2O:MeCN. The reaction progress was monitored by decay of an absorption for $\mathbf{[1]PF_6}$ at 280 nm. Two isosbestic points, at 335 and 362 nm, were observed for the reaction (Figure S7). These isosbestic points show that the decay of $\mathbf{1}^+$ and growth of product **1** are nearly symmetrical with no measurable buildup of an intermediate. A striking feature of all kinetic experiments is the slightly sigmoidal decay of $\mathbf{1}^+$ over the course of the reaction. The least-squares fit of the dependence of $[\mathbf{1}^+]_0$ on the initial rate at 10 mM $[OH^-]$ gives a mixed-order rate law containing a second-order term (k_{obs2} = 21000 ± 4000 $M^{-1}\,s^{-1}$) and a first-order term, (k_{obs1} = 0.8 ± 0.1 s^{-1}) (Figure 4A, eq 2).

$$v_i = k_{obs1}[\mathbf{1}^+]_0 + k_{obs2}[\mathbf{1}^+]_0^2 \qquad (2)$$

Scheme 2. Proposed mechanism for the reduction of $\mathbf{1}^+$ to **1** by hydroxide

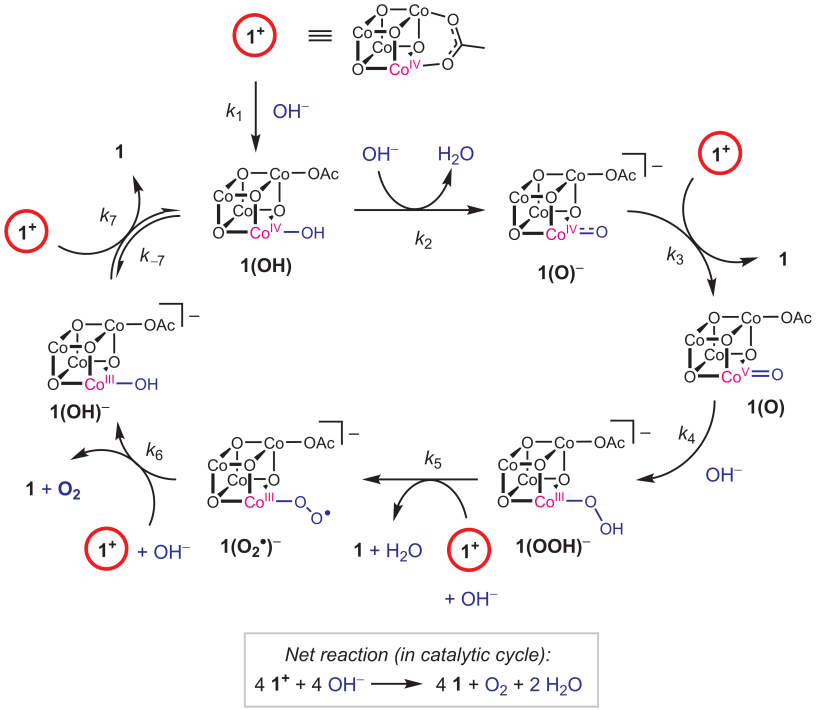

The second-order term strongly implicates the involvement of two molecules of $\mathbf{1}^+$ in the pathway to O–O bond formation, while the first-order term is consistent with either an activation of $\mathbf{1}^+$ or a concurrent pathway involving $\mathbf{1}^+$. Also, the rate of the reaction increased with increasing concentration of NaOH, but reached an asymptote at about 110 equivs of NaOH (6 mM, Figure 4B). This saturation behavior for NaOH suggests that OH^- reacts with an intermediate species whose concentration is limited. Four observations – the symmetry of growth and decay, the sigmoidal shape of the kinetic profile, the first- and second-order [$\mathbf{1}^+$] terms in the rate law, and the saturation behavior of [OH^-] – are most consistent with a chain reaction propagated by a small amount of non-steady-state catalytic intermediate.[40] In this type of chain reaction mechanism, the reactant is both a pre-catalyst and a participant in a catalytic cycle. The precatalyst activation step gives rise to the first-order term, and the reaction of the precatalyst with a catalytic intermediate gives the second-order term. Saturation behavior in [OH^-] is thus explained by reaction(s) of OH^- with catalytic intermediate(s). Pyridine has only a very weak inhibitory effect at high concentrations (16% rate decrease at 300 equivalents pyridine), implying that the reaction does not require dissociation of a pyridine ligand (Figure 4B). At 298 K, the activation free energy $\Delta G^{\ddagger}$ can be estimated from k_{obs2} to be 12 kcal/mol. When adjusted for the three steps involving H^+-transfer at pH 12 (–1.36ΔpH kcal/mol per deprotonation step) and a redox potential of 1.25 V (the redox potential for $\mathbf{1}/\mathbf{1}^+$), Siegbahn's calculated activation energy for O–O bond formation starting from Co(III) is 11.2 kcal/mol, which is very close to the value obtained from the kinetics.[30]

The proposed mechanism of Scheme 2 is consistent with all the experimental results described above. On the basis of the saturation behavior of hydroxide in this

system, and the first-order term in the rate law (*vide supra*), catalyst generation likely results from formation of **1(OH)**, by deprotonation of $\mathbf{1(H_2O)^+}$ or by addition of hydroxide ion to $\mathbf{1}^+$. The second-order term in $[\mathbf{1}^+]_0$ is explained by the participation of $\mathbf{1}^+$ as an oxidant in a proton-coupled electron transfer (PCET) process with **1(OH)**, represented in Scheme 2 by two steps (deprotonation followed by electron transfer) that generate the formally $[Co(III)_3Co(V)]$ species **1(O)**. Note, however, that the order of deprotonation and electron-transfer in the proposed mechanism is not distinguishable with these data. This unusually high oxidation state for cobalt is predicted to be favored over the $[Co(III)_2Co(IV)_2]$ state by several theoretical calculations; the oxidation state assignment is discussed in the following section.[30,32,33]

The reactions described above are consistent with the DFT calculations by Siegbahn for water oxidation, which indicate that $\mathbf{1(O)}^-$ is unable to engage in O–O bond formation by reaction with water; however, the higher oxidation state of **1(O)** should allow attack by water to produce the hydroperoxy species $\mathbf{1(OOH)}^-$.[30] Peroxide intermediates for cobalt catalysts have been speculated to exist based on observations by the groups of Frei and Stahl.[17,41] Finally, the OOH^- ligand may be readily oxidized to superoxide ($\mathbf{1(O_2^{\bullet})}^-$), then finally to O_2. The plausibility of the peroxide oxidation was tested by the reaction of $\mathbf{[1]PF_6}$ with hydrogen peroxide, which gave O_2 and the reduced and protonated cubane, $\mathbf{[1H]PF_6}$, characterized by ^1H NMR spectroscopy and single crystal X-ray diffraction (Figure S8). Kinetic measurements on the reaction in 9:1 MeCN:H_2O by stopped-flow UV-vis indicate clean first-order behavior for $[\mathbf{1}^+]$ and $[H_2O_2]$, with a second order rate constant of $k = 78 \pm 3\ M^{-1}\ s^{-1}$ at 25 °C. Replacement of **1(OH)** by $\mathbf{2}^-$ in the catalytic cycle should give the analogous intermediates, with the only difference being that an OAc^- ligand is replaced by an OH^- ligand.

A possible, related mechanism (Scheme S1) could involve displacement of acetate from **1(OH)** by hydroxide, to produce the dihydroxide **2**. This reaction would be analogous to that observed between **1** and OH^-, which leads to $\mathbf{2}^-$ and acetate (*vide supra*). The more oxidized dihydroxide **2**, with a $[Co(III)_3Co(IV)](OH)_2$ diamond core moiety, would then have to be oxidized (by $\mathbf{1}^+$) to a $[Co(III)_2Co(IV)_2]$ or $[Co(III)_3Co(V)]$ analogue before engaging in O–O bond formation across one face of the cubane. DFT calculations indicate that dicobalt centers like this may undergo O–O bond formation from the Co(IV)Co(IV) state, perhaps *via* deprotonation to an oxo-hydroxy intermediate.[31,42] Note that Siegbahn's DFT calculation indicates that a direct coupling mechanism of this type is less preferred in cubanes, by ~3 kcal/mol.[30]

This complex mechanism was modeled numerically with global kinetics analysis, which successfully reproduced the initial rates, as well as the entire kinetic profile (Figures 4C and 4D). The model utilized eight rate constants (see Supporting Information); however, a sensitivity analysis (Figure S8) revealed that only the values of k_1, k_3, and k_7 were major contributors for a good fit. Not surprisingly, those rate constants (k_1, k_3, and k_7) represent the key features of the mechanism: catalyst activation, oxidation to a formal Co(V) by disproportionation, and catalyst turnover. Similar conclusions about the rate equation could also be derived analytically, as follows. A rate law for the initial rates with excess $[OH^-]$ can be derived for the proposed mechanism using the steady-state approximation for all intermediates except **1(OH)** (see Supporting Information), which

describes the experimental observations: the first- and second-order terms in $[\mathbf{1}^+]_0$, and the saturation behavior in $[OH^-]$ (eq. 3). At very high concentrations of $[OH^-]$, low concentrations of product ($[\mathbf{1}] \approx 0$), and for $[\mathbf{1}^+] = f[\mathbf{1}^+]_0$ (where $0 < f < 1$), the rate law reduces to eq. 2 with the expressions for k_{obs1} and k_{obs2} given in eqs. 4 and 5. Again, it is shown that the kinetics (under excess $[OH^-]$ conditions) depend only on k_1, k_3, and k_7, in good agreement with the numerical fitting. Additionally, it can be shown that the exact expression of $[\mathbf{1}^+](t)$ over *all time* is a sigmoidal curve (eq. S12 and Figure S9). The consistency of this model with all the observations is compelling evidence for the proposed mechanism.

$$-\frac{d[\mathbf{1}^+]}{dt} = k_1[\mathbf{1}^+][OH^-] + \frac{2k_2\left([\mathbf{1}^+]_0 - [\mathbf{1}^+] - [\mathbf{1}]\right)[OH^-]}{k_2\frac{[OH^-]}{[\mathbf{1}^+]}\left(\frac{k_3+k_7}{k_3k_7}\right) + \frac{k_2}{k_4} + \frac{k_2}{k_5[\mathbf{1}^+]} + \frac{k_2}{k_6[\mathbf{1}^+]} + \frac{k_{-7}[\mathbf{1}]}{k_7[\mathbf{1}^+]} + 1} \quad (3)$$

$$k_{obs1} = k_1 f[OH^-] \quad (4)$$

$$k_{obs2} = \frac{2k_3k_7}{k_3+k_7}\left(f - f^2\right) \quad (5)$$

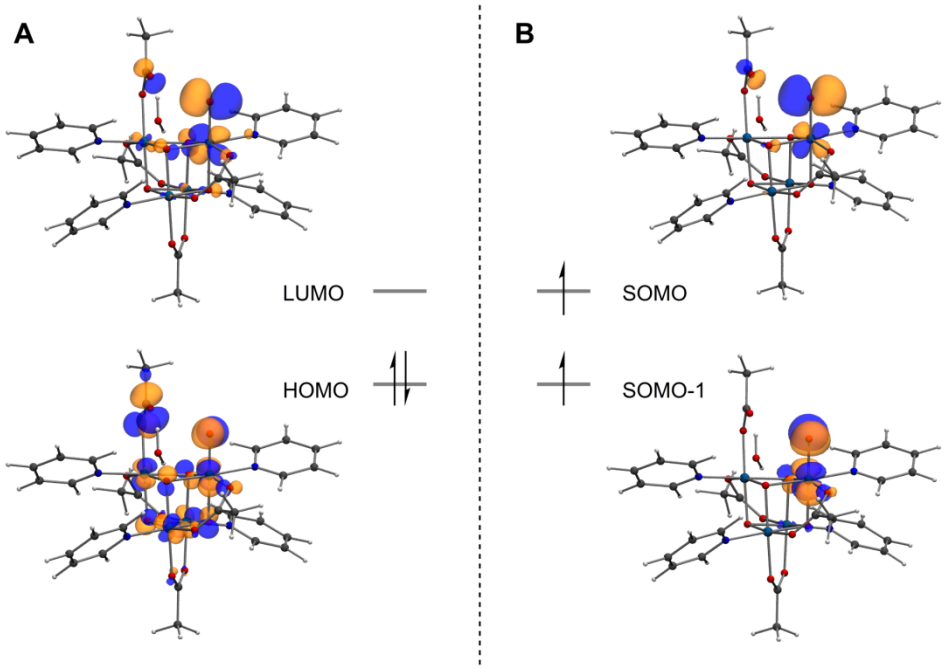

Figure 5. Density functional theory (DFT) calculated molecular orbitals of **1(O)·H₂O** using B3LYP/6-31G+d,p: (a) The singlet state frontier orbitals, and (b) the triplet state frontier orbitals (β-spin).

2.4 Nature of the Highly Oxidized Intermediate

The kinetic experiments discussed above suggest that the formal $[Co(III)_3Co(IV)]$ oxidation state disproportionates into the $[Co(III)_4]$ state and a higher oxidation state, $[Co(III)_2Co(IV)_2]$ or $[Co(III)_3Co(V)]$. Of course, the concept of oxidation state is merely a formalism having a defined set of rules,[43] and extrapolation of this formalism to actual charge distributions must be made with caution. Nonetheless, it may be instructive to determine the location of the electron hole in the oxidized cluster. Significantly, Co(V) has never been observed spectroscopically but it has often been suggested by calculations. If the mechanism suggested by the kinetic data is correct, it would not be possible to build up significant concentrations of the formal $[Co(III)_3Co(V)]$ species **1(O)** for typical spectroscopic investigations. Therefore, we choose to investigate the nature of this intermediate species with DFT calculations.

First, the feasibility of the Co(V) oxidation state may be considered on the basis of simple ligand-field arguments. While it has been demonstrated that the electron hole in the $[Co(III)_3Co(IV)]$ complex ($\mathbf{1}^+$) is completely delocalized over the cubane (each Co is better described with an "oxidation state"/charge of +3.125),[25] introduction of the strongly π-basic terminal oxo ligand at one cobalt center in the cubane ($\mathbf{1(O)}^-$) is expected to raise the energy of the corresponding t_{2g}-like orbitals to effectively localize the electron hole at that particular cobalt ion. Stated another way, the electron hole should be most stable on the cobalt ion associated with the π-basic terminal oxo ligand. Thus, the terminal oxo ligand should cause a shift from $[Co(+3.125)_4]$ toward $[Co(III)_3Co(IV)]$. By the same argument, the $[Co(III)_3Co(V)]$ state should also be a better description than $[Co(III)_2Co(IV)_2]$ in the **1(O)** complex, as the presence of the terminal oxo ligand should also cause preferential localization of the hole. These ligand-field rationalizations provide an intuitive albeit rough guide for possible oxidation state assignments.

Density-functional theory (DFT) can potentially provide a more quantitative description of the oxidation state. Complex **1(O)** has been described by Siegbahn[30] to have an $S = 1$ ground state, with an $S = 0$ excited state 5.6 kcal/mol higher in energy. Inspection of the molecular orbitals in both the triplet and singlet states indicates significant localization of the SOMO and LUMO, respectively, on the terminal Co–oxo moiety (Figure 5). In the triplet state, the β-spin wavefunctions reside predominately on the Co–O unit, while the α-electron wavefunctions are more delocalized throughout the cubane (Figure S11). Similarly, in the singlet state, the LUMO is localized on the Co–O unit. These results reiterate the spin-density calculations by Siegbahn, and are also more consistent with the formal $[Co(III)_3Co(V)]$ oxidation state. In summary, both ligand-field arguments and DFT calculations support the formal oxidation state in **1(O)** as being described as $[Co(III)_3Co(V)]$ rather than $[Co(III)_2Co(IV)_2]$.

2.5 Conclusions

The characterization of species implicated by electrochemical experiments over a wide pH range provides important insights into the reactivity of a cobalt cubane cluster. The $[Co(III)_4]$ cubane **1** reacts with H^+ as well as OH^- to give observable products. Although it is difficult to establish the identity of the electrocatalyst implicated by CV studies, stoichiometric reactivity demonstrates that cobalt cubane **1** reacts with OH^- to

produce a likely WOC, and the [Co(III)$_3$Co(IV)] cubane (**[1]PF$_6$**) reacts with OH^- to produce O_2 with quantitative reduction to **1**. These reactions strongly suggest that there exists at least one molecular, homogeneous pathway for O_2 evolution by cobalt cubane complexes. Kinetic experiments on the stoichiometric oxygen evolution from **1**$^+$ provide strong, direct evidence for the homogenous nature of the reaction, especially as it obeys a rate law consistent with the proposed mechanism. The second-order term in [**1**$^+$] indicates that a more oxidized state for the cubane, formally [Co(III)$_3$Co(V)], must be reached *via* disproportionation of the [Co(III)$_3$Co(IV)] state, before O_2 evolution. The participation of a terminal cobalt-oxo intermediate is supported by several observations, including the noninvolvement of cubane oxo ligands in the formation of O_2, the viability of intermediates **1(H$_2$O)**$^+$ and **1(OH)**, and the dependence of the rate on [OH^-]. Furthermore, the experimentally determined activation energy is consistent with theoretical values reported in the literature. This study helps solidify the role of cobalt cubane complexes as water oxidation catalysts, and as useful structural and functional models for cobalt-oxide materials. Significantly, this work suggests that O–O bond formation on cobalt oxide occurs *via* terminal oxo, rather than bridging oxo ligands present at edge sites.

These results provide several guidelines relevant to future catalyst design strategies. The most relevant formal oxidation states for cobalt WOCs appear to be +3, +4, and +5, while the +2 oxidation state does not appear to be necessary in the catalytic cycle. Thus, supporting frameworks should be designed to stabilize the higher oxidation states such as Co(IV) and Co(V). Multi-metallic oxido systems, such as the cobalt cubane described herein, are well suited to stabilize such states as they can relieve the burden of an unstable oxidation state by sharing an electron hole throughout the cluster. Ancillary ligands may play a key role in tuning a cluster's redox potentials to those appropriate for efficient water oxidation. In addition, catalyst design must allow for water or hydroxide to bind to the cobalt center, as this is the first step towards generating the putative high-valent cobalt-oxo intermediate. Finally, since bridging oxo ligands do not appear to play a direct role in O_2 formation, design elements that allow formation of terminal cobalt-oxo moieties, while stabilizing the [Co_4O_4] core, may prove advantageous to WOCs.

2.6 Acknowledgements

We thank Heinz Frei for help with the mass spectrometry measurements of O_2, Anthony T. Iavarone for electrospray-ionization mass spectrometry (ESI-MS) (QB3 Chemistry Mass Spectrometry Facility), and Kurt van Allsburg, Gavin R. Kiel, Patrick W. Smith, Robert G. Bergman, and Richard G. Finke for helpful discussions. We also would like to thank Antonio DiPasquale for assistance with solving X-ray diffraction structures, and the NIH Shared Instrumentation Grant S10-RR027172. This work was supported by the Director, Office of Science, Office of Basic Energy Sciences of the US Department of Energy under contract No. DE-AC02-05CH11231. P.O.-B. thanks the grant PIOF-GA-2011–299571 (7th FP, People Marie Curie Actions) for funding.

2.7 References

(1) IPCC. Climate Change 2014: Synthesis Report. Contribution of Working Groups I, II and III to the Fifth Assessment Report of the Intergovernmental Panel on Climate Change; Core Writing Team, Rajendra K. Pachauri, Leo Meyer, Series Eds.; Cambridge University Press: United Kingdom and New York, NY, USA, 2014; p 138.
(2) Lewis, N. S.; Nocera, D. G. *Proc. Natl. Acad. Sci.* **2006**, 103 (43), 15729.
(3) Barber, *J. Chem. Soc. Rev.* **2008**, 38 (1), 185.
(4) Moore, G. F.; Brudvig, G. W. *Annu. Rev. Condens. Matter Phys.* **2011**, 2 (1), 303.
(5) Eisenberg, R.; Gray, H. B. *Inorg. Chem.* **2008**, 47 (6), 1697.
(6) Rüttinger, W.; Dismukes, G. C. *Chem. Rev.* **1997**, 97 (1), 1.
(7) Walter, M. G.; Warren, E. L.; McKone, J. R.; Boettcher, S. W.; Mi, Q.; Santori, E. A.; Lewis, N. S. *Chem. Rev.* **2010**, 110 (11), 6446.
(8) Kärkäs, M. D.; Verho, O.; Johnston, E. V.; Åkermark, B. *Chem. Rev.* **2014**, 114 (24), 11863.
(9) Cox, N.; Retegan, M.; Neese, F.; Pantazis, D. A.; Boussac, A.; Lubitz, W. *Science* **2014**, 345 (6198), 804.
(10) Kern, J.; Alonso-Mori, R.; Tran, R.; Hattne, J.; Gildea, R. J.; Echols, N.; Glöckner, C.; Hellmich, J.; Laksmono, H.; Sierra, R. G.; Lassalle-Kaiser, B.; Koroidov, S.; Lampe, A.; Han, G.; Gul, S.; DiFiore, D.; Milathianaki, D.; Fry, A. R.; Miahnahri, A.; Schafer, D. W.; Messerschmidt, M.; Seibert, M. M.; Koglin, J. E.; Sokaras, D.; Weng, T.-C.; Sellberg, J.; Latimer, M. J.; Grosse-Kunstleve, R. W.; Zwart, P. H.; White, W. E.; Glatzel, P.; Adams, P. D.; Bogan, M. J.; Williams, G. J.; Boutet, S.; Messinger, J.; Zouni, A.; Sauter, N. K.; Yachandra, V. K.; Bergmann, U.; Yano, J. *Science* **2013**, 340 (6131), 491.
(11) Betley, T. A.; Wu, Q.; Van Voorhis, T.; Nocera, D. G. *Inorg. Chem.* **2008**, 47 (6), 1849.
(12) Delaplane, R. G.; Ibers, J. A.; Ferraro, J. R.; Rush, J. J. *J. Chem. Phys.* **1969**, 50 (5), 1920.
(13) Kanan, M. W.; Nocera, D. G. *Science* **2008**, 321 (5892), 1072.
(14) Jiao, F.; Frei, H. *Angew. Chem. Int. Ed.* **2009**, 48 (10), 1841.
(15) Esswein, A. J.; McMurdo, M. J.; Ross, P. N.; Bell, A. T.; Tilley, T. D. *J. Phys. Chem. C* **2009**, 113 (33), 15068.
(16) Hans Wedepohl, K. *Geochim. Cosmochim. Acta* **1995**, 59 (7), 1217.
(17) Zhang, M.; de Respinis, M.; Frei, H. *Nat. Chem.* **2014**, 6 (4), 362.
(18) Ahn, H. S.; Yano, J.; Tilley, T. D. *Energy Environ. Sci.* **2013**, 6 (10), 3080.
(19) Yin, Q.; Tan, J. M.; Besson, C.; Geletii, Y. V.; Musaev, D. G.; Kuznetsov, A. E.; Luo, Z.; Hardcastle, K. I.; Hill, C. L. *Science* **2010**, 1185372.
(20) Wasylenko, D. J.; Ganesamoorthy, C.; Borau-Garcia, J.; Berlinguette, C. P. *Chem. Commun.* **2011**, 47 (14), 4249.
(21) Wang, D.; Groves, J. T. *Proc. Natl. Acad. Sci.* **2013**, 110 (39), 15579.
(22) Stracke, J. J.; Finke, R. G. ACS Catal. **2014**, 4 (3), 909.
(23) Stracke, J. J.; Finke, R. G. *J. Am. Chem. Soc.* **2011**, 133 (38), 14872.

(24) Beattie, J. K.; Hambley, T. W.; Klepetko, J. A.; Masters, A. F.; Turner, P. *Polyhedron* **1998**, 17 (8), 1343.
(25) McAlpin, J. G.; Stich, T. A.; Ohlin, C. A.; Surendranath, Y.; Nocera, D. G.; Casey, W. H.; Britt, R. D. *J. Am. Chem. Soc.* **2011**, 133 (39), 15444.
(26) McCool, N. S.; Robinson, D. M.; Sheats, J. E.; Dismukes, G. C. *J. Am. Chem. Soc.* **2011**, 133 (30), 11446.
(27) Ganga, G. L.; Puntoriero, F.; Campagna, S.; Bazzan, I.; Berardi, S.; Bonchio, M.; Sartorel, A.; Natali, M.; Scandola, F. *Faraday Discuss.* **2012**, 155 (0), 177.
(28) Zhang, B.; Li, F.; Yu, F.; Wang, X.; Zhou, X.; Li, H.; Jiang, Y.; Sun, L. *ACS Catal.* **2014**, 4 (3), 804.
(29) Ullman, A. M.; Liu, Y.; Huynh, M.; Bediako, D. K.; Wang, H.; Anderson, B. L.; Powers, D. C.; Breen, J. J.; Abruña, H. D.; Nocera, D. G. *J. Am. Chem. Soc.* **2014**, 136 (50), 17681.
(30) Li, X.; Siegbahn, P. E. M. *J. Am. Chem. Soc.* **2013**, 135 (37), 13804.
(31) Wang, L.-P.; Van Voorhis, T. *J. Phys. Chem. Lett.* **2011**, 2 (17), 2200.
(32) Fernando, A.; Aikens, C. M. *J. Phys. Chem. C* [Online Early Access]. DOI: 10.1021/jp511805x.
(33) Mattioli, G.; Giannozzi, P.; Amore Bonapasta, A.; Guidoni, L. *J. Am. Chem. Soc.* **2013**, 135 (41), 15353.
(34) Chakrabarty, R.; Bora, S. J.; Das, B. K. *Inorg. Chem.* **2007**, 46 (22), 9450.
(35) Symes, M. D.; Surendranath, Y.; Lutterman, D. A.; Nocera, D. G. *J. Am. Chem. Soc.* **2011**, 133 (14), 5174.
(36) Pakalapati, S. N. R.; Popov, B. N.; White, R. E. *J. Electrochem. Soc.* **1996**, 143 (5), 1636.
(37) Eckenhoff, W. T.; Eisenberg, R. *Dalton Trans.* **2012**, 41 (42), 13004.
(38) Stich, T. A.; Krzystek, J.; Mercado, B. Q.; McAlpin, J. G.; Ohlin, C. A.; Olmstead, M. M.; Casey, W. H.; David Britt, R. *Polyhedron* **2013**, 64, 304.
(39) Surendranath, Y.; Kanan, M. W.; Nocera, D. G. *J. Am. Chem. Soc.* **2010**, 132 (46), 16501.
(40) Mower, M. P.; Blackmond, D. G. *J. Am. Chem. Soc.* **2015**, 137, 2386-2391.
(41) Gerken, J. B.; McAlpin, J. G.; Chen, J. Y. C.; Rigsby, M. L.; Casey, W. H.; Britt, R. D.; Stahl, S. S. *J. Am. Chem. Soc.* **2011**, 133 (36), 14431.
(42) Davenport, T. C.; Ahn, H. S.; Ziegler, M. S.; Tilley, T. D. *Chem. Commun.* **2014**, 50 (48), 6326.
(43) IUPAC. Compendium of Chemical Terminology, 2nd ed. (the "Gold Book"). Compiled by A. D. McNaught and A. Wilkinson. Blackwell Scientific Publications, Oxford (1997).

Supporting Information for **Chapter 2**

General considerations. Cobalt(II) nitrate hexahydrate, pyridine, hydrogen peroxide (34-37% in water), ceric ammonium nitrate, ammonium hexafluorophosphate, tosylic acid monohydrate, and sodium metal were purchased from Sigma-Aldrich and used without further purification. Sodium acetate trihydrate was purchased from EMD. Solvents were purchased from Fisher-Scientific and used without any further purification. $H_2{}^{18}O$ (97%) was purchased from Cambridge Isotopes. Routine NMR spectra were recorded on Bruker AVB-400, AVQ-400 and AV-300 spectrometers at room temperature. d_3-MeCN and D_2O were purchased from Cambridge Isotopes. ^{1}H NMR spectra were referenced to residual protio-solvent peaks (δ 2.94 for CD_3CN, δ 4.79 for D_2O). Electrospray ionization mass spectrometry measurements were performed at the QB3 Mass Spectrometry Facility at UC Berkeley using a quadrupole time-of-flight mass spectrometer (Q-TOF Premier, Waters, Milford, MA) that was equipped with an electrospray ionization (ESI) source. ESI source voltages were adjusted for optimum desolvation and transmission of ions of interest prior to recording mass spectra. Elemental analyses were carried out by the College of Chemistry Microanalytical Laboratory at the University of California, Berkeley. Infrared spectra were recorded on a Bruker Alpha P attenuated total reflectance instrument.

Synthesis of 1. Cobalt(II) nitrate hexahydrate (10.00 g, 34.3 mmol) and sodium acetate trihydrate (9.35 g, 68.6 mmol) were dissolved in 100 mL of methanol, and then pyridine (2.8 mL, 34 mmol) was added. Hydrogen peroxide (34-37% w/w in water, 17.1 mL, 170 mmol) was added dropwise to this solution, and then the reaction mixture was refluxed for 2 h. The dark brown-green solution was dried *in vacuo*, and the solid was partitioned between 20 mL of water and 100 mL of dichloromethane. The organic layer was collected, and the aqueous layer was extracted with 2 x 100 mL of dichloromethane. The combined extracts were dried with $MgSO_4$ and concentrated to ~50 mL, to which 500 mL of hexanes was added to induce crystallization. The solid was dry-loaded onto a silica column and eluted with 5% methanol in acetone. The fractions were dried to give a dark-green solid (2.01 g, 27%), which was pure by ^{1}H NMR spectroscopy. To remove trace Co(II), the solid (0.580 g) was dissolved in 5 mL of 0.10 M Na_4EDTA, extracted with dichloromethane (5 x 50 mL), dried with $MgSO_4$, and volatiles were removed *in vacuo* to yield a green solid (0.280 g). The cyclic voltammogram of **1** in Na_2SO_4 electrolyte at pH 12 is shown in Figure S1A. A control experiment with 280 ppb Co(II) (5.7 μM $Co(OAc)_2(H_2O)_4$) under identical conditions was conducted, since it had been noted by Nocera and coworkers[1] that in theory, the decomposition of only 70 ppb of **1** could result in observable catalysis from the resulting Co(II) species. This control experiment showed that Co(II) at this concentration is not nearly as active as solutions containing purified **1** (Figure S1A).

To check purity by electrochemistry, CV of **1** was also performed in 0.1 KP_i buffer (pH 7), Figure S1C. The current at 1.3 V vs Ag/AgCl can be used to estimate [Co(II)]. Using the equation i_{pa} = 0.0109 mA = 0.018 x [Co(II)]mM – 0.6,[1] an upper limit of 0.03 mM Co(II) was extracted, assuming a linear trend of i_{pa} for all [Co(II)]. In the presence of 0.25 mM Na_4EDTA, the upper limit of [Co(II)] is 6.6 x 10^{-19} M (using

the K_f for $Co(EDTA)^{2+}$ = 2 x 10^{16}) corresponding to 6 x 10^{-10} ppb Co(II). Thus the experiment with 280 ppb Co(II) already demonstrates that Co(II) cannot be responsible for the observed electrocatalysis.

Synthesis of [1]PF_6. Compound **1** (1.00 g, 1.17 mmol) was dissolved in 30 mL of water. Ceric ammonium nitrate (0.708 g, 1.30 mmol) in 10 mL of water was added to the solution of **1**, and the resulting solution was stirred for 3 min. Ammonium hexafluorophosphate (0.191 g, 1.17 mmol) in 20 mL of water was added to the reaction mixture, producing a black solid. The solid was collected by filtration and washed with 3 x 50 mL water. The air-dried solid was then dissolved in 10 mL of dichloromethane and filtered. Hexanes (40 mL) was added to form black crystals of **[1]PF_6•CH_2Cl_2** which were collected by decantation (0.880 g, 70%). Pure **[1]PF_6** was obtained by drying the solid under vacuum for 24 h. The ^{1}H NMR and EPR spectra are consistent with those previously reported. The presence of Co(II) species was examined by dissolving 10 mg of **1[PF_6]** in 10 mL of 0.1 M Na_2SO_4 at pH 12, and then obtaining the cyclic voltammogram (CV). The CV of the material is nearly identical to the CV of pure **1** (Figure S1B).
Anal. Calcd for $C_{28}H_{32}Co_4F_6N_4O_{12}P$: C, 33.72; H, 3.23; N, 5.62. Found: C, 34.07; H, 3.54; N, 6.12.

Synthesis of [1-H]OTs. Tosylic acid monohydrate (0.0450 g, 0.234 mmol) was added to **1** (0.200 g, 0.234 mmol) in 10 mL of methanol. The solution was stirred for 10 min, and then the volatile components were removed to yield a brown solid (100%). Single crystals of **[1-H]OTs•4MeCN** were grown by vapor diffusion of diethyl ether into an acetonitrile solution. ^{1}H NMR (300 MHz, CD_3CN) δ: 2.01 (s, 6H, acetate-CH_3), 2.16 (s, 6H, acetate-CH_3), 2.45 (s, 3H, tosylate-CH_3) 7.16-7.24 (m, 8H, *m*-pyridine-*H*), 7.42 (br, 2H, tosylate-aryl-*H*), 7.71 (m, 4H, *p*-pyridine-*H*), 8.24 (br, 2H, tosylate-aryl-*H*), 8.43-8.48 (br, 8H, *o*-pyridine-*H*). Anal. Calcd for $C_{35}H_{40}Co_4N_4O_{15}S$•$CH_3CN$: C, 41.71; H, 4.07; N, 6.57. Found: C, 41.19; H, 4.30; N, 6.24.

Synthesis of [1-H]PF_6. Hydrogen peroxide (34-37%, 9 μL, 0.1 mmol) was added to **[1]PF_6** (0.100 g, 0.100 mmol) in 10 mL of dichloromethane, and the reaction mixture was stirred for 16 h at room temperature. The volatile materials were removed to give a black solid (0.10 g, 100%). Layering hexanes over a dichloromethane solution of **[1-H]PF_6** gave single crystals of **[1-H]PF_6•(x > 1)CH_2Cl_2•$2H_2O$**. ^{1}H NMR (300 MHz, CD_3CN) δ: 2.15 (s, 12H, acetate-CH_3), 7.24 (br, 8H, *m*-pyridine-*H*), 7.70 (br, 4H, *p*-pyridine-*H*), 8.31 (br, 8H, *o*-pyridine-*H*). Anal. Calcd for $C_{28}H_{37}Co_4F_6N_4O_{14}P$: C, 32.52; H, 3.61; N, 5.42. Found: C, 32.21; H, 3.49; N, 5.34.

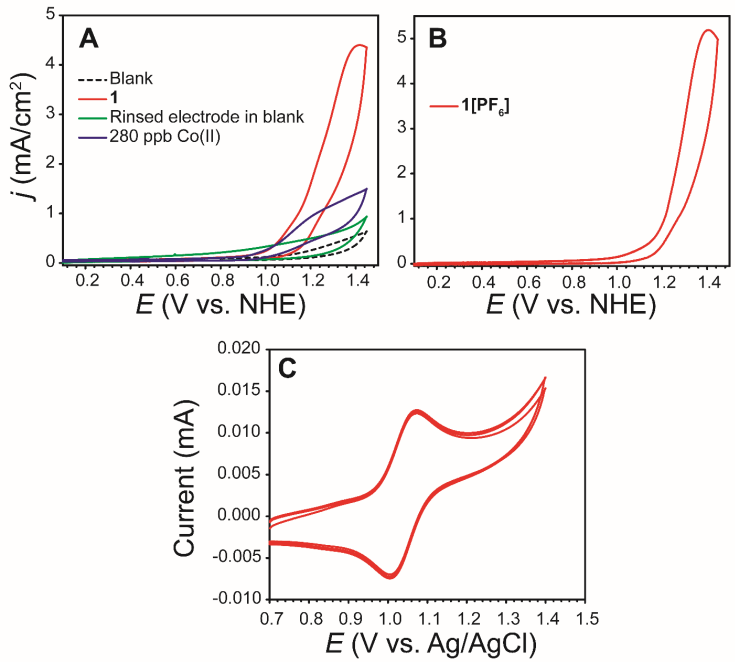

Figure S1. Cyclic voltammograms at 100 mV/s of 1 mM **1** (A) and 1 mM **1[PF_6]** (B) in 0.10 M Na_2SO_4 at pH 12. Scan rate is 100 mV/s. (C) 1 mM of **1** in 0.1 M KPi buffer at pH 7.

Reaction of NaOH with 1[PF_6] in CD_3CN. A ^1H NMR spectrum of **1[PF_6]•CH_2Cl_2** (0.021g, 0.019 mmol) in 600 µL CD_3CN was taken. Then sodium hydroxide (42 µL of 0.50 M in H_2O, 0.021 mmol) was added to the solution. After 10 minutes, the ^1H NMR spectrum was acquired. Using the CH_2Cl_2 resonance as the internal standard, the reaction formed **1** in 100% yield.

Preparation of 0.50 M $Na^{18}OH$ in $H_2{}^{18}O$. Sodium metal (0.0115g, 0.5 mmol) was added carefully to 1.0 mL of $H_2{}^{18}O$ (97%). The reaction was complete in seconds.

Determination of oxygen evolution. Oxygen was detected using an Ocean Optics Multi-Frequency Phase Fluorimeter (MFPF-100) with a FOSPOR-R probe inserted in the headspace of a sealed flask. The probe was calibrated at a single temperature by fitting a second order polynomial to eight O_2 concentrations between 0.0 and 10.6%, which were produced using pair of mass-flow controllers. Henry's Law was used to account for oxygen that remained dissolved in solution.

Baseline O_2. A 50 mL round bottom flask was filled with 25 mL water, and equipped with a stir bar. The flask was stoppered with a rubber septum holding the Ocean Optics O_2 sensor probe. Silicone grease was used to seal around the probe. The flask was then purged by bubbling N_2 (*via* an inlet needle and an exit needle) for 20 minutes. The purging needle was removed and the O_2 was measured for ~10 minutes, at which point, a

0.40 mL solution of 0.50 M NaOH was added. The O_2 measurement was continued for 1 hour.

*With **1[PF_6]***. A 50 mL round bottom flask was filled with 25 mL of water, and then equipped with a stir bar. Solid **1[PF_6]** was suspended in the solution. The flask was stoppered with a rubber septum holding the Ocean Optics O_2 sensor probe. Silicone grease was used to seal around the probe. The flask was then purged by bubbling N_2 (*via* an inlet needle and an exit needle) for 20 minutes. The purging needle was removed and the O_2 was measured for ~10 minutes, at which point, a 0.40 mL solution of 0.50 M NaOH was added. The O_2 measurement was continued for 1 hour.

Mass spectroscopic monitoring of oxygen evolution

$^{18}O_2$ measurement. A solution containing 0.200 g **[1]PF_6•CH_2Cl_2** in 10 mL of dry MeCN was added to a 40 mL round bottom flask equipped with an attachment for an evacuated 7 mL Teflon-sealed bulb and a stir bar, and stoppered with a rubber septum. The solution was purged with N_2 for 10 min. A solution of $Na^{18}OH$ (0.40 mL, 0.50 M) in 97% $H_2{}^{18}O$ was injected by syringe and stirred for 10 min. The headspace was sampled by opening the Teflon seal and closing it. The headspace aliquot was analyzed by a quadruple mass spectrometer (Pfeiffer model Omnistar 422).

$^{16}O_2$ measurement. The experiment was repeated using $Na^{16}OH$ in $H_2{}^{16}O$ instead.

Control measurement. The control experiment was run with exact same procedure except without **[1]PF_6**.

Electrospray-Ionization Mass Spectrometry (ESI-MS). An aliquot of the solution from the $^{18}O_2$ measurement experiment was diluted with MeCN, and analyzed with high-resolution ESI-MS. The spectrum is shown below in Figure S2 (The vertical lines and masses in parentheses denote the predicted masses):

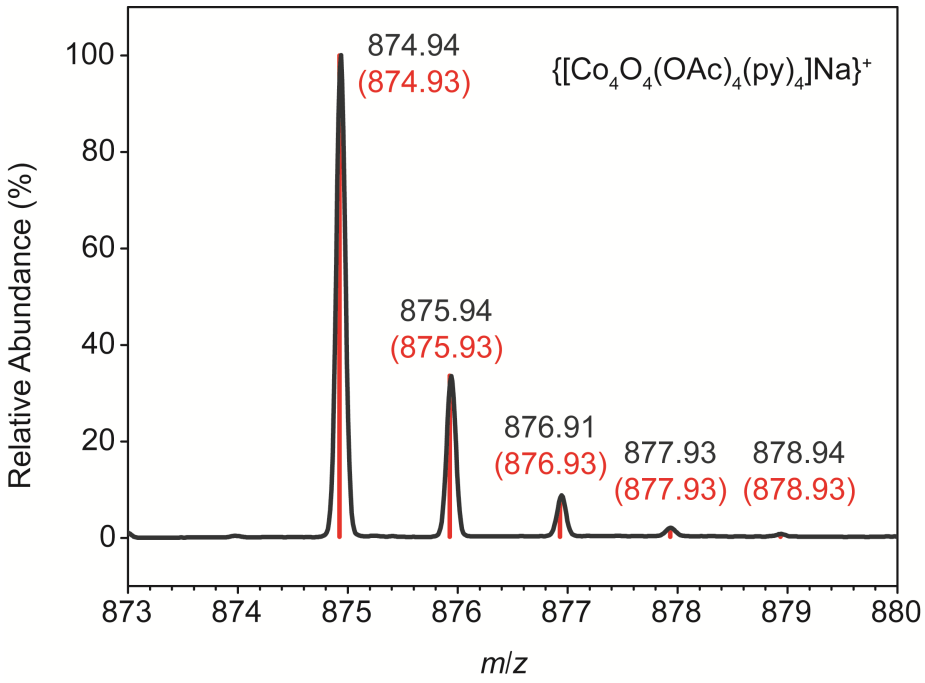

Figure S2. High-resolution electrospray mass spectrum post reaction of **[1]PF$_6$** with Na^{18}OH.

Electrochemistry.

Cyclic voltammograms were obtained on a BASi Epsilon potentiostat at 25°C, in water with 0.10 M sodium sulfate electrolyte, platinum wire counter electrode, glassy carbon working electrode (7 mm diameter, polished with 0.05 μm alumina), and either Ag/AgCl (for pH 0 – 8) or Hg/HgO (for pH 9 – 12) reference electrodes. The pH was adjusted by addition of tosylic acid monohydrate or NaOH. A Thermo Orion 2-Star Benchtop pH meter used to determine pH and was calibrated using three points: pH 4, 7, 10 buffer solutions. Turnover frequencies (TOF) were calculated using the equation below.[2]

$$\frac{i_{cat}}{i_p} = \frac{n}{0.466}\sqrt{\frac{RT \times TOF}{F\upsilon}}$$

n = number of electrons (4 electrons)
T = 298 K
R = 8.314 J K^{-1} mol^{-1}
F = 94865 C mol^{-1}
υ = scan rate (0.10 V s^{-1})

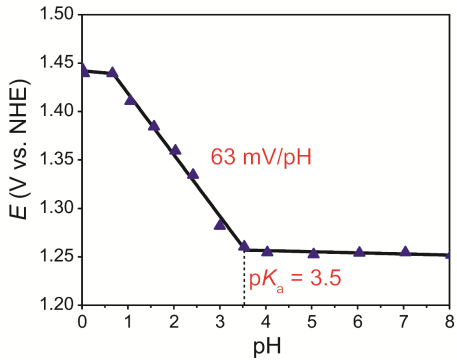

Figure S3. Pourbaix diagram (*E* vs pH plot) of **1**. The dashed line indicates the intercept on the pH axis.

Stability of compound 1 in pH 12

A solution of **1** at 10 mM in D_2O at pD 12 was monitored over 5.5 hours by ^1H NMR spectroscopy. Residual protio-solvent and added MeCN were used as internal standards. Figure S4 shows the ^1H NMR stacked spectra over the course of 5.5 hours and the integration of the cobalt species versus time.

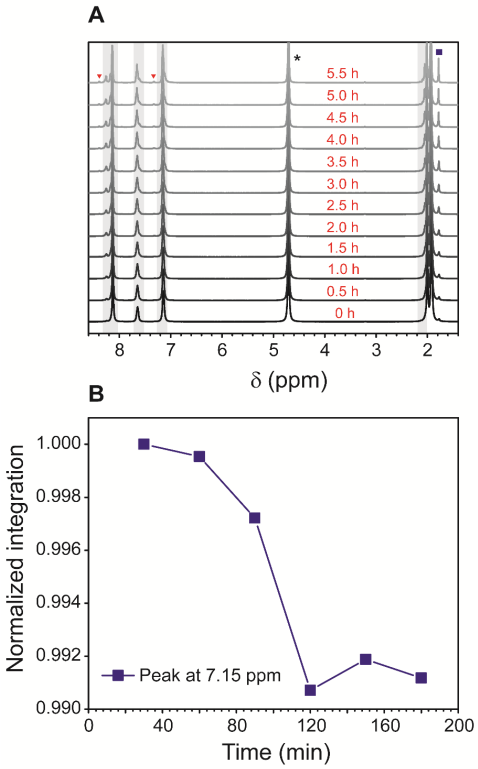

Figure S4. (A) ^1H NMR spectra of **1** at pH 12. The highlighted regions are all the diamagnetic cobalt species, including **1** and **2**$^-$. The red triangles (▼) denote free pyridine, the blue square (■) denotes free acetate, and the asterisk (*) denotes H_2O. (B) The normalized integration of the region centered around 7.15 ppm over time.

^{1}H NMR of 1[PF$_6$] in 9:1 water:MeCN. Compound **1[PF$_6$]** (0.001 g) was dissolved in 0.1 mL acetonitrile-d_3. D_2O (0.9 mL) was added to the solution, and the reaction was filtered to remove any precipitated material. The mixture was allowed to stand for 1 hour before acquisition of ^{1}H NMR spectrum. Apodization was used to increase signal-to-noise (Gaussian = 1.00 Hz, exponential = 0.30 Hz, and sine square = 90°).

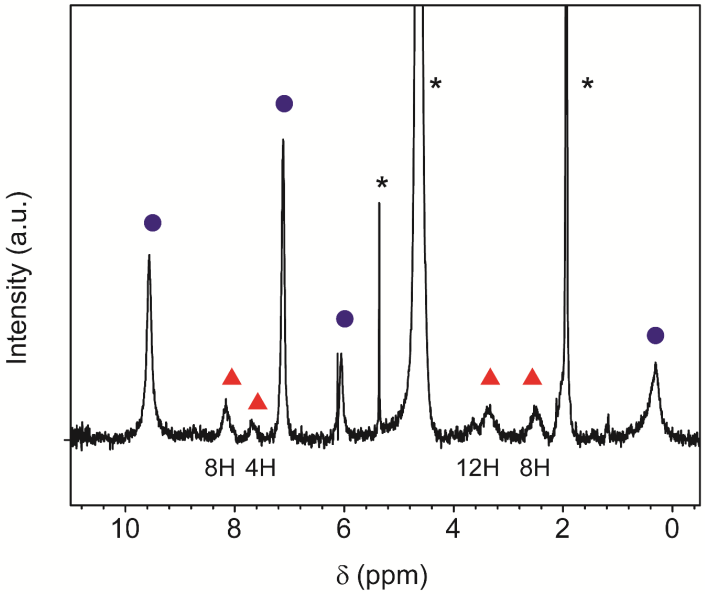

Figure S5. ^{1}H NMR spectrum of **[1]PF$_6$•CH$_2$Cl$_2$** in 9:1 D_2O:CD_3CN at 298 K. The asterisks (*) denote solvent (D_2O, CD_3CN, and CH_2Cl_2). The blue circles (●) indicate **[1]PF$_6$**, and the red triangles (▲) indicate the new species assigned as **1(H$_2$O)$^+$**.

NMR Spectroscopy (TOCSY, PGSE)

NMR spectra for these experiments were recorded on a Bruker Avance III HD 500 spectrometer. Chemical shifts are referenced relative to internal solvent resonances in ppm. The spectral references used were TMS for ^{1}H NMR spectra.

The 1D gTocsy ^{1}H NMR spectra were acquired at 500.1 MHz, by using the sequence selmlgp, 1D homonuclear Hartman-Hahn transfer. This sequence uses MLEV17 for mixing and shape pulse for selective refocusing.[3-5] The TOCSY mixing time employed was 120 ms, the number of scans was 64, the acquisition time was 2s and the relaxation time was 1s. Figure S6 shows the 1D TOCSY for **1** with NaOH in D_2O after 2 hours.

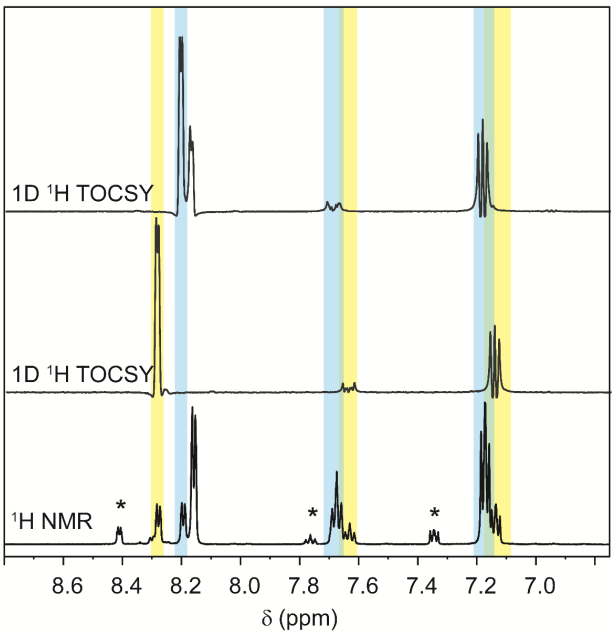

Figure S6. ^{1}H NMR and the 1D ^{1}H TOCSY spectra of **1** with NaOH in D_2O at 298 K. The color of the highlighted resonances indicates which resonances correlate with one another in the TOCSY experiment. The asterisks (*) denote free pyridine.

Diffusion NMR measurements were performed using the Stimulated Echo Pulse Sequence[6] without spinning. The shape of the gradient pulse was sine, and its strength varied automatically in the course of the experiments. The D values were determined from the slope of the regression line $\ln(I/I_0)$ versus G^2, according to Equation S1. I/I_0 = observed spin echo intensity/intensity without gradients, G = gradient strength, Δ = delay between the mid-points of the gradients, D = diffusion coefficient, δ = gradient length, and γ = the gyromagnetic ratio.

(eq S1)

$$\ln(\frac{I}{I_0}) = -(\gamma\delta)^2(\Delta - \frac{\delta}{3})DG^2$$

The calibration of the gradients was carried out *via* a diffusion measurement of HDO in D_2O, which afforded a slope of 2.18 x 10^{-4}. We estimate the experimental error in the D values to be ± 2%. All of the data leading to the reported D values afforded lines whose correlation coefficients were > 0.9999 and 8-12 points have been used for regression analysis. To check reproducibility, three different measurements with different diffusion parameters (δ and/or Δ) were always carried out. The gradient strength was incremented in 8 % steps from 10 % to 98 % and the recovery delay set to 5 times T_1. In ^{1}H diffusion experiments δ was set to 2 ms, employing an overall Δ of 68-118.5 ms. The number of scans was 8-64 per increment, with a recovery delay of 10 to 60 s. Typical experimental times were 1-4 h. All the diffusion processing and molecular size estimation was performed using the DiffAtOnce software available at www.diffatonce.com.

The ^{1}H PGSE NMR results for D_2O solutions of **1** and **1** + NaOH, all at 295 K, are given in Table S1.

Table S1. Diffusion coefficient (D) and hydrodynamic radius (r_H) values for of **1** and **1** + NaOH at 295 K in D_2O.

Chemical shift (ppm)	T_1 **(s)**	D^a **(10^{-10} m^2s^{-1})**	r_H **(Å)**^{b}
Solution of **1** with NaOH			
8.41 *o*-pyridine, free	19.7	9.47	2.3
8.30 *o*-pyridine, Unknown	1.4	3.30	6.7[a]
8.26 *o*-pyridine, **2**$^-$	1.4	3.24	6.8
8.19 *o*-pyridine, **2**$^-$	1.9	3.24	6.8
8.16 *o*-pyridine, **1**	1.5	3.16	7.0
2.07 Acetate, **2**$^-$	2.0	3.26	6.8
2.02 Acetate, **1**	2.0	3.17	7.0
1.94 Acetate, **2**$^-$	2.0	3.25	6.8
1.79 Acetate, free	9.6	9.00	2.5
Solution of **1**			
8.14 *o*-pyridine		3.14	7.1
7.66 *p*-pyridine		3.14	7.1
7.16 *m*-pyridine		3.14	7.1
2.02 Acetate		3.14	7.1

[a] The experimental error in the D values is ±2 %. [b] The viscosity η used in the Stokes-Einstein equation for H_2O was taken from Perry's Chemical Engineers' Handbook 8th Edition (www.knovel.com) and is 0.9748 x10^{-3} kg m^{-1} s^{-1}.

Stopped-flow kinetics.

A solution of **[1]PF$_6$** was prepared as a 100 μM stock solution in 80:20 H_2O:MeCN and left for 1 hour for equilibration of **1**$^+$ and **1(H$_2$O)**$^+$, and was shielded from light. Sodium hydroxide was prepared as a 0.198 M stock solution in water. All solutions were diluted to a final concentration before mixing. All concentrations given for the kinetic

experiments are given after mixing unless otherwise indicated. The table below lists the concentrations used for each experiment.

Kinetics studies were carried out with an Olis RSM 1000 stopped-flow spetrophotometer in symmetric mixing mode at ambient pressure and different temperatures. The center wavelength was set to 320 nm covering a spectral range from 244 to 394 nm with a 600 line/mm grating blazed at 300 nm. *For each data point at least 10 single measurements were performed and averaged*. Unless otherwise noted, all kinetic experiments were done at 25 °C. Figure S7 is a representative difference absorption spectrum of the reaction.

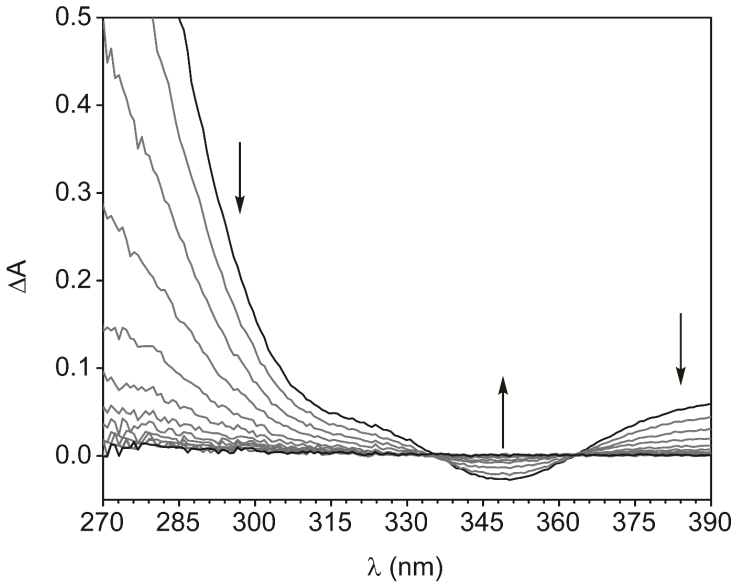

Figure S7. Difference absorption spectrum for the reaction of **1[PF$_6$]** (5.0 x 10^{-5} M) with NaOH (1.0 x 10^{-2} M).

The kinetics data were analyzed using the method of initial rates (data from 0 to 0.1 seconds, 3 –10% consumption of **1**$^+$).

Table S2.

Experiment	[**[1]PF$_6$**]] (M)	[OH^-] (M)	[pyridine] (M)
1	5.0 x 10^{-5}	1.0 x 10^{-2}	0
2	5.0 x 10^{-5}	7.5 x 10^{-3}	0
3	5.0 x 10^{-5}	5.5 x 10^{-3}	0
4	5.0 x 10^{-5}	3.5 x 10^{-3}	0
5	5.0 x 10^{-5}	2.5 x 10^{-3}	0
6	5.0 x 10^{-5}	1.5 x 10^{-3}	0
7	4.0 x 10^{-5}	1.0 x 10^{-2}	0
8	3.0 x 10^{-5}	1.0 x 10^{-2}	0
9	2.0 x 10^{-5}	1.0 x 10^{-2}	0

10	1.0×10^{-5}	1.0×10^{-2}	0
11	5.0×10^{-5}	5.0×10^{-4}	5.0×10^{-4}
12	5.0×10^{-5}	5.0×10^{-4}	2.5×10^{-3}
13	5.0×10^{-5}	5.0×10^{-4}	5.0×10^{-3}
14	5.0×10^{-5}	5.0×10^{-4}	1.0×10^{-2}
15	5.0×10^{-5}	5.0×10^{-4}	1.5×10^{-2}

Table S3.

Experiment	[[1]PF_6]] (M)	[H_2O_2] (M)
1	5.0×10^{-5}	5.0×10^{-3}
2	5.0×10^{-5}	1.0×10^{-2}
3	5.0×10^{-5}	1.5×10^{-2}
4	5.0×10^{-5}	2.0×10^{-2}
5	5.0×10^{-5}	2.5×10^{-2}

COPASI fitting.

The data for each kinetic run were averaged and converted from units of absorbance to concentrations. *COPASI* software was used to fit the kinetic traces with global rate constants through a combination of genetic algorithm and differential evolution methods. The fitting also allowed for the variance of the initial concentrations of **1(OH)** since experimentally observed existing simultaneously in equilibrium. The following reactions were used for the model:

$$\mathbf{1}^+ + OH^- \xrightarrow{k_1} \mathbf{1(OH)}$$

$$\mathbf{1(OH)} + OH^- \xrightarrow{k_2} \mathbf{1(O)}^-$$

$$\mathbf{1}^+ + \mathbf{1(O)}^- \xrightarrow{k_3} \mathbf{1(O)} + \mathbf{1}$$

$$\mathbf{1(O)} + OH^- \xrightarrow{k_4} \mathbf{1(OOH)}^-$$

$$\mathbf{1(OOH)}^- + \mathbf{1}^+ + OH^- \xrightarrow{k_5} \mathbf{1(O_2)}^- + \mathbf{1} + H_2O$$

$$\mathbf{1(O_2)}^- + \mathbf{1}^+ + OH^- \xrightarrow{k_6} O_2 + \mathbf{1(OH)}^- + \mathbf{1}$$

$$\mathbf{1}^+ + \mathbf{1(OH)}^- \underset{k_{-7}}{\overset{k_7}{\rightleftharpoons}} \mathbf{1} + \mathbf{1(OH)}$$

The following rate constants and initial concentrations were extracted from the fitting:

Table S4.

Parameter	Lower Bound	Value	Upper Bound	Coeff. of Variation (%)
k_1	1.0e-06	1.277e+01	1.0e+09	1.6e+00
k_2	1.0e-06	4.431e+05	1.0e+09	1.3e+02
k_3	1.0e-06	4.430e+05	1.0e+09	3.1e+00
k_4	1.0e-06	8.790e+08	1.0e+09	4.6e+02
k_5	1.0e-06	8.520e+08	1.0e+09	9.6e+01
k_6	1.0e-06	1.000e+09	1.0e+09	1.1e+02
k_7	1.0e-06	3.515e+05	1.0e+09	3.2e+00
k_{-7}	1.0e-06	9.329e-01	1.0e+09	5.75e+02
[**1(OH)**_1]$_0$ [a]	4.50e-07	1.22e-06	1.3e-05	5.96e-01
[**1(OH)**_2]$_0$ [a]	4.50e-07	1.31e-06	1.30e-05	4.83e-01
[**1(OH)**_3]$_0$ [a]	4.50e-07	1.31e-06	1.30e-05	4.10e-01
[**1(OH)**_4]$_0$ [a]	4.50e-07	1.25e-06	1.30e-05	3.35e-01
[**1(OH)**_5]$_0$ [a]	4.50e-07	1.18e-06	1.30e-05	2.94e-01
[**1(OH)**_6]$_0$ [a]	4.50e-07	1.20e-06	1.30e-05	2.34e-01
[**1(OH)**_7]$_0$ [a]	4.50e-07	1.00e-06	1.30e-05	7.50e-01
[**1(OH)**_8]$_0$ [a]	4.50e-07	7.00e-07	1.30e-05	1.09e+00
[**1(OH)**_9]$_0$ [a]	4.50e-07	4.70e-07	1.30e-05	1.73e+00

[a] The "_#" notation denotes the [**1(OH)**] belonging to the corresponding experiment number (See Table S2 under the "Stopped flow kinetics" section).

The sensitivity of each kinetic parameter was evaluated by increasing or decreasing its value, and then allowing the other parameters to refine until the goodness of fit no longer improved. The plot of the change in least squares function ($\partial E/\partial k$) versus a multiple of the respective kinetic parameter is shown below (Figure S8). Parameters which have a near zero slope do not affect fit significantly when altered.

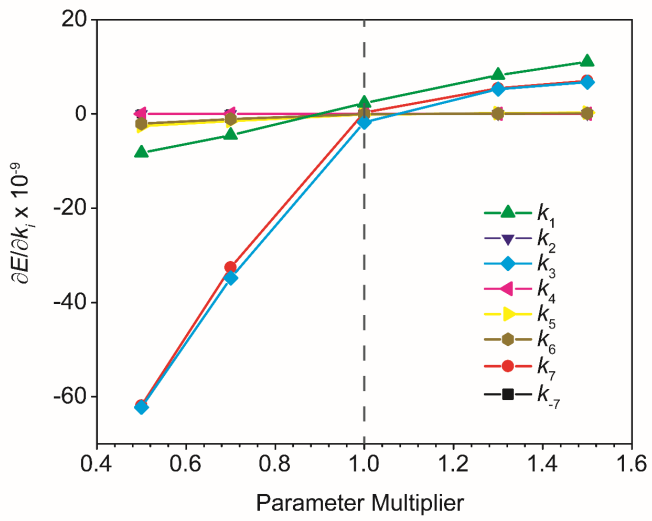

Figure S8. Sensitivity of the fit with respect to a change in one parameter.

Derivation of rate law.

Since all reactions were carried out in pseudo-first order conditions:

$$[OH^-]_0 = [OH^-]$$

Since the kinetic profile is sigmoidal, this necessarily implies a non-steady state concentration in at least one intermediate. We assume the concentration of **1(OH)** is non-steady state. The concentrations of **1(O)**$^-$, **1(O)**, **1(OOH)**$^-$, **1(O$_2$)**$^-$, and **1(OH)**$^-$ were assumed to be in steady state (eq S2-S5).

(eq S2-S5)

$$\frac{d[\mathbf{1(O)}^-]}{dt} = 0 = k_4[\mathbf{1(OH)}][OH^-] - k_3[\mathbf{1(O)}^-][\mathbf{1}^+]$$

$$\frac{d[\mathbf{1(O)}]}{dt} = 0 = k_3[\mathbf{1(O)}^-][\mathbf{1}^+] - k_4[\mathbf{1(O)}][OH^-]$$

$$\frac{d[\mathbf{1(OOH)}^-]}{dt} = 0 = k_4[\mathbf{1(O)}][OH^-] - k_5[\mathbf{1(OOH)}^-][OH^-]$$

$$\frac{d[\mathbf{1(O_2)}^-]}{dt} = 0 = k_5[\mathbf{1(OOH)}^-][OH^-][\mathbf{1}^+] - k_6[\mathbf{1(O_2^-}][OH^-][\mathbf{1}^+]$$

$$\frac{d[\mathbf{1(OH)}^-]}{dt} = 0 = k_6[\mathbf{1(O_2)}^-][OH^-][\mathbf{1}^+] + k_{-7}[\mathbf{1(OH)}][\mathbf{1}] - k_7[\mathbf{1(OH)}^-][\mathbf{1}^+]$$

[**1(OH)**] can be solved for using the mass balance equation (eq S6 and S7):
(eq S6)

$$[\mathbf{1}^+]_0 = [\mathbf{1}^+] + [\mathbf{1(OH)}] + [\mathbf{1(O)}^-] + [\mathbf{1(O)}] + [\mathbf{1(OOH)}^-] + [\mathbf{1(O_2)}^-] + [\mathbf{1(OH)}^-] + [\mathbf{1}]$$

(eq S7)

$$[\mathbf{1(OH)}] = \frac{[\mathbf{1}^+]_0 - [\mathbf{1}^+] - [\mathbf{1}]}{k_2 \dfrac{[\mathrm{OH}^-]}{[\mathbf{1}^+]}\left(\dfrac{k_3 + k_6}{k_3 k_6}\right) + \dfrac{k_2}{k_4} + \dfrac{k_2}{k_5} + \dfrac{k_{-6}[\mathbf{1}]}{k_6[\mathbf{1}^+]} + 1}$$

Substitution into $-d[\mathbf{1}^+]/dt$ (Eq. S8) gives the full rate law (Eq. S9):

(eq S8)

$$-\frac{d[\mathbf{1}^+]}{dt} = k_1[\mathbf{1}^+][\mathrm{OH}^-] + k_3[\mathbf{1(O)}^-][\mathbf{1}^+] - k_6[\mathbf{1(OH)}^-][\mathbf{1}^+] + k_{-6}[\mathbf{1(OH)}][\mathbf{1}]$$

(eq S9)

$$-\frac{d[\mathbf{1}^+]}{dt} = k_1[\mathbf{1}^+][\mathrm{OH}^-] + \frac{2k_2\left([\mathbf{1}^+]_0 - [\mathbf{1}^+] - [\mathbf{1}]\right)[\mathrm{OH}^-]}{k_2 \dfrac{[\mathrm{OH}^-]}{[\mathbf{1}^+]}\left(\dfrac{k_3 + k_7}{k_3 k_7}\right) + \dfrac{k_2}{k_4} + \dfrac{k_2}{k_5[\mathbf{1}^+]} + \dfrac{k_2}{k_6[\mathbf{1}^+]} + \dfrac{k_{-7}[\mathbf{1}]}{k_7[\mathbf{1}^+]} + 1}$$

For conditions where $[\mathrm{OH}^-]$ is very high, $\lim_{[\mathrm{OH}^-]\to\infty} -\dfrac{d[\mathbf{1}^+]}{dt}$ (Eq. S10):

(eq S10)

$$-\frac{d[\mathbf{1}^+]}{dt} = k_1[\mathbf{1}^+][\mathrm{OH}^-] + \frac{2k_3k_7}{k_3 + k_7}[\mathbf{1}^+]\left([\mathbf{1}^+]_0 - [\mathbf{1}^+] - [\mathbf{1}]\right)$$

Since:
(eq S11)

$$\frac{d[\mathbf{1}]}{dt} = -\frac{d[\mathbf{1}^+]}{dt} - k_1[\mathbf{1}^+][\mathrm{OH}^-]$$

The solution to this system of first-order non-linear differential equations (Eqs. S10 and S11), with the boundary conditions $[\mathbf{1}^+](t = 0) = [\mathbf{1}^+]_0$ and $[\mathbf{1}](t = 0) = 0$, is the sigmoid curve:

(Eq. S12)

$$[\mathbf{1}^+](t) = \frac{C\left(k_3 + k_7\right)}{4k_3k_7}\operatorname{sech}^2\left(\frac{\sqrt{k_1[\mathrm{OH}^-]C}}{2}t + \tanh^{-1}\frac{\sqrt{k_1[\mathrm{OH}^-]C}}{C}\right)$$

Where:

$$C = k_1[\mathrm{OH}^-] + \frac{4k_3k_7}{k_3 + k_7}[\mathbf{1}^+]_0$$

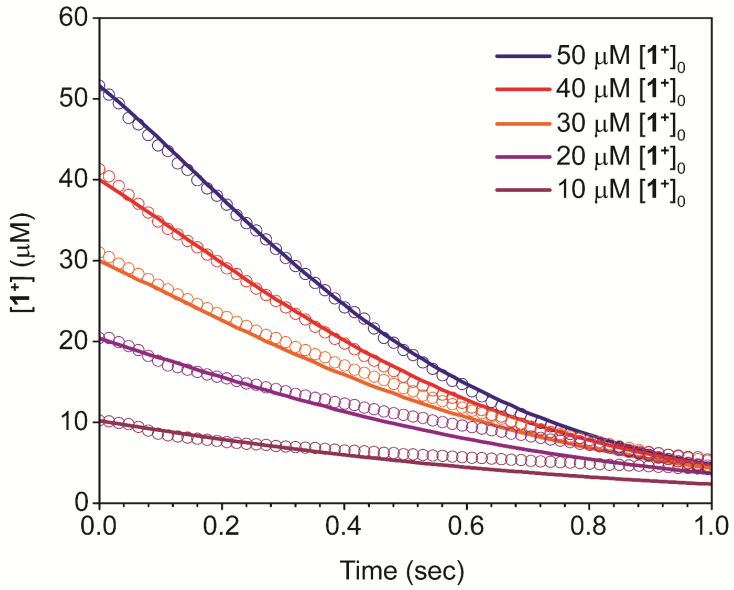

Figure S9. Fitting of the measured kinetic profiles using Eq. S12 with $k_{obs1} = k_1[\mathrm{OH}^-] = 1.2$ and $k_{obs2} = k_3k_7/(k_3 + k_7) = 65000$. These fitted rate constants are within an order of magnitude of the measured values. The open circles are the measured values of $[\mathbf{1}^+]$ and the solid lines are the fit.

For initial rates:
Since $[\mathbf{1}^+]$ represents a fraction of $[\mathbf{1}^+]_0$, we can define:

$$[\mathbf{1}^+] = f[\mathbf{1}^+]_0$$

$$0 < f < 1$$

And:

$$[\mathbf{1}] \approx 0$$

The equation then becomes:
(eq S13)

$$-\frac{d[\mathbf{1}^+]}{dt} = k_1 f[\mathbf{1}^+]_0[\mathrm{OH}^-] + \frac{2k_3k_7}{k_3 + k_7}(f - f^2)[\mathbf{1}^+]_0^2$$

Scheme S1. Alternative (direct-coupling) mechanism for reduction of $\mathbf{1}^{+}$ by hydroxide.

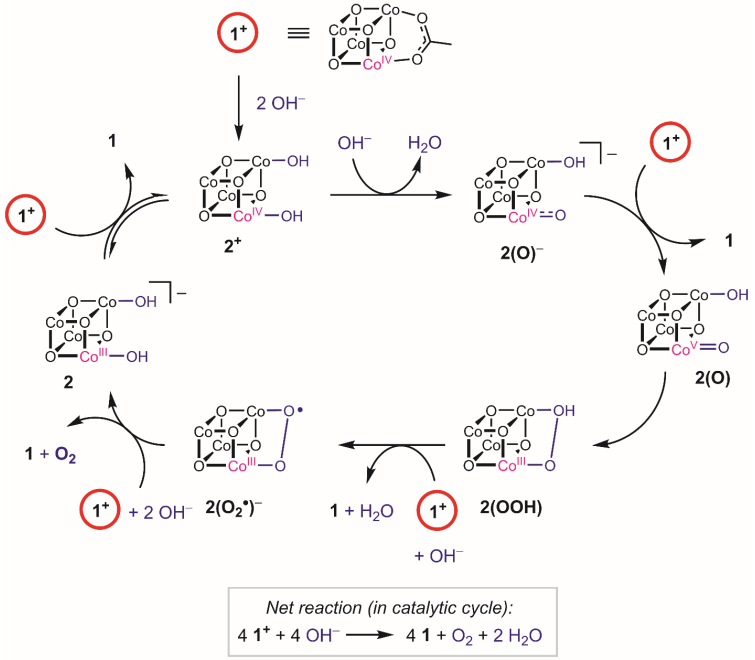

Single crystal X-ray diffraction.

X-ray diffraction data were collected using Bruker AXS three-circle diffractometers coupled to APEX-II CCD detectors with either QUAZAR multilayer mirror- or graphite-monochromated Mo Kα radiation (λ = 0.71073 Å). The structures were solved by direct methods using SHELXS or by employing SHELXT and were refined against F^2 on all data by full-matrix least squares with SHELXL-97 or -2014. All non-hydrogen atoms were refined anisotropically; hydrogen atoms were included into the model at their geometrically calculated positions and refined using a riding model. In the structure of **[1H]PF_6**, co-crystallizing solvent molecules and a component of a positionally disordered hexafluorophosphate anion could not be satisfactorily modeled, so Squeeze was employed to treat the diffuse electron density in the void space they occupied. The metrical parameters for these structures can be obtained free of charge from the Cambridge Crystallographic Data Centre under reference numbers CCDC-1054644, CCDC-1054645, and CCDC-1054646.

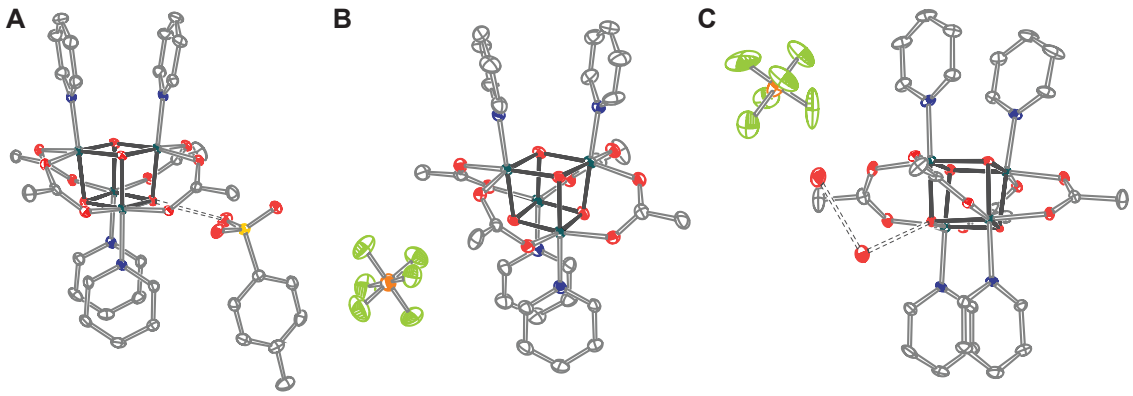

Figure S10. ORTEP diagrams of (A) **[1H]OTs**, (B) **[1]PF$_6$**, and (C) **[1H]PF$_6$•2H$_2$O**. Thermal ellipsoids are drawn at 50% probability. Solvent molecules and hydrogen atoms are excluded for clarity.

Computational Details.

DFT calculations were carried out with the unrestricted B3LYP functional and 6-31G+(d,p) basis set using the Gaussian 09 RevD01 software package. Electronic energy calculations were performed using optimized geometry coordinates of **1(O)**•H$_2$O taken from Siegbahn et. al..[8] The coordinates are listed below in Table S5. The Kohn-Sham orbitals for the α and β spin of the triplet state are shown in Figure S9.

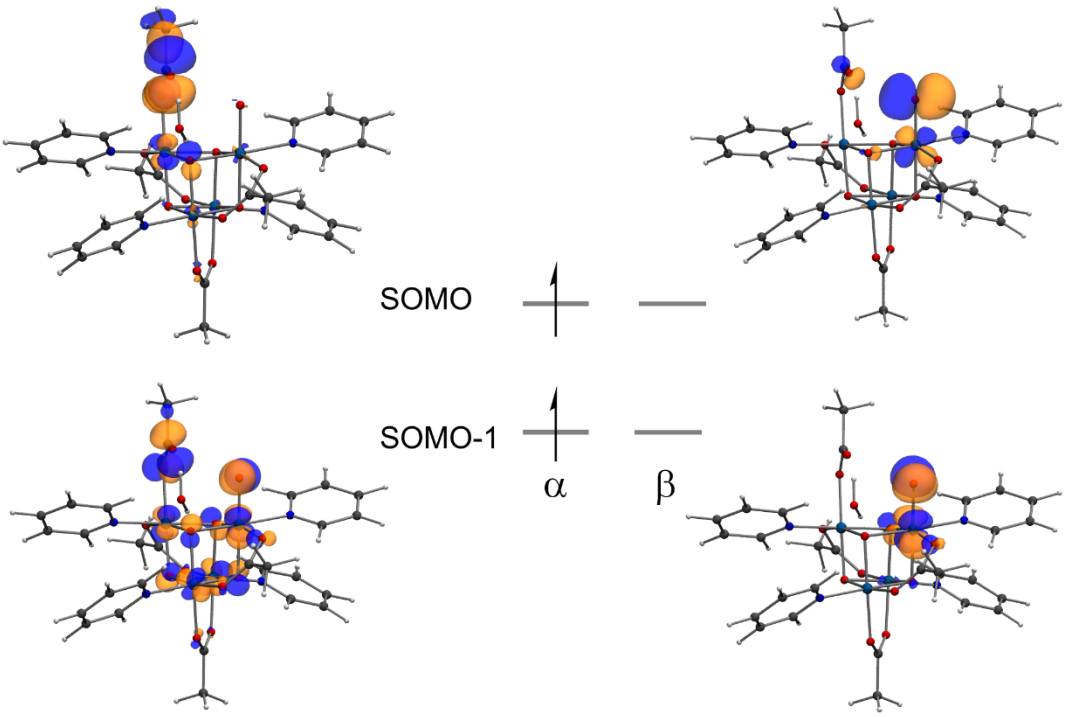

Figure S11. The frontier Kohn-Sham orbitals of ^{3}**1(O)**•H$_2$O.

Table S5. Atomic coordinates for **1(O)•H_2O**

Co	6.07032	-4.90576	9.36819
Co	4.81001	-6.56153	11.34711
Co	7.48816	-6.00999	11.37979
Co	6.37108	-7.62944	9.28915
O	5.91521	-5.02043	11.21847
O	4.92465	-6.42948	9.50387
N	4.6274	-3.49821	9.2062
O	7.46396	-6.11539	9.52645
C	4.44103	-2.66683	10.24493
C	3.94364	-3.2961	8.06912
O	6.39149	-7.53945	11.21093
N	7.88998	-8.91037	9.1174
C	3.55284	-1.59703	10.18143
C	3.03448	-2.25081	7.92979
C	8.07153	-9.86286	10.05068
C	8.6832	-8.88848	8.03294
C	2.83632	-1.38407	9.00357
C	9.06177	-10.83393	9.91776
C	9.69036	-9.8264	7.83417
C	9.8826	-10.82137	8.79256
O	5.02961	-6.35285	13.30605
C	6.15644	-6.18501	13.88293
C	6.12925	-6.26989	15.39721
O	7.2823	-5.99641	13.33906
O	7.35647	-3.44684	9.52429
C	8.26339	-3.4458	10.41698
O	8.50761	-4.33289	11.29264
C	9.18653	-2.23701	10.41022
O	5.15797	-9.0759	8.88704
C	4.73974	-10.01596	9.66772
O	5.08908	-10.22939	10.8401
C	3.68649	-10.91515	9.01708
O	6.1652	-5.03128	7.4111
C	6.29116	-6.15048	6.82092
C	6.28989	-6.1149	5.30002
O	6.3906	-7.30061	7.34434
N	9.20696	-7.00256	11.55738
C	9.45584	-7.82459	12.59006
C	10.16647	-6.76906	10.64614
C	10.69594	-8.43686	12.75358
C	11.42899	-7.34325	10.7449
C	11.70104	-8.18869	11.82127
N	3.0448	-5.56537	11.40556
C	2.62765	-4.91361	12.5008
C	2.23769	-5.67835	10.33758
C	1.36744	-4.32608	12.56194
C	0.96325	-5.11921	10.32891
C	0.52063	-4.43141	11.45883
H	5.02205	-2.90271	11.12996

H	4.1644	-3.98643	7.26418
H	3.43168	-0.94561	11.04132
H	2.50176	-2.12158	6.99264
H	7.40461	-9.83883	10.9038
H	8.47226	-8.1065	7.31579
H	2.13805	-0.55504	8.92301
H	9.17126	-11.58621	10.69234
H	10.30406	-9.77414	6.94006
H	10.65714	-11.57293	8.66268
H	9.92893	-2.36365	9.61279
H	9.70681	-2.14328	11.36547
H	8.61876	-1.32857	10.19154
H	2.70578	-10.4339	9.12095
H	3.65019	-11.88269	9.52407
H	3.88457	-11.04854	7.94971
H	8.63862	-7.99486	13.27853
H	9.87901	-6.1205	9.82726
H	10.85623	-9.09891	13.59843
H	12.17831	-7.13019	9.98897
H	12.67917	-8.65075	11.9269
H	3.32783	-4.89529	13.32744
H	2.65757	-6.22176	9.49732
H	1.05971	-3.80505	13.46305
H	0.33403	-5.23064	9.45157
H	-0.47181	-3.98905	11.48151
H	6.97126	-5.72408	15.82844
H	5.18185	-5.89407	15.79181
H	6.21378	-7.3298	15.66599
H	7.01666	-6.8293	4.9035
H	5.30026	-6.42269	4.94109
H	6.50637	-5.10934	4.93366
O	3.84097	-7.95606	11.49439
O	6.63596	-9.47966	13.16358
H	5.98691	-10.11726	12.81978
H	6.48729	-8.74492	12.52801

Spin-State	Energy (Hartree)
S = 0	-7890.71942806
S = 1	-7890.76558592

Supporting Information References

(1) Ullman, A. M.; Liu, Y.; Huynh, M.; Bediako, D. K.; Wang, H.; Anderson, B. L.; Powers, D. C.; Breen, J. J.; Abruña, H. D.; Nocera, D. G. *J. Am. Chem. Soc.* **2014**, 136 (50), 17681

(2) Bard, A. J., Faulkner, L. R., *Electrochemical Methods: Fundamentals and Applications*, 2nd ed.; John Wiley & Sons, 2001.

(3) H. Kessler, H. Oschkinat, C. Griesinger, W. Bermel, *J. Magn. Reson. 1969*. **70**, 106–133 (1986).

(4) J. Stonehouse, P. Adell, J. Keeler, A. J. Shaka, *J. Am. Chem. Soc.* **116**, 6037–6038 (1994).

(5) K. Stott, J. Stonehouse, J. Keeler, T.-L. Hwang, A. J. Shaka, *J. Am. Chem. Soc.* **117**, 4199–4200 (1995).

(6) P. Stilbs, *Prog. Nucl. Magn. Reson. Spectrosc.* **19**, 1–45 (1987).

(7) R. M. Silva, M. D. Smith, J. R. Gardinier, *J. Org. Chem.* **70**, 8755–8763 (2005).

(8) Li, X.; Siegbahn, P. E. M. *J. Am. Chem. Soc.* **2013**, 135 (37), 13804.

Chapter 3:

Prediction of redox potentials for Co_4O_4 cubanes over a 1400 mV range: Implications for the feasibility of formal Co(V)–Oxo species*

* This work is based upon work a manuscript to be published, included with permission from all authors:

Nguyen, A. I., Wang, J., Levine, D. S., Ziegler, M. S., Tilley, T. D. *In preparation*

Author contributions: Andy I. Nguyen formulated the project. A.I.N and Jianing Wang synthesized materials and performed electrochemical studies. A.I.N. analyzed the data. Daniel S. Levine performed DFT calculations. Micah S. Ziegler contributed to the solving of crystal structures obtained from x-ray diffraction.

3.1 Introduction

The development of catalysts for the oxygen evolving reaction (OER), motivated by the goal of creating an artificial photosynthesis system, has generated a number of hypotheses that challenge traditional ideas regarding transition-metal oxidation states and bonding. Thus, catalytic OER cycles often invoke unusually high and rare oxidation states at the metal centers, which are bound to reactive terminal (μ^1) oxido ligands.[1–8] For the intensely studied cobalt-based OER catalysts, a Co(IV)-oxo intermediate is commonly proposed.[3,6,9] However, the Co(IV) oxidation state is quite rare, and ligand field considerations seem to suggest a high instability for a terminal oxo ligand bound to Co(IV).[10] Recently, many experiments have confirmed the Co(IV) oxidation state during water oxidation catalysis, but evidence for any Co(IV)–μ^1-oxo still remains circumstantial.[3,9,11,12] Remarkably, many density functional theory (DFT) calculations of cobalt-catalyzed OER suggest yet an even more unconventional species, a Co(V)-oxo intermediate that is sometimes described as a Co(IV)-oxyl radical.[4,5,13] So far, the only experimental evidence for this type of intermediate comes from kinetic analysis of OER mediated by a molecular Co_4O_4 cubane.[6] The validity of Co(V)-oxo needs to be verified with more experimental data; specifically, a method for predicting the redox potential required to access Co(V) should be quite useful in determining whether or not such an oxidation state is feasible. As cobalt compounds bearing terminal oxo- ligands have never been isolated, direct measurement of its potential is not possible. In the case of the Co_4O_4 cubane, a stable Co(III)-hydroxide has been synthesized, and would be a promising starting point for accessing Co(IV)-oxo or Co(V)-oxo complexes. A strategy to estimate the Co(IV)/Co(V) redox potential of nonisolable intermediates could come from an extrapolation of a linear free-energy relationship (LFER). We hypothesize that analysis of a large and diverse set of cubanes comprising a large ligand range could yield a LFER from which the redox potentials could be confidently predicted.

This report describes the analysis of a substantial library of homologous cubanes with the general formula $Co_4O_4X_{4-n}X'_nL_4$ (X, X′ are anionic ligands; L is a neutral ligand). Synthetic methods were developed to obtain relatively electron-rich or electron poor cubanes, or cubanes with mixed-carboxylate ligand sets or ligands that provide secondary-sphere H-bond donors. Empirical linear relationships describe the redox potentials of the $[Co^{III}_4O_4]^{4+}/[Co^{IV}Co^{III}_3O_4]^{5+}$ and $[Co^{IV}Co^{III}_3O_4]^{5+}/\{[Co^{V}Co^{III}_3O_4]^{6+} \leftrightarrow [Co^{IV}_2Co^{III}_2O_4]^{6+}\}$ couples, based solely on a pK_a descriptor of the ligands bound to the cubane. This model holds for at least seven pK_a units (seven orders of magnitude), over which the redox potentials of the cubanes span a remarkable 1420 mV range. This LFER also accurately predicts the redox potentials of a different cubane series, with the stoichiometry $[Co_4O_4X_2L_4]^{2+}$, supporting the generality of this model. The pK_a-redox relationship provides a unifying description of numerous existing $[Co_4O_4]^{4+}$ cubanes in the literature. Applying this model to $\{[Co^{V}Co^{III}_3O_4]^{6+} \leftrightarrow [Co^{IV}_2Co^{III}_2O_4]^{6+}\}$ cubanes bearing μ^1-hydroxo- and μ^1-oxo- ligands, we predict that redox potentials are indeed low enough to be accessed by an OER mechanism involving $[Co^{IV}Co^{III}_3O_4]$ disproportionation.[12] The predicted values support the mechanistic proposal previously obtained by kinetics.

3.2 Results and Discussion

The numerous cubane complexes to be described in this work differ by varying degrees of ligand substitutions, ranging from simple to complex, and thus a nomenclature was created to concisely, yet descriptively, abbreviate these compound. Compounds of the general formula $[Co^{III}_4O_4X_xL_y]^{+(4-x)}$ are abbreviated as $\mathbf{[}x\mathbf{X}\text{-}y\mathbf{L]}^{+(4-x)}$, where x and y are integers greater than 1, and denote the stoichiometry of **X** (anionic ligand) and **L** (neutral ligand) bound to $[Co_4O_4]^{4+}$, respectively. If multiple types of **X** or **L** are present in the same complex, then the additional x**X** or y**L** is appended in the fashion $\mathbf{[}x_1\mathbf{X}_1,x_2\mathbf{X}_2,..x_n\mathbf{X}_n\text{-}y_1\mathbf{L}_1,y_2\mathbf{L}_2,..y_n\mathbf{L}_n\mathbf{]}^{+(4-x)}$. If the $[Co_4O_4]^{4+}$ unit is oxidized to $[Co_4O_4]^{5+}$ or $[Co_4O_4]^{6+}$, the notation changes to $[x\mathbf{X}\text{-}y\mathbf{L}]^{+(5-x)}$ and $[x\mathbf{X}\text{-}y\mathbf{L}]^{+(6-x)}$, respectively. For example, a cubane with the hypothetical stoichiometry $[Co_4O_4(OAc)_2(OH)(H_2O)_3py_4]^+$ would be abbreviated as $\mathbf{[2OAc,OH\text{-}2H_2O,4py]}^+$, and could be oxidized once or twice to $\mathbf{[2OAc,2OH\text{-}2H_2O,4py]}^{+2}$ and $\mathbf{[2OAc,2OH\text{-}2H_2O,4py]}^{+3}$, respectively.

Three general methods were used to synthesize **4X-4L** derivatives (Chart 1). The "self-assembly" route (Method A, eq 1), patterned after the Das synthesis of $Co_4O_4(OAc)_4py_4$ (**4OAc-4py**) from $Co(NO_3)_2(H_2O)_6$, NaX, L, and H_2O_2, was extended to the preparation of $Co_4O_4(OAc)_4$(*p*-cyanopyridine) (**4OAc-4(CNpy)**).[14] However, in our hands, this method was unsuccessful for the synthesis of cubanes with very electron-rich pyridines, very electron-poor carboxylates, very basic anions, and mixed-carboxylates. The synthesis of cubane derivatives with these types of ligands will be discussed in the following sections.

A useful method involves the exchange of neutral ligands (Method B, eq 2) is used to synthesize cubanes with L = DMAP. Cubane $Co_4O_4(OAc)_4(DMAP)_4$ (**4OAc-4DMAP**) was produced by this method in 67% recrystallized yield. Method B seems to works well for other cases (*vide infra*), also, as long as the $pK_a(L'H^+) > pK_a(LH^+)$. Synthesis of cubane with X′ = CF_3COO^- was achieved by heating **1** with slight excess of CF_3CO_2H to give $Co_4O_4(CF_3CO_2)_4py_4$ (**4TFA-4py**) in 56% yield. This method (Method C, eq 3) is driven by release of HX, thus it works well when $pK_a(HX') < pK_a(HX)$. Methods B and C provide a predictable and divergent route for cubane diversification (Chart 1), and in contrast to Method A, give crude products which are mostly free of Co(II) impurities. Remarkably, substitution of ligands by Method B or C is highly stereoselective, always preserving the X ligands around the equatorial faces and L ligands on the top and bottom faces, as evidenced by NMR spectroscopy and crystallography (Figure 1).

$$Co(NO_3)_2(H_2O)_6 + 2NaX + L + H_2O_2 \rightarrow \frac{1}{4}Co_4O_4X_4L_4 + HX + 2NaNO_3 + 6H_2O \quad (1)$$

$$Co_4O_4X_4L_4 + 4L' \rightleftharpoons Co_4O_4X_4L'_4 + 4L \quad (2)$$

$$Co_4O_4X_4L_4 + nHX' \rightleftharpoons Co_4O_4X_{4-n}X'_nL_4 + nHX \quad (3)$$

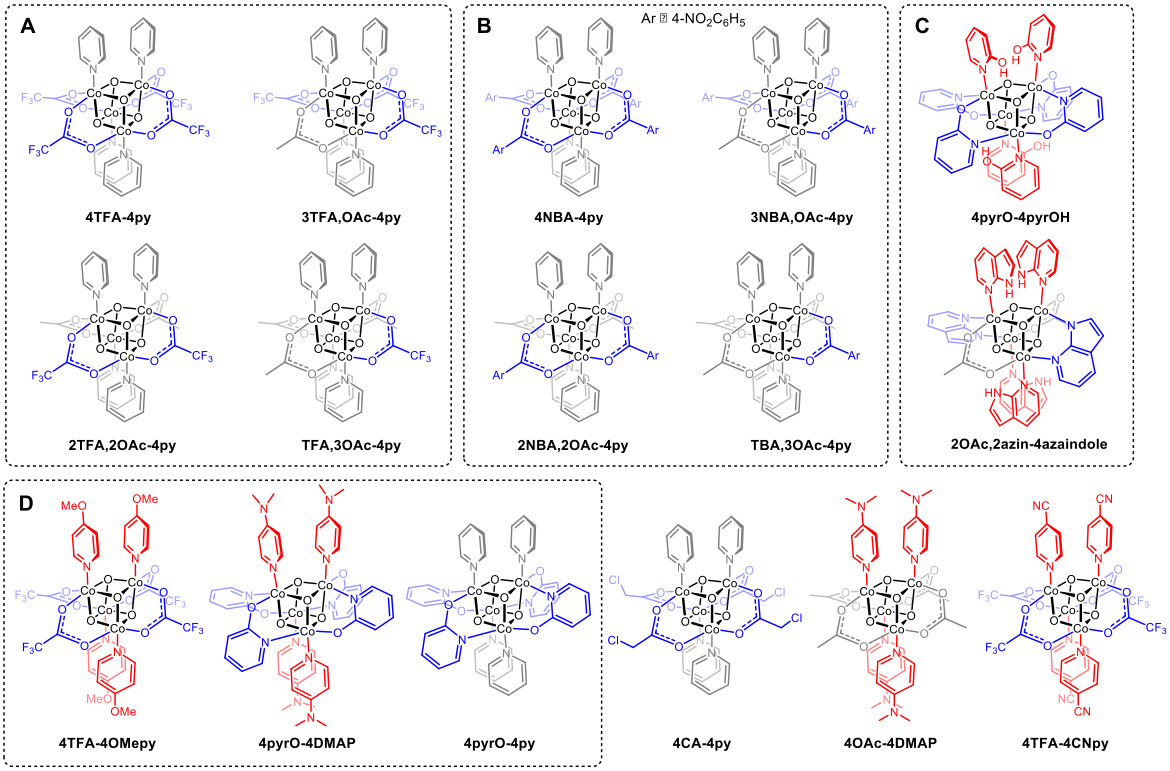

Chart 1. New cubane complexes. (A) Trifluoroacetate series synthesized by Method C; (B) *p*-nitrobenzoate series synthesized by Method C; (C) Hydrogen-bonded cubanes; (D) Cubanes synthesized by a combination of Methods B and C.

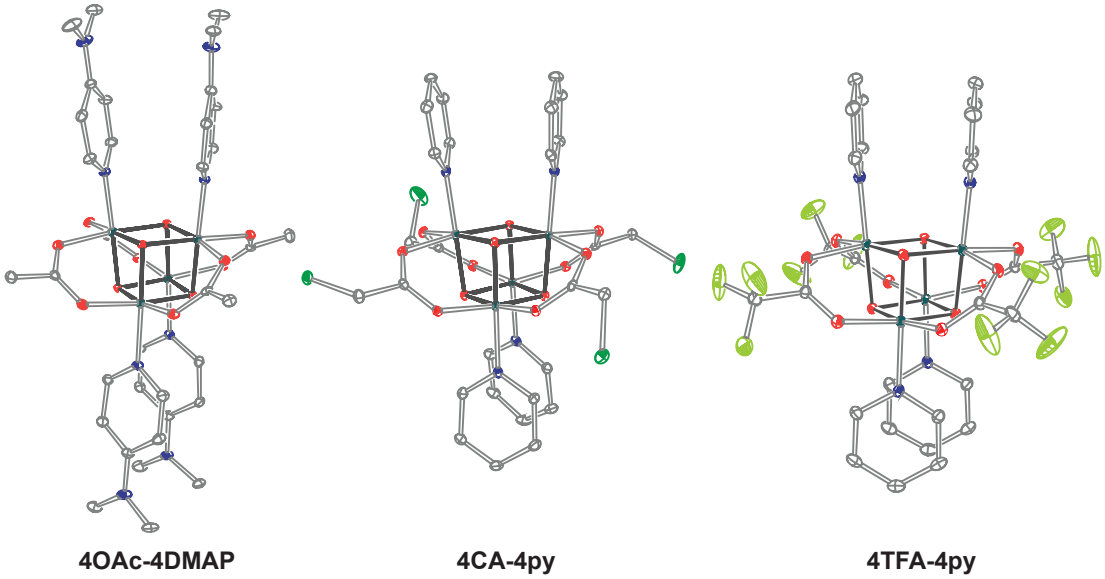

Figure 1. Single-crystal XRD structures of cubanes. Thermal ellipsoids are at 30% probability, with hydrogen atoms and solvent molecules removed for clarity.

The most significant advantage of Method C over Method A is the ability to control the synthesis of unprecedented mixed-carboxylate cubanes. Depending on the equivalents of HX′ in the reaction with a cubane mono- (**3X,X′-4L**), di- (**2X,2X′-4L**), or trisubstituted (**X,3X′-4L**) complexes can form as the major product. The mixture of mono-, di-, tri-, and tetrasubstituted cubane is easily separable by column chromatography since the compounds are highly colored with significantly different R_f values. By this method, $Co_4O_4(OAc)_{4-n}(CF_3CO_2)_npy_4$ and $Co_4O_4(OAc)_{4-n}$(4-nitrobenzoate)$_npy_4$, where n = 1, 2, and 3, have also been synthesized and characterized by NMR spectroscopy. Interestingly, the formation of disubstituted cubanes is stereoselective for *cis*-substitution – that is the two X′ ligands are on adjacent faces of the cubane, as revealed by XRD (Figure 2).

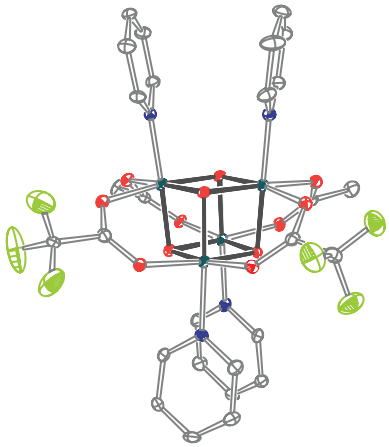

Figure 2. Single-crystal XRD structure of **2TFA,2OAc-4py**. Thermal ellipsoids shown at 30% probability. Hydrogen atoms were removed for clarity.

Cubanes bearing the highly electron-rich X ligands 2-pyridonate (pK_a (O–H) = 8.05)[15] and 7-azainodolate (pK_a (N^1–H) ~ 15)[16] where synthesized in a manner similar to Method C, but the products have a different stoichiometry than those produced by Method C (Scheme 1). Heating **4OAc-4py** with excess 2-hydroxypyridine in acetonitrile gives Co_4O_4(2-pyridonate)$_4$(2-hydroxypyridine)$_4$ (**4pyrO-4pyrOH**) in 37% yield. Similarly, heating **4OAc-4py** with excess 7-azaindole in acetonitrile gives $Co_4O_4(OAc)_2$(7-azin)$_2$(7-azaindole)$_4$ (**2OAc,2azin-4azaindole**) in 48% yield. Though the pK_a values of 2-hydroxypyridine and 7-azaindole are higher than those of HOAc, the reaction is driven by use of excess ligand as well as the insolubility of **4pyrO-4pyrOH** and **2OAc,2azin-4azaindole** in acetonitrile. These reactions differ from Method C in that the X ligands also can act as L ligands (2-hydroxypyridine and 7-azaindole have pyridyl nitrogen atoms), and thus, full substitution of the L-positions on the cubane is also observed. Interestingly, when these ligands act as L-type, their polar O–H or N–H functional groups hydrogen-bond to the μ^3-oxo ions of the [Co_4O_4] cubane. The 2-hydroxypyridine ligand can be substituted for other L ligands by Method B to produce **4pyrO-4py** and **4pyrO-4DMAP**. These compounds were characterized by ^{1}H NMR

spectroscopy and single-crystal x-ray diffraction (XRD) (Figure 3). In the solid state, **4pyrO-4pyrOH** is in the S_4 symmetric confirmation, but solution ^{1}H NMR spectroscopy suggests a variety of conformational H-bonded isomers coexisting at room temperature. For **2OAc,2azin-4azaindole**, two C_2 symmetric isomers co-crystallized which differ by the relative orientation of the 7-azin ligands. The O(X)•••O(X) distances of 2.44 Å in **4pyrO-4pyrOH** and N(X)•••O(X) distances of 2.69 Å in **2OAc,2azin-4azaindole** are consistent with strong to moderate hydrogen-bonding.[17] Thus, these cubanes possess an additional secondary coordination sphere that modulates their reactivity

Scheme 1. Synthesis of cubane complexes containing intramolecular hydrogen-bonding

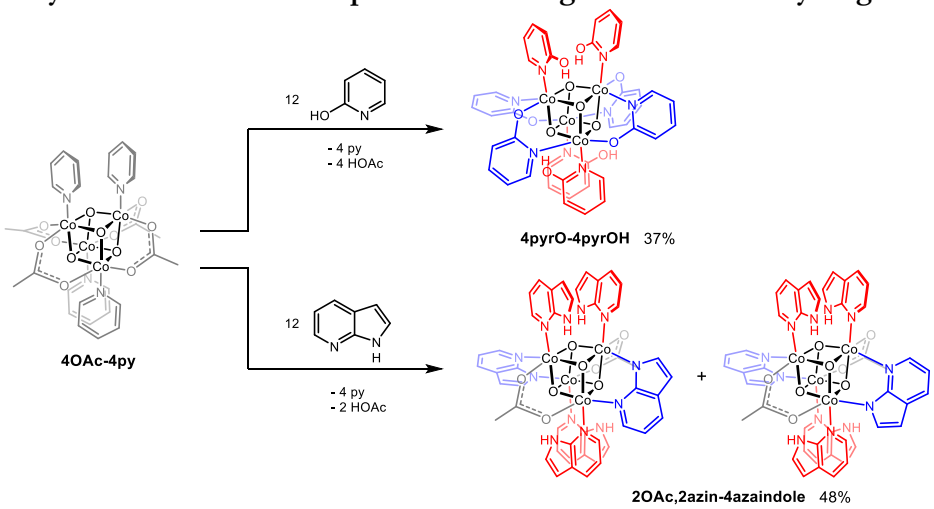

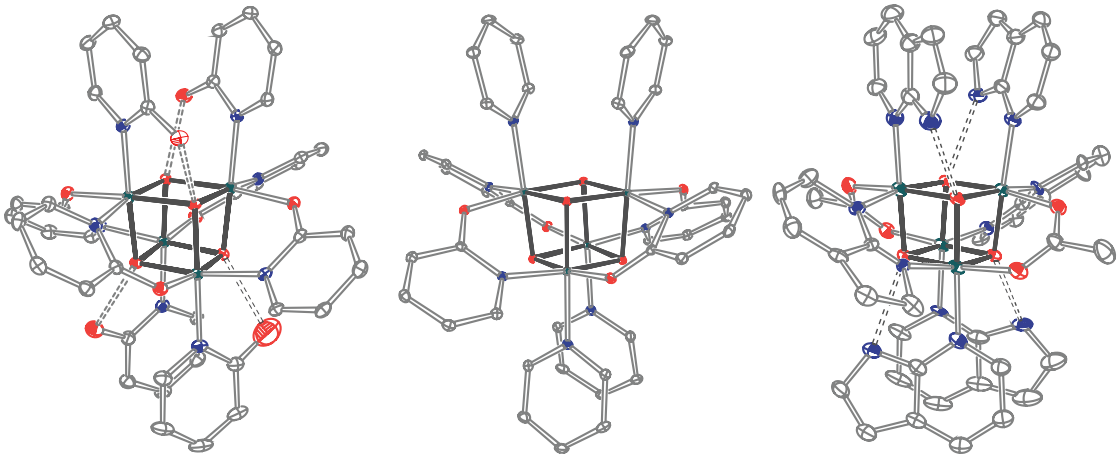

Figure 3. Single-crystal XRD structures of cubanes containing pyrindonate or 7-azaindolate ligands. Intramolecular hydrogen-bond donor-acceptor distances are distinguished as dashed-bonds. Thermal ellipsoids shown at 30% probability. Hydrogen atoms and solvent are removed for clarity.

3.3 Electrochemistry

All cyclic voltammograms of the cubanes exhibit a reversible event for the $[Co^{III}_4O_4]^{4+}/[Co^{IV}Co^{III}_3O_4]^{5+}$ couple (E_1), and depending of the ligand set, either a reversible or irreversible event for the $[Co^{IV}Co^{III}_3O_4]^{5+}/\{[Co^{V}Co^{III}_3O_4]^{6+} \leftrightarrow [Co^{IV}_2Co^{III}_2O_4]^{6+}\}$ couple (E_2) (Figure 4). While the first redox event has long been reported in the literature, the second redox event has not yet been reported, to the best of our knowledge.[14,18–20] The reversibility of E_2 seems to depend on the *combination* of X and L, rather than the individual identity of X or L. When there exists a large asymmetry in the electron-donating properties of X and L, E_2 is irreversible. In other words, if X and L are either all electron-rich or electron-poor, then E_2 will be reversible; however, if X is much more basic than L, or vice versa, E_2 will be irreversible. Four examples corroborate this hypothesis: **4OAc-4DMAP**, **4pyrO-4py**, **4pyrO-4DMAP**, and **4OAc-4py**. The first two cubanes have only electron-rich L (DMAP) or electron-rich X (2-pyridonate), and their cyclic voltammograms show irreversible E_2. However, **4pyrO-4DMAP** and **4OAc-4py** both have either all electron-rich or all electron-poor ligands, and therefore have reversible E_2 events. This observation suggests that redox couple E_2 involves some degree of ligand non-innocence. If there is large difference between the donating properties of X and L, more electron-hole character concentrates on the more donating ligand, leading to oxidative degradation. Conversely, when all the ligands are more equally donating, the electron-hole character is distributed more evenly across all eight ligands, and leads to a more stable complex. The electronic structure of this oxidation state will be discussed in later sections.

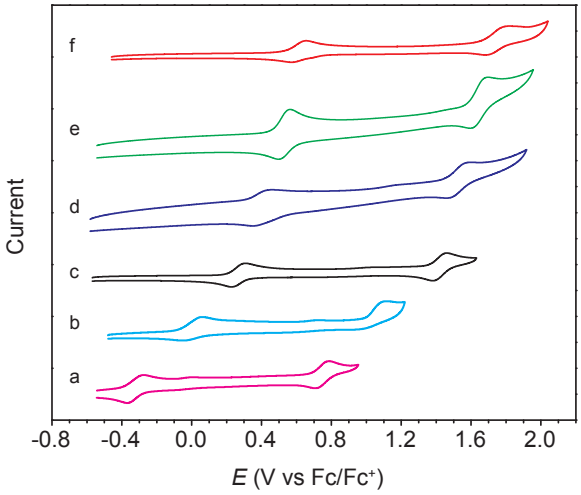

Figure 4. Some representative cyclic voltammograms of cubane complexes in organic solvent (see Table 1 for details, 100 mV/s scan rate, 0.1 M $[^nBu_4N]PF_6$ electrolyte). (a) **4pyrO-4DMAP**; (b) **4pyrO-4py**; (c) **4OAc-4py**; (d) **2NBA,2OAc-4py**; (e) **4NBA-4py**; (f) **4OAc-4CNpy**.

The redox couples show a strong dependence on the ligand basicity, shifting cathodically with electron-withdrawing ligands, and anodically with electron-donating ligands. To decouple the effects of the pyridyl ligand and anionic ligand on redox potentials, a series of cubanes were synthesized holding X = OAc constant while varying

L (**4OAc-4L**, Series 1), and conversely holding L = py constant while varying X (**4X-4py**, Series 2). The redox potentials both Series 1 and 2 correlated linearly with an electron-density descriptor, the average pK_a (aqueous)[15,16,21,22] of HX or HL^+ per cobalt center (eq 4) (Figure 5A). This descriptor will herein be referred to as the *effective basicity*. Here, pK_a is employed as a free-energy representation for the electron-donating ability of the ligand. Previous reports have used Hammett parameters to correlate redox activity, but this analysis is limited to only substituted aryl-based ligands, whereas pK_a is a much more general parameter.[19] The E_1 slopes of Series 1 and 2 is -120 ± 7 mV/dec and -69 ± 9 mV/dec, respectively. The E_2 slopes are very similar at -128 ± 9 mV/dec and -51 ± 9 mV/dec. The magnitude of the slopes demonstrates that the redox couple of the cubane is about twice as sensitive to the X ligand than to the L ligand. The possible cause for this effect will be discussed in the later section. Most surprising is that the redox potentials of asymmetric, mixed-carboxylate cubanes could be predicted simply by considering the summed pK_a values. This fact would seem to suggest that the electronic effects of coordination asymmetry are levelled out by the Co_4O_4 cubane through some communicative mechanism. In this context, all four cobalt ions in the Co_4O_4 unit essentially behave as a single "superion" entity.

The two series could be fit simultaneously with planar surfaces (eq 5 & 6, Figure 5B). To validate the universality of eq 5 and 6 (which were trained on Series 1 and Series 2), the E_1 and E_2 values of cubanes comprising *any* combination of X and L were measured and compared to the predicted values. The E_1 redox potential ranged from 1.12 V to –0.30 V, range of 1420 mV (Table 1). A smaller range of 830 mV was observed for E_2 due to some of the expected events existing outside the solvent's electrochemical window. Satisfyingly, the redox potentials of all the cubanes (without intramolecular hydrogen-bonds) were able to predicted by eq 5 and 6 with a maximum absolute error of 0.099 V and 0.050 V, respectively. Significantly, we found that both cubanes of the type $Co_4O_4X_4L_4$ and $[Co_4O_4X_2L^2{}_4]^{2+}$ (L^2 = 2,2′-bipyridine) behave identically with respect to eq 5 and 6.[20] This observation indicates that the relative number of X to L ligands does not affect the validity of eq 5 and 6, and therefore the coefficients must reflect the intrinsic donor properties of X versus L type ligands. In summary, it appears that eq 5 and 6 holds true for (1) any number of X or L, (2) symmetric and asymmetric ligand coordination environments around the cubane, and (3) X ligands other than carboxylates, as well.

$$\textit{effective bascity} = \frac{1}{4\mathrm{Co}} \sum_i \mathrm{p}K_{ai} \tag{4}$$

$$E_1 = -0.120 \times \frac{1}{4} \sum_i \left[\mathrm{p}K_a(\mathrm{HX})_i + 0.575\mathrm{p}K_a(\mathrm{HL}^+)_i \right] + 1.28 \tag{5}$$

$$E_2 = -0.128 \times \frac{1}{4} \sum_i \left[\mathrm{p}K_a(\mathrm{HX})_i + 0.40\mathrm{p}K_a(\mathrm{HL}^+)_i \right] + 2.32 \tag{6}$$

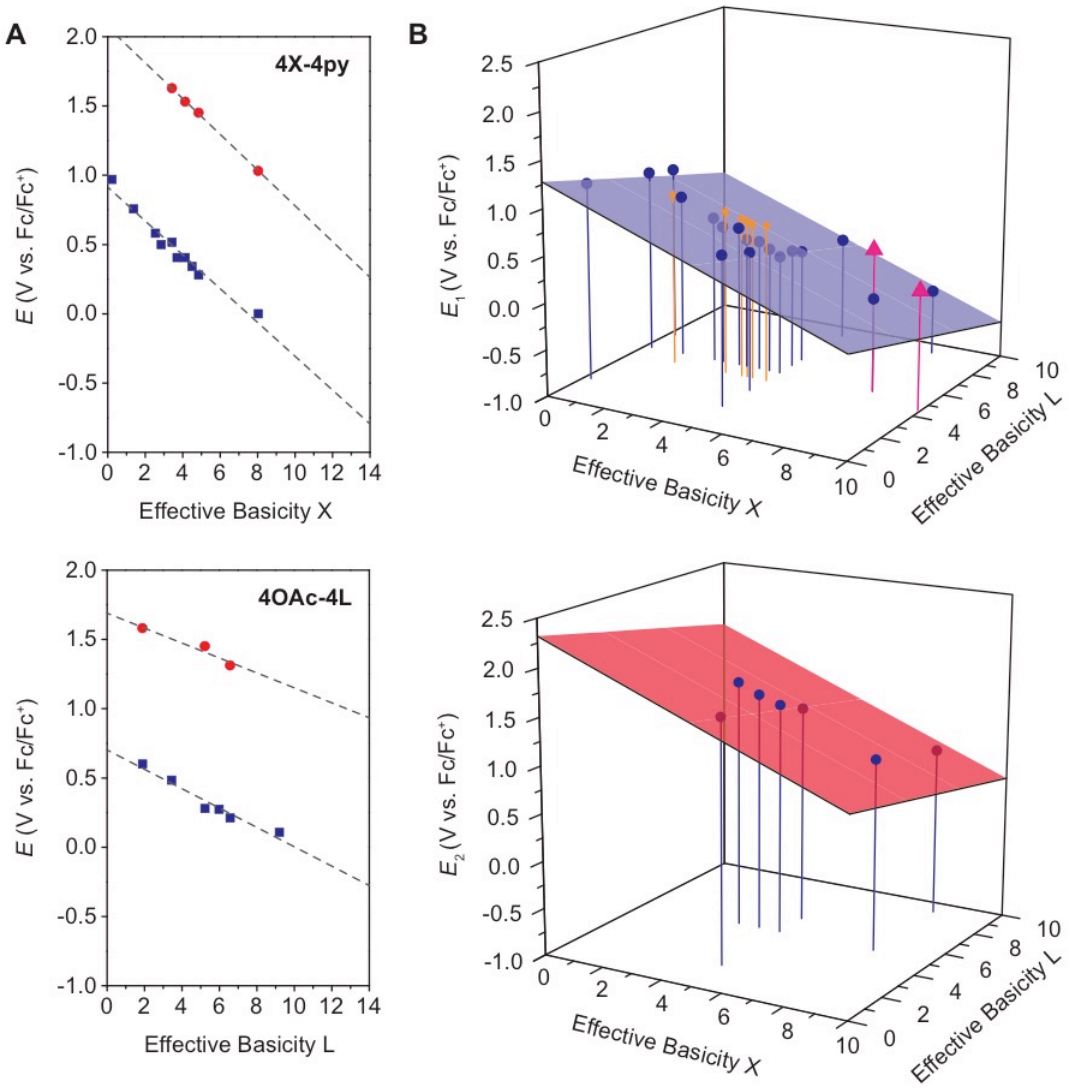

Figure 5. (A) Plots and fits of E_1 and E_2 potentials versus effective basicity for **4X-4py** (Series 1, top) and **4OAc-4L** (Series 2, bottom). The blue squares (■) are the E_1 values and the red circles (●) are the E_2 values. The dashed lines are the linear fits. (B) Surface fits of the E_1 (eq 5, top) and E_2 (Eq. 6, bottom) for all cubane complexes. The blue circles (●) are redox potentials for **4X-4L** cubanes, the orange stars (★) are E_1 values for **[2X-4L]**$^{2+}$ from Christou and coworkers [20], and the purple triangles (▲) are potentials for the hydrogen-bonded cubanes. Vertical drop lines are present for visual guide.

Table 1. Cubane complexes and their redox potentials

Cubane	Effective Basicity X[15,16,21,22]	Effective Basicity L[15,16,21,22]	E_1 (V)	E_2 (V)	Solvent	Reference
4TFA-4CNpy	0.23	1.90	1.12		CH_2Cl_2	
4TFA-4OMepy	0.23	6.39	0.90		MeCN	
4TFA-4py	0.23	5.25	0.97		CH_2Cl_2	
3TFA,OAc-4py	1.37	5.25	0.76		CH_2Cl_2	

2TFA,2OAc-4py	2.54	5.25	0.58		CH_2Cl_2	
TFA,3OAc-4py	3.70	5.25	0.40		CH_2Cl_2	
4CA-4py	2.86	5.25	0.50		MeCN	
4NBA-4py	3.43	5.25	0.52	1.63	MeCN	
3NBA,OAc-4py	3.79	5.25	0.47	1.59	MeCN	
2NBA,2OAc-4py	4.15	5.25	0.41	1.53	MeCN	
NBA,3OAc-4py	4.50	5.25	0.34	1.48	MeCN	
4OAc-4py	4.86	5.25	0.28	1.45	MeCN	
4OAc-4CNpy	4.86	1.90	0.60	1.58	MeCN	[14]
4OAc-4COOEtpy	4.86	3.45	0.48		MeCN	[19]
4OAc-4OMe	4.86	6.39	0.21	1.31[b]	MeCN	[19]
4OAc-4Mepy	4.86	5.99	0.27		MeCN	[19]
4OAc-4DMAP	4.86	9.20	0.11	1.10[b]	MeCN	
4pyrO-4pyrOH	8.04	5.23	0.55		CH_2Cl_2	
4pyrO-4py	8.04	5.25	0.0	1.03	CH_2Cl_2	
4pyrO-4DMAP	8.04	9.20	-0.30	0.80	CH_2Cl_2	
2OAc,2azin-4azaindole	~10	4.45	0.30[b]		DMF	
[a]**[2OAc-4bipy]$^{+2}$**	2.43	4.34	0.69		MeCN	[20]
[a] **[2NBA-4bipy]$^{+2}$**	1.71	4.34	0.77		MeCN	[20]
[a] **[2BA-4bipy]$^{+2}$**	2.10	4.34	0.70		MeCN	[20]
[a] **[2PFBA-4bipy]$^{+2}$**	0.80	4.34	0.86		MeCN	[20]
[a] **[2CBA-4bipy]$^{+2}$**	2.00	4.34	0.72		MeCN	[20]
[a] **[2tBuBA-4bipy]$^{+2}$**	2.19	4.34	0.68		MeCN	[20]

[a] bipy = 2,2-bipyridine, BA = benzoate, PFBA = pentafluorobenzoate, CBA = 4-chlorobenzoate, tBuBA = 4-*t*Butylbenzoate. [b] Value obtained by differential pulse voltammetry (DPV).

The redox potentials reported above were all measured in polar aprotic solvents (MeCN, DCM, or DMF). When measured in water, the E_1 potentials experience an average +553 ± 26 mV potential shift (Table 2). This solvent dependence on redox potentials has been noted for **4OAc-4py** before, but its origin has not been discussed.[6,18] Unfortunately, only a few complexes were water-soluble enough to be measured, and E_2 potentials were not observed, as they would be beyond the electrochemical window of water. We rationalize this positive shift in potential originates from hydrogen-bonding interactions between the cubane μ^3-oxo ligands and water. The hydrogen-bonding reduces the μ^3-oxo donation into each cobalt ion, which in turn, destabilizes higher oxidation states. Interestingly, the preservation of the E_1/pK_a ratio suggests that *relative* cubane-ligand interactions do not significantly change. The hydrogen-bonding effect is clearly demonstrated, even in aprotic solvent, by comparing **4pyrO-4pyrOH** with **4pyrO-4py**. The pK_a of 2-hydroxypyridinium cation and pyridinium are essentially identical (5.23 and 5.25, respectively), and according to eq 5, should give nearly identical E_1 values. However, the observed E_1 value for **4pyrO-4pyrOH** is 550 mV higher than that of **4pyrO-4py**. In the case of **2OAc,2azin-4azaindole**, the experimental E_1 is 519 mV

higher than predicted by eq 5. These raised redox potential differences of the hydrogen-bonded cubanes (519 and 550 mV) and cubanes in water (553 mV) is remarkably similar.

Table 2. Comparison of cubane redox potential in aprotic solvent versus water

Cubane	E_1 (V), aprotic solvent	E_1 (V), water[a]	Reference
4OAc-4COOEtpy	0.48	1.00	[19,23]
NBA,3OAc-4py	0.34	0.89	
4OAc-4py	0.28	0.85	
4OAc-4Mepy	0.27	0.84	[19]
4OAc-4DMAP	0.11	0.68	

[a] Potential versus Fc/Fc^+.[24]

3.4 Computational Results

To quantify the ligands' influence on the redox potential, we performed energy decomposition analysis (EDA) on the cubanes. The results reveal that X ligands stabilize the oxidized cubanes significantly better than L ligands. In **4OAc-4py**, the overall interaction energy between the $[Co^{III}_4O_4]^{4+}$ ion and acetate is -158 kcal/mol, while the energy between $[Co^{III}_4O_4]^{4+}$ and pyridine is only -43 kcal/mol. The interaction energies for the two ligand sets increase upon oxidation to **[4OAc-4py]**$^+$: -243 kcal/mol for acetate and -46 kcal/mol. As can be seen, the $[Co_4O_4]$-acetate bonding is greatly strengthened upon oxidation by -85 kcal/mol, but the pyridine-$[Co_4O_4]$ bonding only slightly increases by -2 kcal/mol. The frozen electron density term, (FRZ) which describes electrostatic and steric contributions to bonding, is at least an order of magnitude larger for the acetate ligand, and doubles in magnitude upon oxidation. The polarization and charge transfer terms are also overall larger for acetate than for pyridine, however they are less than an order of magnitude different. The size of the FRZ term indicates that electrostatic forces dominate the stability of the oxidized cubane. This finding seems intuitive as Co(III) and Co(IV) are both considered hard-type ions, and according to hard-soft acid-base theory, should prefer ionic bonding interactions over dative interactions. To uncover trends in the bonding, EDA was also applied to **4TFA-4py** and **4OAc-4(CNpy)**, as well. The energy difference in frozen component between **[4X-4L]**$^+$ and **4X-4L** ($FRZ_{ox} - FRZ_{red} = \Delta FRZ$) for the $[Co_4O_4]$–X and $[Co_4O_4]$–L bonds plotted against pK_a yields a slope of -0.8 kcal/(mol•pK_a) and -0.5 kcal/(mol•pK_a), respectively (Figure S1). Note that the energy values are within the error of DFT calculations, but there is a qualitative correlation between theory and the experimental redox trends.

The doubly oxidized state, **[4OAc-4py]**$^{2+}$, was analyzed by DFT calculations (See Supporting Information). The calculations determined that the $S = 1$ is favored over the $S = 0$ state by -22 kcal/mol. Negligible spin contamination ($\langle S^2 \rangle = 2.0775$, expected 2) also strongly supports the triplet ground state. Interestingly, the calculations suggest two valence-trapped Co(IV) centers, as opposed to a valence delocalized system. There have been conflicting reports of hole delocalization in cobalt cubane systems by DFT, and delocalization has been suggested as a product of a self-interaction error.[4,25]

3.5 Application of model to OER intermediates

Now, we wish to apply eq 5 and 6 to various fleeting intermediates proposed in the cubane-catalyzed OER mechanism, in order to fortify the previous mechanistic study with some thermodynamic values.[6] It is important to emphasize that the redox values predicted by eq 5 and 6 are under the strict assumption that fundamental bonding interactions between carboxylates, pyridonates, hydroxide, or oxide with Co_4O_4 are similar, in the sense that they are primarily electrostatic (*vide supra*). However, hydroxide and oxide ligands do possess stronger π-donating abilities than carboxylates and pyridonates, and this may cause the true redox potentials of cubanes bound to hydroxide or oxide to deviate from those derived by eq 5 and 6. Nevertheless, from simple ligand-field arguments, the stronger π-donating properties should actually destabilize more the lower oxidation states of cobalt, which should result in *negative* deviations from eq 5 and 6.

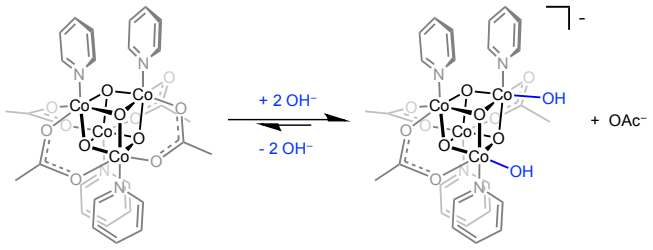

4OAc-4py **3OAc,2OH-4py** (7)

We have reported previously that aqueous solutions $Co_4O_4(OAc)_4py_4$ reacts with hydroxide to produce $[Co_4O_4(OAc)_3(OH)_2py_4]^-$ (**[3OAc,2OH-4py]**$^-$), perhaps in equilibrium with $Co_4O_4(OAc)_3(OH)(H_2O)py_4$ (**3OAc,OH-H_2O,4py**) (eq 7).[6] This species was characterized by NMR spectroscopies, and is proposed to be the active form of the cubane during OER catalysis. During catalysis, the Co(III)-hydroxide moiety undergoes a series of proton- and electron-transfer steps to form putative Co(IV)-oxo and Co(V)-oxo intermediates. Evidence for these intermediates came from kinetic studies and DFT calculations. The kinetics implicated that a key electron-transfer from the Co(IV)-oxo to **[4OAc-4py]**$^+$ generated the Co(V)-oxo intermediate responsible for O–O bond formation. No prior knowledge of the relative redox potentials contributed to the formulation of this disproportionation step. While the mechanistic study revealed that the $[Co_4O_4]^{+6}$ state was achieved and only terminal oxygen ligands were involved, much remains unknown about the specific catalyst speciation. The resting state of the catalyst is presumably **[3OAc,2OH-4py]**$^-$ or **3OAc,OH-H_2O,4py**, but the specifics of proton- and electron-transfer steps have not been elucidated. Specifically, are the redox steps simple electron-transfer, or are proton-transfers required before, during, or after oxidation? Using the conjugate acid pK_a values of 15.7 for OH^- ligand, and ~36 for O^{2-},[21,26] the following E_1 and E_2 redox potentials were obtained for the most likely catalytically-active candidates (Table 3). The E_1 values of these candidates suggest that oxidation from $[Co^{III}{}_4O_4]^{4+}$ to $[Co^{III}{}_3Co^{IV}O_4]^{5+}$ by **[4OAc-4py]**$^+$ occurs spontaneously. The E_2 potentials for the hydroxo-ligated cubanes are significantly higher than the E_1 of **[4OAc-4py]**$^+$ which indicates that a simple electron-transfer is not thermodynamically favored. However, if deprotonation of hydroxide to oxide occurred before electron-

transfer, the oxidation to $[Co^{III}_2Co^{IV}_2O_4]^{+6}$ becomes favorable. Thus, these results suggest that the most likely catalyst is **[3OAc,2OH-4py]**$^-$, which has been previously described by NMR spectroscopies, since it possess reasonable redox couples to allow cycling between $[Co^{III}_4O_4]^{+4}$, $[Co^{III}_3Co^{IV}O_4]^{+5}$, and $\{[Co^{III}_2Co^{IV}_2O_4]^{+6} \leftrightarrow [Co^{III}_3Co^{V}O_4]^{+6}\}$ states during OER catalysis. With this information, we propose a revised OER catalytic cycle (Scheme 2). This updated mechanism allows for two kinetically indistinguishable O–O coupling pathways, acid-base mechanism or radical-coupling. Recently, Nocera and coworkers have found direct evidence for the radical-coupling mechanism at pH 7 in CoP_i, and several DFT calculations have also shown this pathway to be energetically reasonable.[4,27,28]

Table 3. Predicted redox potentials for hydroxo- and oxo-ligated cubanes

Cubane	E_1 (V)[a]	E_2 (V)[a]	$[E_1(4OAc\text{-}4py) - E_1]$ (V)	$[E_1(4OAc\text{-}4py) - E_2]$ (V)
[4OAc,OH-4py]$^-$	-0.09	+0.86	+0.37	-0.58
[4OAc,O-4py]$^{-2}$	-0.70	+0.21	+0.96	-0.07
3OAc,OH-H_2O,4py	0.01	0.96	+0.27	-0.69
[3OAc,2OH-4py]$^-$	-0.41	+0.51	+0.69	-0.23
[3OAc,OH,O-4py]$^{-2}$	-1.02	-0.14	+1.30	+0.42
[3OAc,2O-4py]$^{-3}$	-1.63	-0.78	+1.91	+1.06

[a] Potential versus Fc/Fc^+ in polar aprotic solvent.

Scheme 2. Proposed mechanism for OER catalyzed by **3OAc,2OH-4py**

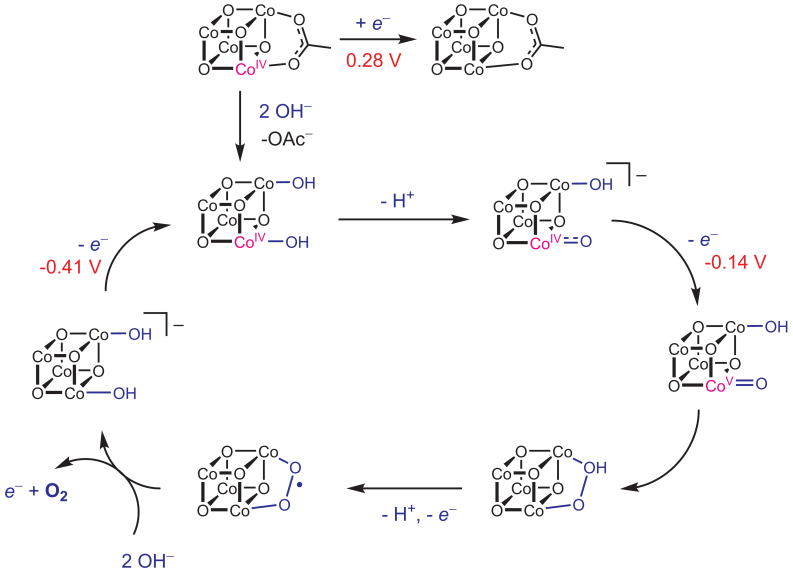

3.6 Conclusions

New synthetic routes to functionalize cubanes were developed to yield a large diversity of cubanes containing very electron-rich to electron-poor ligands. Addition of secondary-sphere hydrogen-bond donors on the cubane caused its redox potentials to increase relative to its non-hydrogen-bonded congener, and thus offered a rationalization

for the observed difference in cubane redox potential in water versus aprotic solvents. The pK_a of the ligands were found to be an excellent, quantitative predictor of the $[Co^{III}_4O_4]^{4+}/[Co^{IV}Co^{III}_3O_4]^{5+}$ and $[Co^{IV}Co^{III}_3O_4]^{5+}/\{[Co^{V}Co^{III}_3O_4]^{6+} \leftrightarrow [Co^{IV}_2Co^{III}_2O_4]^{6+}\}$ redox potentials. DFT results provided a rationalization for the LFER. Thus, there are at least three basic variables which alter the cubane's redox properties: basicity of anion, basicity of neutral ligand, and presence of hydrogen-bond interactions. This LFER was applied to predicting the redox potentials of $[Co_4O_4]$ cluster bound to μ^1-hydroxide and μ^1-oxo-ligands, and supports the plausibility of cubane-catalyzed OER mechanism whereby a Co(V)-μ^1-oxo is formed *via* redox disproportionation of two $[Co^{IV}Co^{III}_3O_4]$ cubanes.[6] These newly developed synthetic methods and predictive model should also aid the rational discovery of better cobalt-based OER catalysts.

3.7 Acknowledgements
We would like to thank the NIH Shared Instrumentation Grant S10-RR027172. This work was supported by the Director, Office of Science, Office of Basic Energy Sciences of the US Department of Energy under contract No. DE-AC02-05CH11231.

3.8 References

(1) Krewald, V.; Retegan, M.; Cox, N.; Messinger, J.; Lubitz, W.; DeBeer, S.; Neese, F.; Pantazis, D. A. *Chem. Sci.* **2015**, *6* (3), 1676.
(2) Fillol, J. L.; Codolà, Z.; Garcia-Bosch, I.; Gómez, L.; Pla, J. J.; Costas, M. *Nat. Chem.* **2011**, *3* (10), 807.
(3) McAlpin, J. G.; Surendranath, Y.; Dincă, M.; Stich, T. A.; Stoian, S. A.; Casey, W. H.; Nocera, D. G.; Britt, R. D. *J. Am. Chem. Soc.* **2010**, *132* (20), 6882.
(4) Li, X.; Siegbahn, P. E. M. *J. Am. Chem. Soc.* **2013**, *135* (37), 13804.
(5) Fernando, A.; Aikens, C. M. *J. Phys. Chem. C* **2015**.
(6) Nguyen, A. I.; Ziegler, M. S.; Oña-Burgos, P.; Sturzbecher-Hohne, M.; Kim, W.; Bellone, D. E.; Tilley, T. D. *J. Am. Chem. Soc.* **2015**, *137* (40), 12865.
(7) Su, X.-J.; Gao, M.; Jiao, L.; Liao, R.-Z.; Siegbahn, P. E. M.; Cheng, J.-P.; Zhang, M.-T. *Angew. Chem. Int. Ed.* **2015**, *54* (16), 4909.
(8) Liu, F.; Concepcion, J. J.; Jurss, J. W.; Cardolaccia, T.; Templeton, J. L.; Meyer, T. J. *Inorg. Chem.* **2008**, *47* (6), 1727.
(9) Gerken, J. B.; McAlpin, J. G.; Chen, J. Y. C.; Rigsby, M. L.; Casey, W. H.; Britt, R. D.; Stahl, S. S. *J. Am. Chem. Soc.* **2011**, *133* (36), 14431.
(10) Winkler, J. R.; Gray, H. B. In *Molecular Electronic Structures of Transition Metal Complexes I*; Mingos, D. M. P., Day, P., Dahl, J. P., Eds.; Structure and Bonding; Springer Berlin Heidelberg, 2011; pp 17–28.
(11) Costentin, C.; Porter, T. R.; Savéant, J.-M. *J. Am. Chem. Soc.* **2016**, *138* (17), 5615.
(12) Nguyen, A. I.; Hadt, R. G.; Solomon, E. I.; Tilley, T. D. *Chem. Sci.* **2014**, *5* (7), 2874.
(13) Smith, P. F.; Hunt, L.; Laursen, A. B.; Sagar, V.; Kaushik, S.; Calvinho, K. U. D.; Marotta, G.; Mosconi, E.; De Angelis, F.; Dismukes, G. C. *J. Am. Chem. Soc.* **2015**, *137* (49), 15460.

(14) Chakrabarty, R.; Bora, S. J.; Das, B. K. *Inorg. Chem.* **2007**, *46* (22), 9450.
(15) Zhou, X.-X.; Welch, C. J.; Chattopadhyaya, J. *Acta Chem. Scand.* **1986**, *40b*, 806.
(16) Dufour, N.; Lebuis, A.-M.; Corbeil, M.-C.; Beauchamp, A. L.; Dufour, P.; Dartiguenave, Y.; Dartiguenave, M. *Can. J. Chem.* **1992**, *70* (12), 2914.
(17) Jeffrey, G. A. *An Introduction to Hydrogen Bonding*; Oxford University Press, 1997.
(18) McCool, N. S.; Robinson, D. M.; Sheats, J. E.; Dismukes, G. C. *J. Am. Chem. Soc.* **2011**, *133* (30), 11446.
(19) Berardi, S.; La Ganga, G.; Natali, M.; Bazzan, I.; Puntoriero, F.; Sartorel, A.; Scandola, F.; Campagna, S.; Bonchio, M. *J. Am. Chem. Soc.* **2012**, *134* (27), 11104.
(20) Dimitrou, K.; Brown, A. D.; Concolino, T. E.; Rheingold, A. L.; Christou, G. *Chem. Commun.* **2001**, No. 14, 1284.
(21) *Handbook of Chemistry and Physics*, 87th ed.; CRC Press: Florida, 2006.
(22) Smith, R. M.; Motekaitis, R. J. *NIST Standard Reference Database 46*, 3.0.; National Institute of Standards and Technology: Washington, D.C., 1997.
(23) Ullman, A. M.; Liu, Y.; Huynh, M.; Bediako, D. K.; Wang, H.; Anderson, B. L.; Powers, D. C.; Breen, J. J.; Abruña, H. D.; Nocera, D. G. *J. Am. Chem. Soc.* **2014**, *136* (50), 17681.
(24) Georges, J.; Desmettre, S. *Electrochimica Acta* **1984**, *29* (4), 521.
(25) McAlpin, J. G.; Stich, T. A.; Ohlin, C. A.; Surendranath, Y.; Nocera, D. G.; Casey, W. H.; Britt, R. D. *J. Am. Chem. Soc.* **2011**, *133* (39), 15444.
(26) Cotton, F. A.; Wilkinson, G.; Murillo, C. A.; Bochmann, M. *Advanced Inorganic Chemistry*, 6th ed.; John Wiley & Sons, 1999.
(27) Ullman, A. M.; Brodsky, C. N.; Li, N.; Zheng, S.-L.; Nocera, D. G. *J. Am. Chem. Soc.* **2016**, *138* (12), 4229.
(28) Wang, L.-P.; Van Voorhis, T. *J. Phys. Chem. Lett.* **2011**, *2* (17), 2200.

Supporting Information for **Chapter 3**

General considerations. Cobalt(II) nitrate hexahydrate, pyridine, hydrogen peroxide (34-37% in water), 4-methoxypyridine, 4-cyanopyridine, 4-*N*,*N*-dimethylaminopyridine, 4-nitrobenzoic acid, chloroacetic acid, 2-hydroxypyridine, and 7-azaindole were purchased from Sigma-Aldrich and used without further purification. Sodium acetate trihydrate was purchased from EMD. Solvents were purchased from Fisher-Scientific and used without any further purification. $Co_4O_4(OAc)_4py_4$,[1] and $Co_4O_4(OAc)_4$(4-cyanopyridine)$_4$[1] were synthesized according to published procedures.

Physical methods. Routine NMR spectra were recorded on Bruker AVB-400 and AVQ-400 spectrometers at room temperature. CD_2Cl_2 and acetonitrile-d_3 were purchased from Cambridge Isotopes. ^{1}H NMR spectra were referenced to residual protio-solvent peaks (δ 5.32 for CD_2Cl_2, δ 1.94 for acetonitrile-d_3). Elemental analyses were carried out by the College of Chemistry Microanalytical Laboratory at the University of California, Berkeley. Electrochemical measurements were collected with three-electrode setup on a BASi Epsilon potentiostat.

$Co_4O_4(OAc)_4$(4-methoxypyridine). 4-methoxypyridine (0.150 g, 1.42 mmol) was added to a 10 mL MeCN solution of $Co_4O_4(OAc)_4py_4$ (0.100 g, 0.118 mmol), and the resulting solution was heated to 90°C for 16 hours, yielding a dark solution. The solution was dried *in vacuo*, and the solid was washed 3 x 10 mL Et_2O to give 0.113 g (100%). ^{1}H NMR spectra is consistent with that reported.[2]

$Co_4O_4(OAc)_4$(4-*N*,*N*-dimethylaminopyridine)$_4$. *N*,*N*-dimethylaminopyridine (0.860 g, 7.0 mmol) was added to a 30 mL MeCN solution of $Co_4O_4(OAc)_4py_4$ (0.500 g, 0.59 mmol), and the resulting solution was heated to 80°C for 16 hours, yielding a dark solution. The solution was dried *in vacuo*, and the solid was washed 3 x 100 mL Et_2O. The resulting solid was recrystallized from hot MeCN (~10 mL) to yield 0.400 g (67%) of dark solid. Purer material was obtained by recrystallizing layer diffusion of hexanes into a DCM solution. ^{1}H NMR (400 MHz, CD_2Cl_2): 8.19 (d, 8H), 7.01 (d, 8H), 3.57 (s, 24H), 2.59 (s, 12H). Anal. Calc'd for $C_{36}H_{52}Co_4N_8O_{12}$·0.45 CH_2Cl_2: C, 41.19, H, 5.02; N, 10.54. Found: C, 41.03; H, 5.20; N, 10.58.

$Co_4O_4(O_2CH_2Cl)_4py_4$. Chloroacetic acid (0.049 g, 0.96 mmol) was added to a 5 mL solution of $Co_4O_4(OAc)_4py_4$ (0.100 g, 0.125 mmol) in MeCN, and the resulting solution was heated to 60°C for 16 hours, yielding a dark solution. The solution was dried *in vacuo*, and the solid was recrystallized by layer diffusion of hexanes into a DCM solution. ^{1}H NMR (300 MHz, $CDCl_3$): 8.58 (d, 8H), 7.54 (t, 4H), 7.09 (t, 8H), 4.10 (s, 8H). Anal. Calc'd for $C_{24}H_{28}Cl_4Co_4N_4O_4$·0.83 CH_2Cl_2: C, 33.71; H, 3.38; N, 6.33. Found: C, 34.20; H, 3.14; N, 5.84.

$Co_4O_4(O_2CCF_3)_4py_4$. Trifluoroacetic acid (0.110 g, 0.96 mmol) was added to a 5 mL solution of $Co_4O_4(OAc)_4py_4$ (0.200 g, 0.23 mmol) in MeCN, and the resulting solution was heated to 70°C for 16 hours, yielding a dark solution with the product precipitated as

a black crystalline solid. The solid was collected by decanting, and washed 3 x 10 mL Et_2O to give 0.192 g (77%). Anal. Calc'd for $C_{28}H_{20}Co_4F_{12}N_4O_{12}$: C, 31.48; H, 1.89; N, 5.25. Found: C, 31.62; H, 1.97; N, 5.40.

$Co_4O_4(OAc)_3(O_2CCF_3)py_4$, $Co_4O_4(OAc)_2(O_2CCF_3)_2py_4$, $Co_4O_4(OAc)(O_2CCF_3)_3py_4$
Trifluoroacetic acid (0.0334 g, 0.59 mmol) was added to a 10 mL solution of $Co_4O_4(OAc)_4py_4$ (0.25 g, 0.29 mmol) in MeCN, and the resulting solution was heated to 80˚C for 16 hours, yielding a dark solution. TLC in 66.6% hexanes and 33.3% acetone shows 4 spots with R_f values of 0.8, 0.5, 0.2, and 0. Each species was isolated by silica gel column chromatography, and the fractions containing the pure compound was evaporated *in vacuo*. Each compound was recrystallized by layering hexanes onto a dichloromethane solution.
Yields (with respect to $Co_4O_4(OAc)_4py_4$):
$Co_4O_4(OAc)_3(O_2CCF_3)py_4$: 0.050 g, 19%. Anal. Calc'd for $C_{28}H_{29}Co_4F_3N_4O_{12}$: C, 37.11; H, 3.23; N, 6.18. Found: C, 37.30; H, 3.52; N, 5.89.
$Co_4O_4(OAc)_2(O_2CCF_3)_2py_4$: 0.042 g, 15.2%. Anal. Calc'd for $C_{28}H_{26}Co_4F_6N_4O_{12}\cdot C_3H_6O$: C, 36.56; H, 3.17; N, 5.50. Found: C, 36.20 H, 3.12; N, 5.49.
$Co_4O_4(OAc)(O_2CCF_3)_3py_4$: 0.033 g, 11.4%. Anal. Calc'd for $C_{28}H_{23}Co_4F_9N_4O_{12}\cdot C_3H_6O$: C, 34.72; H, 2.73; N, 5.22. Found: C, 34.46; H, 2.59; N, 5.02.

^1H NMR (400 MHz, CD_2Cl_2):
$Co_4O_4(OAc)_3(O_2CCF_3)py_4$: δ 8.46 (m, 8H), 7.56 (t, 4H), 7.08 (t, 8H), 2.16 (s, 6H), 2.09 (s, 3H).
$Co_4O_4(OAc)_2(O_2CCF_3)_2py_4$: δ 8.36 (m, 8H), 7.50 (t, 4H), 7.01 (t, 8H), 2.07 (s, 6H).
$Co_4O_4(OAc)(O_2CCF_3)_3py_4$: δ 8.39 (m, 8H), 7.60 (t, 4H), 7.13 (t, 8H), 2.22 (s, 3H).

$Co_4O_4(O_2CCF_3)_4$(4-methoxypyridine)$_4$. Trifluoroacetic acid (0.028 g, 0.24 mmol) was added to a 5 mL solution of $Co_4O_4(OAc)_4py_4$ (0.0575 g, 0.067 mmol) in MeCN, and the resulting solution was heated to 70˚C for 16 hours, yielding a dark solution. The solution was dried *in vacuo*, and the solid was dissolved in a minimum amount of DCM, and purified by silica chromatography with 6:4 hexanes:acetone. ^1H NMR (400 MHz, CD_3CN): 8.08 (d, 8H), 6.83 (d, 8H), 3.89 (s, 12H).

$Co_4O_4(O_2CCF_3)_4$(4-cyanopyridine)$_4$. Trifluoroacetic acid (0.245 g, 2.15 mmol) was added to a 10 mL solution of $Co_4O_4(OAc)_4py_4$ (0.500 g, 0.587 mmol) in MeCN, and the resulting solution was heated to 70˚C for 16 hours, yielding a dark solution. The solution was dry-loaded onto silica, and then purified by column chromatography with 7:3 hexanes:acetone. The solid was by precipitation from MeCN by Et_2O (0.164 g, 24%). Anal. Calc'd for $C_{32}H_{16}Co_4F_{12}N_8O_{12}\cdot 2\ H_2O$: C, 31.92; H, 1.67; N, 9.3. Found: C, 31.6; H, 1.57; N, 9.12.

$Co_4O_4(OAc)_3$(4-nitrobenzoate)py_4, $Co_4O_4(OAc)_2$(4-nitrobenzoate)$_2py_4$, $Co_4O_4(OAc)$(4-nitrobenzoate)$_3py_4$, Co_4O_4(4-nitrobenzoate)$_4py_4$

4-nitrobenzoic acid (0.029 g, 0.17 mmol) was added to a 10 mL solution of $Co_4O_4(OAc)_4py_4$ (0.073 g, 0.086 mmol) in MeCN, and the resulting solution was heated to 80˚C for 16 hours, yielding a dark orange solution. TLC in 66.6% hexanes and 33.3% acetone shows 5 spots with R_f values of 0.9, 0.7, 0.5, 0.2 and 0. Silica gel column chromatography was performed to isolate the above species. Each species was isolated by silica gel column chromatography, and the fractions containing the pure compound was evaporated *in vacuo*. Each compound was recrystallized by layering hexanes onto a dichloromethane solution.

Yields (with respect to $Co_4O_4(OAc)_4py_4$):

$Co_4O_4(OAc)_3$(4-nitrobenzoate)py_4: 0.012 g, 15%

$Co_4O_4(OAc)_2$(4-nitrobenzoate)$_2py_4$: 0.007 g, 7.7%. Anal. Calc'd for $C_{43}H_{35}Co_4N_7O_{18}$·0.3 CH_2Cl_2: C, 43.38; H, 2.99; N, 8.18. Found: C, 43.16; H, 3.23; N, 7.94.

$Co_4O_4(OAc)$(4-nitrobenzoate)$_3py_4$: 0.017 g, 17%

Co_4O_4(4-nitrobenzoate)$_4py_4$: 0.005 g, 4.6%. Anal. Calc'd for $C_{48}H_{36}Co_4N_8O_{20}$·1.2 CH_2Cl_2: C, 42.74; H, 2.80; N, 8.11. Found: C, 43.08; H, 2.86; N, 7.76.

^{1}H NMR (400 MHz, CD_2Cl_2):

$Co_4O_4(OAc)_3$(4-nitrobenzoate)py_4: δ 8.51 (m, 8H), 8.11 (m, 4H), 7.56 (m, 4H), 7.10 (m, 8H).

$Co_4O_4(OAc)_2$(4-nitrobenzoate)$_2py_4$: δ 8.47 (d, 8H), 8.13 (d, 4H), 7.99 (d, 4H), 7.63 (m, 4H), 7.13 (d, 8H).

$Co_4O_4(OAc)$(4-nitrobenzoate)$_3py_4$: δ 8.59 (d, 8H), 8.13 (m, 12H), 7.63 (t, 4H), 7.14 (t, 8H).

Co_4O_4(4-nitrobenzoate)$_4py_4$: δ 8.64 (d, 8H), 8.17 (m, 16H), 7.67 (t, 4H), 7.17 (t, 8H).

Co_4O_4(2-pyridonate)$_4$(2-hydroxypyridine)$_4$

2-hydroxypyridine (0.268 g, 2.81 mmol) was added to a 10 mL solution of $Co_4O_4(OAc)_4py_4$ (0.2 g, 0.24 mmol) in MeCN, and the resulting solution was heated at 80˚C for 16 hours, yielding a dark solution. TLC in 60% hexanes and 40% acetone shows three spots with R_f value of around 0.8, 0.7, 0.6. Silica gel column chromatography was performed to isolate the product (R_f = 0.8). Yield: 0.047 g, 37%

Co_4O_4(2-pyridonate)$_4$(4-*N*,*N*-dimethylaminopyridine)$_4$

4-*N*,*N*-dimethylaminopyridine (1.287 g, 10.5 mmol) was added to a 10 mL solution of Co_4O_4(2-pyridonate)$_4$(2-hydroxypyridine)$_4$ (0.15 g, 0.13 mmol), and the resulting solution was heated to 80˚C for 16 hours, yielding a dark solution with solid precipitate. The solution was decanted and solids heated with acetonitrile (10 mL) to 80˚C for 15 minutes, then washed with acetonitrile (3 x 10). Recrystallized by layer diffusion of hexanes into a dichloromethane solution to yield 0.081 g (49%). Anal. Calc'd for $C_{48}H_{56}Co_4N_{12}O_8$·3 H_2O: C, 47.3; H, 5.13; N, 13.79. Found: C, 47.03; H, 5.35; N, 13.49.

Co_4O_4(2-pyridonate)$_4$py$_4$
Pyridine (1.157 g, 1.18 mL, 14.6 mmol) was added to a 10 mL solution of Co_4O_4(2-pyridonate)$_4$(2-hydroxypyridine)$_4$ (0.386 g, 0.034 mmol) in MeCN, and the resulting solution was heated to 80°C for 16 hours, yielding a dark solution with black solid. The solid was collected and recrystallized by layer diffusion of hexanes into a dichloromethane solution. Yield: 0.018 g, 45%. Anal. Calc'd for $C_{40}H_{36}Co_4N_8O_8 \cdot CH_2Cl_2$: C, 45.71; H, 3.55; N, 10.40. Found: C, 46.09; H, 3.74; N, 10.78.

$Co_4O_4(OAc)_2$(7-azin)$_2$(7-azaindole)$_4$. 7-azaindole (0.078 g, 0.66 mmol) was added to a 10 mL solution of $Co_4O_4(OAc)_4py_4$ (0.047 g, 0.055 mmol) in MeCN, and the resulting solution was heated at 80°C for 16 hours, yielding a dark solution with a black crystalline precipitate (single-crystal XRD quality). The solid was collected by filtration. Yield: 0.030 g, 48%. Anal. Calc'd for $C_{46}H_{40}Co_4N_{12}O_8 \cdot 0.55\ C_2H_3N$: C, 49.31; H, 3.66; N, 15.32. Found: C, 49.37; H, 3.51; N, 15.47.

Figure S1. Plot of FRZ energies differences as a function of ligand basicity.

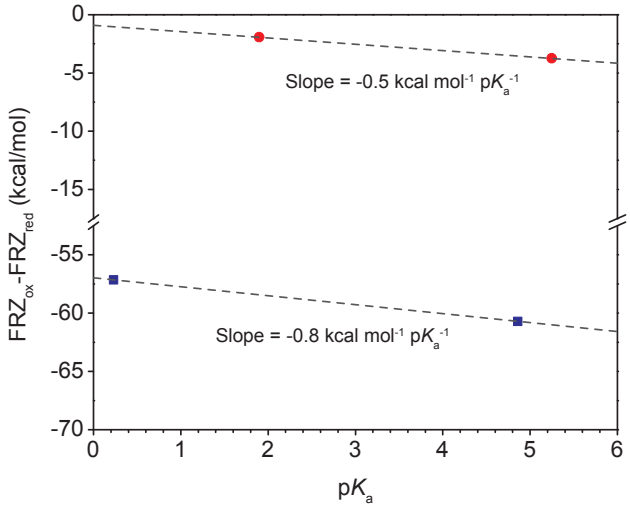

References.

(1) Chakrabarty, R.; Bora, S. J.; Das, B. K. *Inorg. Chem.* **2007**, *46* (22), 9450.
(2) Berardi, S.; La Ganga, G.; Natali, M.; Bazzan, I.; Puntoriero, F.; Sartorel, A.; Scandola, F.; Campagna, S.; Bonchio, M. *J. Am. Chem. Soc.* **2012**, *134* (27), 11104.

Chapter 4:

Tunable, site-isolated Co_4O_4 oxygen-evolution catalysts uniformly dispersed within porous frameworks*

---

* This work is based upon work from a manuscript to be published, included with permission from all authors:

Nguyen, A. I.,* Van Allsburg,* K. M., Terban, M. W., Bajdich, M. Oktawiec, J., Ziegler, M. S., Dombrowski, J. P., Lakshmi, K. V., Drisdell, W. S., Yano, J., Billinge, S. J. L., Tilley, T. D. *In preparation* (*Denotes equal contribution)

Author contributions: Synthetic work in this chapter was a collaborative effort involving Andy I. Nguyen (for pyridyl-linked materials) and Kurt M. Van Allsburg (for carboxylate-linked materials). Both of these authors (A.I.N. and K.M.V.) also conducted spectroscopic and physical characterizations of the new materials. The structural models were constructed by K.M.V. and optimized by Michal Bajdich (Stanford University) using DFT. The X-ray scattering experiments and PDF analyses were performed by Maxwell W. Terban and Simon J. L. Billinge (Columbia University and Brookhaven National Lab). A.I.N., Julia Oktawiec and James P. Dombrowski performed gas sorption experiments. A.I.N. and Micah S. Ziegler contributed the stoichiometric and electrocatalytic OER experiments, and K. V. Lakshmi (Rensselaer Polytechnic Institute) peformed the EPR experiments. A.I.N., K.M.V., and Walter S. Drisdell (LBNL) performed the XAS experiments, and the data analyzed by K.M.V., A.I.N., W.S.D., and Junko Yano (LBNL).

4.1 Introduction

Petrochemicals power the modern lifestyle, providing ubiquitous energy and goods cheaply. However, with mounting evidence of this scheme's unsustainability, the need for solar-derived fuel has never been greater.[1] Storing solar energy via artificial photosynthesis (AP), the light-driven conversion of abundant materials to produce energetically dense chemical fuel, is elegant and highly compatible with existing energy systems. Artificial photosynthesis, whether it is used to produce dihydrogen or carbon-based fuels, requires the oxidation of water to dioxygen.[2] This reaction is termed the oxygen-evolution reaction (OER), and requires catalysts for efficient performance.

Heterogeneous catalyst materials, e.g. metal oxides, uniquely satisfy the demanding requirements of systems for AP (durability, ease of synthesis and device integration), but fuels derived from AP devices using current materials are not yet competitive with fossil fuels.[3] The most critical knowledge, namely how catalytic materials function, and consequently, how they can be improved, often remains elusive. Yet, another disadvantage of metal oxide catalysts is the low ratio of active sites to bulk material; for example, the active sites are often limited to the edges or defect sites, while the majority of the material is inactive.[4,5]

On the other hand, molecular coordination complexes, used as models for heterogeneous catalysts, have offered extensive mechanistic and structural information due to their relative ease of characterization and tunability.[6] However, despite immense effort in this area, many model complexes fail to meet the requirements for practical AP implementation (*vide supra*).[7]

To proceed in light of these limitations, a class of materials recommends itself: three-dimensional coordination polymers.[8,9] These materials elegantly marry molecular tunability with heterogeneous practicality. Moreover, the highly porous nature of many coordination polymers reduces or eliminates the significance of surface/bulk and active/passive distinctions in catalysis, because the metal sites are identical and accessible. Furthermore, the choice of organic linker offers an enormous range of chemical tunability for catalyst design (Scheme 1).

Molecular OER catalysts based on the cobalt(III)-oxo cubane motif (Co_4O_4) are attractive building blocks for polymeric structures, and recent studies on Co_4O_4 have already revealed detailed information on the criteria for efficient catalysis.[10] While an example of an OER catalyst appended onto the linker of a framework structure exists,[11] no example of a framework material with intrinsic OER activity has been reported; this latter structure would significantly have higher catalyst loading by mass. Thus, the Co_4O_4 system is ideal for testing whether the reactivity and mechanism of molecular OER catalysts can be directly translated into heterogeneous materials.

Scheme 1. Strategy to create a porous material derived from a metal oxide catalyst

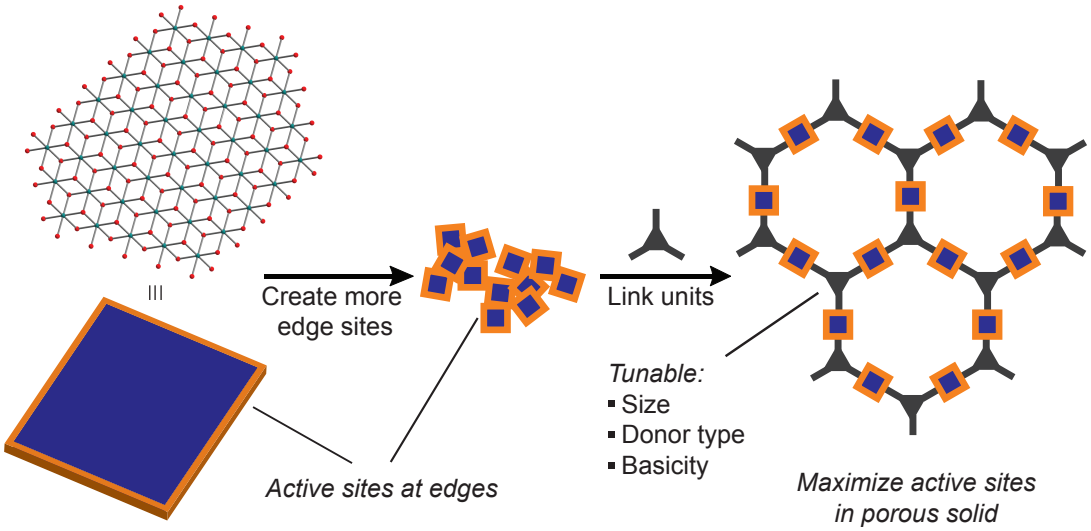

Herein, we report a series of coordination polymers based on Co_4O_4 nodes that catalyze the OER. Through a suite of techniques, we establish structure despite the absence of long-range crystallographic order. The use of different linker ligands was found to have a profound impact on the reactivity and stability of these materials. From an initial set of five different linkers in combination with the parent molecular catalyst, two materials were found to exhibit exceptional stability and OER activity. These optimized Co_4O_4-polymers are significantly more stable than their molecular analogues, yet they retain the chemical and electrocatalytic OER activity. These polymers represent a new class of highly tunable hetereogeneous OER electrocatalysts, and their synthetic strategy provides a rational method for improving AP device efficiency.

4.2 Synthesis

All materials were synthesized in a single step by heating the parent cubane, $Co_4O_4(OAc)_4py_4$ (**1**), with an appropriate linker. The syntheses of Co_4O_4 coordination polymers bridged by carboxylate-based linkers were achieved (Scheme 2) by heating a solution of **1** with stoichiometric amounts of either 1,3,5-benzenetricarboxylic acid (H_3BTC) or 1,3,5-benzenetribenzoic acid (H_3BTB) at 60 °C in methanol. After stirring for 1.5 h, **Co_4-BTC** and **Co_4-BTB** were isolated by filtration as green powders. Analogously, syntheses of Co_4O_4 coordination polymers bridged by pyridyl-based linkers were achieved by heating a solution of **1** with stoichiometric amounts of either 2,4,6-tris(4-pyridyl)triazine (TPT), 2,4,6-tris(4-pyridyl)pyridine (TPP), or 2,4,6-tris(4-pyridyl)benzene (TPB) in benzonitrile at 90–100 °C. To provide a driving force for these reactions, active vacuum was applied to remove pyridine by distillation as it was released from **1**. The resulting solids **Co_4-TPT**, **Co_4-TPP**, and **Co_4-TPB** were isolated by filtration. The proposed structures for these solids are shown in Chart 1. **Co_4-TPT** is a dark-red solid, **Co_4-TPP** is red-brown, and **Co_4-TPB** is dark green. Two strong bands, similar to that of the molecular cubane, **1**, in dominate the diffuse-reflectance UV-visible absorbance spectra (Chart 1A). The band at longer wavelength likely originates from the

$^1A_1 \rightarrow {}^1T_1$ *d*-*d* transition of the low-spin, pseudo-O_h cobalt(III) centers.[12] This transition in **Co$_4$-TPB**, **Co$_4$-TPP**, and **Co$_4$-TPT** occurs at ~700 nm, 650 nm, and 600 nm, respectively. The blue-shifting of the band signifies an increasing t_{2g}-e_g gap correlated with the increasing π-acidity traversing from TPB to TPP to TPT. In **Co$_4$-BTC** and **Co$_4$-BTB**, this transition is blue-shifted relative to that of **1**; in this case the weaker σ-donation of the aryl-carboxylate ligands relative to that of acetate also results in a diminished t_{2g}-e_g gap. These color differences are a first glimpse at the electronic tunability of these materials.

Scheme 2. Two routes for synthesis of cubane-derived polymers.

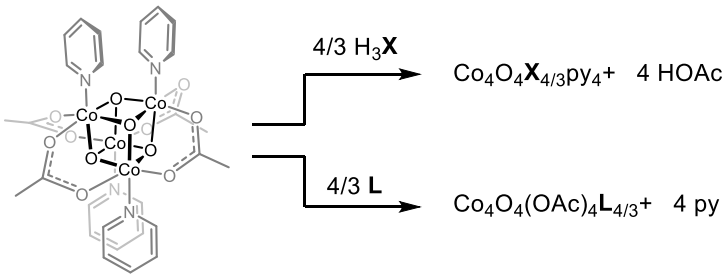

1

Chart 1. Proposed structures of (A) polymers synthesized by carboxylate exchange, and (B) polymers synthesized by pyridine exchange.

A

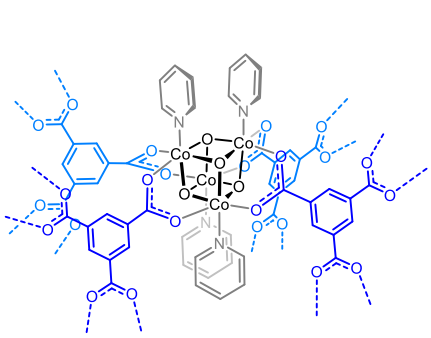

Co_4-BTC

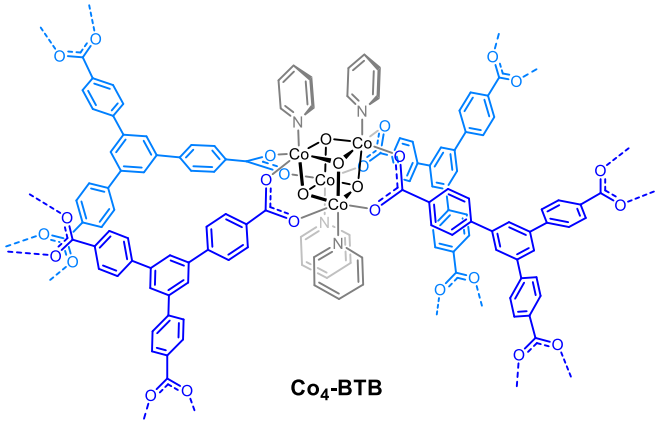

Co_4-BTB

B

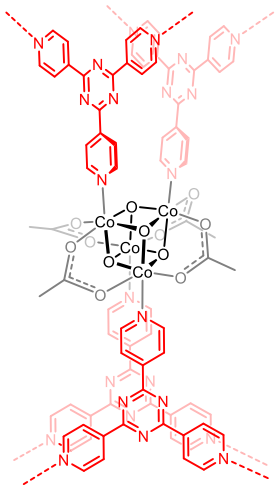

Co_4-TPT

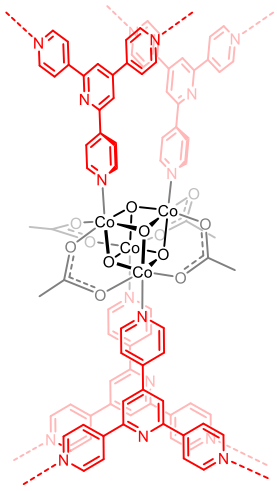

Co_4-TPP

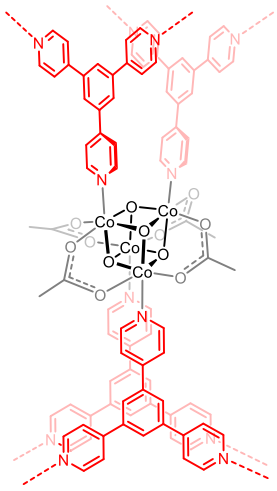

Co_4-TPB

The polymers were further purified of any Co(II) formed during the synthesis by stirring in water with an Empore SPE chelating membrane (Supporting Information). Elimination of Co(II) impurity is a crucial step for investigations into the inherent OER activity of any new Co OER catalyst.[13] The physical separation of the membrane from the coordination polymer avoids the modification of the polymer surface that would be possible with EDTA or a similar reagent, while still allowing the sequestration of any leached metal ions. Indeed, the Empore SPE membrane turned a strong pink color after stirring for 5 days in the presence of each polymer, indicating adsorption of leached Co(II) ions (Supporting Information). This process was repeated until no pink color was observed on the chelating membrane, demonstrating that all soluble forms of Co(II) had been removed from the polymer. This decrease in Co(II) capture over time also demonstrates that Co(II) does not originate from cubane degradation. An alternative purification method found to provide material of similar purity is Soxhlet extraction in methanol over 16 h. This method is significantly faster than the chelation method and

also produces material that is free of Co(II), as evidenced by the absence of any pink color in an Empore membrane when the Soxhlet-treated solids were stirred for five days together with the membrane.

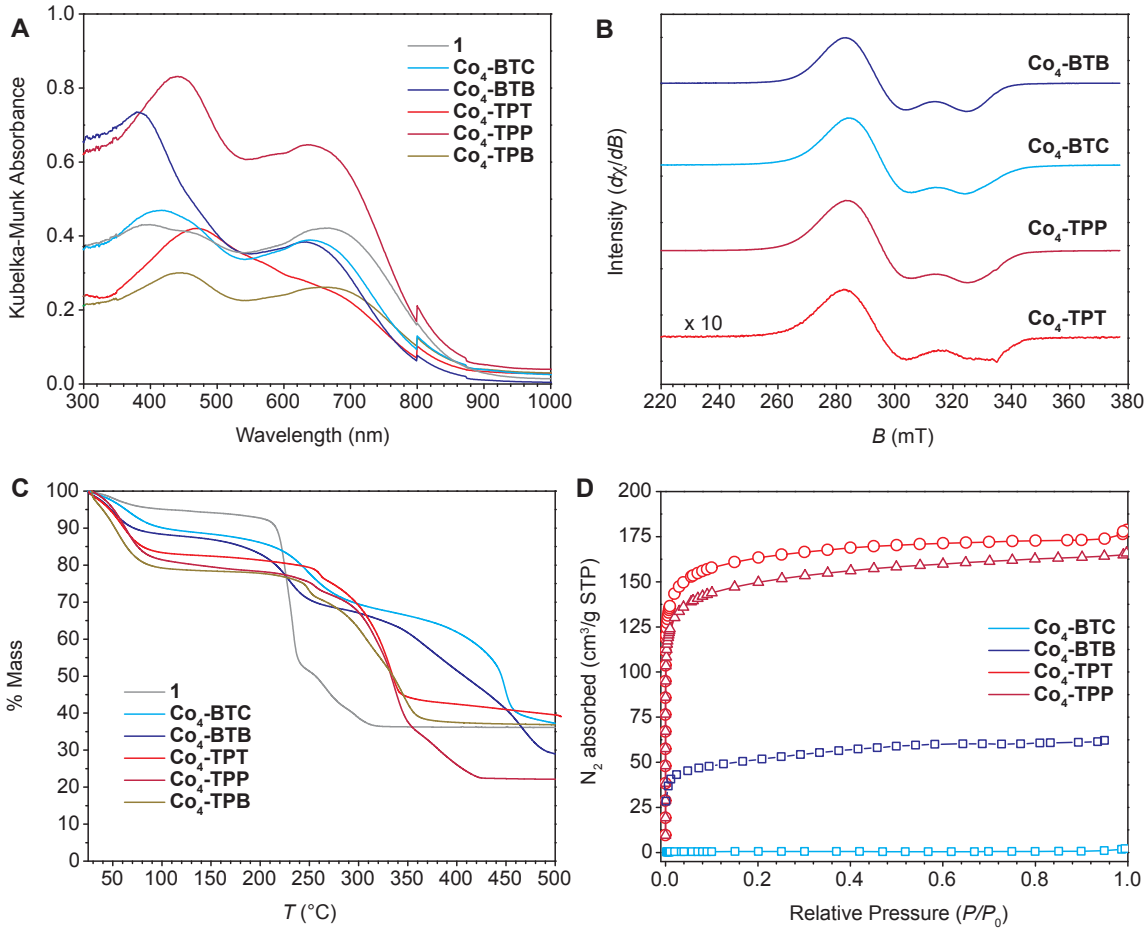

Figure 1. Characterization of Co_4O_4 polymers, with complex **1** for comparison: (A) diffuse reflectance ultraviolet/visible absorbance spectroscopy, (B) electron paramagnetic resonance spectroscopy (microwave frequency = 9.39 GHz, power = 1.19 mW, modulation amplitude = 4 G, modulation frequency = 100 kHz), (C) thermogravimetric analysis under flowing N_2 (heat rate = 10 °C/min), (D) nitrogen adsorption isotherms.

4.3 Structural Characterization

The empirical formulations of these materials were determined by a combination of ^{1}H NMR spectroscopy on acid-digested samples and combustion elemental analysis (EA). The relative ratios of ligands were determined using the integrated intensities of their ^{1}H NMR signals, after digestion in 37% DCl in D_2O. For digested **Co₄-TPT**, **Co₄-TPP**, and **Co₄-TPB**, only the pyridyl-linker and acetic acid were observed in ^{1}H NMR spectra, indicating that all pyridine ligands of **1** were replaced in the synthesis. The molar ratios of the pyridyl-linkers to acetate gave empirical formulas of 1.89, 1.70, and 1.34, for **Co₄-TPT**, **Co₄-TPP**, and **Co₄-TPB**, respectively (Supporting Information). These ratios

are slightly higher than the ideal stoichiometric ratio of 1.33. Combustion EA of the materials also were consistent with the NMR integration of the respective digested samples. Trapped free ligand is an unlikely source of the observed stoichiometric excess, since the materials were purified by Soxhlet extraction with methanol, in which all linker ligands are soluble, prior to analysis. These observations suggest that the average domains of **Co_4-TPT**, **Co_4-TPP**, and **Co_4-TPB** must be small, and thus the edge sites, which are capped by extra-stoichiometric linker ligands, contribute significantly to the overall stoichiometry of these materials. For **Co_4-BTC** and **Co_4-BTB**, the BTC/py and BTB/py molar ratios were both 1.47, slightly larger than the ideal 1.33.

Retention of the reactivity and structure associated with the Co_4O_4 unit in the polymers was probed *via* chemical oxidation (Scheme 3). For reference, the molecular cubane **1** is reported to have a reversible $[Co_4O_4]^{4+}/[Co_4O_4]^{5+}$ redox event,[10] and the oxidized form, **1**$^+$, was synthesized by chemical oxidation using ceric ammonium nitrate and studied by EPR spectroscopy. The polymers stirred with aqueous ceric ammonium nitrate for 1 h reproduced the signature EPR spectrum of **1**$^+$, providing preliminary evidence for the presence of Co_4O_4 units, and that the materials retained the redox chemistry of their molecular analogue (Figure 1B).

Scheme 3. Representative oxidation of the materials (e.g. **Co_4-TPP**) by Ce(IV).

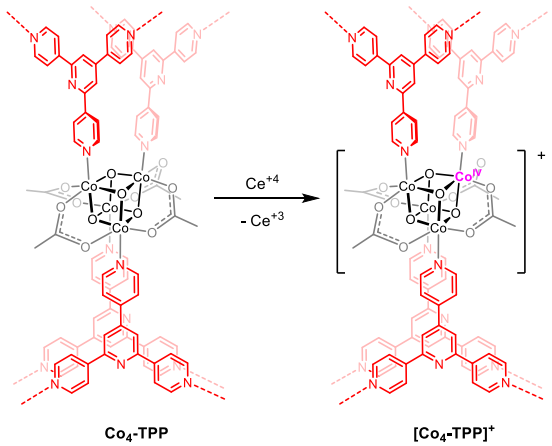

Porosity and surface area of the polymers were estimated by BET (Brunauer-Emmett-Teller) analysis of the N_2 adsorption isotherms of the solvent-free materials. These surface areas are measured for the solvent-free materials, which were prepared by heating under vacuum for 12 h. An ideal porous material will display *permanent* porosity, that is, no collapse of the pores occurs upon solvent removal, but many porous materials demonstrate a lower-than-expected measured surface area due to partial or total framework collapse during this drying process.[14] While permanent porosity is necessary for applications such as gas separations, it is not required for chemistries in solution. Nonetheless, N_2 adsorption isotherms can provide a lower-bound estimate of pore structure and surface areas for these materials. To determine the ideal temperature for solvent removal, thermogravimetric analyses (TGA) were performed. TGA of all the solids showed a significant mass loss (12-22%) at low temperature (60-100˚C), consistent

with a large amount of methanol solvent associated within the materials' pores as synthesized (4 to 9 mol MeOH per mol Co_4O_4, Supporting Information) (Figure 1C). The magnitude of this mass loss is typical of what has been observed for many porous metal-organic frameworks.[15] After solvent removal, all solids appear stable up to 200–250°C. **Co_4-BTC** is essentially nonporous with a low BET surface area of S_{BET} = 1.7 m^2/g. The replacement of BTC^{3-} with the isosymmetric, but larger BTB^{-3} linker (in **Co_4-BTB**) produced a type I adsorption isotherm, indicative of a microporous material. Correspondingly, the surface area increased dramatically to S_{BET} = 177 m^2/g. **Co_4-TPT** and **Co_4-TPP** exhibited microporosity and high surface areas of 480 m^2/g and 530 m^2/g, respectively. Interestingly, **Co_4-TPB**, which exhibits a thermogravimetric solvent loss similar to that of its isoreticular homologues, **Co_4-TPT** and **Co_4-TPP**, lacks permanent porosity, as demonstrated by a low surface area of S_{BET} = 11 m^2/g. This low surface area suggests that the pores collapse upon solvent removal.

These as-synthesized materials lack long-range periodicity, as demonstrated by the absence of sharp Bragg diffraction peaks in the powder X-ray diffraction pattern. The lack of long-range order is also consistent with the small domains implied by the empirical formula. Scanning electron microscopy (SEM) images do not reveal crystalline facets (Figure 2). The as-synthesized particle sizes and morphologies varied significantly between the different samples (and even between different particles of the same sample), as demonstrated in Figure 2. However, interestingly, **Co_4-BTC** formed monodisperse ~3 μm diameter spheres (Figure S3). Synthetic efforts to improve crystallinity using higher temperatures, longer reaction times, different solvents, and slow diffusion of reactants were unsuccessful. The difficulty in obtaining crystalline material is attributed to low reversibility of the reaction arising from the sluggish ligand exchange kinetics inherent in the t_{2g}^6 electron configuration of Co(III) ions of the cubane.[16] Attempts to overcome the exchange kinetics with higher temperatures, longer reaction times, or acid led to reduction of Co(III) to Co(II) as evidenced by formation of purple or pink solids and solutions.

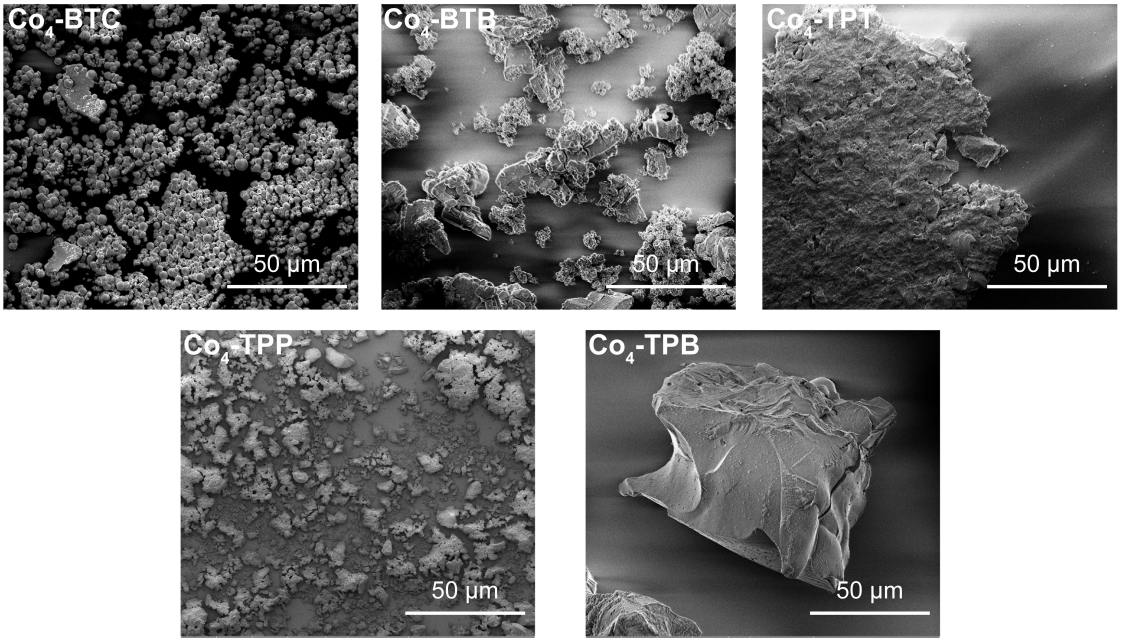

Figure 2. SEM images of materials obtained directly from synthesis.

While structures of most crystalline materials are easily modeled solely through the use of X-ray crystallography, structural solutions for less crystalline materials are achieved *via* refinement of a model against several measurements and observations. A structural solution of these materials must be consistent with all the following observables: (1) the stoichiometry, (2) the identity and structure of the individual building unit(s), and (3) the arrangement of these building units into an extended framework. Stoichiometry and identity of ligands have already been established by combustion EA and NMR spectroscopy. The next step in structural interrogation is direct observation of Co_4O_4 building units.

X-ray absorption spectroscopy (XAS) at the Co K-edge was used to identify intact Co_4O_4 units within the framework materials (Figure 3). This technique has been used previously for the Photosystem II active site,[17-22] the cobalt oxide water-oxidation catalyst,[23,24] and Mn-oxo cubanes.[25-28] The X-ray absorption near edge structure (XANES) part of the spectra provides an element-specific probe of the oxidation state of the Co centers in the framework materials, while the extended X-ray absorption fine structure (EXAFS) part of the spectra is sensitive to the local atomic structure within ~ 5 Å of the excited Co atoms. This makes XAS an ideal technique to probe the specific coordination of the Co centers in the framework materials and determine whether the Co_4O_4 units are intact. Results from XANES spectroscopy demonstrate that the oxidation state of Co(III) from $Co_4O_4(OAc)_4(py)_4$ (**1**) is preserved in the new materials (Figure 3A). Results from extended X-ray absorption fine structure (EXAFS) spectroscopy reveal that both the first (Co-O, Co-N) and second (Co-Co, Co-C, etc.) nearest-neighbor peaks are similar in the molecular species and the materials (Figure 3B).

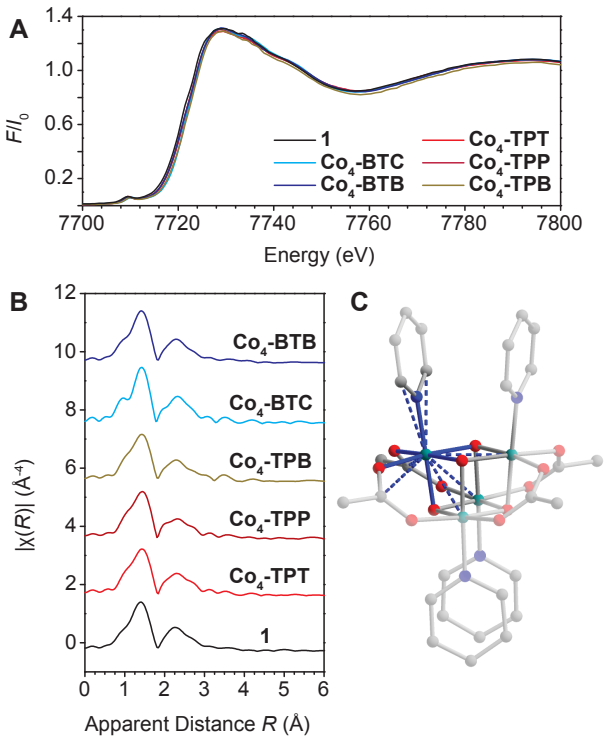

Figure 3. (A) Co K-edge absorption spectra, comparing polymers (colored) to complex **1** (black). (B) Fourier transformed EXAFS spectra. The spectra are vertically stacked for clarity, and thus the *y*-axis values are relative. (C) The XRD structure of **1** used as a model for EXAFS spectra fitting. The blue lines, solid and dashed, represent the Co-containing scattering paths used in the fit.

Additionally, a crystal structure-based fit to the EXAFS spectrum for complex **1** was used as a starting point for quantitative structural comparisons of the Co coordination environment of the polymers to **1** (Figure 3C). The key results are provided below in Table 1. Importantly, the bond lengths resulting from structural fits to each new material are within the uncertainty associated with the original fit to complex **1**.

Table 1. Co EXAFS curve fitting parameters.

Sample	Shell	N	*R* / Å	σ^2 / Å	R / %
1					
	Co–O	3	1.86	0.001	2.2
	Co–O	2	1.95	0.003	
	Co–N	1	1.95	0.003	
	Co–Co	2	2.71	0.005	
	Co–Co	1	2.75	0.005	
	Co–C	4	2.88	0.003	
	Co–O/N–C	8	3.01	0.002	
				E_0 (eV) =	0.7
Co_4-TPT					
	Co–O	3	1.88	0.003	2.0
	Co–O	2	1.94	0.003	
	Co–N	1	1.99	0.003	
	Co–Co	2	2.73	0.005	
	Co–Co	1	2.75	0.005	
	Co–C	4	2.88	0.002	
	Co–O/N–C	8	3.02	0.002	
				E_0 (eV) =	1.5
Co_4-BTC					
	Co–O	3	1.92	0.003	1.8
	Co–O	2	1.89	0.002	
	Co–N	1	1.89	0.002	
	Co–Co	2	2.73	0.004	
	Co–Co	1	2.75	0.004	
	Co–C	4	2.87	0.002	
	Co–O/N–C	8	3.01	0.002	
				E_0 (eV) =	0.9

S_0^2 was set to 0.75. σ^2 is the Debye-Waller factor, R(%) shows the goodness of fit. The fit range of all the spectra are k = 2.6 – 11.2 Å^{-1} (R = 1 – 4.0 Å).

A description of these materials would be incomplete without information on their extended framework and pore structure. For materials without observable Bragg diffraction, analysis of diffuse X-ray scattering *via* its Fourier transform, the pair distribution function (PDF), provides substantial information on their metrical parameters. Like EXAFS, PDF presents structural information as a histogram of interatomic distances. EXAFS does so with elemental specificity and provides highly local information. Conversely, PDF is not specific to a particular element and its local environment but probes *all* interatomic pairs, and thus it can be used to elucidate the extended structure.

Experimental data from X-ray scattering and PDF analysis must be compared to calculated data from a three-dimensional structural model, much like that used in X-ray crystallography. In this case, however, the models must be generated *a priori*, as the

spherically averaged experimental PDF data does not contain sufficient information to "solve" the structure directly.

The three-dimensional models for correlation with PDF data were assembled as follows: atomic coordinates from the crystal structure of molecular analogue **1** were placed at appropriate sites of candidate framework structures, linker atoms were added, and the structures were optimized using density functional theory (DFT) with periodic boundary conditions. Candidate structures were determined by comparing cubane and linker symmetry to known framework structures in the Reticular Chemistry Structure Resource (RCSR).[29] Complex **1** has idealized D_{2d} site symmetry (neglecting acetate methyl groups), where κ^2-carboxylates cap four equatorial faces (~90° apart) and pyridine ligands cap the two remaining, opposite faces (180° apart) of the cubane. The BTC and BTB linkers have idealized D_{3h} symmetry, which is expected to reduce to D_3 in the **Co$_4$-BTC** and **Co$_4$-BTB** polymers because the cubane units cannot be arranged to maintain the mirror planes in D_{3h}. The structures compatible with these requirements are **pto**[30] and **tbo**[30] (Supporting Information). These abbreviations refer to specific, known topologies from previously characterized solid-state materials (*e.g.* **pto** is derived from, and named for, the coordination network of crystalline Pt_3O_4). In the case of **tbo** (*Fm*-3*m*), the formal crystallographic symmetry of the net – *mmm* (D_{2h}) for four-coordinate sites and 3*m* (C_{3v}) for three-coordinate sites – is different from that expected for **Co$_4$-BTC** and **Co$_4$-BTB** and thus a "pseudo-**tbo**" structure that lacks some of the symmetry operations of *Fm*-3*m* was constructed. For **Co$_4$-TPT**, **Co$_4$-TPP**, and **Co$_4$-TPB**, the only vertex is the pyridyl linker, with idealized D_{3h} symmetry, and the edges with Co_4 cubanes have idealized D_{2d} symmetry. Searching the RCSR for structures with one three-coordinate vertex and one edge produces only the **srs**[31] net (and its interpenetrated analogues **srs-c**, **srs-c4**, and **srs-c8**). Site symmetry in **srs** (*I*4(1)32) – 32 (D_3) for vertices and 222 (D_2) for edges – is a subset of the idealized symmetry above and thus compatible. The structural models were refined by DFT in the Vienna *Ab initio* Simulation Package (VASP)[32-34] to improve the chemical soundness of their metrical parameters.

The PDF information obtained by analysis of diffuse X-ray scattering data is consistent with the structural models for all of the polymer materials. The experimental PDF results for the five materials are shown in Figure 4, including oscillations to at least 20 Å. **Co$_4$-TPT**, **Co$_4$-TPP**, and **Co$_4$-TPB** are consistent with the corresponding **srs** structural models. The calculated PDF's for **Co$_4$-TPT-srs** and **Co$_4$-TPT-srs-c** are quite similar and similarly consistent with the experimental data, but the N_2 adsorption isotherm data is more consistent with the microporous **srs-c** interpenetrated network than the mesoporous **srs** network. **Co$_4$-BTC** and **Co$_4$-BTB** experimental PDF data is consistent with the pseudo-**tbo** structural model, however, the **pto** structure accessible for **Co$_4$-BTB** gives a better fit for that material. Detailed information on the PDF analysis, including structural refinements, isolation of cubane and linker contributions to the observed data, reduced structure function data, and estimation of crystallite size, is included in the Supporting Information. Figure 5 shows an example of the agreement between a structural model and the experimental data for **Co$_4$-TPT**. Figure 6 depicts representative structures confirmed by PDF analysis.

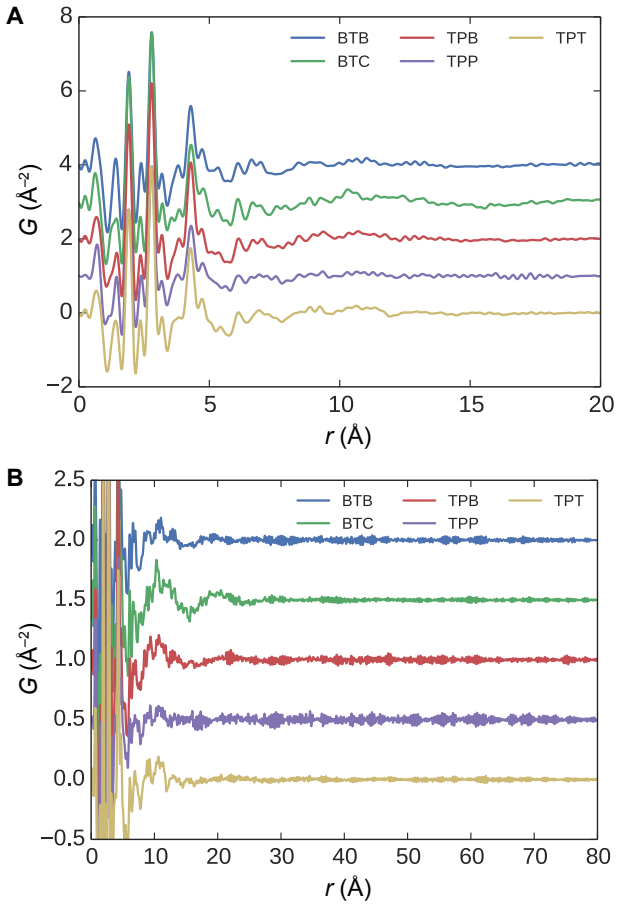

Figure 4. Experimental PDF from diffuse X-ray total scattering measurements for each of the Co polymer materials: (A) short (0–20 Å) pair range and (B) long (0–80 Å) pair range.

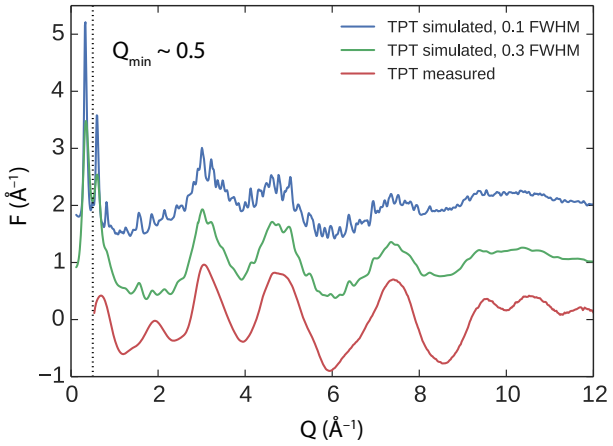

Figure 5. Comparison of experimental (red) and simulated (green, blue) structure factors for **Co_4-TPT** from diffuse X-ray total scattering measurements.

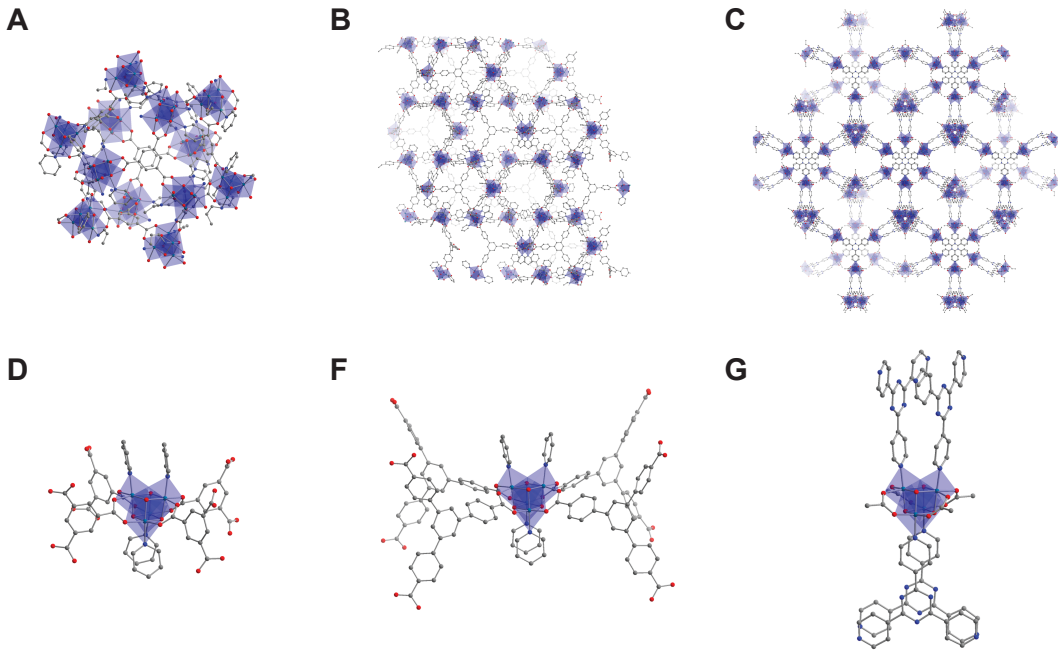

Figure 6. Representative segments of the proposed extended structures of (A) **Co_4-BTC** (**tbo** topology), (B) **Co_4-BTB** (pseudo-**tbo** topology), and (C) **Co_4-TPT** (**srs-c** topology). Building units of (D) **Co_4-BTC**, (E) **Co_4-BTB** (pseudo-**tbo** topology), and (F) **Co_4-TPT**.

Raman spectroscopy proved useful as a fingerprint identification method for the new materials. Raman spectra were collected at λ = 633 nm (or 532 nm), in order to benefit from resonance with broad electronic absorption modes of **1** and all new materials. Detailed analysis, e.g. to identify common structural features of the polymers and complex **1**, was not performed with Raman spectra, as XAS and PDF analyses were found to be more suitable.

4.4 Stability to high pH conditions

The site-isolation of the cubane units within a rigid, porous framework results in chemical properties that are distinct from those of the molecular cubane **1**. On the bais of solution NMR studies, it has been shown that one acetate ligand of **1** is displaced by hydroxide ions at pH > 11, to generate a dicobalt *syn*-dihydroxide molecular complex (**2**).[10] Notably, this *syn*-dihydroxide motif is thought to correspond to the active site for OER as catalyzed by cobalt oxide materials.[5] However, molecular complexes **1** and **2** are unstable at higher pH's, since the hydroxide ligands engage in condensation reactions that result in precipitation of CoO_x over the course of 1 h.

Spatial isolation of the cubane clusters in the rigid framework was expected to prevent unwanted Co_4O_4 aggregation, thereby stabilizing the desired, dicobalt *syn*-dihydroxide active site. Indeed, Co_4O_4 units of **Co_4-TPT**, **Co_4-TPP**, and **Co_4-TPB** remain intact after treatment at pH 14 for at least 5 h, as evidenced by XAS (Figure 7). ^{1}H NMR spectroscopy of D_2O solutions at pD 14 (1.0 M NaOD) containing suspensions of these

materials showed the release of acetate ligands from the framework into solution over time, reaching 50-60% displacement after 5 h (Supporting Information for details). Sodium was not detected by X-ray photoelectron spectroscopy (XPS) on the materials after the 5 h of soaking, signifying that on average, no more than four OH^- ligands bind to each Co_4O_4 site; otherwise, Na^+ would be required for charge balance. The XAS, NMR, and XPS data together suggest that each cubane unit has an approximate formulation, aside from the pyridyl linker, of $[Co_4O_4(OH)_2(H_2O)_2(OAc)_2]$ (Scheme 4). These materials are abbreviated hereafter as **Co_4O_4-TPT-OH**, **Co_4O_4-TPP-OH**, and **Co_4O_4-TPB-OH**.

Scheme 4. Reactions of polymers at pH 14

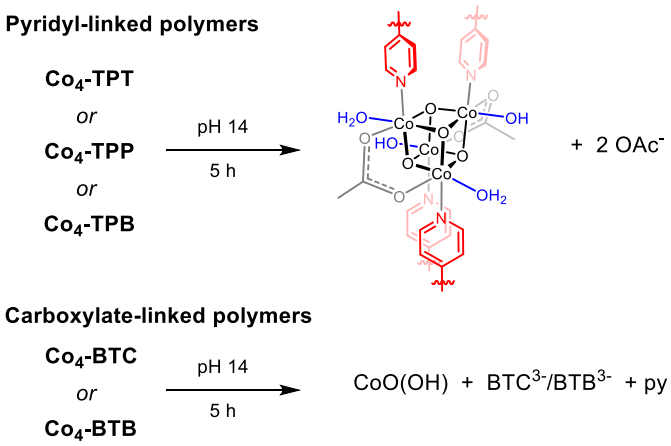

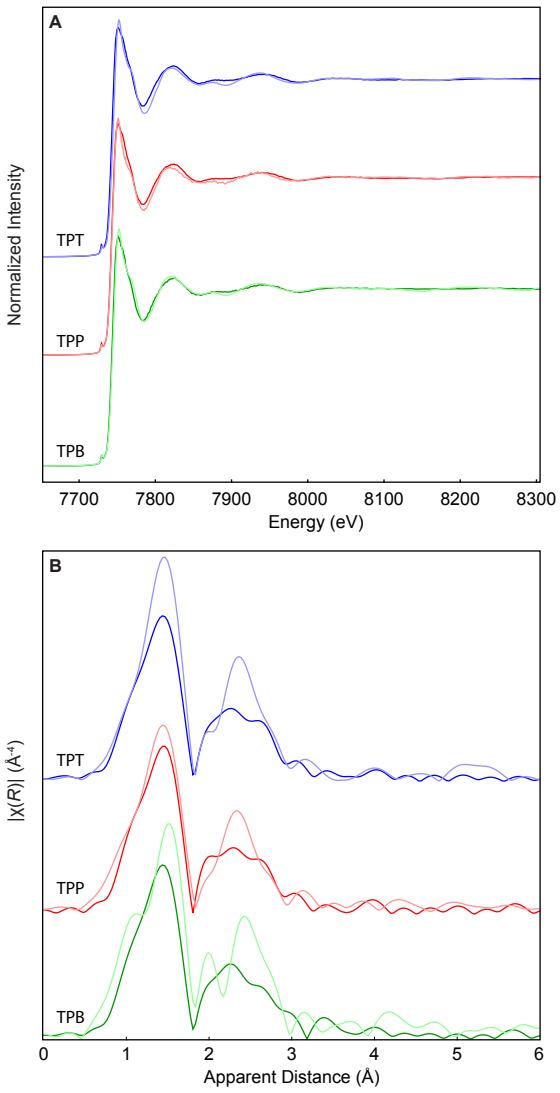

Figure 7. Comparison of **Co_4O_4-TPT**, **Co_4O_4-TPP**, and **Co_4O_4-TPB** (solid colors) to their hydroxide-exchanged analogues, **Co_4O_4-TPT-OH**, **Co_4O_4-TPP-OH**, and **Co_4O_4-TPB-OH** (light colors) by Co K-edge absorbance spectroscopy: (A) XANES and (B) FT-EXAFS.

Interestingly, the carboxylate-linked materials, **Co_4-BTC** and **Co_4-BTB**, are quite *unstable* in alkaline water (Scheme 4). **Co_4-BTC** immediately dissolves upon addition of pH 14 water, followed by precipitation of a brown solid after 1 h. For **Co_4-BTB**, EXAFS and Raman analyses confirm the absence of the Co_4O_4 cubane core, and formation of cobalt oxyhydroxide (CoOOH) after 5 h of stirring in pH 14 solution (Figure 7). These results are consistent with the previous observation that hydroxide ions displace the carboxylate ligands in preference to the pyridyl ligands of **1**,[10] which explains the rapid decomposition of frameworks built upon carboxylate linkages, **Co_4-BTC** and **Co_4-BTB**, at pH 14. The contrast in stability between the carboxylate-linked and pyridyl-linked

classes showcases the power of well-defined, three-dimensional polymers, in which principles of molecular chemistry remain relevant even as favorable materials properties are achieved.

4.5 Water oxidation by oxidized materials

The molecular cubane **1** has been demonstrated as a water oxidation catalyst at pH > 11, and key features of its mechanism have recently been elucidated.[10] As discussed in the previous section, **1** exhibits long-term instability at high pH due to intermolecular aggregation, but immobilization in a rigid framework greatly increases stability. Mechanistic studies on OER by **1** demonstrate that displacement of acetate by hydroxide forms the activated catalyst,[10] and therefore only the pyridyl-linked materials **Co_4-TPT**, **Co_4-TPP**, and **Co_4-TPB** can be activated by hydroxide without framework decomposition (*vide supra*). In the molecular species, OER catalysis is initiated by oxidation to $\mathbf{1}^+$ by an electrode or chemical oxidant. Analogously, **Co_4-TPT**, **Co_4-TPP**, and **Co_4-TPB** can be oxidized by ceric ammonium nitrate to form **[Co_4-TPT]$^+$**, **[Co_4-TPP]$^+$**, and [**Co_4-TPB**]$^+$ (*vide supra*). Satisfyingly, addition of one equivalent of NaOH to **[Co_4-TPT]$^+$**, **[Co_4-TPP]$^+$**, and [**Co_4-TPB**]$^+$ produced O_2, in 12%, 44%, and 30% yield with respect to the polymer (Figure 8A). Yields of O_2 lower than 100% and varying between the materials could result from incomplete oxidation by Ce(IV), clogging of pores by residual Ce species (*vide infra*), or partial reduction of oxidized polymer during workup prior to hydroxide addition. Nonetheless, the stoichiometric OER experiment demonstrates the retention of molecular reactivity in heterogeneous, porous solids. Raman spectroscopy on each material after OER produced a spectrum identical to that of the starting material with some admixture of the hydroxide-exchanged material, indicating that the structure was not substantially changed by its oxidation (by Ce^{4+}) and subsequent reduction (by OH^-) (Figure 8C). The mechanism for these OERs is assumed to be similar to that determined for **1** (Scheme 5). The electron transfer steps would occur between oxidized cubane sites within the lattice, perhaps *via* a redox hopping mechanism. Surprisingly, attempts to reuse the material for OER proved unsuccessful. Evidence from XPS offers an explanation that may reconcile the evidence of intact **Co_4-TPT** from Raman with the reduction in activity: significant levels of cerium were detected at the surface (Supporting Information). Clogging of porous catalysts by cerium ions or particles has been reported previously.[35,36] Even hydrated cerium (III), with a diameter of ~5 Å,[37] might be capable of blocking the pores of **Co_4-TPT** (*vide supra*). Moreover, at the high pH used for OER, decomposition of Ce ions to larger cerium oxide particles is likely. This result indicates that conditions that reduce or eliminate remaining chemical oxidant from the polymers before OER are needed, and therefore electrochemical OER with these materials is ultimately preferred. Nonetheless, the OER capability of **Co_4-TPT** demonstrates an unprecedented feat: OER by a porous polymeric material made from earth-abundant metals.

Scheme 5. Proposed OER mechanism by the polymers

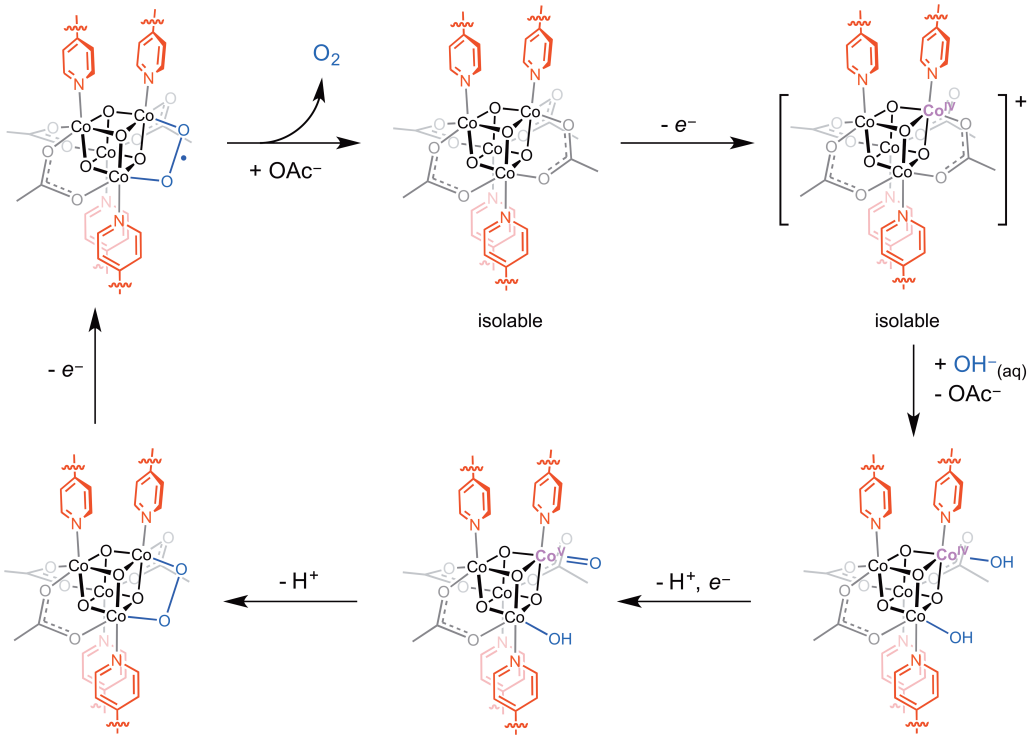

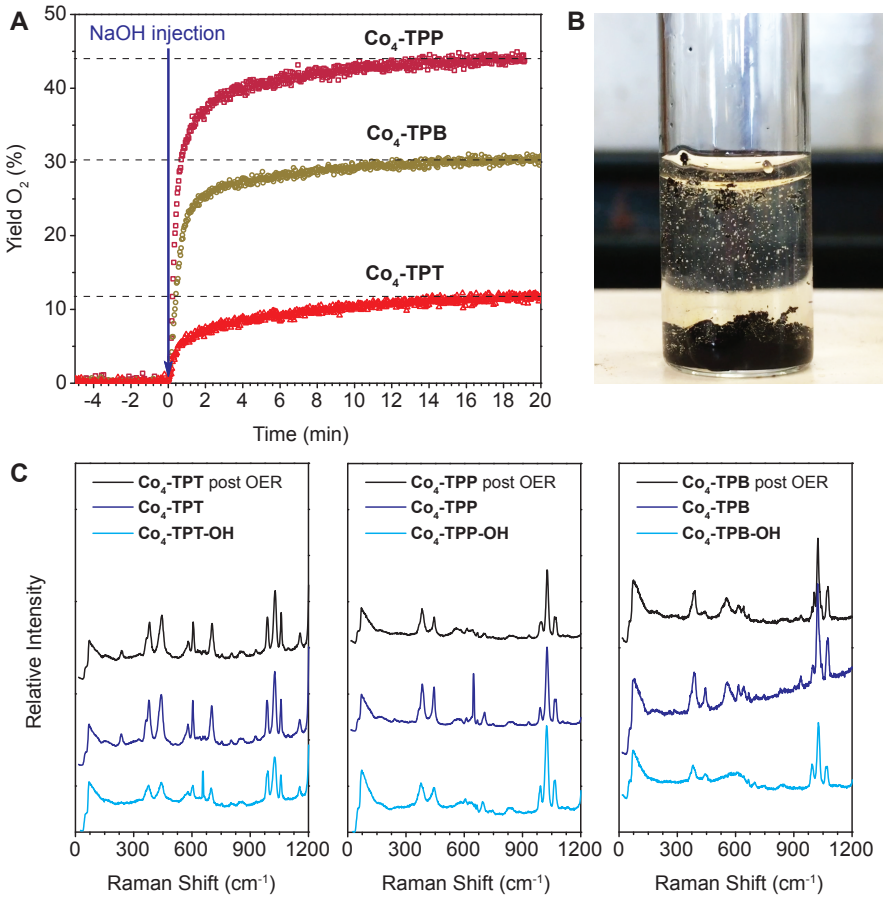

Figure 8. (A) Quantification of O_2 evolved from oxidized polymers upon addition of 1 M NaOH. (B) A photograph showing the bubbles of O_2 upon addition of 1 M NaOH to **[Co$_4$-TPP]**$^+$. (C) Raman spectra comparing the materials post OER to the starting polymers and the polymers treated at pH 14 for 5 h.

Electrochemistry of **Co$_4$-TPT**, **Co$_4$-TPP**, and **Co$_4$-TPB** revealed that both a reversible Co(III)/Co(IV) wave and electrocatalytic OER activity is preserved from complex **1**. A permanent colloid ink of each material was generated by sonication in ethanol or isopropanol. This ink was drop-cast onto a glassy carbon electrode. In our hands, **Co$_4$-BTC** and **Co$_4$-BTB** suspended poorly, and thus, no electrochemical data was obtained. Reversible Co(III)/Co(IV) waves were observed in acetonitrile with an [*n*Bu$_4$N]PF$_6$ electrolyte. The redox couples shifted towards more positive potentials moving from **Co$_4$-TPB** to **Co$_4$-TPP** to **Co$_4$-TPT**, following the trend of decreasing electron-donation of the pyridyl linker (Figure 9, Table 2). These redox waves displayed scan-rate dependent currents characteristic of diffusion-controlled electron-transfer (Randles-Sevcik equation);[38] this behavior is suggestive of an electron-hopping charge transport mechanism within the material under applied potential.[39] Consistent with low conductivity for these materials, the percentage of the polymer films accessed electrochemically during a CV sweep is small. At 100 mV/s, the electroactive fraction was 4.0% of **Co$_4$-TPT**, 5.7% of **Co$_4$-TPP**, and 3.2% of **Co$_4$-TPB** (Supporting Information for calculation). This observation suggests that only the surface of the materials is

electroactive on the timescale of cyclic voltammetry. In pH 7 (0.1 M KP_i buffer) aqueous solution clear redox waves were seen for **Co_4-TPP** and **Co_4-TPB** by CV (Figure 10), but peaks for **Co_4-TPT** were too broad to observe. The well-defined CVs of **Co_4-TPP** and **Co_4-TPB** with low current signal at 1300 mV vs Ag/AgCl are also consistent with pure material, free of Co(II)-impurities.[13] Again, the redox potential of **Co_4-TPP** was higher than that of **Co_4-TPB** due to TPP being more electron-withdrawing than TPB (Table 2). Increasing the pH to 11 and 12 led to an OER electrocatalytic current originating from the Co(III)/Co(IV) redox couple. The potential of this electrocatalytic wave is comparable to that of molecular cubane, **1**.[10] The onset overpotential is clearly lower for **Co_4-TPB** than for **Co_4-TPP**, reflecting the intrinsic electronic differences of these materials, and their ability to be precisely tuned *via* the choice of ancillary ligands.

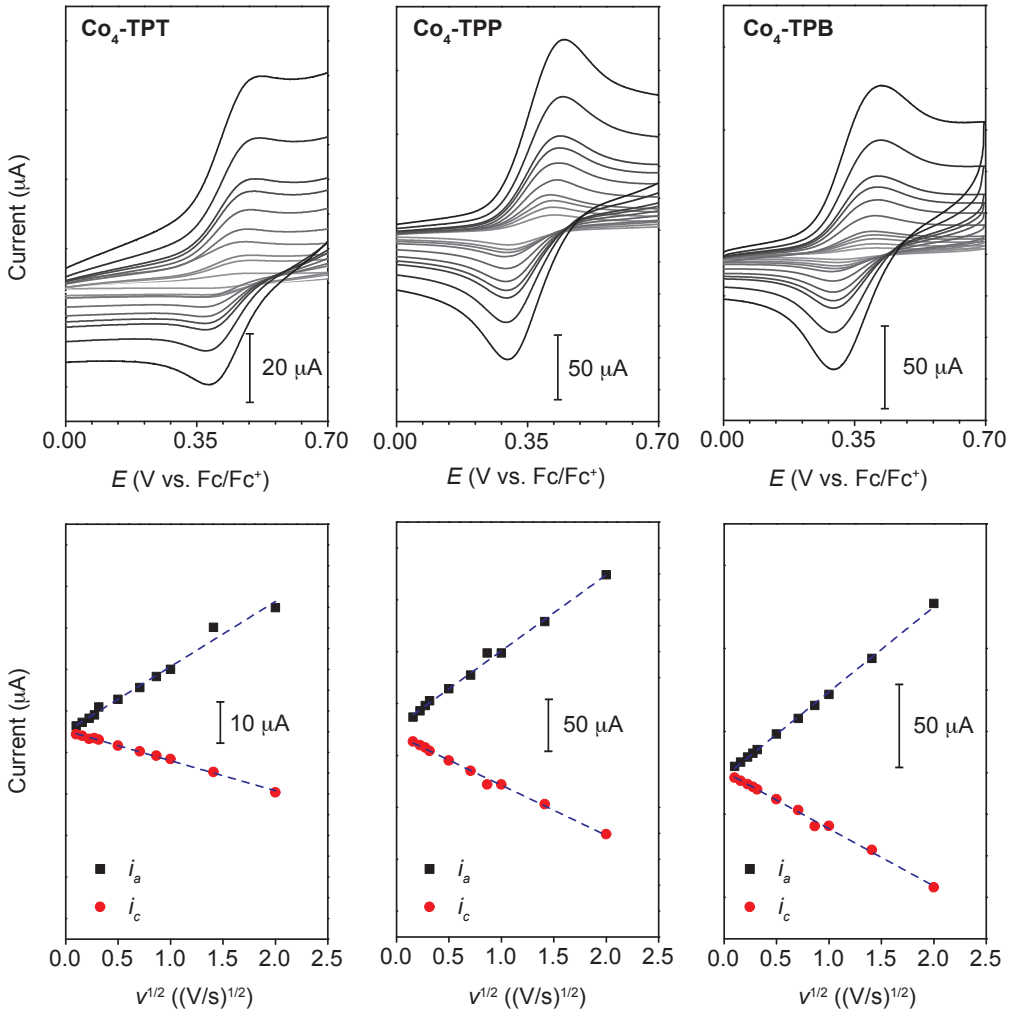

Figure 9. (Top panels) Cyclic voltammetry trace in acetonitrile with 0.1 M [nBu$_4$N]PF$_6$ at varying scan rates. (Bottom panels) Plots of peak current versus the square root of scan rate showing linear correlations consistent with diffusion-controlled electron-transfer.

Table 2. Cyclic voltammetry data for **Co_4-TPT**, **Co_4-TPP**, and **Co_4-TPB**.

Compound	$E^{1/2}$ in MeCN (V vs. Fc/Fc^+)	$E^{1/2}$ in H_2O (V vs. Ag/AgCl)
1	0.280	1.008
Co_4-TPT	0.438	–
Co_4-TPP	0.351	1.052
Co_4-TPB	0.346	1.036

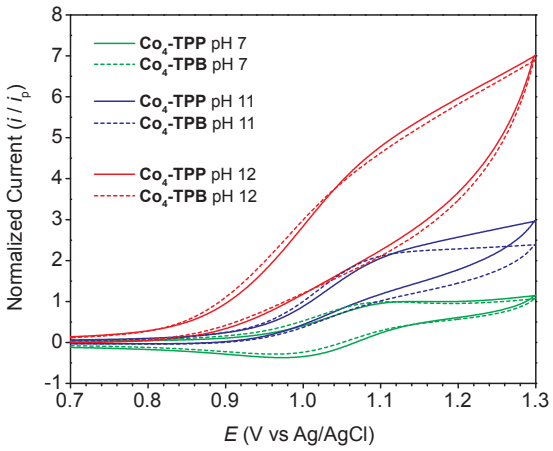

Figure 10. Cyclic voltammetry trace in 0.1 M KP_i (aq.) at pH = 7, 11, & 12 and 100 mV/s scan rate.

The hydroxide-exchanged materials **Co_4-TPP-OH** and **Co_4-TPB-OH** are highly active OER catalysts. The overpotentials required to reach a current density of 10 mA/cm^2 in pH 14 water were 464 mV for **Co_4-TPP-OH** and 430 mV for **Co_4-TPB-OH**, which are comparable to those observed for cobalt oxide.[3] Again, the differences in overpotentials are correlated with the basicity of the pyridyl linker, reinforcing the concept of molecular-level tunability (Figure 11). The Tafel slopes for **Co_4-TPP-OH** and **Co_4-TPB-OH** were 69 and 63 mV/dec, respectively, indicative of a mechanism where catalysis involves an electron-transfer pre-equilibrium prior to a rate-determining chemical step. This mechanism is consistent with that proposed for OER by **1** and cobalt oxide catalysts.[10,40]

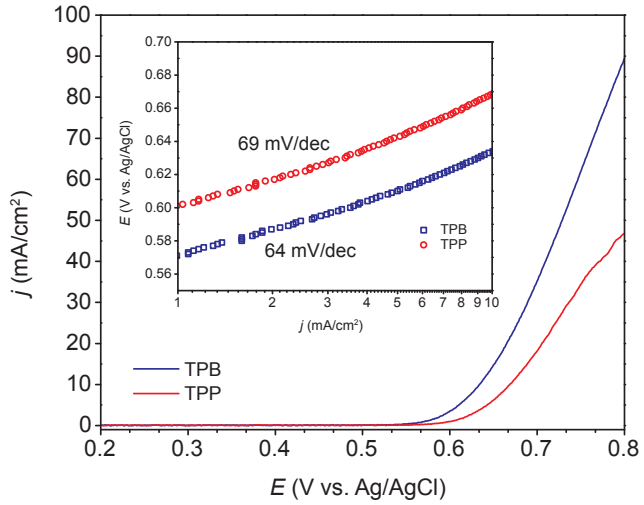

Figure 11. Linear sweep voltammograms (2 mV/s) of **Co_4-TPP-OH** and **Co_4-TPB-OH** films casted on glassy carbon electrodes in pH 14.

4.6 Conclusions

A porous, solid-state material derived from a Co_4O_4 cubane, one of the most intriguing molecular structures capable of water oxidation, has been prepared. A suite of techniques, including UV-visible absorption, EPR, and X-ray absorption spectroscopies confirmed the preservation of Co_4O_4 units in the resulting coordination polymers. Nitrogen adsorption and PDF analysis provided experimental confirmation of the porous DFT-refined structural models for all materials, even though long-range crystallographic order was not observed. Favorable properties attained by the coordination polymers include high porosity, good thermal stability, and resistance to water oxidizing conditions that exceeds that of the parent cubane complex **1**. Most significantly, these new materials can be synthesized by a general, one-step method, and they retain a molecular level of electronic tunability. The simplicity of the synthesis should allow rapid development and screening of new derivatives. Stoichiometric oxidation with Ce(IV) provided evidence that the polymers operate *via* a well defined OER mechanism analogous to that by **1**,[10] and electrocatalysis experiments revealed activity trends among the polymer materials while demonstrating their suitability for practical heterogeneous catalysis. However, these materials are nonconductive and only small fractions of the materials are electrochemically active. Thus, new catalyst designs should incorporate features, such as redox-active linker ligands, that promote charge transport. The results presented in this work provide the basic design and synthesis of new metal-organic polymers for OER catalysis and underscore the potential of applying molecular design principles to heterogeneous catalysis.

4.7 Acknowledgements

This material is based upon work performed by the Joint Center for Artificial Photosynthesis, a DOE Energy Innovation Hub, supported through the Office of Science of the U.S. Department of Energy under Award Number DE-SC0004993. The

Advanced Light Source is supported by the Director, Office of Science, Office of Basic Energy Sciences, of the U.S. Department of Energy under Contract No. DE-AC02-05CH11231. Use of the Stanford Synchrotron Radiation Lightsource, SLAC National Accelerator Laboratory, is supported by the U.S. Department of Energy, Office of Science, Office of Basic Energy Sciences under Contract No. DE-AC02-76SF00515. DFT optimizations were performed using the resources of the National Energy Research Scientific Computing Center, a DOE Office of Science User Facility supported by the Office of Science of the U.S. Department of Energy under Contract No. DE-AC02-05CH11231. We thank Michael L. Aubrey and Miguel I. Gonzales for helpful discussions.

4.8 References

(1) *Climate Change 2014: Synthesis Report*; p 138.
(2) Moore, G. F.; Brudvig, G. W. *Annu Rev Condens Matter Phys* **2011**.
(3) McCrory, C. C. L.; Jung, S.; Ferrer, I. M.; Chatman, S. M.; Peters, J. C.; Jaramillo, T. F. *J. Am. Chem. Soc.* **2015**, *137* (13), 4347–4357.
(4) Somorjai, G. A.; Li, Y. *Introduction to surface chemistry and catalysis*; Wiley: New York, 2010.
(5) Ullman, A. M.; Brodsky, C. N.; Li, N.; Zheng, S.-L.; Nocera, D. G. *J. Am. Chem. Soc.* **2016**, *138* (12), 4229–4236.
(6) Kärkäs, M. D.; Åkermark, B. *Dalton Trans.* **2016**.
(7) Stracke, J. J.; Finke, R. G. *ACS Catal.* **2014**, *4* (3), 909–933.
(8) Batten, S. R.; Champness, N. R.; Chen, X.-M.; Garcia-Martinez, J.; Kitagawa, S.; Öhrström, L.; O'Keeffe, M.; Suh, M. P.; Reedijk, J. *CrystEngComm* **2012**, *14* (9), 3001–3004.
(9) Zhou, H.-C.; Long, J. R.; Yaghi, O. M. *Chem. Rev.* **2012**, *112* (2), 673–674.
(10) Nguyen, A. I.; Ziegler, M. S.; Oña-Burgos, P.; Sturzbecher-Hohne, M.; Kim, W.; Bellone, D. E.; Tilley, T. D. *J. Am. Chem. Soc.* **2015**, *137* (40), 12865–12872.
(11) Wang, C.; Wang, J.-L.; Lin, W. *J. Am. Chem. Soc.* **2012**, *134* (48), 19895–19908.
(12) Chakrabarty, R.; Bora, S.; Das, B. K. *Inorg. Chem.* **2007**, *46* (22), 9450–9462.
(13) Ullman, A. M.; Liu, Y.; Huynh, M.; Bediako, D. K.; Wang, H.; Anderson, B. L.; Powers, D. C.; Breen, J. J.; Abruña, H. D.; Nocera, D. G. *J. Am. Chem. Soc.* **2014**, *136* (50), 141118215154009–17688.
(14) Feldblyum, J. I.; Liu, M.; Gidley, D. W.; Matzger, A. J. *J. Am. Chem. Soc.* **2011**, *133* (45), 18257–18263.
(15) McDonald, T. M.; Bloch, E. D.; Long, J. R. *Chem. Commun.* **2015**, *51* (24), 4985–4988.
(16) Langford, C. H.; Gray, H. B. *Ligand Substitution Processes*; W. A. Benjamin, Inc.: New York, New York, 1966.
(17) Ono, T.-A.; Noguchi, T.; Inoue, Y.; Kusunoki, M.; Matsushita, T.; Oyanagi, H. *Science* **1992**, *258* (5086), 1335–1337.
(18) Yachandra, V. K.; Sauer, K.; Klein, M. P. *Chem. Rev.* **1996**, *96* (7), 2927–2950.
(19) Iuzzolino, L.; Dittmer, J.; Dörner, W.; Meyer-Klaucke, W.; Dau, H. *Biochemistry* **1998**, *37* (49), 17112–17119.

(20) Messinger, J.; Robblee, J. H.; Bergmann, U. *Journal of the …* **2001**.
(21) Yano, J.; Yachandra, V. K. *Photosynthesis Research* **2007**, *92* (3), 289–303.
(22) Brena, B.; Siegbahn, P. E. M.; Ågren, H. *J. Am. Chem. Soc.* **2012**, *134* (41), 121003072852009.
(23) Risch, M.; Khare, V.; Zaharieva, I.; Gerencser, L.; Chernev, P.; Dau, H. *J. Am. Chem. Soc.* **2009**, *131* (20), 6936–6937.
(24) Kanan, M. W.; Yano, J.; Surendranath, Y.; Dincă, M.; Yachandra, V. K.; Nocera, D. G. *J. Am. Chem. Soc.* **2010**, *132* (39), 13692–13701.
(25) Kanady, J. S.; Tran, R.; Stull, J. A.; Lu, L.; Stich, T. A.; Day, M. W.; Yano, J.; Britt, R. D.; Agapie, T. *Chem. Sci.* **2013**, *4* (10), 3986–3996.
(26) Tsui, E. Y.; Tran, R.; Yano, J.; Agapie, T. *Nature Chemistry* **2013**, *5* (4), 293–299.
(27) Suseno, S.; McCrory, C. C. L.; Tran, R.; Gul, S.; Yano, J.; Agapie, T. *Chem. Eur. J.* **2015**, *21* (38), 13420–13430.
(28) Van Allsburg, K. M.; Anzenberg, E.; Drisdell, W. S.; Yano, J.; Tilley, T. D. *Chem. Eur. J.* **2015**, *21* (12), 4646–4654.
(29) O'Keeffe, M.; Peskov, M. A.; Ramsden, S. J.; Yaghi, O. M. **2008**.
(30) Delgado-Friedrichs, O.; O'Keeffe, M.; Yaghi, O. M. *Acta Crystallogr., Sect. A: Found. Crystallogr.* **2006**, *62* (5), 350–355.
(31) Delgado-Friedrichs, O.; O'Keeffe, M.; Yaghi, O. M. *Acta Crystallogr., Sect. A: Found. Crystallogr.* **2003**, *59* (1), 22–27.
(32) Kresse, G.; Hafner, J. *Phys. Rev. B* **1993**, *47* (1), 558–561.
(33) Kresse, G.; Furthmüller, J. *Computational Materials Science* **1996**, *6* (1), 15–50.
(34) Kresse, G.; Joubert, D. *Phys. Rev. B* **1999**, *59* (3), 1758–1775.
(35) Hansen, R. E.; Das, S. *Energy & Environmental Science* **2014**.
(36) Meyer, K.; Ranocchiari, M.; van Bokhoven, J. A. *Energy Environ. Sci.* **2015**, *8* (7), 1923–1937.
(37) Persson, I.; D'Angelo, P.; De Panfilis, S.; Sandström, M.; Eriksson, L. *Chem. Eur. J.* **2008**, *14* (10), 3056–3066.
(38) Bard, A. J.; Faulkner, L. R. *Electrochemical Methods: Fundamentals and Applications*, 2nd ed.; John Wiley & Sons, 2001.
(39) Ahrenholtz, S. R.; Epley, C. C.; Morris, A. J. *J. Am. Chem. Soc.* **2014**, *136* (6), 2464–2472.
(40) Gerken, J. B.; McAlpin, J. G.; Chen, J. Y. C.; Rigsby, M. L.; Casey, W. H.; Britt, R. D.; Stahl, S. S. *J. Am. Chem. Soc.* **2011**, *133* (36), 14431–14442.

Supporting Information for **Chapter 4**

General considerations. Cobalt(II) nitrate hexahydrate, pyridine, hydrogen peroxide (34-37% in water), ceric ammonium nitrate, benzene-1,3,5-tricarboxylic acid, and 1,3,5-tris(4-carboxyphenyl)benzene were purchased from Sigma-Aldrich and used without further purification. Sodium acetate trihydrate was purchased from EMD. Solvents were purchased from Fisher-Scientific and used without any further purification. Cubane **1**,[1,2] 1,3,5-tris(4-pyridyl)triazine,[3] 2,4,6-tris(4-pyridyl)pyridine,[4] 1,3,5-tris(4-pyridyl)benzene,[5] were synthesized according to published procedures. MilliQ water was used in all experiments involving water.

Physical methods. Routine NMR spectra were recorded on Bruker AVB-400, AVQ-400 and AV-300 spectrometers at room temperature. DMSO-d_6 and 37% DCl in D_2O were purchased from Cambridge Isotopes. ^{1}H NMR spectra were referenced to residual protio-solvent peaks (δ 2.50 for DMSO-d_6, δ 4.79 for D_2O). Elemental analyses were carried out by the College of Chemistry Microanalytical Laboratory at the University of California, Berkeley. Inductively-coupled plasma (ICP) analysis were performed by Galbraith Laboratories. Electrochemical measurements were collected with three-electrode setup on a BASi Epsilon potentiostat. Thermogravimetric analysis were measured on a Seiko Instruments EXSTAR 6000. Scanning electron microscopy (SEM) images were collected using an FEI Quanta FEG 250 microscope at a working distance of 10 mm. A voltage of 1-5 kV was used to minimize sample annealing. pH was measured with a Thermo Orion 2 Star bench top meter.

Raman spectroscopy. Raman spectra were collected using a confocal Raman microscope spectrometer (LabRAM HR, Horiba Yvon Jobin) at 633 nm and laser power 0.19–3.70 mW at the objective. The spot size of the laser beam is approximately 1–2 μm. Total acquisition time per spectrum was 180 s. Using a 600 g/mm grating, the spectral resolution is ~ 1 cm^{-1}. Spectral positions were calibrated using the 520.7 cm^{-1} band of a silicon wafer.

Synthetic procedures.

$Co_4O_4(BTC)_{1.5}py_4$•4MeOH (Co_4-BTC). Cubane **1** (0.200 g, 0.234 mmol) and benzene-1,3,5-tricarboxylic acid (0.066 g, 0.312 mmol) were suspended in 10 mL of methanol in a scintillation vial. The capped vessel was heated to 60°C for 2 h. The dark green solid was collected by filtration and washed 3 x 10 mL of methanol to yield 0.186 g (75%). Samples for elemental analysis were dried under vacuum at 70°C for 12 h. Amount of methanol was determined by TGA mass loss (12%) at the first plateau region (160°C). The solid was dissolved in a mixture of 37% DCl in D_2O and DMSO (1:1) to give a cyan solution. The solution was analyzed by ^{1}H NMR spectroscopy (Figure S1). The Raman spectrum (633 nm excitation) is shown in Figure S2. Anal calc'd for $(C_{20}H_{20}Co_4N_4O_4)(C_9H_3O_6)_{1.7}(H_2O)_9$: C, 41.47; H, 3.07; N, 5.48. Found: C, 41.08; H, 3.07; N, 5.08.

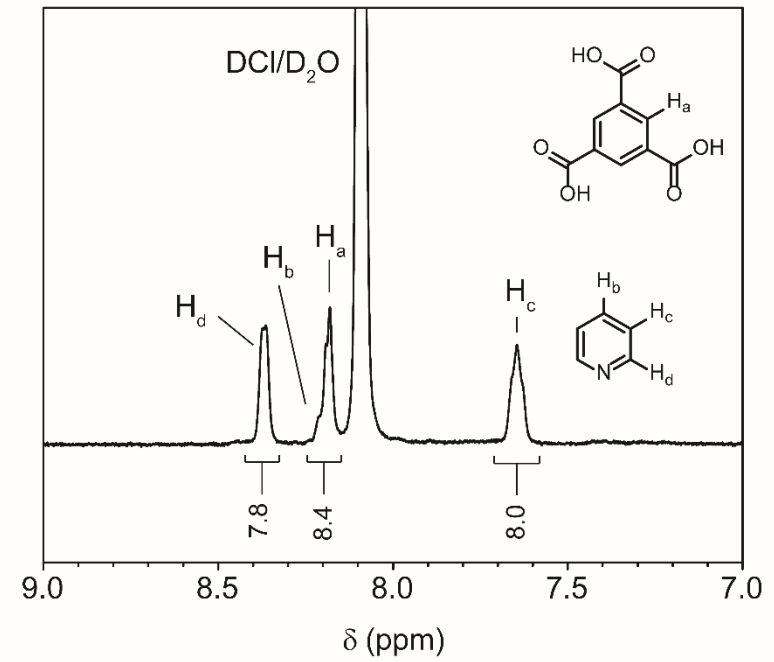

Figure S1. ^{1}H NMR (DMSO-d_6/D_2O) spectrum for **Co_4-BTC** after digestion in DCl/D_2O.

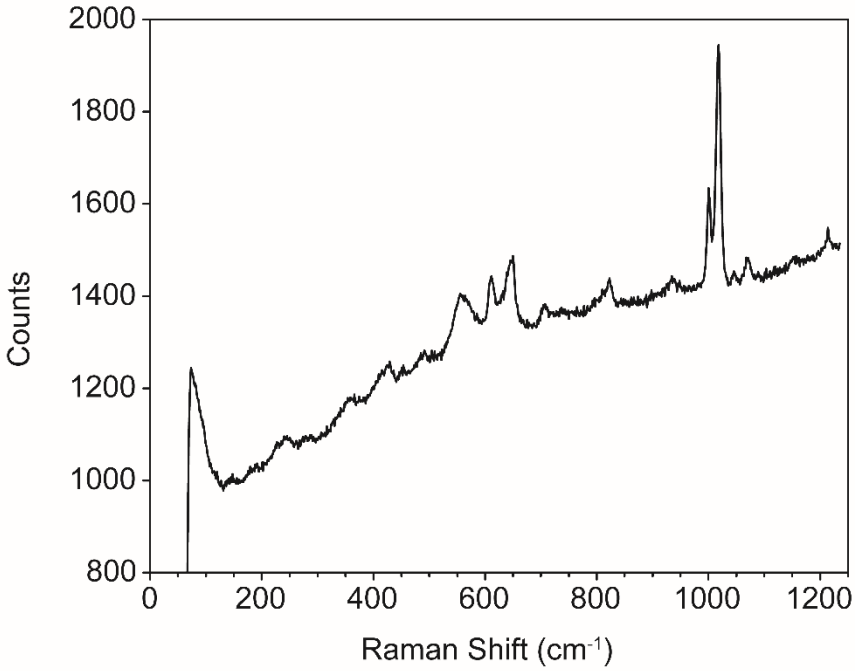

Figure S2. Raman spectrum for **Co_4-BTC**.

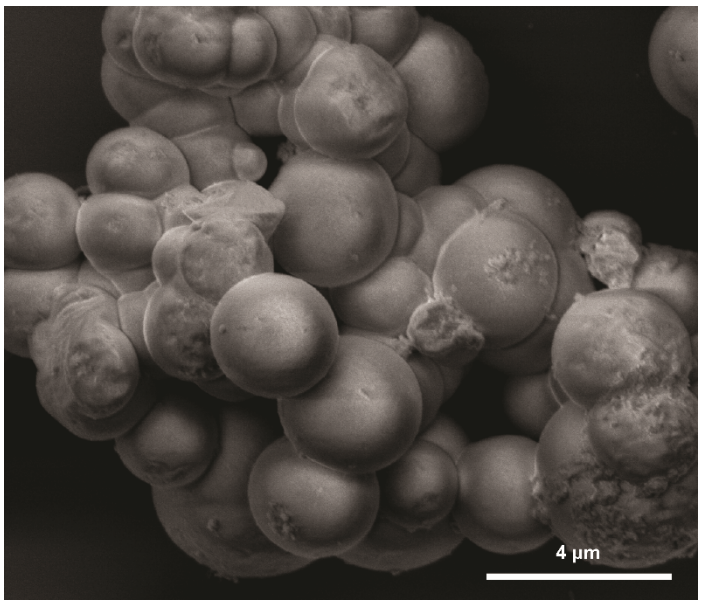

Figure S3. A higher magnification SEM image of as-synthesized **Co_4-BTC**.

$Co_4O_4(BTB)_{1.5}py_4$•5MeOH (Co_4-BTB). Cubane **1** (0.200 g, 0.234 mmol) and 1,3,5-tris(4-carboxyphenyl)benzene (0.137 g, 0.312 mmol) were suspended in 10 mL of methanol in a scintillation vial. The capped vessel was heated to 70˚C for 2 h. The dark green solid was collected by filtration and washed 3 x 10 mL of methanol to yield 0.247 g (72 %). Samples for elemental analysis were dried under vacuum at 70˚C for 12 h. Amount of methanol was determined by TGA mass loss (13%) at the first plateau region (160˚C). The solid was dissolved in a mixture of 37% DCl in D_2O and DMSO (1:1) to give a cyan solution. The solution was analyzed by ^{1}H NMR spectroscopy (Figure S4). The Raman spectrum (633 nm excitation) is shown in Figure S5. Anal calc'd for $C_{56}H_{40}Co_4N_4O_{12}$: C, 56.21; H, 3.37; N, 4.68. Found: C, 56.06; H, 3.51; N, 4.30.

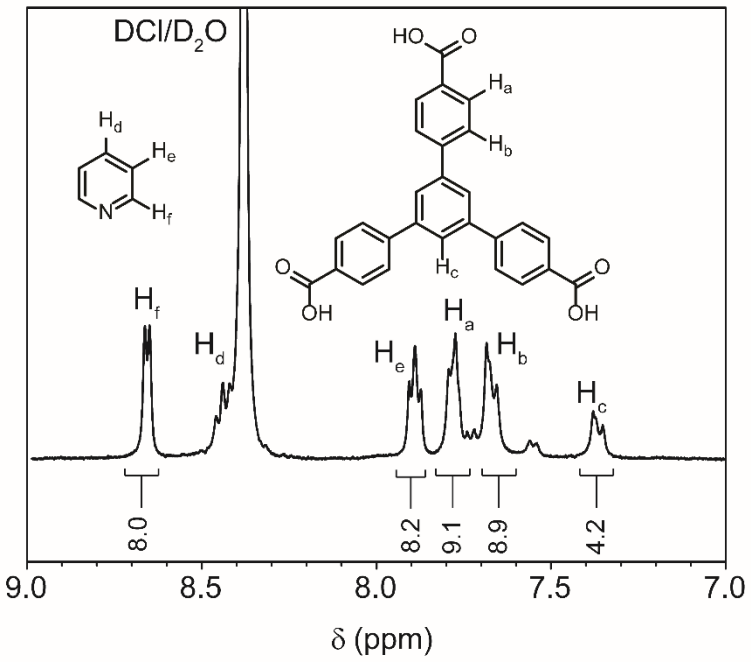

Figure S4. ^{1}H NMR (DMSO-d_6/D_2O) spectrum for **Co_4-BTB** after digestion in DCl/D_2O.

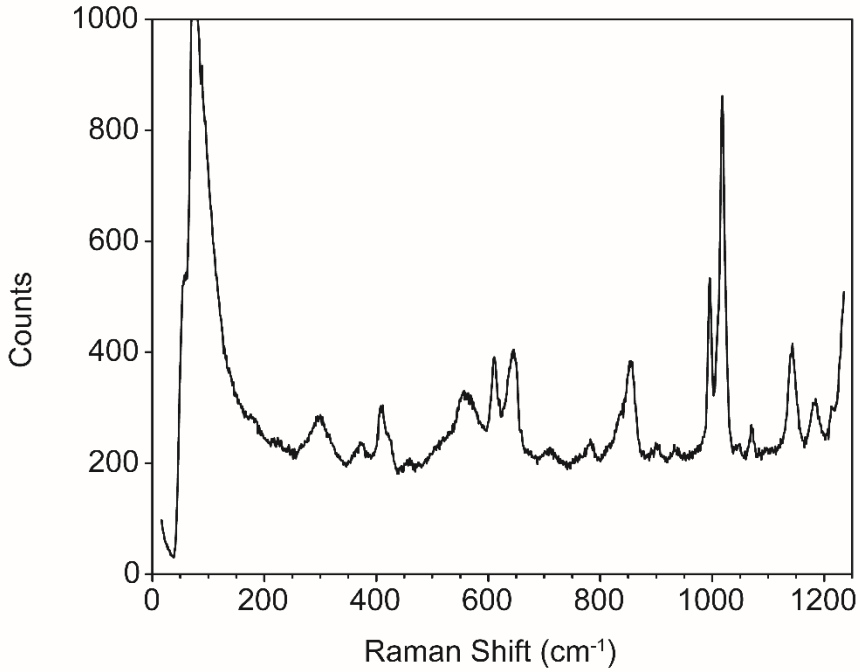

Figure S5. Raman spectrum for **Co_4-BTB**.

$Co_4O_4(OAc)_4(TPT)_{1.9}$•8MeOH ($Co_4$-TPT). Cubane **1** (0.050 g, 0.059 mmol) and 1,3,5-tris(4-pyridyl)triazine (0.025 g, 0.080 mmol) were suspended in 10 mL of benzonitrile in a Schlenk tube. An active vacuum was applied and the vessel was heated to 100˚C for 2 days. The dark red solid was collected by filtration and washed 3 x 20 mL of methanol. The solid was transferred to a Soxhlet apparatus, and extracted with

methanol for 24 h to yield 0.047 g (58 %). Samples for elemental analysis were dried under vacuum at 70°C for 12 h. Amount of methanol was determined by TGA mass loss (18%) at the first plateau region (160°C). The solid was dissolved in a mixture of 37% DCl in D_2O to give a cyan solution. The solution was analyzed by ^1H NMR spectroscopy (Figure S6). The Raman spectrum (633 nm excitation) is shown in Figure S7. Anal calc'd for $(C_8H_{12}Co_4O_{12})(C_{18}N_{12}N_6)_{1.57}$: C, 42.41; H, 3.03; N, 12.87. Found: C, 42.63; H, 3.23; N, 12.67.

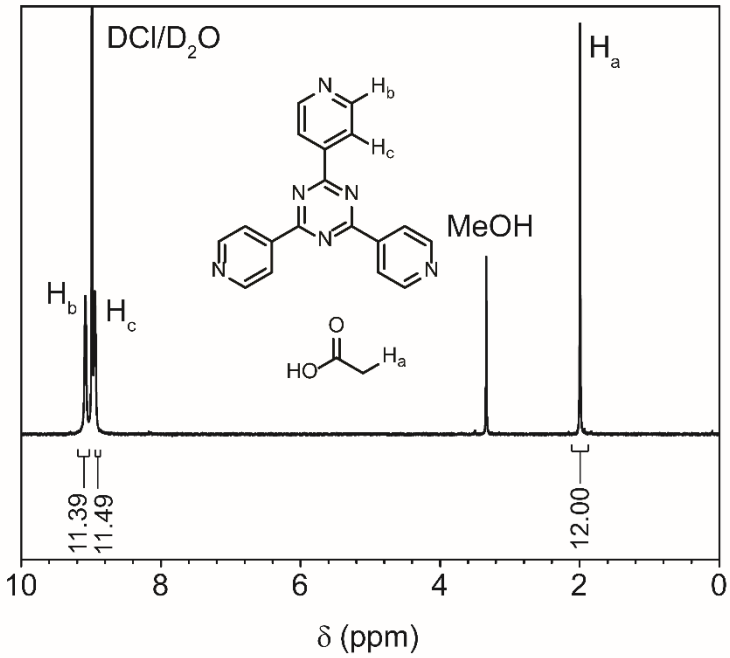

Figure S6. ^1H NMR (D_2O) spectrum for **Co_4-TPT** after digestion in DCl/D_2O.

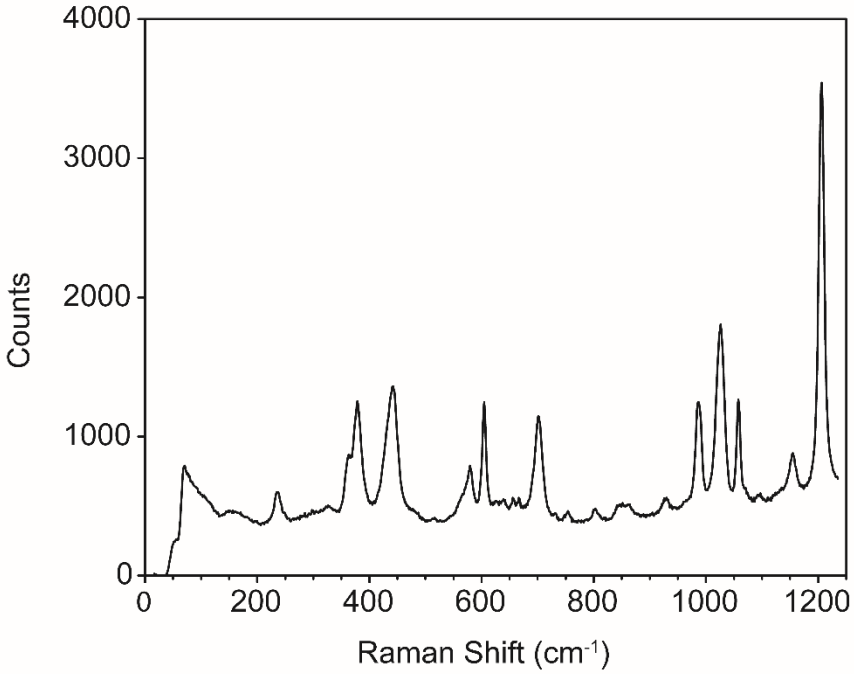

Figure S7. Raman spectrum for **Co_4-TPT**.

$Co_4O_4(OAc)_4(TPP)_{1.7}$•9MeOH ($Co_4$-TPP). Cubane **1** (0.500 g, 0.587 mmol) and 2,4,6-tris(4-pyridyl)pyridine (0.243 g, 0.782 mmol) were suspended in 30 mL of benzonitrile in a Schlenk tube. An active vacuum was applied and the vessel was heated to 90˚C for 2 days. The dark solid was collected by filtration and washed 50 mL of methanol. The solid was transferred to a Soxhlet apparatus, and extracted with methanol for 24 h to yield 0.614 g (68 %). Samples for elemental analysis were dried under vacuum at 70˚C for 12 h. Amount of methanol was determined by TGA mass loss (20 %) at the first plateau region (160˚C). The solid was dissolved in a mixture of 37% DCl in D_2O to give a cyan solution. The solution was analyzed by ^{1}H NMR spectroscopy (Figure S8). The Raman spectrum (633 nm excitation) is shown in Figure S9. Anal calc'd for $(C_8H_{12}Co_4O_{12})(C_{18}N_{12}N_6)_{1.73}$: C, 47.02; H, 3.50; N, 9.42. Found: C, 47.72; H, 3.40; N, 9.04

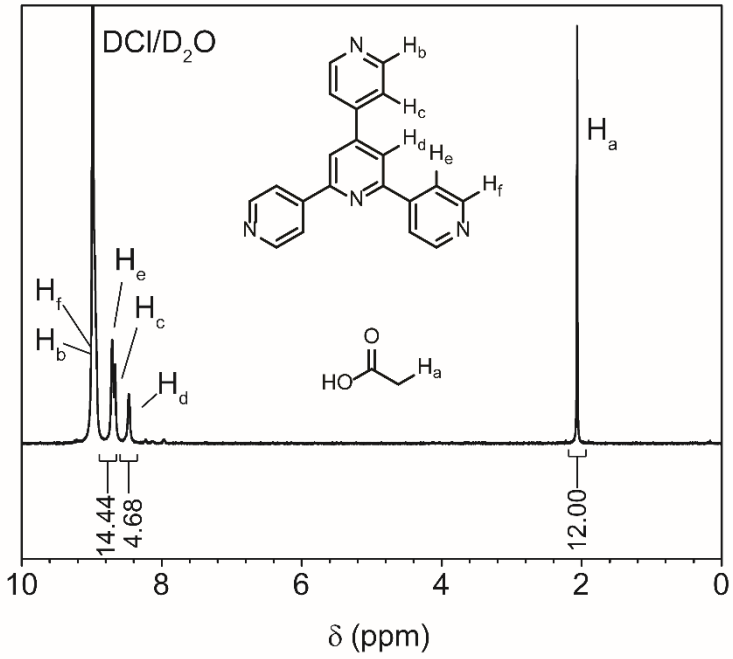

Figure S8. ^{1}H NMR (D_2O) spectrum for **Co_4-TPP** after digestion in DCl/D_2O.

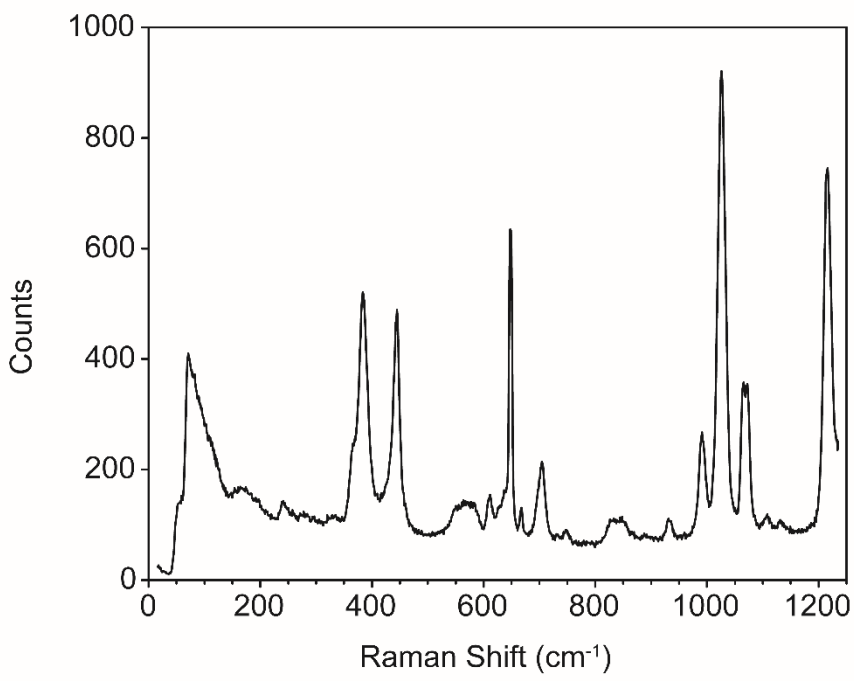

Figure S9. Raman spectrum for **Co_4-TPP**.

$Co_4O_4(OAc)_4(TPB)_{1.33}$•8MeOH ($Co_4$-TPB). Cubane **1** (0.500 g, 0.587 mmol) and 1,3,5-tris(4-pyridyl)benzene (0.242 g, 0.782 mmol) were suspended in 30 mL of benzonitrile in a Schlenk tube. An active vacuum was applied and the vessel was heated to 90˚C for 2 days. The dark solid was collected by filtration and washed 50 mL of methanol. The solid was transferred to a Soxhlet apparatus, and extracted with methanol for 24 h to yield 0.578 g (82 %). Samples for elemental analysis were dried under vacuum at 70˚C for 12 h. Amount of methanol was determined by TGA mass loss (22 %) at the first plateau region (160˚C). The solid was dissolved in a mixture of 37% DCl in D_2O to give a cyan solution. The solution was analyzed by ^{1}H NMR spectroscopy (Figure S10). The Raman spectrum (633 nm excitation) is shown in Figure S11. Anal calc'd for $(C_8H_{12}Co_4O_{12})(C_{18}N_{12}N_6)_{1.33}(H_2O)_4$: C, 44.47; H, 3.59; N, 5.76. Found: C, 44.23; H, 3.43; N, 6.01.

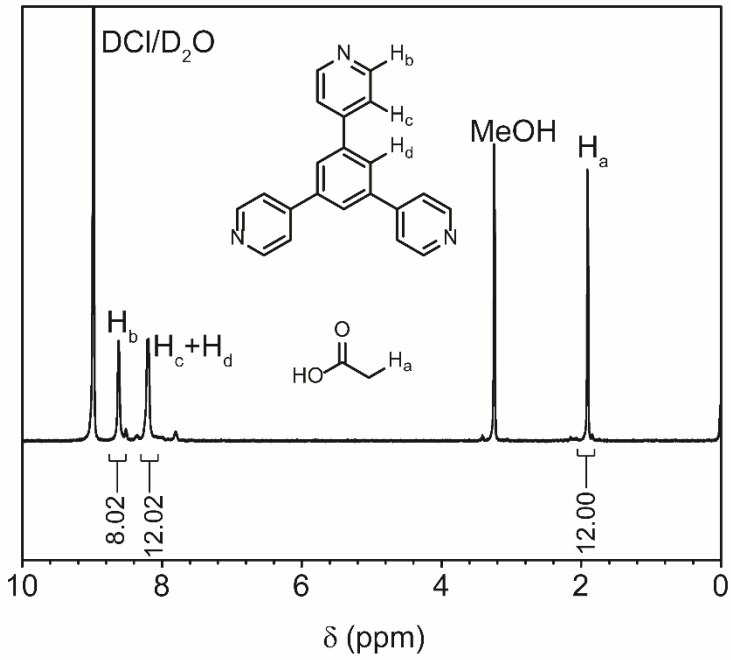

Figure S10. ^{1}H NMR (D_2O) spectrum for **Co_4-TPT** after digestion in DCl/D_2O.

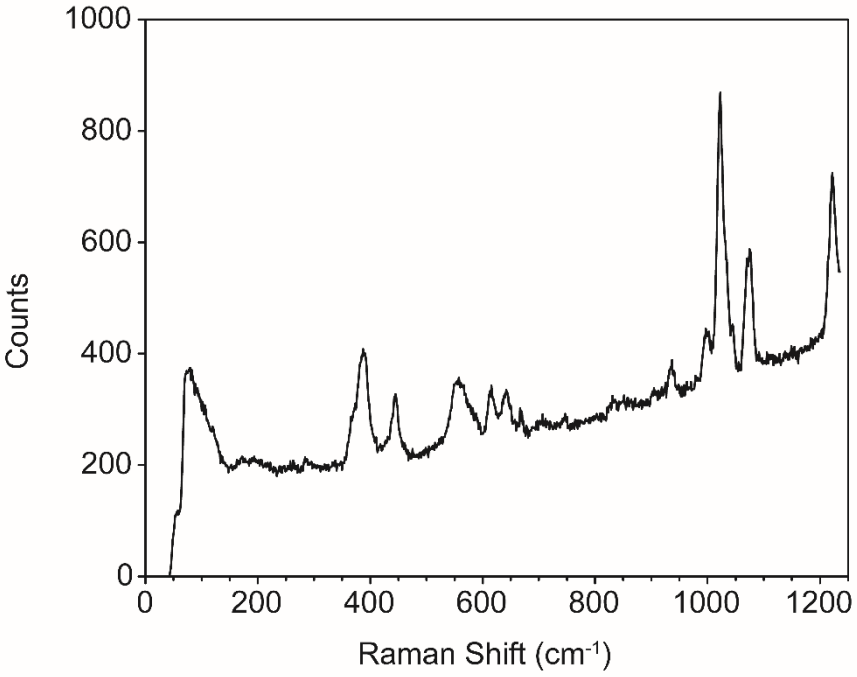

Figure S11. Raman spectrum for **Co_4-TPB**.

Removal of trace Co(II) impurities by chelation. The following procedure was used to allow stirring of polymer materials during chelation while ensuring that the chelating membrane was not mechanically degraded and could be separated from the polymer after chelation (Figure S12). Polymer samples were placed in a small (e.g. 100 mL) beaker equipped with a stir bar. A filter paper basket was folded over the edge of the beaker so

that it hung down ~ 1 cm into the beaker. A section of Empore SPE chelating membrane was placed into the basket and the basket was filled partially with water. Then, water was carefully added to the lower compartment (below the filter paper basket, containing the polymer), until no air remained below the filter paper. The filter paper was then sealed to the outside of the beaker by wrapping with Teflon tape. The upper compartment was then filled with water and the entire assembly sealed carefully with Parafilm. The chelation experiments were stirred for 5 days at a time, after which the chelating membrane was checked for pink color. If color was observed, the procedure was repeated until no more color, indicative of the presence of Co(II), was observed. Samples required 1-5 treatments to reach this point.

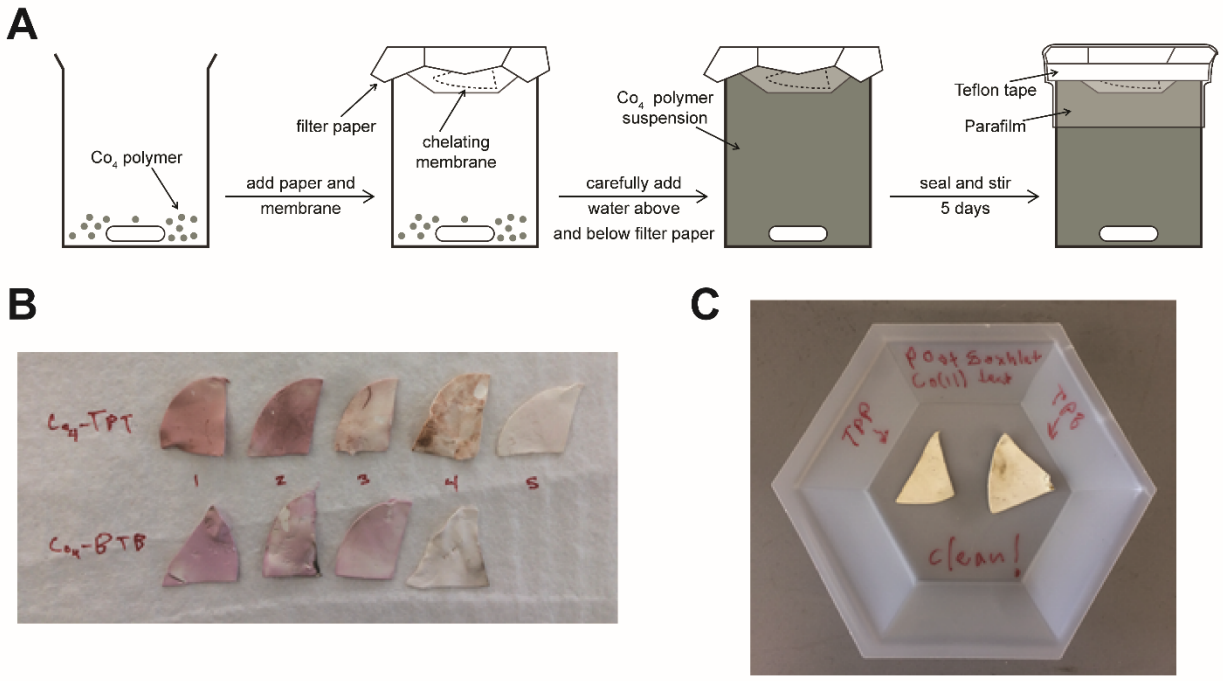

Figure S12. (A) Chelation procedure used to remove Co(II) impurities from polymer materials. (B) Empore SPE chelating membranes after successive chelation experiments with selected polymer samples, showing the decrease in pink color with successive treatments.

Replacement of carboxylate ligands in polymers by NaOH exchange. Each sample (0.1 g) was suspended in 1 M NaOH solution (10 mL) and stirred gently for 5 h. The solids were collected by filtration and washed with water (3 x 10 mL), then soaked in water (5 mL) for 12 h with stirring. The pH of the aqueous solution after soaking was observed to be near neutral (7–8). The solids were then filtered and washed with water (3 x 10 mL). The Raman spectra for the products from the reaction of NaOH with the polymers are shown in Figure S13.

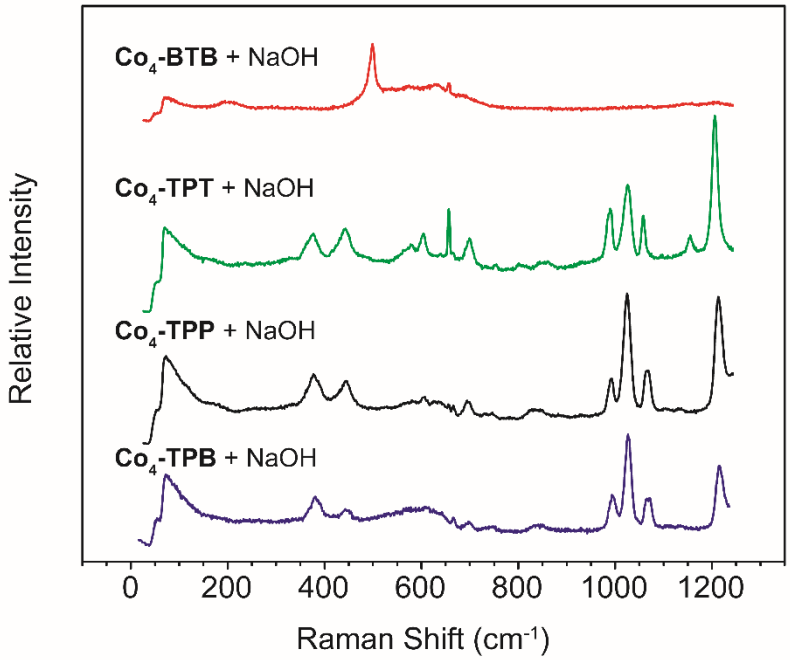

Figure S13. Raman spectra for the products from the reaction of NaOH with the polymers.

Thermogravimetric analysis. Samples (3-5 mg) were analyzed under N_2 flow, at a ramp rate of 10°C/min, from room temperature to 500°C.

Gas sorption measurements. Nitrogen adsorption isotherms for pressures in the range 0–1.2 bar were measured using a volumetric method using either a Micromeritics ASAP2020 or ASAP2420 instrument. Samples were transferred into preweighed analysis tubes, then capped with a Transeal. Samples were first activated under vacuum with applied heat in a gas sorption tube (70°C for **Co_4-BTC** and **Co_4-BTB**, 100°C for **Co_4-TPT**, **Co_4-TPP**, and **Co_4-TPB**) for 12 h to remove solvent (until the outgas rate was <1 μbar/min), at which point the tube was weighed to determine the mass of the activated sample. The tube was transferred to the analysis port of the instrument and the outgas rate was again checked to ensure that it was <1 μbar/min. UHP-grade (99.999% purity) N_2 and He were used for all adsorption measurements. For all isotherms, warm and cold free spaces were measured using He; N_2 at 77 were measured in liquid nitrogen. BET surface areas were calculated from the linear region of the N_2 isotherms at 77 K were determined using Micromeritics software.

Oxidation of polymers. The samples (0.075 g) were stirred gently in 5 mL of 0.2 M $Ce(NO_3)_6(NH_4)_2$ for 1 h. The solids were collected by filtration and washed with water (3 x 5 mL), then soaked in water (5 mL) for 15 min with stirring. The washed solids were collected by filtration, washed with water (3 x 5 mL), and used immediately for EPR measurements or stoichiometric water oxidation. Note that the oxidized samples decomposed over the course of hours at room temperature, as observed by changes in their EPR spectra.

EPR Spectroscopy. X-band EPR spectroscopy was carried out using a Bruker Instruments (Billerica, MA) Elexsys EPR spectrometer equipped with a dual mode cavity. Temperature was controlled with an Oxford Instruments liquid helium cryostat. Samples were finely ground and placed into 4 mm quartz tubes for measurement.

Construction of structural models. Complex **1** has idealized D_{2d} site symmetry (neglecting acetate methyl groups), where κ^2-carboxylates cap four equatorial faces (~90˚ apart) and pyridine ligands cap the two remaining, opposite faces (180˚ apart) of the cubane. The BTC and BTB linkers have idealized D_{3h} symmetry, which is expected to reduce to D_3 in the **Co$_4$-BTC** and **Co$_4$-BTB** polymers because the cubane units cannot be arranged to maintain the mirror planes in D_{3h}. Searching the RCSR for known framework structures with one four-coordinate vertex, one three-coordinate vertex, and one edge type yields eight candidates – **bor**, **bor-c**, **bor-c***, **ctn**, b, **mhq-z**, **pto**, and **tbo** – of which **bor**, **ctn**, **mhq-z**, **pto**, and **tbo** are unique. The remaining three are interpenetrated versions of these structures. Two of the five candidates – **bor** and **ctn** – were discarded because their four-coordinate vertices, while having D_{2d} site symmetry or a subset thereof, are tetrahedrally coordinated and therefore incompatible with the tetragonal arrangement of carboxylate edge sites around the cube. A third, **mhq-z**, was eliminated because its topological density appears too high for the axial pyridine ligands to fit in the structure. The remaining structures – **pto** and **tbo** – differ in the dihedral angle between the threefold axis and the rotation axis of the S_4 operation. In **tbo** it is 90˚, while in **pto** it is smaller (e.g. 55˚ for MOF-143). Both structures were used to construct models. In the case of **pto** (*Pm*-3*m*), the symmetry of the four-coordinate vertices, -42*m* (D_{2d}), matches the cubane and that of the three-coordinate vertices, 32 (D_3), matches BTC/BTB. In the case of **tbo** (*Fm*-3*m*), the formal crystallographic symmetry of the net – *mmm* (D_{2h}) for four-coordinate sites and 3*m* (C_{3v}) for three-coordinate sites – is different from that expected for **Co$_4$-BTC** and **Co$_4$-BTB** and thus a "pseudo-**tbo**" structure that lacks some of the symmetry operations of *Fm*-3*m* was constructed.

For **Co$_4$-TPT**, **Co$_4$-TPP**, and **Co$_4$-TPB**, the only vertex is the pyridyl linker, with idealized D_{3h} symmetry, and the edges with Co_4 cubanes have idealized D_{2d} symmetry. Searching the RCSR for structures with one three-coordinate vertex and one edge produces only the **srs** net (and its interpenetrated analogues **srs-c**, **srs-c4**, and **srs-c8**). Site symmetry in **srs** (*I*4(1)32) – 32 (D_3) for vertices and 222 (D_2) for edges – is a subset of the idealized symmetry above and thus compatible.

For each of the candidate structures, the unit cell was sized by applying an estimate of the edge length, from atomic coordinates in **1** and linker molecules, to the fractional edge length defined by the space group. Atomic coordinates from the molecular complex **1** were then transformed to be correctly sized, oriented, and positioned on the appropriate Wyckoff positions. Finally, linker molecules were constructed along edge sites, using previously published structural parameters (e.g. from HKUST-1[6] and MOF-143[7]) where needed.

DFT optimization of structural models. The structural models were relaxed by density functional theory (DFT+U) calculations within the Vienna *Ab-initio* Simulation Package

(VASP).[8-10] Structures with centered unit cells (**tbo** and **srs**) were reduced to primitive cells to minimize computational burden. To meet the requirements of VASP, all crystallographically related atoms were treated independently (*i.e.* all structures were converted to *P*1). As with other studies of Co^{III}-oxides,[11-13] the Perdew-Burke-Ernzerhof (PBE)[14] exchange-correlation functional was employed with the Hubbard-U correction[15] and a value of U = 3.32 eV[16,17] for Co atoms. Next, all the atomic positions, cell shape and volume of all the systems were optimized using high energy cutoff of 600 eV to reach a maximum force threshold of 0.05 eV/Å and stress below 0.01 kBar.

X-ray photoelectron spectroscopy. X-ray photoelectron spectra were collected using a Kratos Axis Ultra DLD system with a monochromatized Al Kα source (hν = 1486.6 eV), at power = 225 W. A pass energy for survey spectra of 160 eV and for elemental spectra of 20 eV was used. Spectra were fit using CasaXPS. Energy positions were corrected by shifting the C 1s core level position to 284.8 eV.

X-ray absorption spectroscopy. X-ray absorption spectra were taken at the Advanced Light Source (ALS) on Beamline 10.3.2. The radiation was monochromatized by a Si (111) double-crystal monochromator. The intensity of the incident X-ray (I_0) was monitored by an N_2-filled ionization chamber in front of the sample. The energy was calibrated using a glitch in I_0 relative to the absorption edge of a Co foil. Samples were cooled to –20 ˚C using a Peltier cooling stage. All data were collected using a quick XAS scan mode, and the data collection was carried out under the threshold of X-ray radiation damage, by monitoring with the XANES edge shift. Data reduction was performed using custom software (Matthew Markus, BL 10.3.2, ALS). Pre-edge and post-edge contributions were subtracted from the XAS spectra, and the result was normalized with respect to the edge jump.

X-ray total scattering and pair distribution function. The experiments were carried out at Beamline 28-ID-1 at NSLS-II at Brookhaven National Laboratory using the rapid acquisition PDF method (RAPDF).[18] A 2D Perkin Elmer detector was placed 218.7025 mm behind the samples which were loaded in 1 mm ID Kapton capillaries. The incident wavelength of the X-rays was λ = 0.1827 Å. Calibration of the experimental setup was done using a Ni standard as a calibrant. Datasets were collected at 100 K using a flowing nitrogen cryostream cooler. The detector exposure time was adjusted for each sample to avoid detector saturation, and the number of frames taken for each sample was adjusted to obtain sufficient counting statistics on the data. Raw data were summed and corrected for polarization effects before being integrated along arcs of constant angle to produce 1D powder diffraction patterns using the program fit2D.[19] Corrections were then made to the data and normalizations carried out to obtain the total scattering structure function, $F(Q)$, which was Fourier transformed to obtain the PDF using PDFgetX3[20] within xPDFsuite.[21] The maximum range of data used in the Fourier transform (Q_{max}, where $Q = (4\pi \sin\theta)/\lambda$ is the magnitude of the momentum transfer on scattering) was varied depending on the quality of the data. Figure S14 shows the data in various stages of the analysis, from raw intensity at the top, through $F(Q)$ in the middle, to $G(r)$ at the bottom.

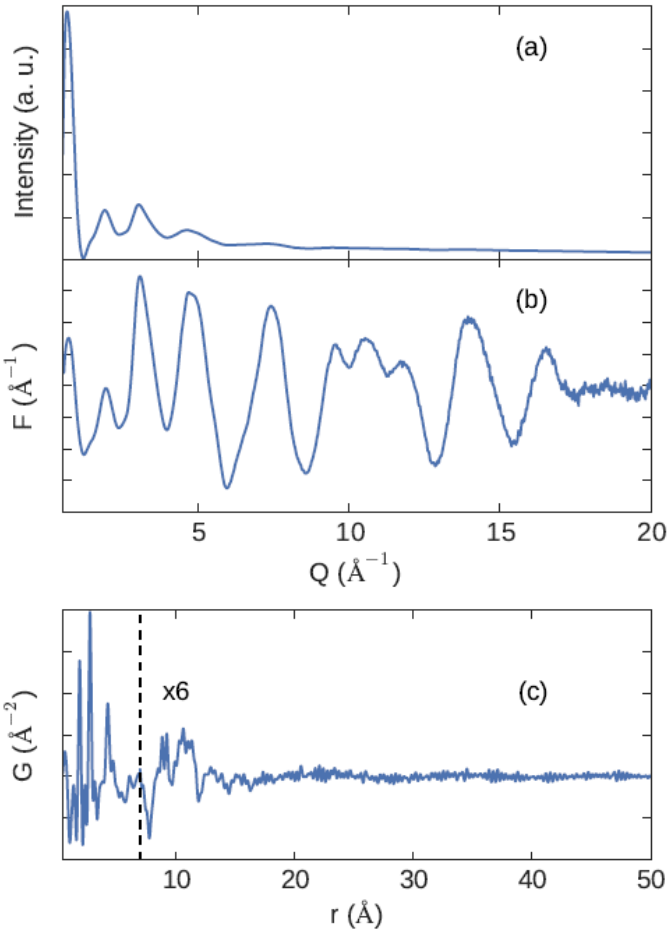

Figure S14. Representative raw intensities (background subtracted) (a), *F*(*Q*) (b) and *G*(*r*) (c) curves from **Co_4-TPT** sample. Note that after processing a clear signal at high-Q is evident in *F*(*Q*) that is not so clear in the raw data.

General procedure for stoichiometric OER. Oxygen was detected using an Ocean Optics Multi-Frequency Phase Fluorimeter (MFPF-100) with a FOSPOR-R probe inserted in the headspace of a sealed flask. The probe was calibrated at a single temperature by fitting a second order polynomial to eight O_2 concentrations between 0.0 and 10.6%, which were produced using pair of mass-flow controllers. Henry's Law was used to account for oxygen that remained dissolved in solution.

Baseline O_2: A 10 mL round bottom flask was equipped with a stir bar. The flask was stoppered with a rubber septum holding the Ocean Optics O_2 sensor probe. Silicone grease was used to seal around the probe. The flask was then purged with N_2 (*via* an inlet needle and an exit needle) for 10 minutes. The purging needle was removed and the O_2 was measured for ~10 minutes, at which point, a 1.0 mL solution of 1 M NaOH was added. The O_2 measurement was continued for 25 min.

With [Co_4-TPT]$^+$: A 10 mL round bottom flask was filled with solid **[Co_4-TPT]$^+$** (*vide supra*, 0.058 g). The flask was stoppered with a rubber septum holding the Ocean Optics

O_2 sensor probe. Silicone grease was used to seal around the probe. The flask was then purged with N_2 (*via* an inlet needle and an exit needle) for 10 minutes. The purging needle was removed and the O_2 was measured for ~5 minutes, at which point, a 1.0 mL solution of 1 M NaOH was added. The O_2 measurement was continued for ~25 min.

With ***[Co₄-TPP]***$^+$: A 10 mL round bottom flask was filled with solid **[Co₄-TPP]**$^+$ (*vide supra*, 0.100 g). The flask was stoppered with a rubber septum holding the Ocean Optics O_2 sensor probe. Silicone grease was used to seal around the probe. The flask was then purged with N_2 (*via* an inlet needle and an exit needle) for 10 minutes. The purging needle was removed and the O_2 was measured for ~5 minutes, at which point, a 1.0 mL solution of 1 M NaOH was added. The O_2 measurement was continued for ~25 min.

With ***[Co₄-TPB]***$^+$: A 10 mL round bottom flask was filled with solid **[Co₄-TPB]**$^+$ (*vide supra*, 0.100 g). The flask was stoppered with a rubber septum holding the Ocean Optics O_2 sensor probe. Silicone grease was used to seal around the probe. The flask was then purged with N_2 (*via* an inlet needle and an exit needle) for 10 minutes. The purging needle was removed and the O_2 was measured for ~5 minutes, at which point, a 1.0 mL solution of 1 M NaOH was added. The O_2 measurement was continued for ~25 min.

Recycling experiment. After the stoichiometric OER experiment ended, is collected by filtration, **Co₄-TPT** was collected and washed with water (~50 mL). **Figure SX** compares the Raman spectra before and after OER. The solid was collected and oxidized again by the procedure described above, and the stoichiometric OER reaction was repeated.

Electrochemistry. Samples analyzed by electrochemistry were first suspended in solution by the following procedure. A small amount of solid (~1-2 mg) is ground by mortar and pestle in 0.5 mL ethanol (for **Co₄-BTC**, **Co₄-BTB**, **Co₄-TPP**, and **Co₄-TPB**) or isopropanol (**Co₄-TPT**). These solvent choices gave the best suspension in our hands. The slurry is transferred to a polypropylene tube, diluted to 2 mL with the same solvent, and then sonicated for 1 h. The suspension was allowed to settle for 24 h, and the colored colloidal solution was decanted for use. Only **Co₄-TPP**, **Co₄-TPB**, and **Co₄-TPT** had colored solutions indicative of colloids. The cobalt concentrations were determined by ICP analysis, and the results are listed in Table S1.

Table S1. Concentration of polymer in suspended solutions by ICP analysis.

Polymer	Solvent	[Co] (mM)	[Co_4O_4] (mM)
Co₄-TPT	*i*PrOH	0.271	0.0678
Co₄-TPP	EtOH	0.680	0.170
Co₄-TPB	EtOH	0.477	0.119

To prepare the electrodes, two drops (22.8 ± 0.28 μL for EtOH, 20.2 ± 0.66 μL for *i*PrOH) of the solution was drop-cast onto a glassy carbon disk electrode ($A_{electrode}$ = 0.0707 cm^2) surrounded by a Teflon casing (A_{total} = 0.322 cm^2). The solution was evaporated at room temperature to give a film. The loading of Co_4O_4 on the glassy carbon disk was calculated by the method below and listed in Table S2. Electrodes with

Co_4-TPP-OH and **Co_4-TPB-OH** were prepared by soaking electrodes coated with **Co_4-TPP** and **Co_4-TPB** in pH 14 for 5 h.

Calculation of electrode loading:
Loading = *volume suspension* (L) x [Co_4O_4] (mol/L) x $A_{electrode}/A_{total}$

Table S2. Calculated loadings of polymer on electrode

Polymer	Co_4O_4/Area (mol/cm^2)	Loading on electrode (mol)
Co_4-TPT	4.24 x 10^{-9}	2.99 x 10^{-10}
Co_4-TPP	1.20 x 10^{-8}	8.55 x 10^{-10}
Co_4-TPB	8.46 x 10^{-9}	5.98 x 10^{-10}

SEM images of the drop-cast films are shown in Figure S15, demonstrating particle sizes on the order of a micron.

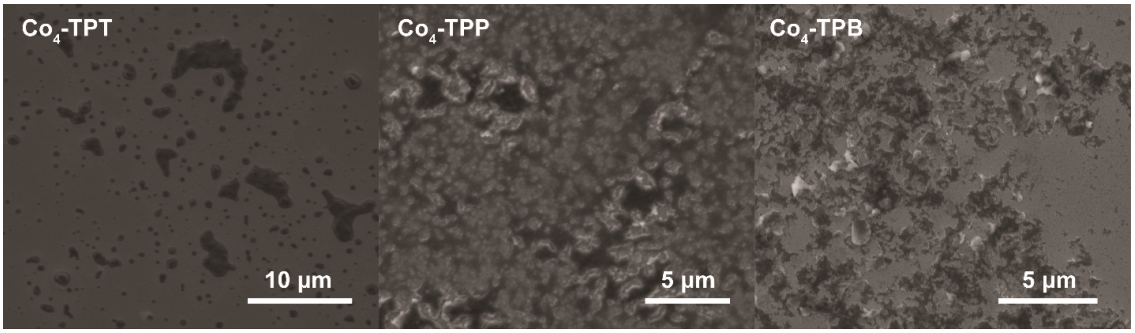

Figure S15. SEM images of drop-cast polymers on silicon wafer.

Nonaqueous CV. Cyclic voltammograms were collected in 0.1 M ^{n}Bu$_4$NPF$_6$ electrolyte in MeCN at room temperature with *iR* compensation. Ag wire was used as a floating reference, and Pt wire was used as the counter electrode. Ferrocene was added as an internal standard. The scan rate was varied from 10 mV/s to 4000 mV/s. The integrated peak areas are show in Figure S16 and listed in Table S3.

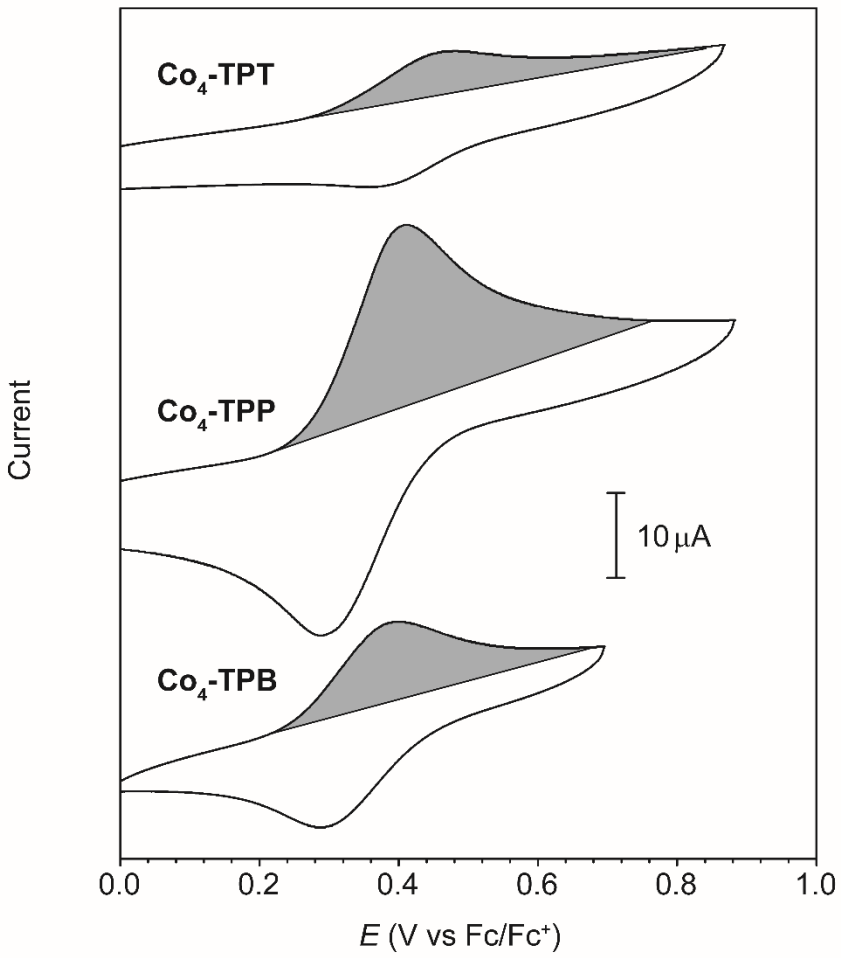

Figure S16. Integration of anodic peaks for CVs in MeCN at 100 mV/s.

Table S3. Integrated areas of anodic peaks

Polymer	Anodic peak area (coulombs)	mol e^-/mol Co_4O_4 (%)
Co_4-TPT	1.15×10^{-6}	4.0%
Co_4-TPP	4.72×10^{-6}	5.7%
Co_4-TPB	1.82×10^{-6}	3.2%

Aqueous CV. Aqueous electrochemical data were collected in 0.1 M KPi buffer at pH 7, 11, and 12. The pH was adjusted by addition of 1.0 M NaOH and measured by a pH meter. No *iR* compensation was applied since solution resistance was assumed to be negligible. Note that the application of *iR* compensation occasionally lead to deleterious potentiostat oscillations and damaging of the electrode.

Supporting Information References

(1) Chakrabarty, R.; Bora, S.; Das, B. K. *Inorg. Chem.* **2007**, *46* (22), 9450–9462.
(2) Nguyen, A. I.; Ziegler, M. S.; Oña-Burgos, P.; Sturzbecher-Hohne, M.; Kim, W.; Bellone, D. E.; Tilley, T. D. *J. Am. Chem. Soc.* **2015**, *137* (40), 12865–12872.
(3) Anderson, H. L.; Anderson, S.; Sanders, J. K. M. *J. Chem. Soc., Perkin Trans. 1* **1995**, No. 18, 2231–2245.
(4) Constable, E. C.; Zhang, G.; Housecroft, C. E.; Zampese, J. A. *CrystEngComm* **2011**, *13* (22), 6864–6870.
(5) Schmittel, M.; He, B.; Mal, P. *Org. Lett.* **2008**, *10* (12), 2513–2516.
(6) Chui, S.; Lo, S.; Charmant, J.; Orpen, A.; Williams, I. *Science* **1999**, *283* (5405), 1148–1150.
(7) Furukawa, H.; Go, Y. B.; Ko, N.; Park, Y. K.; Uribe-Romo, F. J.; Kim, J.; O'Keeffe, M.; Yaghi, O. M. *Inorg. Chem.* **2011**, *50* (18), 9147–9152.
(8) Kresse, G.; Hafner, J. *Phys. Rev. B* **1993**, *47* (1), 558–561.
(9) Kresse, G.; Furthmüller, J. *Computational Materials Science* **1996**, *6* (1), 15–50.
(10) Kresse, G.; Joubert, D. *Phys. Rev. B* **1999**, *59* (3), 1758–1775.
(11) Friebel, D.; Bajdich, M.; Yeo, B. S.; Louie, M. W.; Miller, D. J.; Casalongue, H. S.; Mbuga, F.; Weng, T.-C.; Nordlund, D.; Sokaras, D.; Alonso-Mori, R.; Bell, A. T.; Nilsson, A. *Phys. Chem. Chem. Phys.* **2013**, *15* (40), 17460–17467.
(12) Zhou, M.; Cai, L.; Bajdich, M.; García-Melchor, M.; Li, H.; He, J.; Wilcox, J.; Wu, W.; Vojvodic, A.; Zheng, X. *ACS Catal.* **2015**, *5* (8), 4485–4491.
(13) Zhang, B.; Zheng, X.; Voznyy, O.; Comin, R.; Bajdich, M.; Garcia-Melchor, M.; Han, L.; Xu, J.; Liu, M.; Zheng, L.; Garcia de Arquer, F. P.; Dinh, C. T.; Fan, F.; Yuan, M.; Yassitepe, E.; Chen, N.; Regier, T.; Liu, P.; Li, Y.; De Luna, P.; Janmohamed, A.; Xin, H. L.; Yang, H.; Vojvodic, A.; Sargent, E. H. *Science* **2016**, *352* (6283), 333–337.
(14) Perdew, J. P.; Burke, K.; Ernzerhof, M. *Phys. Rev. Lett.* **1996**, *77* (18), 3865–3868.
(15) Dudarev, S. L.; Botton, G. A.; Savrasov, S. Y.; Humphreys, C. J.; Sutton, A. P. *Phys. Rev. B* **1998**, *57* (3), 1505–1509.
(16) Wang, L.; Maxisch, T.; Ceder, G. *Phys. Rev. B* **2006**, *73* (19), 195107.
(17) Jain, A.; Ong, S. P.; Hautier, G.; Chen, W.; Richards, W. D.; Dacek, S.; Cholia, S.; Gunter, D.; Skinner, D.; Ceder, G.; Persson, K. A. *APL Mater.* **2013**, *1* (1), 011002.
(18) Chupas, P. J.; Qiu, X.; Hanson, J. C.; Lee, P. L.; Grey, C. P.; Billinge, S. J. L. *J. Appl. Crystallogr.* **2003**, *36* (6), 1342–1347.
(19) Hammersley, A. P.; Svensson, S. O.; Hanfland, M.; Fitch, A. N.; Hausermann, D. *High Pressure Res.* **2006**, *14* (4-6), 235–248.
(20) Juhás, P.; Davis, T.; Farrow, C. L.; Billinge, S. J. L. *J. Appl. Crystallogr.* **2013**, *46* (2), 560–566.
(21) Yang, X.; Juhas, P.; Farrow, C. L.; Billinge, S. J. L. *J. Appl. Crystallogr.* **2014**, 1402.3163.

Chapter 5:

Carboxylate-Supported Mixed Manganese-Cobalt Oxido Cubane and Dangler Clusters*

---

* This work is based upon work in a manuscript to be published, included with permission from all authors:

Nguyen, A. I., Suess, D. L. M., Darago, L. E., Levine, D. S., Ziegler, M. S., Britt, R. D., Tilley, T. D. *In preparation*

Author contributions: Andy I. Nguyen formulated the project, synthesized all materials, and performed electrochemical studies. Daniel L. M. Suess and R. David Britt (UC Davis) measured and analyzed all EPR spectra. Lucy E. Darago measured and analyzed magnetometry data. Daniel S. Levine performed DFT calculations. A.I.N. and Micah S. Ziegler solved x-ray diffraction crystal structures.

5.1 Introduction

Many well-known catalysts for the oxygen-evolution reaction (OER), such as nickel oxide (NiO_x) and cobalt oxide (CoO_x), owe their high activity to serendipitous doping by Fe impurities.[1,2] This effect is also observed in the enhanced OER catalysis by CoO_x doped with Mn.[3,4] Curiously, the pure oxides are not as efficient for the OER as are the heterometallic oxides. The prevalence of heterometallic oxide OER catalysts extends to Nature: the oxygen-evolving center (OEC) in photosystem II is a mixed calcium-manganese oxido cluster.[5] These observations suggest that there are cooperative mechanisms unique to heterometallic systems.

Molecular models of heterometallic oxide catalysts could immensely facilitate understanding of these complex systems, but the rational synthesis of molecular oxido clusters is nontrivial. The high basicity, multiple bonding modes, and the lack of reliably general chemical sources of the oxide ligand contribute to difficulties in the development of rational synthetic approaches. In addition, the precise incorporation of a heterometal presents a significant synthetic challenge. For these reasons, many known examples of molecular metal oxido clusters were initially discovered *via* serendipitous self-assembly rather than *via* a designed approach.[6–11] Furthermore, examples of post-synthetic modifications of oxido clusters as a means of probing reactivity and electronic perturbations are uncommon. A notable exception is the work of Agapie and coworkers, who have made significant progress towards the rational synthesis and post-synthetic modification of several metal oxido clusters supported by a trialkoxide ligand.[12–17] While this elegant approach has provided homo- and hetero-metallic oxido clusters, the necessity of the chelating trialkoxide ligand is a constraint on the bonding and reactivity of these complexes. Thus, there is still a need for development of rational routes to fundamentally simple oxido clusters.

This contribution describes the first syntheses of mixed manganese-cobalt oxido cubane and dangler clusters using a rational approach. These $[MnCo_3O_4]$-based clusters are ligated by simple, biologically relevant carboxylate and pyridine ligands, though these can be systematically exchanged for additional types of ligands. Relevant to developing an understanding of the heterometallic effects on OER catalysis, the $[MnCo_3O_4]$ cubane is essentially a Mn-doped version of the $[Co_4O_4]$ cubane OER catalyst, and could be a useful model for Mn-doped CoO_x.[18] A fifth metal can be intentionally appended onto the cubane to generate a pentametallic $[MnCo_4O_4]$ cluster bearing a resemblance to the "dangler" motif in photosystem II.[5] There is only one other example of a synthetic 3*d*-transition metal "dangler" complex, which came from a self-assembled synthesis.[8] The synthetic protocols of these clusters demonstrate design principles for furthering molecular metal-oxido chemistry. Electronic properties of the clusters were probed by a range of spectroscopy, magnetometry, electrochemistry, and theory to provide evidence for cooperativity between Mn and Co mediated by the cubane structure.

Scheme 1. Synthesis of $[MnCo_3O_4]^{5+}$ congeners

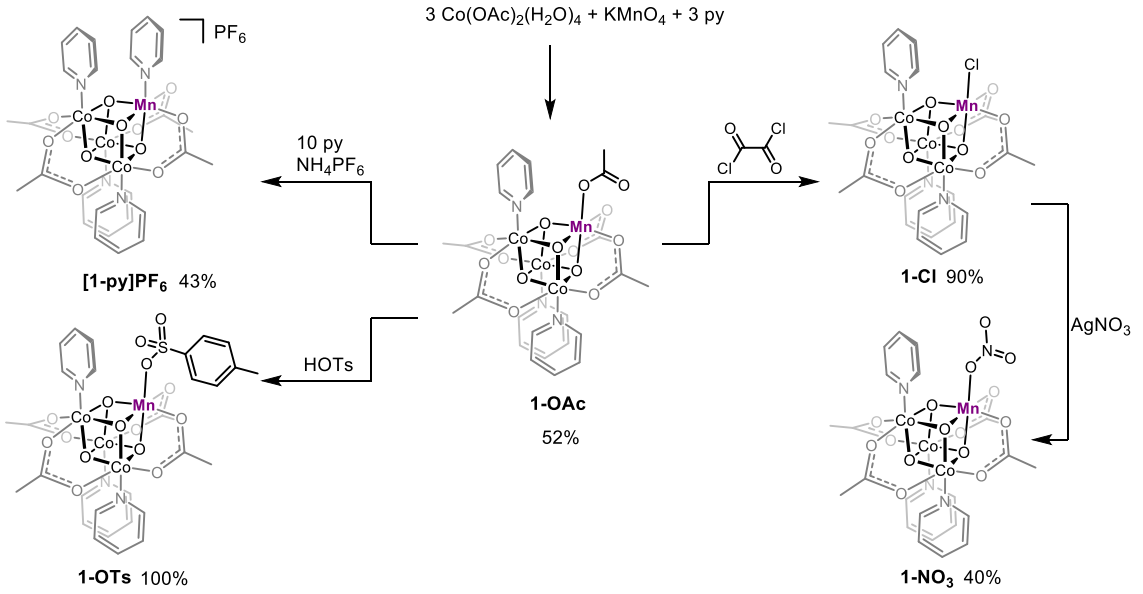

5.2 Synthesis and Structure

The asymmetry in oxidation states of the manganese and cobalt reagents was exploited to control the Mn:Co ratio in the cluster. Permanganate (MnO_4^-) with its Mn(VII) oxidation state was expected to oxidize three equivs of Co(II) to Co(III) with concurrent reduction to Mn(IV). Additionally, MnO_4^- is a possible source of the four oxo-ligands of a cubane core. Indeed, three equivs of cobalt(II) acetate tetrahydrate reacted with potassium permanganate, in the presence of pyridine, to afford the tetrametallic oxido cluster, $MnCo_3O_4(OAc)_5py_3$ (**1-OAc**) in 52% isolated yield as black-brown crystals (Scheme 1). The elemental composition of **1-OAc** was conclusively determined by high-resolution electrospray-ionization-mass spectrometry (HR-ESI-MS) (*m*/*z* = 850.90, $[MnCo_3O_4(OAc)_5py_3Na]^+$). Single-crystal X-ray diffraction (XRD) confirmed **1-OAc** as a C_s-symmetric oxo-cubane, with three Co(III) ions and one Mn(IV), each in a pseudo-O_h ligand environment, defining four corners of the $[MnCo_3O_4]^{5+}$ core (Figure 1). The somewhat shorter average metal-oxo bond distances about one metal ion identified it as the Mn(IV) ion; the average Mn–O(oxo) bond length is 1.859(2) Å, while the average Co–O(oxo) distances are 1.875(1) Å. This is consistent with stronger ionic bonding between the oxo ligand and a 4+ (*vs.* 3+) ion. Four μ^2-acetate ligands cap four equatorial faces of the cubane, and the fifth μ^1-acetate is bound to Mn(IV) on an axial face of the cubane. Notably, the average Mn–O(μ^2-acetate) distances are 1.992(3) Å, *longer* than the average Co–O(μ^2-acetate) distance of 1.933(3) Å. This difference between the Mn–O(μ^2-acetate) and Co–O(μ^2-acetate) bond lengths may be rationalized by the stronger Mn–O(oxo) versus Co–O(oxo) bond (*vide supra*), giving rise to a stronger *trans*-influence on the Mn–O(μ^2-acetate) bonds. Finally, three pyridine ligands on the axial faces of the cubane complete the coordination spheres of the three Co(III) ions. Notably, **1-OAc** is quite soluble and stable in water, as well as in organic solvents (such as dichloromethane, acetonitrile, and methanol). Aqueous conductivity

measurements of dissolved **1-OAc** do not indicate ionization at 25°C, presumably due to the strong ligand-field stabilization of both the t_{2g}^6 and t_{2g}^3 electron configurations of Co(III) and Mn(IV), respectively.

The axial μ^1-acetate ligand of Mn(IV) in **1-OAc** can be substituted for a wide variety of ligands. Efficient exchange of the acetate ligand for a chloride ligand was achieved by reaction of **1-OAc** with oxalyl chloride, to afford **1-Cl** in 90% yield (Scheme 1). Single crystal XRD confirmed exchange of the μ^1-acetate for chloride ligand, and provided a Mn–Cl bond length of 2.270(2) Å (Figure 1). The bond distances within the cubane core are nearly identical to those of **1-OAc**. The chloride derivative **1-Cl** is a useful starting point for ligand substitutions *via* elimination of metal chloride salts. For example, exchange for nitrate (NO_3^-) upon reaction of **1-Cl** with silver nitrate produced **1-NO$_3$** (Scheme 1). The structure of complex **1-NO$_3$** was established by single crystal XRD (Figure 1). A contraction of the Mn–O bond *trans* to the nitrate, from 1.864(4) Å in 1-OAc to 1.846(4) Å, is consistent with weaker σ-donation and a lower *trans*-influence from nitrate, which results in a strengthening of the Mn–O(oxo) bond. The average Co–O bond lengths remain essentially unchanged.

Use of the strong acid 4-toluenesulfonic acid (HOTs) readily exchanged the μ^1-acetate of **1-OAc** for μ^1-OTs, driven by formation of acetic acid, to generate **1-OTs** in 100% yield. The cubane bond metrics, determined by single crystal XRD, are similar to those of **1-NO$_3$**, consistent with the low Lewis basicity of 4-toluenesulfonate. Generation of a cationic species was achieved by displacement of the μ^1-acetate ligand of Mn(IV) in 1-OAc with a neutral ligand. Heating an aqueous solution of **1-OAc** and excess pyridine in the presence of hexafluorophosphate anion (PF_6^-) resulted in precipitation of $[Co_3MnO_4(OAc)_4py_4]PF_6$, **[1-py]PF$_6$**, as dark brown crystals (43%). Compound **[1-py]PF$_6$** crystallizes in *Cc*, resulting in positional disorder of Co and Mn atoms, however HR-ESI-MS unambiguously established the elemental composition (m/z = 847.94, $[Co_3MnO_4(OAc)_4py_4]^+$). It is noteworthy that **[1-py]PF$_6$** is isostructural, but not isoelectronic, to the previously described all-cobalt derivative $[Co_4O_4(OAc)_4py_4]^+$.[18–20]

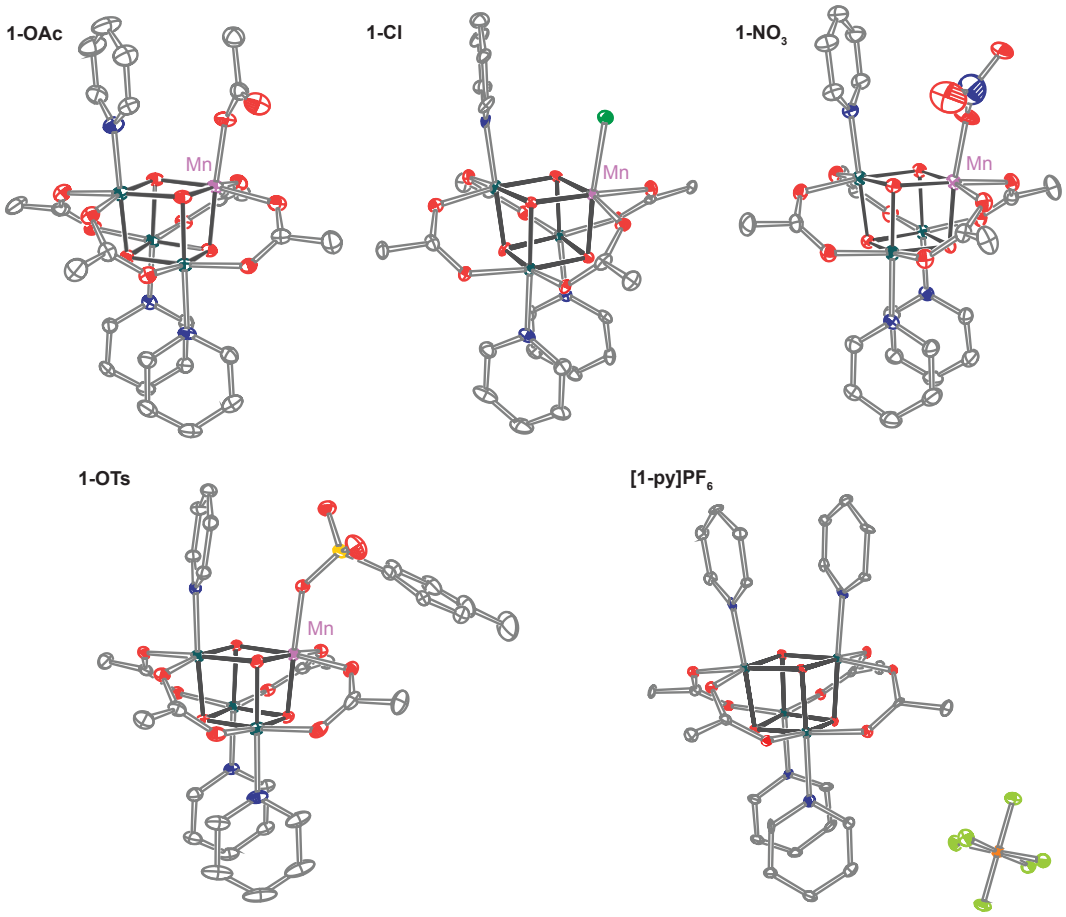

Figure 1. Thermal ellipsoids of $[MnCo_3O_4]$ cubanes at 30% probability. Hydrogen atoms and solvent molecules were removed for clarity.

The μ^1-acetate ligand of Mn(IV) in **1-OAc** also coordinates an additional metal ion to become a μ^2-acetate ligand. Attempts to coordinate $M(OAc)_2$ salts, where M = Zn, Ni, and Cu to **1-OAc** did not produce a new product. However, $Co(OAc)(NO_3)$, produced *in situ* by a 1:1 mixture of $Co(OAc)_2$ and $Co(NO_3)_2$, successfully incorporated a fifth metal to generate the pentametallic, "dangler" complex $Co_4Mn_4(OAc)_6(NO_3)py_3$ (**2**) (eq 1, Figure 2). The crystal structure of **2** reveals that the "dangling" Co(II) is attached to the tetrametallic cubane core *via* three μ^2-acetate ligands and a μ^4-oxo ligand. The nitrate ligand is bound in a bidentate fashion to the Co(II) dangler to complete the local, pseudo-octahedral coordination sphere for this metal center (Figure 2). One of the acetate ligands bound to the dangler is derived from rearrangement of a face-capping acetate ligand. The bond distances within the cubane core of **2** have significantly changed with respect to those in **1-OAc**. Notably, the metal–μ^4-O bond distances significantly elongate upon coordination of the dangler; the average Co(III)–μ^4-O and Mn–μ^4-O bond lengths are lengthened by 0.045(8) Å and 0.025(7) Å, respectively. However, the other cubane metal–O(oxo) bond lengths have contracted such that the *total* average bond distance is only 0.007(2) Å longer than that of the parent cubane, **1-OAc**. These bond metrics suggest that the oxo-cubane moiety is somewhat flexible.

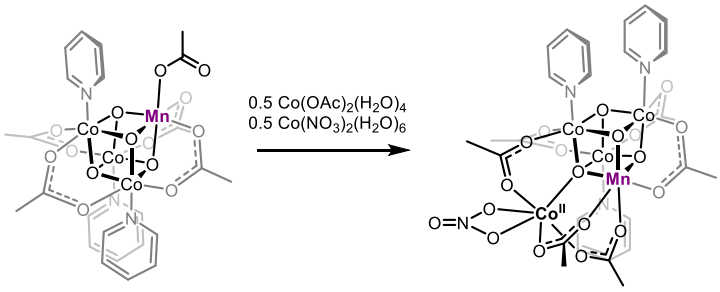

(1)

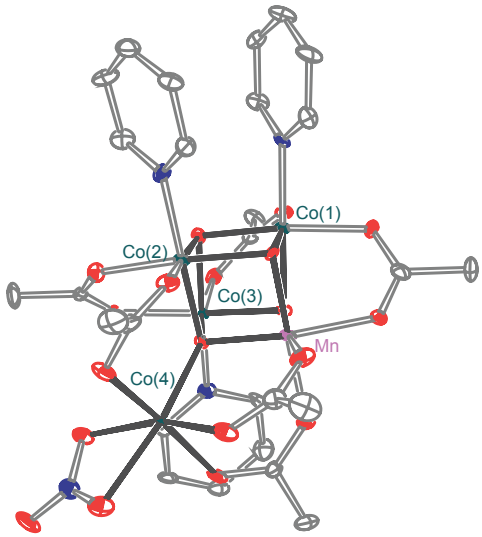

Figure 2. The single-crystal XRD structure of **2** (30% thermal ellipsoid probability) with hydrogen atoms and solvent removed for clarity.

5.3 Redox Chemistry

Complex **1-OAc** exhibits a quasi-reversible redox couple in the cyclic voltammogram (CV) at $E_{1/2} \approx 1.15$ V (all potentials are referenced against Fc/Fc^{+}) and a second reversible redox event at $E_{1/2} \approx 1.49$ V. With increasing scan rates ($v > 0.10$ V/s), the anodic and cathodic peak current of the 1.15 V couple grows to about twice those associated with the 1.49 V couple. The plot of normalized current versus potential clearly demonstrates that the 1.15 V redox couple becomes more reversible (i_a/i_p approaches unity) at faster scan rates, while the 1.49 V redox couple diminishes in current (Figure 3A and 3B). This suggests that the electrochemical event at 1.15 V is followed by a chemical reaction, to produce a daughter species with a redox couple at 1.49 V (ECE mechanism). The first electrochemical event is assigned as a one-electron couple for $[MnCo_3O_4]^{5+}/[MnCo_3O_4]^{6+}$. The derivatives **1-Cl**, **1-NO$_3$**, and **[1-py]$^+$** exhibit only one redox event at a potential similar to that of the first redox event for **1-OAc**, but are more positively shifted. The ranking of clusters with respect to redox potential (lowest to highest) is: **1-OAc** (1.15 V) > **1-Cl** (1.18 V) > **1-NO$_3$** (~1.2 V) > **[1-py]$^+$** (1.48 V) (Figure 3A). This ranking correlates with the magnitude of the electrostatic interaction between the μ^1 ligand and Mn: the more basic ligand better stabilizes the oxidized cluster. The reversibility of the redox couple for **1-NO$_3$** is noteworthy, in that it is completely

irreversible at $v \leq 100$ mV/s but becomes almost fully reversible at $v = 4000$ mV/s (Figure 3A and 3C). This indicates an irreversible chemical transformation following electrochemical oxidation to **[1-NO$_3$]$^+$**. Presumably, at faster scan rates the back reduction to **1-NO$_3$** occurs before chemical decomposition (by an EC mechanism) can take place. Though the identity of this decomposition product is not yet known, a possible decomposition route involves loss of $NO_2^{\bullet}$ *via* homolytic cleavage of the N–O bond of the nitrato ligand, with concurrent one-electron reduction of the cluster. The nature of the oxidized cubane complexes, and specifically the location of the electron hole, is discussed in the following section.

The Co(II)-dangler complex **2** exhibits an interesting voltammogram possessing four quasireversible redox events between 1.0 and 2.0 V (Figure 3A). The general shapes of these peaks do not vary with scan rate. The four events are better distinguished by differential pulsed voltammetry (DPV) as four peaks at 1.04 V, 1.12 V, 1.48 V, and 1.72 V (Figure 3D). Scanning in the reverse direction by DPV produces an approximate mirror image of the forward voltammogram. The results of the CV and DPV experiments suggest that these redox events are electron transfers associated with with some structural reorganization of the dangler group during each event. Compared to the parent cubane **1-OAc**, the addition of the Co(II)-dangler in compound **2** increases the number of accessible redox states from two to four; this ability of a dangler to expand the redox capacity of a system could provide insight into the mechanism of the oxygen-evolving center (OEC) in photosystem II. Whereas the [Mn_4CaO_5] dangler core of the OEC is able to undergo four redox events,[21,22] synthetic [Mn_3CaO_4] models of the OEC lacking a dangler ion exhibit only a single redox event.[12,16]

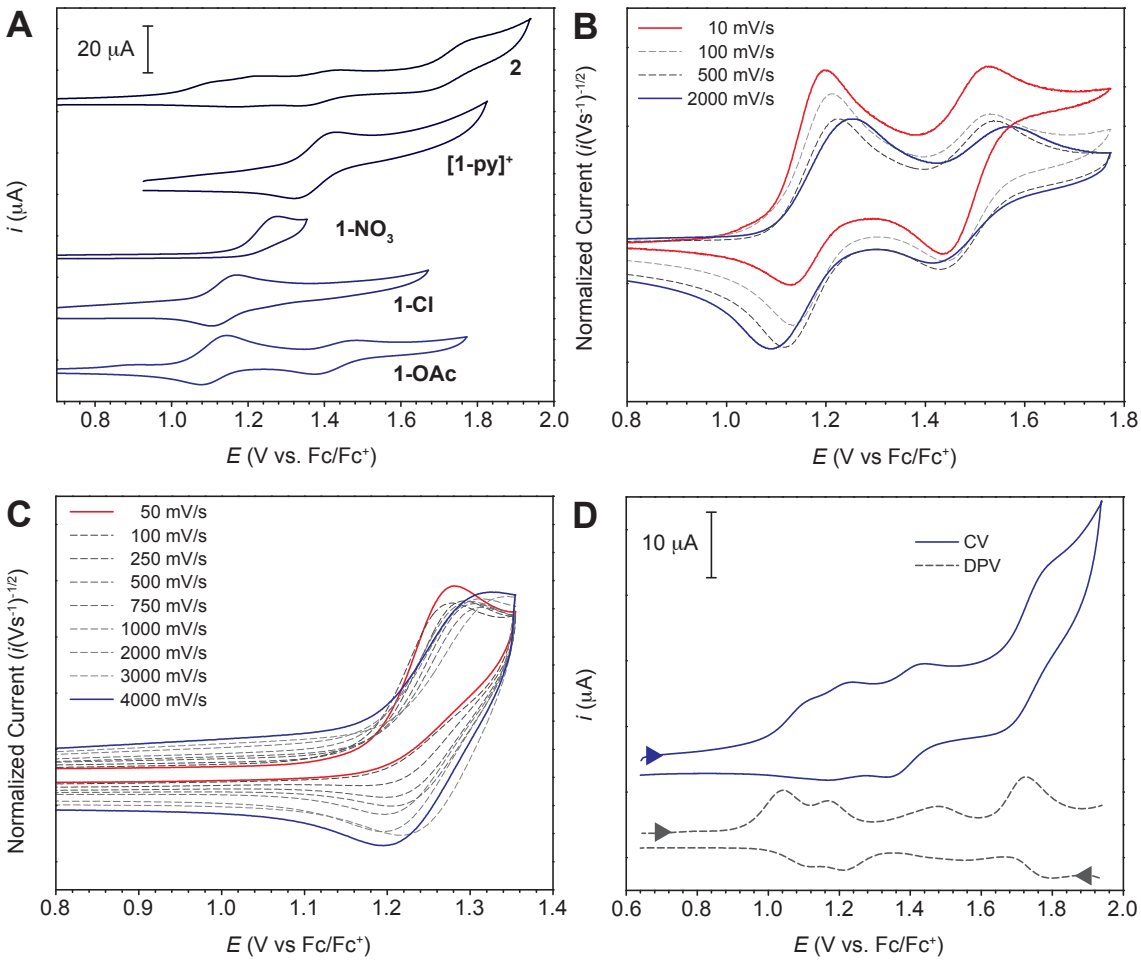

Figure 3. Electrochemical data. (A) Cyclic voltammograms of cubane and dangler complexes (υ = 100 mV/s, 0.1 M $^{n}Bu_4NPF_6$ supporting electrolyte in MeCN (except for **1-NO$_3$** is in DCM)). (B) Scan rate dependence of 1-OAc. (C) Scan rate dependence of **1-NO$_3$**. (D) Detailed view of the CV and DPV for the dangler (**2**).

In comparison to $Co_4O_4(OAc)_4py_4$, the $[MnCo_3O_4]$ cubanes all require higher applied potentials to become oxidized. This effect can be ascribed to the difficulty in removing an electron from the more positively charged $[MnCo_3O_4]^{5+}$ (versus the $[Co_4O_4]^{4+}$) core. This difference is dramatically illustrated by comparison of the isostructural $[MnCo_3O_4(OAc)_4py_4]^+$ (**[1-py]$^+$**) and $Co_4O_4(OAc)_4py_4$ clusters, which shows that **[1-py]$^+$** requires a 1.2 V higher potential for oxidation. Agapie and coworkers have quantified this effect on a series of $[MMn_3O_4]$ (M = metal) clusters, relating the redox potential of the overall cluster with the Brønsted acidity of the hydrated M^{n+} ion.[16] A similar effect appears to be operative in the $[MCo_3O_4]$ series. Additionally, it is observed that the ligand bound to Mn(IV) has a strong influence on the redox properties of the core. A redox range of nearly 300 mV is spanned by simple modulation of the electron-donating properties of the ligand bound to Mn(IV).

5.4 Spectroscopy

The valences of the Mn and Co ions in the cubane complexes appear to be localized on their respective ions (Robin-Day class I) as indicated by the absence of an intervalence charge-transfer (IVCT) band in the near-infrared (NIR) spectrum (900-1600 nm) (Figure S1). Even the dangler complex, **2**, lacks bands in the NIR, suggesting that even the dangler Co(II) ion lacks strong electronic coupling with the $MnCo_3O4$ cubane.

Multifrequency EPR spectroscopic experiments were performed in order to obtain further insight into the electronic structures of cubane complexes **1-OAc**, **1-Cl**, **1-NO_3**, **[1-py]PF_6,** and the dangler complex, **2.** In general, EPR spectra of Kramers spin systems with $S > {}^1/_2$ are strongly influenced by the relative magnitudes of the zero-field splitting (ZFS), D, and the microwave frequency, $h\nu$, that corresponds to the electron Zeeman splitting. Spectra recorded under a weak-field regime (where $D >> h\nu$) display features whose positions are determined primarily by the ratio of the zero-field splitting parameters E/D. Spectra recorded under an intermediate-field regime (where $D \approx h\nu$) can be exceedingly complicated with the spectral features highly sensitive to small changes in E and/or D. At X-band (9.4 GHz), the EPR spectra of complexes **1-OAc**, **1-Cl**, **1-NO_3**, **[1-py]PF_6,** and **2** display features whose field positions are consistent with $S = {}^3/_2$ spin systems recorded under the weak-to-intermediate-field regime (Figure 4). For example, the broad positive features centered around 130 mT ($g_{eff} \approx 5$) that are present in each of the spectra arise from the low-field components of the $m_S = \pm {}^1/_2$ and $m_S = \pm {}^3/_2$ transitions that are characteristic of $S = {}^3/_2$ spin systems. The spectra are broadened due to a distribution in E and D (presumably due to small differences in molecular structure upon in the frozen solution) and by unresolved hyperfine coupling to ^{55}Mn, ^{59}Co, and other nuclei. Thus, although the X-band CW EPR spectroscopic data establish an $S = {}^3/_2$ spin system for each complex, the values of E and D and the spin distribution are obscured by the broadness and complexity of the spectra.

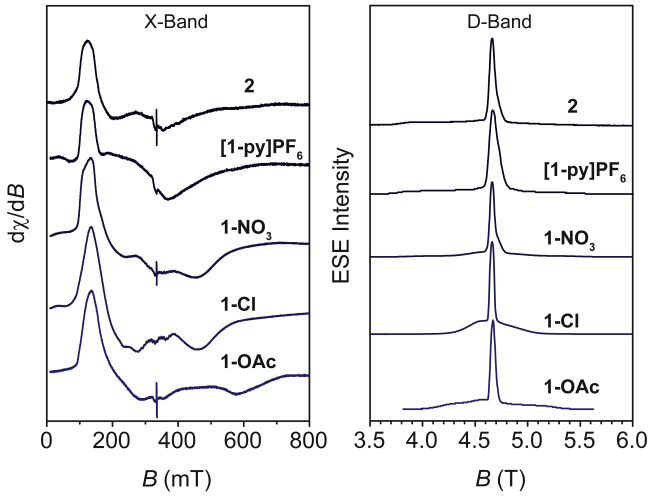

Figure 4. Solution-state EPR spectra for clusters in 1:1 DCM:toluene. (Left panel) X-band (9.38 GHz) at 6K. (Right panel) D-band (130 GHz) at 7K (except 5K for **1-OAc**).

Table 1. Mn-ZFS parameters determined by EPR spectroscopy

Cluster	D (cm^{-1})	E/D
1-OAc	0.29	0.22
1-Cl	0.18	0.14
1-NO_3	0.40	0.27
[1-py]PF_6	0.44	0.32
2	0.43	0.31

In order to gain further insight into the zero-field splitting parameters, we recorded the EPR spectra of complexes **1-OAc**, **1-Cl**, **1-NO_3**, **[1-py]PF_6**, and **2** at D-band (130 GHz) using a Hahn-echo detection sequence ($\pi/2$–τ–π) (Figure 4). At this higher frequency, $D << h\nu$ which results in a sharp, central-field transition corresponding to the $m_S = -1/2$ to $+1/2$ transition, as well as broader transitions corresponding to the $m_S = -3/2$ to $-1/2$ and $m_S = +1/2$ to $+3/2$ transitions. The breadth of the latter transitions corresponds to D, and their shapes are sensitive to E/D. Thus, analysis of the D-band spectra gives more precise values for D and E than analysis of the relatively complex X-band spectra. The values obtained by spectral simulation show that both D and E are sensitive to ligand substitution at the Mn center, and the magnitude of the D values is consistent with those observed for other Mn(IV) complexes (Table 1).[23] Thus, the ZFS parameters corroborate the X-ray spectroscopic data in the $Mn(IV)Co(III)_3$ valence assignments for the heterometallic cubanes complexes **1-OAc**, **1-Cl**, **1-NO_3**, **[1-py]PF_6**, and **2**. However, these data alone cannot rule out the possibility of other electronic structures (e.g. $Mn(III)Co(III)_2Co(IV)$) that give rise to ZFS parameters that are coincidentally similar to those known for mononuclear Mn(IV).[24]

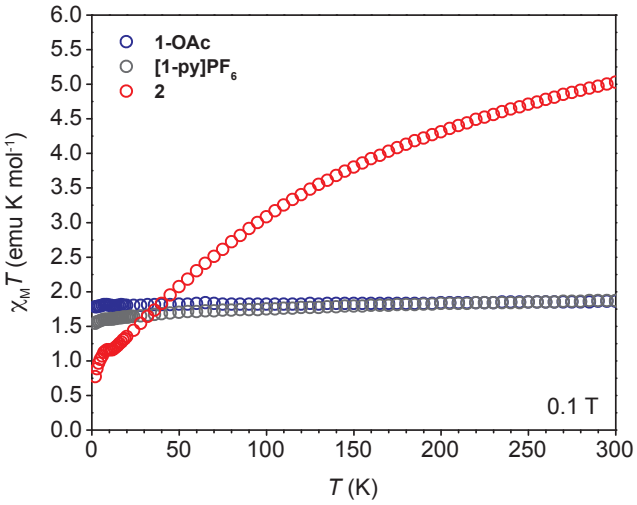

Figure 5. Solid-state magnetic susceptibility data for **1-OAc**, **[1-py]PF_6**, and **2**.

5.5 Magnetism

Dc magnetic susceptibility measurements were performed under an applied magnetic field of 0.1 T for compounds **1-OAc**, **[1-py]PF_6**, and **2** (Figure 5). Both **1-OAc**

and **[1-py]PF$_6$** show room temperature $\chi_M T$ products consistent with the value expected for the isotropic S = 3/2 spin associated with Mn(IV). These values are 1.86 emu·K/mol and 1.87 emu·K/mol for **1-OAc** and **[1-py]PF$_6$**, respectively, compared to the expected value of 1.876 emu·K/mol. Next, variable temperature magnetization data were collected at applied magnetic fields of 1, 2, 3, 4, 5, 6, and 7 T and temperatures from 2 – 15 K in order to investigate the magnetic anisotropy in these systems. Slight non-superimposibility of the isofield lines when plotted vs. H/T indicated **1-OAc** and **[1-py]PF$_6$** display some magnetic anisotropy, presumably determined by the coordination environment of the Mn(IV) in each system. Molecules containing Mn(IV) have been shown to exhibit very small axial anisotropy (D) values before.[23] The M vs. H/T data were fit to the Hamiltonian $\hat{H} = D\hat{S}_z^2 + E(\hat{S}_x^2 + \hat{S}_y^2) + \mu_B g\hat{S}\hat{H}$ using the program PHI.[25] Values of D = 0.84 cm^{-1} and E = 0.008 cm^{-1} with $g_x = g_y = 1.97$ and $g_z = 1.94$ were extracted for **1-OAc**, in good agreement with EPR data, especially given that SQUID magnetometry was performed in the solid state, while EPR data was obtained with the samples in comparatively dilute frozen solutions. In contrast to **1-OAc**, the M vs. H/T data for **[1-py]PF$_6$** could not be fit with reasonable values of D and E for an Mn(IV) ion, possibly due to intermolecular magnetic couplings of a similar order of magnitude compared to the zero-field splitting. Since EPR was performed in solution for **[1-py]PF$_6$**, it provides the a better estimate of D and E for **[1-py]PF$_6$**.

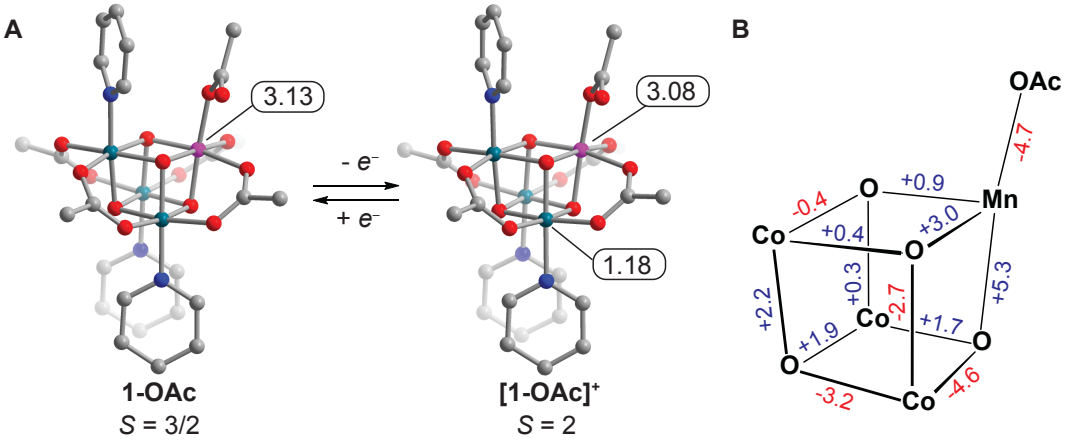

Figure 6. (A) Unpaired spin densities for **1-OAc** and **[1-OAc]**$^+$ from DFT calculations. (B) Cubane bond distance differences (pm) upon oxidation to **[1-OAc]**$^+$.

Compound **2** shows much more complex magnetic behavior than that of **1-OAc** or **[1-py]PF_6**. The $\chi_M T$ product at 300 K and 0.1 T is 5.03 emu·K/mol, a reasonable value for an uncoupled S =3/2 Mn(IV) spin combined with a S = 3/2 Co(II) spin with substantial magnetic anisotropy, a common circumstance for octahedral high-spin Co(II).[26] The $\chi_M T$ product then decreases with decreasing temperature to reach a value of 0.77 emu·K/mol at 2 K. Fitting of this data with a Hamiltonian that reflects (1) the zero-field splitting parameters D and E for the high-spin Co(II) ion and (2) additionally includes a coupling parameter between the Mn(IV) and Co(II) spins is in progress.

5.6 Computational Results

Density functional theory (DFT) calculations corroborated the localization of valence within the clusters. Mulliken spin densities for the DFT-optimized structure of **1-OAc** demonstrated three unpaired spins residing mainly on the Mn ion, and thus indicates a Mn(IV) assignment (Figure 6A). No significant spin density was found on the Co ions, consistent with the expected t_{2g}^6 configuration for Co(III).

Unfortunately, the dangler complex, **2**, resisted characterization by DFT. For unknown reasons, the dangler did not converge in any of the possible spin-states.

The oxidized cubane, **[1-OAc]$^+$**, was also subjected to DFT calculations, in order to address the question of whether the electron is lost from Mn(IV) or the Co(III) during oxidation. The calculations first determined a quintet spin state (S = 2) as the most correct (low spin contamination). From the Mulliken analysis, one of the Co(III) is oxidized to a Co(IV) center. Again, DFT suggests a ground state with localized Mn(IV) and Co(IV) valencies (Figure 6A). Significant bond length changes also occur upon oxidation (Figure 6B). For **[1-OAc]$^+$**, there is a marked contraction of the Mn–OAc bond even though the oxidation state of Mn does not change upon oxidation of the cluster. Simultaneously, the three Co(IVμ)–μ^3-O contract significantly, while the other Co(III)–μ^3-O bonds elongate to compensate. Thus, the oxidation at a distal cobalt ion propagates structural changes throughout the entire cluster, yet, notably, the nature of the ligand at Mn(IV) modulates the redox potential of the distal Co ion (*vide supra*). These results demonstrate a cooperative communication between the Mn and Co ions within the cluster that affects reactivity.

5.7 Conclusions

A heterometallic oxo-cubane with Mn and Co ions has been rationally synthesized by a one-step method, supported only by simple carboxylate and pyridine ligands. This synthesis demonstrates that complex heterometallic clusters can be made in a designed manner and without tailored ligands. The $MnCo_3O_4(OAc)_5py_3$ cubane, **1-OAc**, is the first example of a Mn-Co oxo-cubane. Derivatives of this cubane were accessed by post-synthetic treatment of **1-OAc** with different reagents, producing homologous with Cl^-, NO_3^-, and OTs^- functionalities. A cationic $[MnCo_3O_4(OAc)_4py_4]^+$ derivative was also made, and this complex is isostructural to the well-studied cobalt cubane OER catalyst, $Co_4O_4(OAc)_4py_4$. Comparison of these related complexes may give insight on the different properties of heterogeneous CoO_x and Mn-doped-CoO_x OER

catalysts. Moreover, the [$MnCo_3O_4$] clusters are water-stable, and most are also water-soluble, which will allow studies of chemistries in OER relevant conditions in the future.

Remarkably, the $MnCo_3O_4$ cubane incorporated a fifth metal, a Co(II) ion, generating a so-called dangler complex. Dangler complexes are exceedingly rare, and there is only one other structurally characterized example containing a 3*d*-transition metal, which had been synthesized by self-assembly.[8] In our case, the dangler was added in an intentional, rational manner. We demonstrate, by electrochemistry, that the presence of the Co(II) dangler ion increases the accessible redox states for the clusters from two to four. Though the exact reason for this increase in redox states is so far unclear, future examination of this may shed light on the role(s) of the OEC's dangler in photosystem II.

Spectroscopy, magnetometry, and computation methods described the electronic properties of the cubane and dangler clusters. While DFT proved useful in probing the cubane structures, calculations on the more complex dangler cluster was unsuccessful. In spite of this, the combination of multifrequency EPR and SQUID magnetometry succeeded in elucidating the electronic structure of these systems.

Interestingly, DFT suggests oxidation of the cubanes occurs from a Co(III) site rather than the Mn(IV) site, yet the structural consequences of the oxidation are felt throughout the cluster. While most of the non-redox chemistry, so far demonstrated, occurs at the Mn site, the redox chemistry occurs in the remaining [Co_3O_4] subcluster. Thus, the [Co_3O_4] moiety is conceptually a redox-active ligand for the Mn. Meanwhile, the ligand on Mn modulates the redox potentials of the distal Co, thus demonstrating cooperativity between Mn and Co. Such cooperativity may be operative in Mn-doped-CoO_x, as well: the Mn-sites are better suited to generate terminal-oxo moieties necessary for O–O bond formation,[27,28] while the Co-sites help store electron-hole equivalents. This modulation of reactivity by distal redox changes was also recently observed in an molecular [Fe_4O] cluster by Agapie and coworkers,[29] and could be a more general phenomenon in cluster chemistry.

5.8 Acknowledgements

We would like to thank the NIH Shared Instrumentation Grant S10-RR027172. This work was supported by the Director, Office of Science, Office of Basic Energy Sciences of the US Department of Energy under contract No. DE-AC02-05CH11231.

5.9 References

(1) Burke, M. S.; Kast, M. G.; Trotochaud, L.; Smith, A. M.; Boettcher, S. W. *J. Am. Chem. Soc.* **2015**, *137* (10), 3638.
(2) Trotochaud, L.; Young, S. L.; Ranney, J. K.; Boettcher, S. W. *J. Am. Chem. Soc.* **2014**, *136* (18), 6744.
(3) Song, F.; Hu, X. *J. Am. Chem. Soc.* **2014**, *136* (47), 16481.
(4) Li, D.; Baydoun, H.; Verani, C. N.; Brock, S. L. *J. Am. Chem. Soc.* **2016**.
(5) Umena, Y.; Kawakami, K.; Shen, J.-R.; Kamiya, N. *Nature* **2011**, *473* (7345), 55.
(6) Lis, T. *Acta Crystallogr. B* **1980**, *36* (9), 2042.

(7) Long, D.-L.; Burkholder, E.; Cronin, L. *Chem. Soc. Rev.* **2006**, *36* (1), 105.
(8) Zhang, C.; Chen, C.; Dong, H.; Shen, J.-R.; Dau, H.; Zhao, J. *Science* **2015**, *348* (6235), 690.
(9) Mukherjee, S.; Stull, J. A.; Yano, J.; Stamatatos, T. C.; Pringouri, K.; Stich, T. A.; Abboud, K. A.; Britt, R. D.; Yachandra, V. K.; Christou, G. *Proc. Natl. Acad. Sci.* **2012**, *109* (7), 2257.
(10) Beattie, J. K.; Hambley, T. W.; Klepetko, J. A.; Masters, A. F.; Turner, P. *Polyhedron* **1998**, *17* (8), 1343.
(11) Chakrabarty, R.; Bora, S. J.; Das, B. K. *Inorg. Chem.* **2007**, *46* (22), 9450.
(12) Kanady, J. S.; Tsui, E. Y.; Day, M. W.; Agapie, T. *Science* **2011**, *333* (6043), 733.
(13) Kanady, J. S.; Mendoza-Cortes, J. L.; Tsui, E. Y.; Nielsen, R. J.; Goddard, W. A.; Agapie, T. *J. Am. Chem. Soc.* **2013**, *135* (3), 1073.
(14) Kanady, J. S.; Tran, R.; Stull, J. A.; Lu, L.; Stich, T. A.; Day, M. W.; Yano, J.; Britt, R. D.; Agapie, T. *Chem. Sci.* **2013**, *4* (10), 3986.
(15) Shinagawa, T.; Garcia-Esparza, A. T.; Takanabe, K. *Sci. Rep.* **2015**, *5*, 13801.
(16) Tsui, E. Y.; Agapie, T. *Proc. Natl. Acad. Sci.* **2013**, *110* (25), 10084.
(17) Tsui, E. Y.; Day, M. W.; Agapie, T. *Angew. Chem. Int. Ed.* **2011**, *50* (7), 1668.
(18) Nguyen, A. I.; Ziegler, M. S.; Oña-Burgos, P.; Sturzbecher-Hohne, M.; Kim, W.; Bellone, D. E.; Tilley, T. D. *J. Am. Chem. Soc.* **2015**, *137* (40), 12865.
(19) Ullman, A. M.; Liu, Y.; Huynh, M.; Bediako, D. K.; Wang, H.; Anderson, B. L.; Powers, D. C.; Breen, J. J.; Abruña, H. D.; Nocera, D. G. *J. Am. Chem. Soc.* **2014**, *136* (50), 17681.
(20) McAlpin, J. G.; Stich, T. A.; Ohlin, C. A.; Surendranath, Y.; Nocera, D. G.; Casey, W. H.; Britt, R. D. *J. Am. Chem. Soc.* **2011**, *133* (39), 15444.
(21) Cox, N.; Retegan, M.; Neese, F.; Pantazis, D. A.; Boussac, A.; Lubitz, W. *Science* **2014**, *345* (6198), 804.
(22) Krewald, V.; Retegan, M.; Cox, N.; Messinger, J.; Lubitz, W.; DeBeer, S.; Neese, F.; Pantazis, D. A. *Chem. Sci.* **2015**, *6* (3), 1676.
(23) Zlatar, M.; Gruden, M.; Vassilyeva, O. Y.; Buvaylo, E. A.; Ponomarev, A. N.; Zvyagin, S. A.; Wosnitza, J.; Krzystek, J.; Garcia-Fernandez, P.; Duboc, C. *Inorg. Chem.* **2016**, *55* (3), 1192.
(24) Horitani, M.; Yashiro, H.; Hagiwara, M.; Hori, H. *J. Inorg. Biochem.* **2008**, *102* (4), 781.
(25) Chilton, N. F.; Anderson, R. P.; Turner, L. D.; Soncini, A.; Murray, K. S. *J. Comput. Chem.* **2013**, *34* (13), 1164.
(26) Barefield, E. K.; Busch, D. H.; Nelson, S. M. *Q. Rev. Chem. Soc.* **1968**, *22* (4), 457.
(27) Gao, Y.; Åkermark, T.; Liu, J.; Sun, L.; Åkermark, B. *J. Am. Chem. Soc.* **2009**, *131* (25), 8726.
(28) Betley, T. A.; Wu, Q.; Van Voorhis, T.; Nocera, D. G. *Inorg. Chem.* **2008**, *47* (6), 1849.
(29) de Ruiter, G.; Thompson, N. B.; Lionetti, D.; Agapie, T. *J. Am. Chem. Soc.* **2015**, *137* (44), 14094.

Supporting Information for **Chapter 5**

General considerations. Cobalt(II) acetate tetrahydrate, cobalt(II) nitrate hexahydrate, pyridine, and 4-toluene sulfonic acid monohydrate, were purchased from Sigma-Aldrich and used without further purification. Potassium permanganate was purchased from EMD. Solvents were purchased from Fisher-Scientific and used without any further purification. Routine NMR spectra were recorded on Bruker AVB-400, AVQ-400 and AV-300 spectrometers at room temperature. d_3-MeCN, CD_2Cl_2 and D_2O were purchased from Cambridge Isotopes. ^{1}H NMR spectra were referenced to residual protio-solvent peaks (δ 5.32 for CD_2Cl_2, δ 2.94 for CD_3CN, δ 4.79 for D_2O). Electrospray ionization mass spectrometry measurements were performed at the QB3 Mass Spectrometry Facility at UC Berkeley using a quadrupole time-of-flight mass spectrometer (Q-TOF Premier, Waters, Milford, MA) that was equipped with an electrospray ionization (ESI) source. ESI source voltages were adjusted for optimum desolvation and transmission of ions of interest prior to recording mass spectra. Elemental analyses were carried out by the College of Chemistry Microanalytical Laboratory at the University of California, Berkeley. Cyclic voltammograms were obtained on a BASi Epsilon potentiostat at 25˚C, in acetonitrile or dichloromethane with 0.10 M tetra-*n*-butylammonium hexafluorphosphate electrolyte, platinum wire counter electrode, glassy carbon working electrode (7 mm diameter, polished with 0.05 μm alumina), floating silver reference, and ferrocene was added as an internal reference.

$MnCo_3O_4(OAc)_5py_3$, (1-OAc). Cobalt(II) acetate tetrahydrate (10.00 g, 40 mmol) and pyridine (3.3 mL, 40 mmol) were dissolved in 200 mL of MeOH. With rapid stirring, potassium permanganate (2.11 g, 13.3 mmol) was introduced, and the dark-brown reaction mixture was stirred at room temperature for 16 hours. The reaction mixture was then refluxed for an additional 4 hours, followed by removal of solvent by rotary evaporation. The black residue was partitioned between 50 mL dichloromethane (DCM) and 50 mL water. The DCM layer was collected, and the water layer was extracted with additional DCM 4 x 50 mL. The consolidated DCM extractions were dried with $MgSO_4$, and then poured onto a silica plug in a 350 mL coarse-fritted filter funnel. The plug was washed with 2% MeOH-acetone solution until the liquid ran clear, and then discarded. Product **1-OAc** was then eluted using *ca.* 1.5 L of 10% MeOH-acetone. Thin-layer chromatography of the eluted fraction showed one spot (R_f = 0.2, 1:9 MeOH:acetone). The fraction was dried by rotary evaporation to yield 5.70 g (52 % based on cobalt acetate). Additionally, the product can be recrystallized by layer-diffusion of hexanes into a DCM solution of **1-OAc** to yield **1-OAc•DCM** as black blocks. ^{1}H NMR (600 MHz, CD_2Cl_2): 10.7 (br), 9.46 (br), 8.34 (br), 8.13 (br), 7.82 (br), 3.82 (br). Anal. Calcd for $C_{25}H_{30}Co_3MnN_3O_{14}$•$CH_2Cl_2$: C, 34.20; H, 3.53; N, 4.60. Found: C, 34.00; H, 3.75; N, 4.68. HR-ESI MS: m/z = 850.90, $[MnCo_3O_4(OAc)_5py_3Na]^+$.

$MnCo_3O_4(OAc)_4py_3Cl$, (1-Cl). Compound **1-OAc•DCM** (1.64 g, 1.79 mmol) was dissolved in 20 mL of DCM. Oxalyl chloride (150 μL, 1.75 mmol) was added to the

stirred solution of **1-OAc**. After 1 h, the solution was dried *in vacuo* to give of a black crystalline solid. Single crystals were obtained by recrystallization *via* layer diffusion of hexanes into a DCM solution to give 1.60 g of **1-Cl•2DCM** (91% based on **1-OAc**). R_f = 0.8 (acetone). Anal. Calcd for $C_{23}H_{27}ClCo_3MnN_3O_{12}$•1.4$CH_2Cl_2$: C, 31.73; H, 3.25; N, 4.55. Found: C, 31.45; H, 3.60; N, 4.75.

$MnCo_3O_4(OAc)_4py_3NO_3$, (1-NO_3). Compound **1-Cl•2DCM** (0.100 g, 0.1 mmol) and silver nitrate (0.021 g, 0.12 mmol) were stirred in 10 mL of acetone for 16 h. The solution was dried *in vacuo* and then extracted with 2 mL DCM. The extract was layered with hexanes to yield a crude solid overnight. The solid was washed three times with 3 mL of acetonitrile to leave behind 0.037 g of **1-NO_3** (37 % based on **1-Cl**). Single crystals were grown from layer-diffusion of hexanes into a solution of **1-NO_3** in DCM. R_f = 0.8 (acetone). Anal. Calcd for $C_{23}H_{27}Co_3MnN_4O_{15}$•$CH_2Cl_2$: C, 31.46; H, 3.19; N, 6.12. Found: C, 31.27; H, 3.63; N, 6.12. . HR-ESI MS: *m*/*z* = 831.89, $[MnCo_3O_4(OAc)_4py_3NO_3Na]^+$.

$MnCo_3O_4(OAc)_4py_3$(*p*-$CH_3C_6H_5SO_3$), (1-OTs). *p*-Toluenesulfonic acid monohydrate (0.024 g, 0.12 mmol) was added to **1-OAc** (0.100 g, 0.12 mmol) in 5 mL of dichloromethane. After 16 h, TLC showed complete conversion to product. The solution was filtered and the volatile material was removed *in vacuo*. The resulting solid was dried under vacuum at 60°C for 16 h to give 0.113 g of a black solid (100% based on **1-OAc**). Single crystals suitable for X-ray diffraction were grown from vapor-diffusion of diethyl ether into an acetonitrile solution. R_f = 0.8 (1:9 MeOH:acetone). Anal. Calcd for $C_{30}H_{34}Co_3MnN_3O_{15}S$•0.25$CH_2Cl_2$: C, 37.78; H, 3.62; N, 4.37. Found: C, 37.60; H, 3.82; N, 4.32.

$[MnCo_3O_4(OAc)_4py_4]PF_6$, ([1-py]$PF_6$). In 10 mL of water was dissolved **1-OAc** (0.250 g, 0.30 mmol), pyridine (0.477 g, 6.0 mmol), and ammonium hexafluorophosphate (0.049 g, 0.30 mol). The solution was heated at 70°C for 16 h. Black plates of the crystalline solid formed from the solution. The solid was collected by filtration and washed with 3 x 10 mL of water, then recrystallized by layer diffusion of hexanes into a DCM solution to yield **[1-py]PF_6•2DCM** (0.163 g, 43% based on **1-OAc**). R_f = 0 (acetone). Anal. Calcd for $C_{28}H_{32}Co_3F_6MnN_4O_{12}P$•0.7$CH_2Cl_2$: C, 32.74; H, 3.20; N, 5.32. Found: C, 32.65; H, 3.14; N, 5.44. HR-ESI MS: *m*/*z* = 847.93, $[MnCo_3O_4(OAc)_4py_4]^+$.

$MnCo_4O_4(OAc)_6py_3NO_3$, (2). In 10 mL of methanol was dissolved cobalt acetate tetrahydrate (0.030 g, 0.12 mmol) and cobalt nitrate hexahydrate (0.035 g, 0.12 mmol). This solution was added to **1-OAc** (0.200 g, 0.24 mmol) and the resulting mixture was stirred for 16 h. The solvent was evaporated *in vacuo*, and the resulting solid was extracted into 5 mL of DCM. Hexanes (*ca.* 10 mL) was layered on top of the DCM solution. After 24 h, black plates crystallized from the solution (0.180 g, 74 % based on

1-OAc). R_f = 0.2 (1:9 MeOH:acetone). ^{1}H NMR (500 MHz, CD_3CN): 66.25 (s, 3H), 42.87 (s, 3H), 10.22 (s, 1H), 9.58 (s, 1H), 9.06 (s, 1H), 8.80 (s, 1H), 8.48 (s, 4H), 7.81 (s, 3H), 3.90 (s, 3H), 2.61 (s, 3H), 1.77 (s, 2H), 1.56 (s, 2H), -1.38 (s, 3H), -3.04 (s, 3H). Anal. Calcd for $C_{27}H_{33}Co_4MnN_4O_{19}$•0.2$CH_2Cl_2$: C, 31.87; H, 3.28; N, 5.46. Found: C, 31.61; H, 3.54; N, 5.45. HR-ESI MS: *m*/*z* = 945.86, $[MnCo_4O_4(OAc)_6py_3]^+$; 948.84, $[MnCo_4O_4(OAc)_5py_3NO_3]^+$.

UV-vis-NIR spectroscopy.
Samples were dissolved in MeCN to make a 0.1 mM solution. Spectra were recorded in a 1 cm quartz cell from 200-1600 nm.

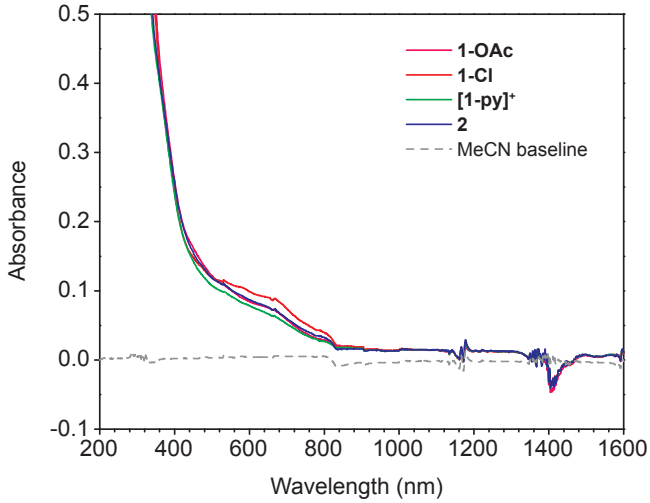

Figure S1. UV-vis-NIR spectra of cluster complexes (0.1 mM) in MeCN at room temperature.

Magnetometry.
Samples were prepared by adding crystalline powder of **1-OAc**, **[1-py]PF_6**, and **2** (35 mg, 67 mg, and 26.1 mg for **1-OAc**, **[1-py]PF_6**, and **2**, respectively) to Quantum Design polycarbonate capsules. In the cases of **1-OAc**, solid eicosane was added to cover the samples to prevent crystallite torqueing and provide good thermal contact between the sample and the cryostat. The solid eicosane was then melted over the sample. Melting of eicosane over **1-py]PF_6 and 2** provoked some solvent evaporation from the sample, preventing determination of an accurate sample mass and possibly causing some sample decomposition. Thus, powdered **1-py]PF_6 and 2** were instead restrained with a plug of glass wool. Sample capsules were then mounted inside standard Quantum Design straws. Magnetic susceptibility measurements were performed using a Quantum Design MPMS2 SQUID magnetometer. Dc magnetic susceptibility measurements were collected in the temperature range 2-300 K under applied magnetic fields of 0.1 T, 0.5 T, and 1 T. Diamagnetic corrections were applied to the data using Pascal's constants to give χ_D = −0.0004573 emu/mol (**1-OAc**), χ_D = −0.00050216 emu/mol (**[1-py]PF_6**), χ_D = −0.000454 emu/mol (**2**), and χ_D = −0.00024306 emu/mol (eicosane). *M* vs. *H*/*T* data was fit using the program PHI using the simplex method.